APPLICATION OF SEISMIC SURFACE-WAVES IN CONCRETE BRIDGE-DECK EVALUATION

by

FARHAD FETRAT

A Dissertation submitted to the

Graduate School-New Brunswick

Rutgers, The State University of New Jersey

in partial fulfillment of the requirements

for the degree of

Doctor of Philosophy

Graduate Program in Civil and Environmental Engineering

written under the direction of

Dr. Nenad Gucunski

and approved by

_____

_____

_____

_____

New Brunswick, New Jersey

January 2016

ABSTRACT OF THE DISSERTATION

APPLICATION OF SEISMIC SURFACE-WAVES IN CONCRETE BRIDGE-DECK EVALUATION

By FARHAD FETRAT

Dissertation Director:

Dr. Nenad Gucunski

Accurate and timely condition assessment of bridge decks is essential for economic management of aging highway bridges. The ability to evaluate concrete modulus profile in a bridge deck can help the detection of early signs of deterioration and optimize the bridge maintenance procedures. This study presents a new method for modulus profiling of concrete bridge decks. The stiffness matrix method is used to simulate wave propagation in a layered media. The results are compared to numerical finite element models. Dispersion analysis is done using the multi-channel analysis of surface waves

(MASW) and phase-shift methods. The characteristics of dispersion surface are analyzed and the effects of model parameters on dispersion surface are examined through a series of parametric studies. An inversion technique is proposed for a fast inversion of surface-wave data collected on bridge decks. This technique utilizes a database of pre-calculated dispersion surfaces and takes advantage of the observed patterns in the parametric study as a priori information for the inversion process.

Dedication

To My Father and Mother

Acknowledgement

The author wishes to express his deep gratitude to all his teachers for their guidance and consultation and to his colleagues and friends for their friendship. Special thanks are addressed to the following for their invaluable assistance in the completion of this work:

- To Professor Nenad Gucunski, his advisor, for his invaluable and continuous support, help and guidance throughout the graduate program;
- To Professor Ali Maher, for his support during the program and this research.
- To CAIT (Center for Advanced Infrastructure and Transportation) for the Research Assistant appointments during the five years of graduate study.
- To John Hencken and Ken Lee for their help in construction of the test specimens.
- To Seong-Hoon Kee for his help with the numerical analysis work.
- And finally to his colleague, Hooman Parvardeh, for his help and support during different phases of the research and for his friendship.

Table of Contents

Table of Figures

Table of Tables

1 Introduction

1.1 Problem Statement

The key problem that this research will address is that of completing a rapid and accurate modulus profiling method for concrete bridge decks. Specifically it will study the wave propagation in concrete bridge decks and examine the current practices in Ultrasonic Surface-waves (USW) technique and use the findings to recommend methods to complete an accurate and in-situ concrete moduli evaluation of the entire thickness of the concrete bridge-deck.

A key difficulty in assessing bridge-deck deterioration is that it most often takes place below the surface and it is not easy to detect until the very progressive stages. Therefore, the techniques commonly used by the state departments of transportation (DOTs), such as visual inspection or those based on acoustic methods are not effective in detecting or assessing the variation in concrete modulus throughout the thickness. Visual inspection, by definition, will be ineffective while acoustic methods such as chain drag, hammer sounding provide information about presence of delamination only. Measuring modulus on the retrieved cores is expensive and can cause structural damage. A group of evaluation techniques commonly referred to as Non-Destructive Testing (NDT) techniques have shown promise in assessing under-the-surface deteriorated conditions in bridge decks. Modern NDT techniques for concrete bridge decks utilize various physical phenomena such as seismic, electric, thermal or electromagnetic to detect and characterize deterioration in bridge decks.

In the Second Strategic Highway Research Program (SHRP2), multiple teams of researchers assessed the capabilities and limitations of an array of NDT techniques in detecting and characterizing four deterioration types – corrosion, delamination, vertical cracking, and concrete degradation. Based on their findings, the team ranked the NDT techniques, in terms of speed, accuracy, precision, ease of use and cost. The summarized results of the project are presented in the table below. As is clear from the results, Ultrasonic Surface-waves (USW) is the most effective technique in detecting and characterizing concrete degradation.

Table 1.1 Grades for NDE techniques based on accuracy, precision, speed, ease of use and cost (Gucunski N. , et al., 2013)

NDT Technology	Deterioration Type	Accuracy	Precision (Repeatability)	Speed	Ease of Use	Cost	Overall Deterioration
		WF = 0.3	WF = 0.3	WF = 0.2	WF = 0.1	WF = 0.1	Type Grade
Impact echo	Delamination	2.8	4.0	2.3	2.1	3.0	3.0
Ultrasonic surface waves	Delamination	2.8	3.0	2.4	1.4	3.0	2.7
	Crack depth	2.5	3.0	1.0	1.4	3.0	2.3
	Concrete deterioration	3.8	4.0	2.4	1.4	3.0	3.3
Ground-penetrating radar	Delamination	2.1	4.0	3.9	2.2	3.0	3.1
	Corrosion	1.6	4.0	3.9	2.2	3.0	3.0
Half-cell potential	Corrosion	3.0	3.0	3.8	3.4	4.0	3.3
Galvanostatic pulse measurement	Corrosion	2.4	3.0	2.4	2.6	4.0	2.8
Electrical resistivity	Corrosion	3.0	4.0	3.8	3.6	4.0	3.6
Infrared thermography	Delamination	2.2	2.0	4.1	4.0	4.0	2.9
Chain dragging	Delamination	2.2	3.0	3.2	4.0	3.0	2.9

Note: WF = weight factor.

Ultrasonic surface waves (USW) technique is an offshoot of the Spectral analysis of surface-waves (SASW) method. It is used to evaluate the elastic moduli and layer thicknesses of layered systems such as pavement systems. It is based on the dispersion phenomenon of surface (Rayleigh) waves. Dispersive aspect makes it highly suitable for

generating a profile of the concrete bridge-deck. A modulus profile can provide critical information about the health of the bridge-deck. By contrast, many of the other NDT techniques such as impact echo focuses on the 2D planar surface of the concrete deck (by using a preset grid for testing only on certain) and thereby miss valuable information about the variations in material properties throughout the deck thickness.

SASW test consists of generation of Rayleigh waves by an impact on the surface of a medium, and measurement of the subsequent vibrations at two receivers located a specific distance from the impulse source. The detected signals are transformed into the frequency domain using the fast Fourier transform (FFT). The phase of the cross-power spectrum of the two sensor records is used to develop the dispersion curve of the profile. By inverting the dispersion curve, information about the properties of the layers (e.g., the thickness and shear-wave velocity) are obtained.

This method is commonly executed using a device called Portable Seismic Property Analyzer (PSPA) that was developed at the University of Texas at El Paso. The main application of the PSPA device is in conducting quality assurance of the pavement top layer and in bridge-deck testing. The PSPA device was designed and constructed as an extension of the Seismic Pavement Analyzer (SPA). It is produced by Geomedia Research and Development Inc., of El Paso, Texas (Nazarian, Baker, & Crain, 1997). The device consists of a high-frequency source and two accelerometers. The receivers are connected to a data acquisition system that consists of a portable computer with data acquisition software. A test sequence typically requires less than 15 seconds, during which the surface is hit multiple times by the source and the two accelerometers record

the vibrations of the surface. At the end of the test, the program plots the average modulus for the point being tested.

While the USW method with the PSPA device certainly provides a good tool for concrete bridge-deck testing, it has one main shortcoming which is its ability to do modulus profiling. This is mainly because of the inversion algorithm used in this method PSPA reports the average phase-velocity across the deck thickness for every test point. The results are very sensitive to the location and the distance between receivers since only two receivers are used.

In general, the conventional surface-wave testing technique suffers from inability to extract higher modes because of its inefficient inversion algorithm. Detecting higher modes-thereby increasing the richness of the measurements and accuracy of results, can be made possible by utilizing multiple sensors instead of the single pair utilized in the PSPA device (Ryden N. , Park, Ulriksen, & Miller, 2004).

These inaccuracies can be improved by using more sensors to collect data. Multi-channel analysis of surface waves (MASW) is a technique that employs more sensors and hence can overcome the earlier problems (Park, Miller, & Xia, 1998). The challenge in using this method in practice stems from a single problem, which is the lack of an optimal inversion technique. Most of the existing methods can easily take anywhere from a few hours to a few days to provide complete results when multiple layers are present (Ryden & Park, 2006; Hadidi & Gucunski, 2003). This research will outline a technique that can eliminate the long processing times and deliver results in near real-time.

1.2 Research Goals

To summarize, the key problem that this study will address is that of a rapid and accurate evaluation of concrete modulus profile in concrete bridge decks. To facilitate the development, the fundamental simplifying assumption made in this study is that the concrete deck consists of three layers with varying elastic modulus (Figure 1.1). The desired goal is then to apply the USW to measure the shear-wave velocity and thickness of the layers. A preliminary assumption is made where the concrete deck consists of a 3 layer system, the technique can be extended to systems with more layers.

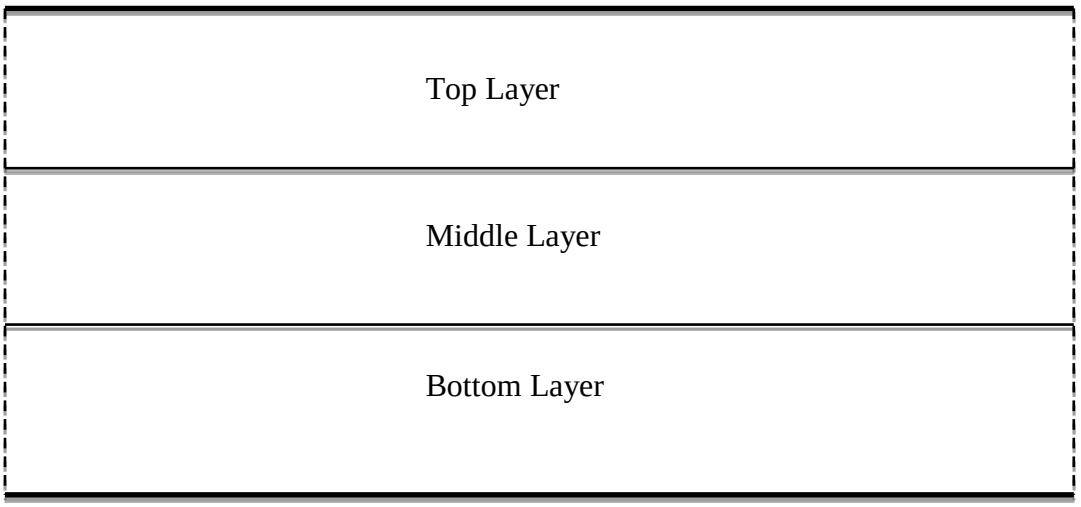

Figure 1.1 A section of a bridge-deck with 3 layers.

This study will demonstrate how to complete a vertical profile for a concrete bridge-deck. For this purpose it will go through the process of dispersion analysis using the multi-channel analysis of surface waves (MASW). It will demonstrate the effects of higher modes in systems with multiple layers. And finally it will develop an inversion technique that can be executed in-situ with instant results.

2 Background on Wave Propagation

This chapter includes the description of the fundamental characteristics of stress-wave propagation in elastic media. Different types of waves are introduced, and matrix methods to solve the wave equations are discussed.

2.1 Introduction to wave propagation in solids

There are two types of waves in solids: body-waves and surface-waves. Body-waves travel through the interior of a solid. Surface-waves diminish as they get further from the surface. Body-waves consist of two wave groups: P-waves and S-Waves. P-waves are pressure waves that travel faster than other waves through solids. They displace alongside the direction of the propagation. Secondary waves (S-waves) arrive after the faster moving P-waves and displace perpendicular to the direction of propagation. Figure 2.1 shows a schematic picture of how each type of body-waves propagates. Surface-waves are discussed later in this chapter.

Waves in solids result from mechanical disturbance of the solid media. Their propagation behavior is related to the material properties of the solid. Wave equation is a differential equation, expressing the properties of motion in waves. The exact solution of the wave equation can be obtained using continuum mechanics. For the purpose of this research, the formulations will follow linear elasticity. This means that the materials are assumed to be both homogeneous and linear elastic. Although concrete is neither homogeneous nor linear-elastic, this assumption is necessary and acceptable for the purpose of

modeling the wave propagation. This is due to the small deformation of the medium during the surface-wave testing.

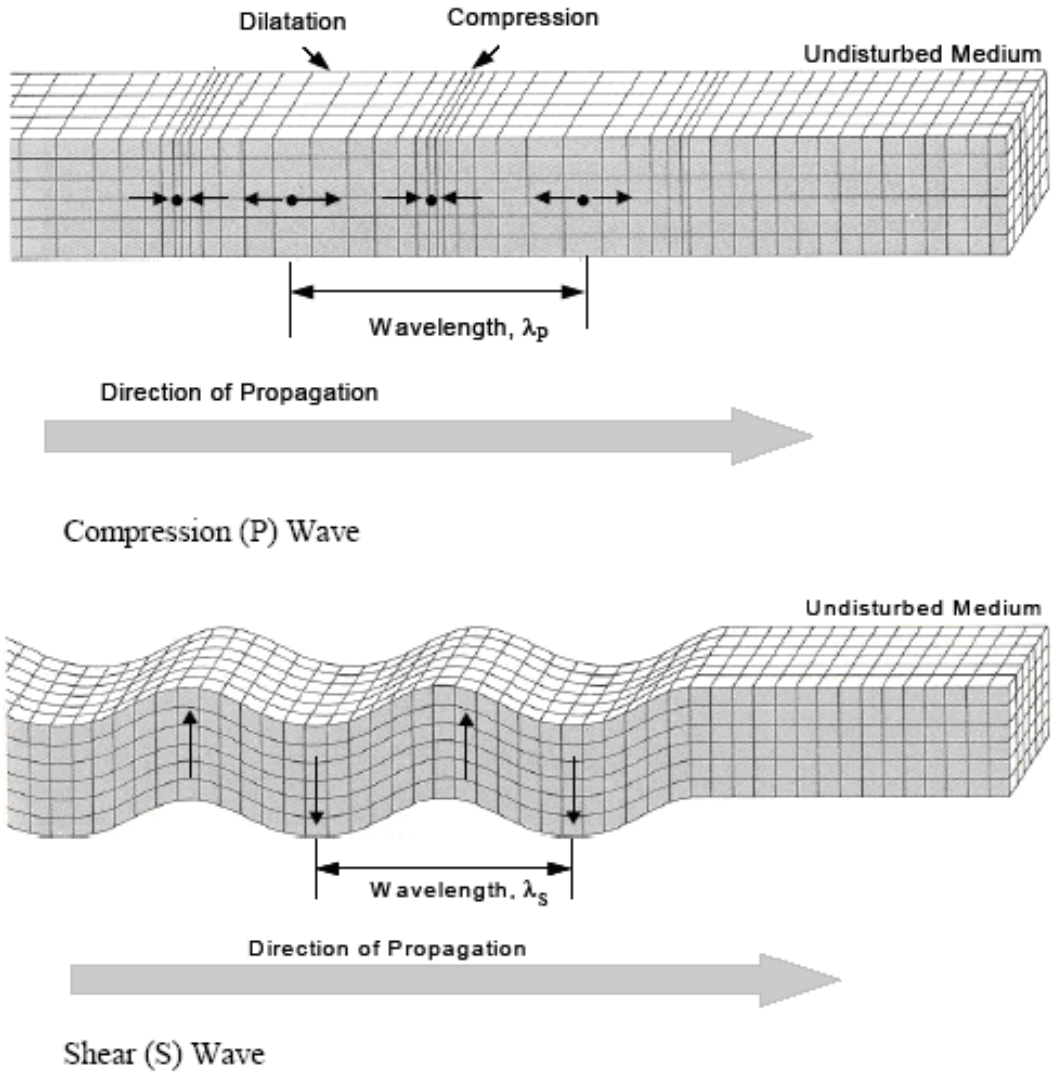

Figure 2.1 Body-waves propagation in solids. P-waves at the top and S-waves at the bottom (Bolt, 1976)

Below are the main equations governing the linear elastic material, stress-strain field. E and ν are Young's modulus and Poisson's ratio, respectively. For the three-dimensional case, shear modulus (G) and bulk modulus (K) parameters are defined as follows:

$$\mathrm{G} = \frac{\mathrm{E}}{2(1 + \nu)} \qquad \text{Equation 2.1}$$

$$K = \frac{E}{3(1 - 2\nu)} \qquad \text{Equation 2.2}$$

Constraint modulus, for uniaxial loading and laterally constraint material, and also Lame's constants (μ and λ) are determined with the following equations. Notice that G and μ are equal. For a more detailed discussion, see (Graff, 1975; Achenbach, 1973; Elmore & Heald, 1969)

$$M = \frac{E(1 - \nu)}{(1 + \nu)(1 - 2\nu)} = B + \frac{4}{3}K \qquad \text{Equation 2.3}$$

$$\lambda = \frac{E\nu}{(1 + \nu)(1 - 2\nu)} \qquad \text{Equation 2.4}$$

$$\mu = G = \frac{E}{2(1 + \nu)} \qquad \text{Equation 2.5}$$

$$E = \frac{\mu(3\lambda + 2\mu)}{\lambda + \mu} \qquad \text{Equation 2.6}$$

$$\nu = \frac{\lambda}{2(\lambda + \mu)} \qquad \text{Equation 2.7}$$

2.2 1-D Wave Propagation

Wave propagation in one dimension is the simplest form of the problem. Only P-waves are considered in this case. If plane sections remain plain, density (ρ) and sectional area (A) remain constant, and maintain a large wavelength with respect to the rod diameter, Newton's second law yields to the following:

$$\frac{\partial F}{\partial x}\Delta x = A\rho\Delta x\frac{\partial^2 u}{\partial t^2} \qquad \text{Equation 2.8}$$

$$F = AE\frac{\partial u}{\partial x} \qquad \text{Equation 2.9}$$

Therefore we have:

$$\frac{\partial^2 u}{\partial x^2} = \frac{1}{Cp^2}\frac{\partial^2 u}{\partial t^2} \qquad \text{Equation 2.10}$$

So the propagation velocity is defined as follows:

$$Cp = \sqrt{\frac{E}{\rho}} \qquad \text{Equation 2.11}$$

2.3 3-D Wave Propagation

In this section the fundamentals of wave propagation in infinite elastic solids is discussed. Many researchers (Graff, 1975; Kolsky, 1963; Rose, 2004; Wolf, 1985) have covered this

topic in detail. Using Newton's second law and given that acceleration and force are partial derivatives of the displacement (u) and normal (σ) and shear stress (τ):

$$-\rho\omega^2 u = \sigma_{x,x} + \tau_{xy,y} + \tau_{xz,z}$$

$$-\rho\omega^2 v = \tau_{yx,x} + \sigma_{y,y} + \tau_{yz,z} \qquad \text{Equation 2.12}$$

$$-\rho\omega^2 w = \tau_{zx,x} + +\tau_{zy,y} + \sigma_{z,z}$$

ρ is the mass density of the infinitesimal cube element in the infinite elastic isotropic solid. *t* represents time. The first subscript shows the direction of the stress, where the second, denotes the direction of the normal of the infinitesimal area on which the stress acts. The comma denotes a partial derivative. Using the strain-displacement equations we have the following:

$$\epsilon_x = u_{,x}$$

$$\epsilon_y = v_{,y}$$

$$\epsilon_z = w_{,z}$$

Equation 2.13

$$\gamma_{xy} = u_{,y} + v_{,x}$$

$$\gamma_{xz} = u_{,z} + w_{,x}$$

$$\gamma_{yz} = v_{,z} + w_{,y}$$

Using the Hook's law, the relationship between stress and strain is as follows:

$$\epsilon_x = \frac{1}{E}\left(\sigma_x - \upsilon\sigma_y - \upsilon\sigma_z\right)$$

$$\epsilon_y = \frac{1}{E}\left(-\upsilon\sigma_x + \sigma_y - \upsilon\sigma_z\right)$$

Equation 2.14

$$\epsilon_z = \frac{1}{E}\left(-\nu\sigma_x - \upsilon\sigma_y + \sigma_z\right)$$

$$\gamma_{xy} = \frac{\tau_{xy}}{G}, \gamma_{xz} = \frac{\tau_{xz}}{G}, \gamma_{yz} = \frac{\tau_{yz}}{G}$$

The basic wave equation in three dimensions for elastic, homogenous and isotropic material can be written as follows:

$$\nabla^2 e = -\frac{\omega^2}{c_p^2} e$$

Equation 2.15

$$\nabla^2\,\Omega = -\frac{\omega^2}{c_s^2}\,\Omega$$

$\nabla^2$is the Laplace operator, and e and Ω are the volumetric strain and rotation strain, respectively.

$$\nabla^2 = \frac{\delta^2}{\delta x_1^2} + \frac{\delta^2}{\delta x_2^2} + \frac{\delta^2}{\delta x_3^2}$$

Equation 2.16

$$e = u_{,x} + v_{,x} + w_{,x} \qquad \text{Equation 2.17}$$

$$\Omega_{x,x} + \Omega_{y,y} + \Omega_{z,z} = 0 \qquad \text{Equation 2.18}$$

Where

$$\Omega_{x,x} = \frac{1}{2}(w_{,y} - v_{,z})$$

$$\Omega_{y,y} = \frac{1}{2}(u_{,z} - w_{,x}) \qquad \text{Equation 2.19}$$

$$\Omega_{x,x} = \frac{1}{2}(v_{,x} - u_{,y})$$

The variable Cp is identified as the dilatational wave velocity as follows:

$$Cp = \sqrt{\frac{E(1-\nu)}{(1+\nu)(1-2\nu)\rho}} = \sqrt{\frac{M}{\rho}} = \sqrt{\frac{\lambda + 2G}{\rho}} \qquad \text{Equation 2.20}$$

And Cs is identified as shear-wave velocity as follows:

$$Cs = \sqrt{\frac{E}{2(1+\nu)\rho}} = \sqrt{\frac{G}{\rho}} \qquad \text{Equation 2.21}$$

2.3.1 Body-waves

The solution of Equation 2.15 is discussed here. Figure 2.2 and Figure 2.3 shows the displacement associated with each type of body wave.

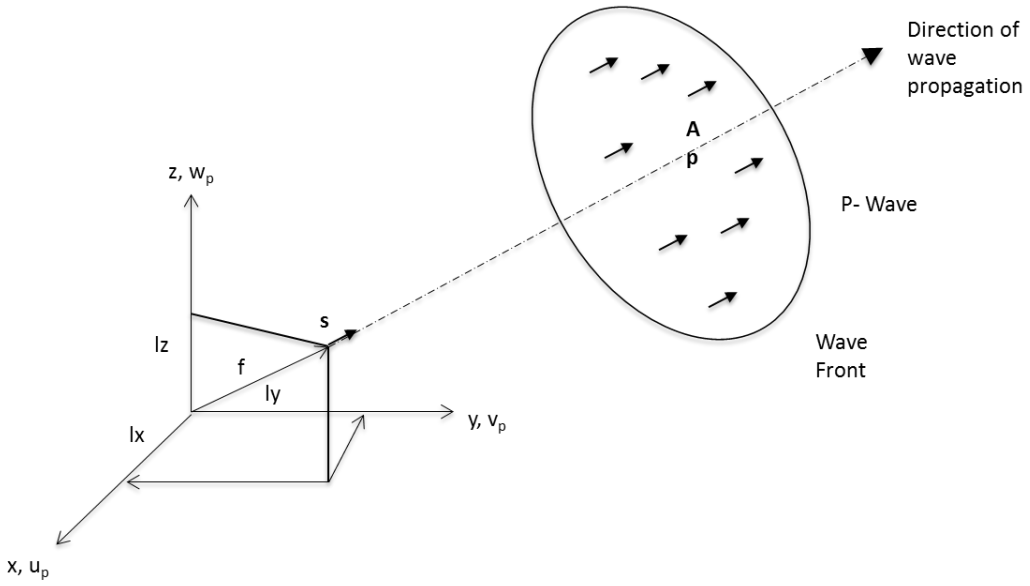

Figure 2.2 Displacement and direction of wave propagation for P-waves

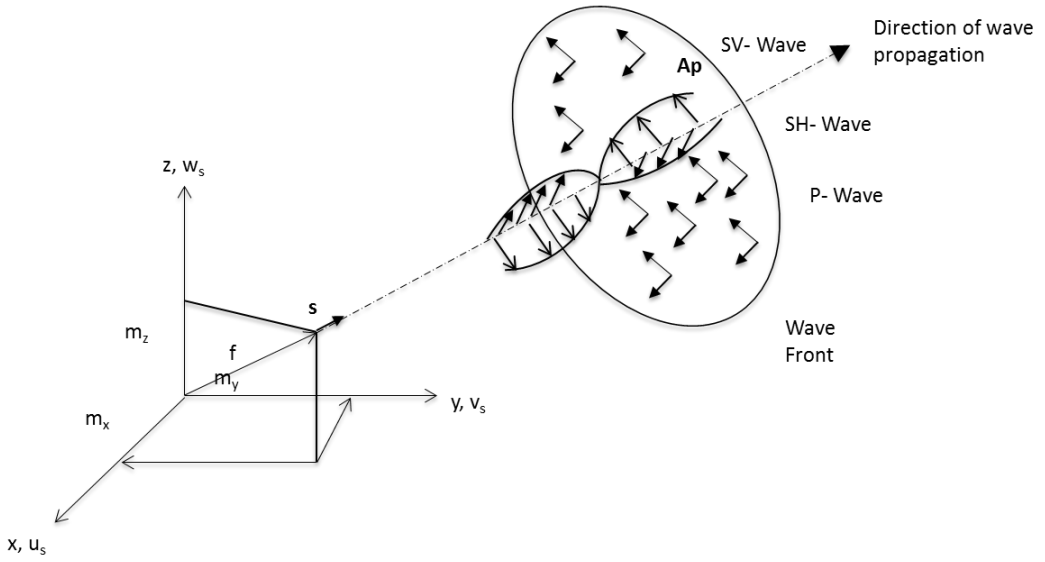

Figure 2.3 Displacement and direction of wave propagation for shear-waves

For the definition of dilatation or P-wave, the corresponding displacements for each direction are equal to the following:

$$u_p = l_x A_p exp\left[\frac{i\omega}{c_p}\left(-l_x x - l_y y - l_z z\right)\right]$$

$$v_p = l_y A_p exp\left[\frac{i\omega}{c_p}\left(-l_x x - l_y y - l_z z\right)\right] \qquad \text{Equation 2.22}$$

$$w_p = l_x A_p exp\left[\frac{i\omega}{c_p}\left(-l_x x - l_y y - l_z z\right)\right]$$

A_p is the amplitude of the wave that coincides with the direction of the wave propagation. The three scalars l_x, l_y and l_z are the direction cosines of the straight line.

$$l_x^2 + l_y^2 + l_z^2 = 1 \qquad \text{Equation 2.23}$$

As illustrated in Figure 2.2 and Equation 2.22 the direction of the propagation coincides with the displacement vector. In addition, the direction of propagation is in positive s direction with velocity c_p.

On the other hand, for the definition of S-wave, the corresponding displacements for each direction are equal to the following:

$$u_s = \frac{(m_x m_z A_{SV} - m_z A_{SH})}{\sqrt{m_x^2 + m_y^2}} exp\left[\frac{i\omega}{c_s}(-m_x x - m_y y - m_z z)\right]$$

$$v_s = \frac{(m_y m_z A_{SV} + m_x A_{SH})}{\sqrt{m_x^2 + m_y^2}} exp\left[\frac{i\omega}{c_s}(-m_x x - m_y y - m_z z)\right] \qquad \text{Equation 2.24}$$

$$w_s = -\sqrt{m_x^2 + m_y^2} A_{SV} exp\left[\frac{i\omega}{c_s}(-m_x x - m_y y - m_z z)\right]$$

With

$$m_x^2 + m_y^2 + m_z^2 = 1 \qquad \text{Equation 2.25}$$

$$m_x c_x + m_y c_y + m_z c_z = 0 \qquad \text{Equation 2.26}$$

And

$$A_{SH} = \frac{C_z}{\sqrt{m_x^2 + m_y^2}} \qquad \text{Equation 2.27}$$

$$A_{SV} = \frac{m_x C_y - m_y C_x}{\sqrt{m_x^2 + m_y^2}} \qquad \text{Equation 2.28}$$

The direction of the propagation is specified by direction cosines m_x, m_y and m_z. Also the displacement vector of S-wave is decomposed into horizontal component A_{SH} and a component lying in the plane, which contains the z-axis A_{SV}. Figure 2.2 shows that the displacement vector is perpendicular to the direction of motion.

Also by introducing the material damping the wave velocities become as follows:

$$c_p^* = c_p\sqrt{1 + 2\zeta_p i} \qquad \text{Equation 2.29}$$

$$c_s^* = c_s\sqrt{1 + 2\zeta_s i} \qquad \text{Equation 2.30}$$

For simplicity, it is reasonable to imagine that the P- wave and S-wave lie on the same plane, the x-z plane, for example. Combining Equation 2.22 and Equation 2.24 yields to the following:

$$u = l_x A_P exp\left[i\omega\left(-\frac{l_x x}{c_p^*} - \frac{l_z z}{c_p^*}\right)\right] + m_z A_{SV} exp\left[i\omega\left(-\frac{m_x x}{c_s^*} - \frac{m_z z}{c_s^*}\right)\right]$$

$$v = A_{SH} exp\left[i\omega\left(-\frac{m_x x}{c_s^*} - \frac{m_z z}{c_s^*}\right)\right] \quad \text{Equation 2.31}$$

$$w = l_z A_P exp\left[i\omega\left(-\frac{l_x x}{c_p^*} - \frac{l_z z}{c_p^*}\right)\right] + m_x A_{SV} exp\left[i\omega\left(-\frac{m_x x}{c_s^*} - \frac{m_z z}{c_s^*}\right)\right]$$

u and w lie in the x-z plane and depend on A_P and A_{SH}, whereas v depends on A_{SH} and forms the out-of-plane motion.

2.4 Guided Waves

In an infinite, homogenous and isotropic medium only body-waves exist. However, in common structures such as plates and rods other types of waves also exist. These waves are called guided waves and formed by the interaction between the P-waves and S-waves at the interface. Guided waves traveling along the free surface are called surface-waves. Rayleigh waves are a special type of guided waves that travel alongside the surface of a plate. They represent the natural mode of wave propagation, and their schematic propagation in solids is depicted in Figure 2.4. This means that Rayleigh waves exist when there is no external force. Stiffness matrix method is one way of solving the wav

equation. This method will be discussed in details later. Here we consider a simplified version where the external surface loads are zero:

$$Su = 0 \qquad \text{Equation 2.32}$$

A nontrivial solution exists when the determinant of the stiffness matrix is equal to zero.

$$|S| = 0 \qquad \text{Equation 2.33}$$

This equation can be viewed as an eigenvalue problem.

$$-st(1+t^2)^2 - \left(2(1+st) - (1+t^2)\right)^2 = 0 \qquad \text{Equation 2.34}$$

Substituting the values for s and t and simplifying yields the following:

$$(2 - \frac{c_R^2}{c_s^2}^2)^2 - 4\left(1 - \frac{c_R^2}{c_p^2}\right)^{\frac{1}{2}}\left(1 - \frac{c_R^2}{c_s^2}\right)^{\frac{1}{2}} = 0 \qquad \text{Equation 2.35}$$

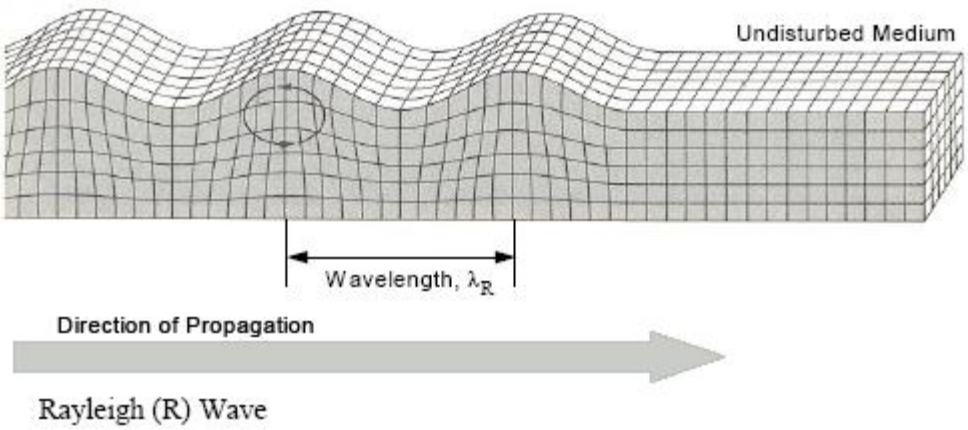

Figure 2.4 Rayleigh waves propagation in solids. (Bolt, 1976)

There is no frequency term in this equation. This proves that Rayleigh waves are non-dispersive in half-space and Poisson's ratio and shear velocity are the only variables that affect the phase-velocity (Achenbach, 1973):

$$C_R = \frac{0.862 + 1.14\nu}{1 + \nu} C_s \qquad \text{Equation 2.36}$$

The importance of Rayleigh waves in radiation of energy comes from the fact that they dominate the transient part of surface response. Approximately 67% of the impact-induced energy in a homogenous half-space propagates as Rayleigh waves (Richart, 1970). The body-waves (P and S waves) propagate through the interior of the medium where R-waves propagate along the surface. Due to hemispherical wave propagation, the amplitude of P- and S- waves which propagate in the interior attenuate with a factor of 1/r and $1/r^2$; but the amplitude of propagation alongside the surface attenuates proportionally

to $1/\sqrt{r}$ due to cylindrical wave propagation. However, because of they are lower velocity; they arrive after body-waves.

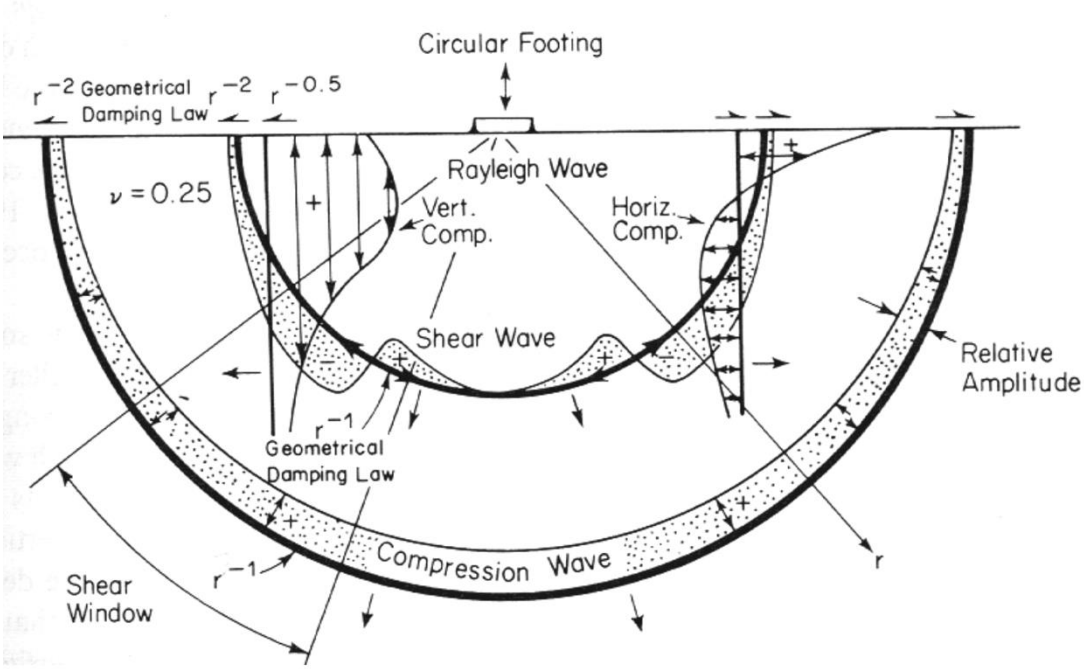

Figure 2.5 Distribution of stress waves from a point source on a homogeneous, isotropic, elastic half-space. The particle motion is visualized at a distance of approximately 2.5 wavelengths from the source. The different wave types are drawn in proportion to the velocity of each wave. (Richart, 1970)

Rayleigh-wave dispersion phenomena provide the basis for SASW and MASW methods. The amplitude of such waves decreases exponentially with depth in the half-space, so the effective depth is usually limited to one wavelength. Only longer wavelength waves can penetrate into deeper layers.

2.5 Lamb Waves in a Uniform plate

Introduced by Horace Lamb (1917), Lamb waves are guided waves that propagate in an elastic, isotropic plate with free boundaries at the top and the bottom, as shown in Figure 2.6. Lamb waves are formed by the interaction of compressional and shear-waves at the plate boundaries. These waves represent a group of wave types that include bending waves, Rayleigh waves and quasi-longitudinal waves. The equations that define the interaction between these waves are called Lamb wave equations.

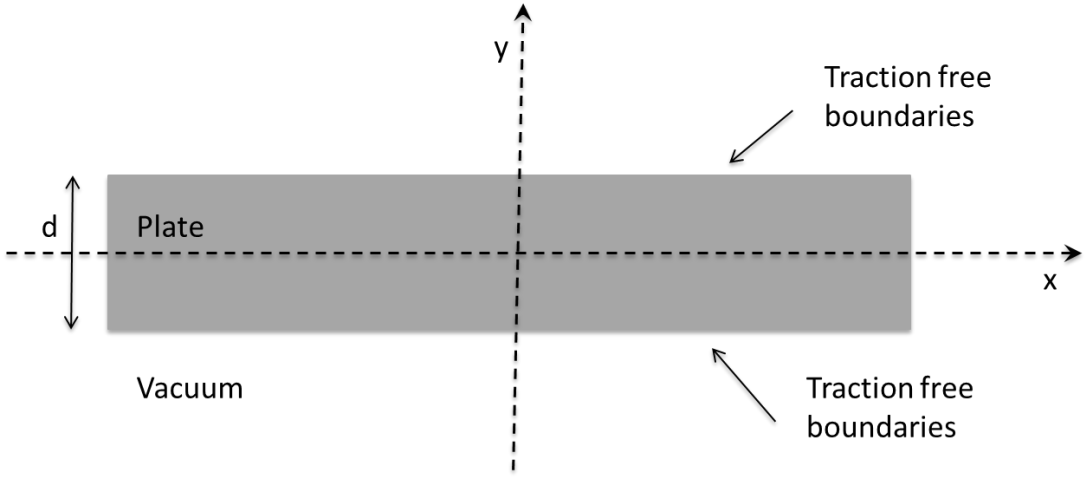

Figure 2.6 Schematic of a plate with isotropic material and traction-free boundaries

To obtain modal phase-velocity, the roots of the Lamb equations should be found. Plates support two infinite sets of Lamb wave modes: Symmetrical and antisymmetrical modes with respect to the middle of the plate. Equation 4.2 and Equation 4.3 are describing symmetrical and antisymmetrical Lamb mode phase velocities. There is a unique phase-velocity for each mode that is dispersive through different frequencies.

$$\frac{\tan\beta\frac{d}{2}}{\tan\alpha\frac{d}{2}}+\frac{4\alpha\beta k^2}{(k^2-\beta^2)^2}=0 \qquad \text{Equation 2.37}$$

$$\frac{\tan\beta\frac{d}{2}}{\tan\alpha\frac{d}{2}}+\frac{(k^2-\beta^2)^2}{4\alpha\beta k^2}=0 \qquad \text{Equation 2.38}$$

$$\alpha^2=\frac{\omega^2}{C_p^2}-k^2 \qquad \text{Equation 2.39}$$

$$\beta^2=\frac{\omega^2}{C_s^2}-k^2 \qquad \text{Equation 2.40}$$

d is the full plate thickness, k is the wave number ($k=\frac{\omega}{c}$) where ω is the circular frequency, and c is the phase wave velocity. C_S and C_P are transverse (shear) and longitudinal wave velocities, respectively.

These equations represent pure Lamb waves with particle motions in x and y directions. To obtain the dispersive phase-velocity, a root-finding algorithm should be used.

2.6 Matrix techniques for solution of wave propagation

In this section matrix techniques are used to simulate wave propagation in layered media. Three methods maybe used to achieve this goal: The transfer-matrix method, the global-matrix method, and the stiffness-matrix method. These methods will be introduced and compared so that an appropriate method is selected for this study.

2.6.1 Transfer Matrix Method:

The transfer matrix method was introduced by Thomson (1950). It describes a matrix that transfers the forces and displacements at the top of the layer to the bottom of the layer. Layer matrices can be coupled to give the system transfer matrix for a layered system. Later on Haskell (1953) corrected a small error in the derivation, so it is now referred to Thomson-Haskell method. This method suffers from numerical of large fd. f and d represent frequency and thickness respectively. The global-matrix method was later proposed to solve this issue.

2.6.2 Global Matrix Method

Proposed by Knopoff (1964), the global matrix method offers an alternative to the Transfer matrix method and can be specially used in cases of large fdA large matrix is used that combines the information from different layers. The advantage of this method is its robustness; however; in the case of many layers the solution can become quite slow. Figure 2.7 shows a three-layer plate with semi-infinite half-space at the bottom.

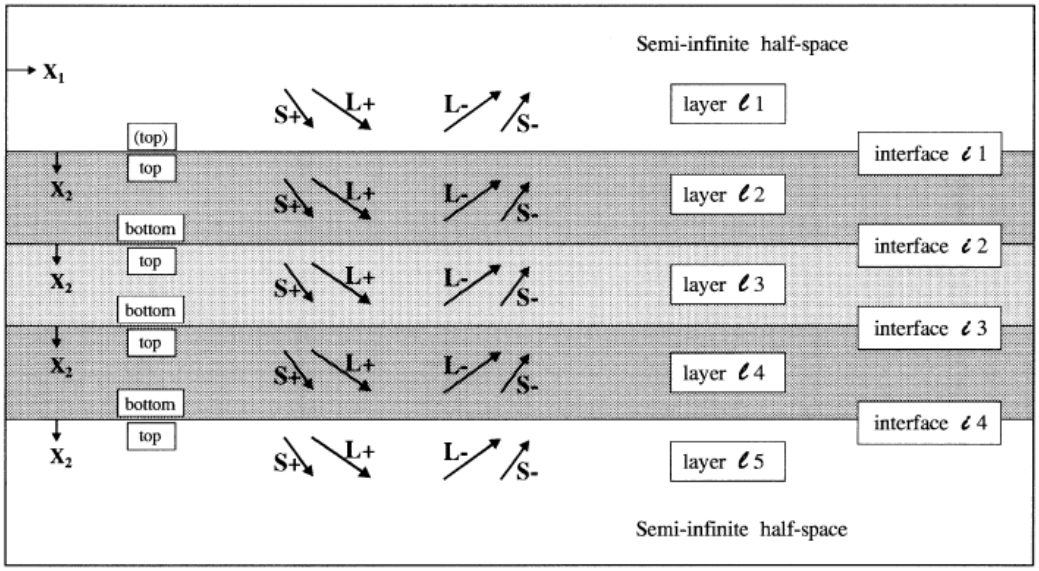

Figure 2.7 A three layers plate with half-space at the bottom (Lowe, 1995)

Displacement in the second layer can be expressed as both amplitudes at the bottom of the second layer and at the top of the third layer:

$$[D]_{l2,bottom} = \begin{bmatrix} A(L+) \\ A(L-) \\ A(S+) \\ A(\mathrm{S}-) \end{bmatrix}_{l2} \qquad \text{Equation 2.41}$$

$$[D]_{l3,top} = \begin{bmatrix} A(L+) \\ A(L-) \\ A(S+) \\ A(S-) \end{bmatrix}_{l3} \qquad \text{Equation 2.42}$$

$A(L+)\& A(L-)$ are the amplitudes of longitudinal waves in the positive and negative directions. $A(S+)\& A(S-)$ are the amplitudes of shear-waves in the positive and negative directions. They can be combined into one equation:

$$[[D_{2b}] \quad [-D_{3t}]] = \begin{bmatrix} A(L+)_2 \\ A(L-)_2 \\ A(S+)_2 \\ A(S-)_2 \\ A(L+)_3 \\ A(L-)_3 \\ A(S+)_3 \\ A(S-)_3 \end{bmatrix} = \{0\} \qquad \text{Equation 2.43}$$

t and b refer to the top and bottom of the layer where 2 and 3 refer to $l2$ and $l3$ layers. The difference with the transfer-matrix method and the global matrix method is that the origin for all waves in the layers is their point of entry to the layer, which could be top or bottom, as opposed to the top of the layer for transfer-matrix method. *D* matrix for the top and bottom of the layer is as follows:

$$[D_t]$$

$$= \begin{bmatrix} k_1 & k_1 g_\alpha & C_\beta & -C_\beta g_\beta \\ C_\alpha & -C_\alpha g_\alpha & -k_1 & -k_1 g_\beta \\ i\rho B & i\rho B g_\alpha & -2i\rho k_1 \beta^2 C_\beta & 2i\rho k_1 \beta^2 C_\beta g_\beta \\ 2i\rho k_1 \beta^2 C_\alpha & -2i\rho k_1 \beta^2 C_\alpha g_\alpha & i\rho B & i\rho B g_\beta \end{bmatrix} \qquad \text{Equation 2.44}$$

$$[D_b]$$

$$= \begin{bmatrix} k_1 g_\alpha & k_1 & C_\beta g_\beta & -C_\beta \\ C_\alpha g_\alpha & -C_\alpha & -k_1 g_\beta & -k_1 \\ i\rho B g_\alpha & i\rho B & -2i\rho k_1 \beta^2 C_\beta g_\beta & 2i\rho k_1 \beta^2 C_\beta \\ 2i\rho k_1 \beta^2 C_\alpha g_\alpha & -2i\rho k_1 \beta^2 C_\alpha & i\rho B g_\beta & i\rho B \end{bmatrix} \qquad \text{Equation 2.45}$$

$$g_\alpha = e^{iC_\alpha x_2} \qquad g_\beta = e^{iC_\beta x_2} \qquad \text{Equation 2.46}$$

$$C_\alpha = \left(\omega^2/_{\alpha^2} - k_1^2\right)^{1/2} \qquad C_\beta = \left(\omega^2/_{\beta^2} - k_1^2\right)^{1/2} \qquad \text{Equation 2.47}$$

$$B = \omega^2 - 2\beta^2 k_1^2 \qquad \text{Equation 2.48}$$

Here **k** is the wavenumber vector and ω is the angular velocity. The wavenumber is in the direction of the wave propagation and contains its velocity and wavelength. $\alpha\&\beta$ describe the longitudinal and shear-wave velocity. The global matrix contains *4n* unknowns and *4(n-1)* equations. For the Figure 2.7 the global matrix is as follows:

$$\mathbf{S} = \begin{bmatrix} [D_{1b}] & [-D_{2t}] & & & \\ & [D_{2b}] & [-D_{3t}] & & \\ & & [D_{3b}] & [-D_{4t}] & \\ & & & [D_{4b}] & [-D_{5t}] \end{bmatrix}. \qquad \text{Equation 2.49}$$

$$\begin{Bmatrix} \{A_1\} \\ \{A_2\} \\ \{A_3\} \\ \{A_4\} \\ \{A_5\} \end{Bmatrix} = \{0\}$$

$\{A_x\}$ is an abbreviation of $A_{(L+)}, A_{(L-)}, A_{(S+)}, A_{(S-)}$ for each layer. Each row in Equation 2.49 represents each interface and each column represents each layer utilizing

the top and bottom half-spaces. For surface-wave applications the top surface is free. In order to avoid modification to the *D matrix,* Lowe (Lowe, 1995) suggests assuming arbitrary bulk wave velocity values for α and β and zero density for bulk density. By this way, the same matrices can be used for both vacuum and half-space. For more detailed discussion, see (Lowe, 1995). The stiffness matrix method follows the same global structure and benefits from higher computational speed (Kausel E. , 2006). This method will be discussed next.

2.6.3 Stiffness Matrix Method:

The stiffness matrix method was first proposed by Eduardo Kausel in 1981 to resolve the numerical instability of the transfer matrix method. There are several advantages to the stiffness matrix method (Kausel E. , 2006):

1. Stiffness matrices only involve displacements, reducing the number of degrees of freedom. This is half compared to the transfer matrix, which involves both displacements and stresses.
2. They are symmetric rather than non-symmetric transfer matrices.
3. The speed of computations is almost 8 times faster; by a factor of 2 because of symmetry and a factor of 4 due to bandwidth. (Kausel E. , 2006) Despite the stability problems of transfer matrices in thick layers or higher frequencies, stiffness matrices remain stable throughout the frequency range.
4. Naturally, when solving for zero loading the stiffness matrix is accompanied by the solution of an eigenvalue problem, which leads to the normal modes without any extra step.

5. Different mode participation amplitudes result from solving the eigenvalue equation. These amplitudes are of main interest for analyzing the characteristics of layered media.

The stiffness matrix was later presented in slightly modified form by Wolf (1985). The following paragraphs summarize the stiffness matrix method presented by this author and the variables needed.

The stiffness matrix method in wave propagation in layered media is very similar to the displacement method in structural analysis. The key difference is that the domain of analysis is frequency-wave number instead of the common spatial domain.

While the description of the next two sections are not used directly in this research, it is provided to give the reader necessary background on the topic.

2.6.3.1 In Plane Wave Motion

The nomenclature of in-plane wave propagation is shown in Figure 2.8. Displacement in the x direction for both P and SV waves can be separated by its variables, x and z:

$$u(z,x) = u(z)\exp(-ikx) \qquad \text{Equation 2.50}$$

$$w(z,x) = w(z)\exp(-ikx) \qquad \text{Equation 2.51}$$

Where k is the frequency wavenumber and c is the velocity defined as follows:

$$k = \frac{\omega}{c}$$ Equation 2.52

$$c = \frac{c_p}{l_x} = \frac{c_s}{m_x}$$ Equation 2.53

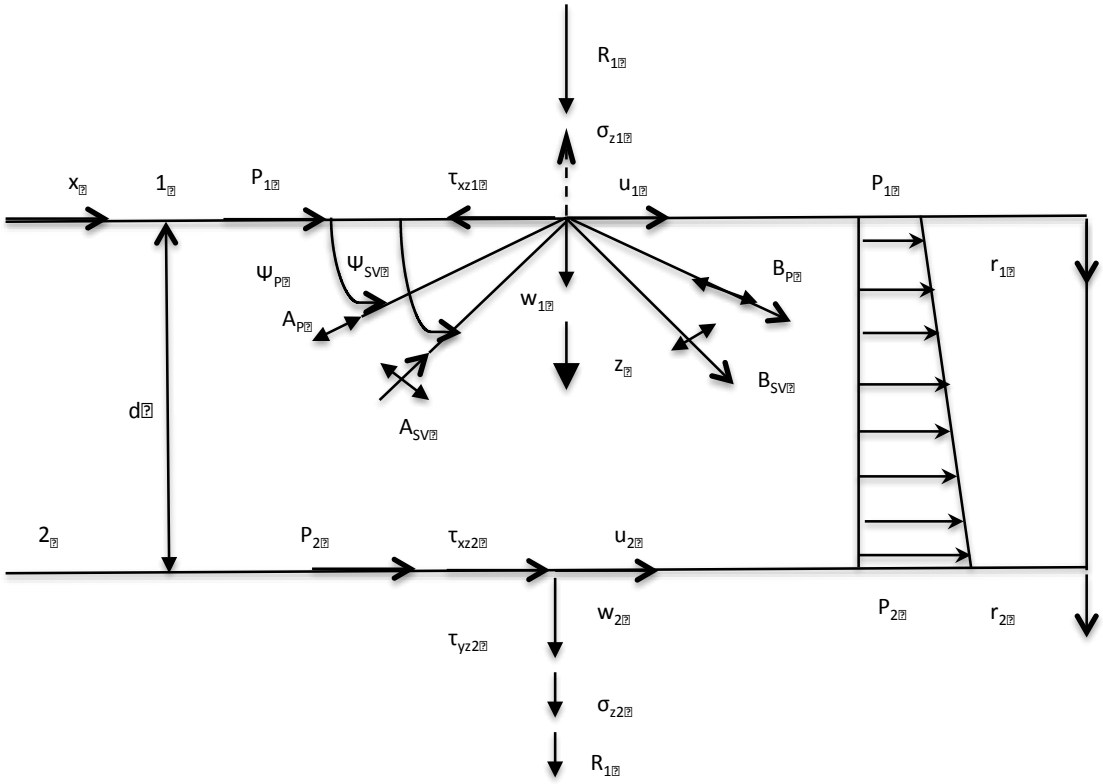

Figure 2.8 Nomenclature of wave propagation in a layer representing In-Plane motion (Wolf, 1985)

By satisfying the boundary conditions at the top and the bottom of the layer shown in Figure 2.8, the in-plane displacement can be expressed as follows:

$$u(z) = l_x\left[A_p \exp(iksz) + B_p \exp(-iksz)\right] - m_x t[A_{SV} \exp(iktz) - B_{SV} \exp(-iktz)] \quad \text{Equation 2.54}$$

$$w(z) = -l_x s\left[A_p \exp(iksz) - B_p \exp(-iksz)\right] - m_x[A_{SV} \exp(iktz) + B_{SV} \exp(-iktz)] \quad \text{Equation 2.55}$$

Where $w(z)$ and $u(z)$ are the amplitudes of the wave travelling in the x direction and

$$s = -i\sqrt{1 - \frac{1}{l_x^2}} \quad \text{Equation 2.56}$$

$$t = -i\sqrt{1 - \frac{1}{m_x^2}} \quad \text{Equation 2.57}$$

A_p and B_p are the amplitudes of the P-wave traveling in the positive and negative directions, respectively. A_{SV} and B_{SV} are the amplitudes of the shear-wave traveling in the positive and the negative directions.

The amplitudes of the shear and normal stresses are then expressed as follows:

$$\sigma_z(z) = \lambda^*(u_{,x} + w_{,x}) + 2G^* w_{,z} \qquad \text{Equation 2.58}$$

$$\tau_{xz}(z) = G^*(u_{,x} + w_{,x}) \qquad \text{Equation 2.59}$$

By imposing the boundary conditions at the top and the bottom of the layer we have the following

$z = 0$ $\quad P_1 = -\tau_{xz1}$ and $R_1 = -\sigma_{z1}$

$z = d$ $\quad P_2 = \tau_{xz2}$ and $R_2 = \sigma_{z2}$

By eliminating the displacement amplitudes the transfer matrix between the top and the bottom of the layer is formed as following:

$$\begin{Bmatrix} u_2 \\ w_2 \\ \tau_{xz2} \\ \sigma_{z2} \end{Bmatrix} = \frac{1}{1+t^2} \begin{bmatrix} T_{11} & T_{12} & T_{13} & T_{14} \\ T_{21} & T_{12} & T_{23} & T_{24} \\ T_{31} & T_{32} & T_{33} & T_{34} \\ T_{41} & T_{42} & T_{43} & T_{44} \end{bmatrix} \begin{Bmatrix} u_1 \\ w_1 \\ \tau_{xz1} \\ \sigma_1 \end{Bmatrix}$$

$$T_{11} = 2\cos ksd \ + (t^2 - 1)\cos ktd \qquad \text{Equation 2.60}$$

$$T_{12} = i\frac{1-t^2}{s}\sin ksd + i2t\sin ktd$$

$$T_{13} = \frac{1}{ksG^*}\sin ksd + \frac{t}{kG^*}\sin ktd$$

$$T_{14} = \frac{i}{kG^*}\cos ksd - \frac{i}{kG^*}\cos ktd$$

$$T_{21} = -2is\sin ksd - i\frac{1-t^2}{t}\sin ktd$$

$$T_{22} = (t^2-1)\cos ksd\ + 2\cos ktd$$

$$T_{23} = \frac{i}{kG^*}\cos ksd - \frac{i}{kG^*}\cos ktd$$

$$T_{24} = \frac{s}{kG^*}\sin ksd + \frac{1}{ktG^*}\sin ktd$$

$$T_{31} = -4kG^*s\sin ksd - kG^*\frac{(1-t^2)^2}{t}\sin ktd$$

$$T_{32} = i2kG^*(t^2-1)\cos ksd - i2kG^*(t^2-1)\cos ktd$$

$$T_{33} = 2\cos ksd\ + (t^2-1)\cos ktd$$

$$T_{34} = -2is\sin ksd - i\frac{1-t^2}{t}\sin ktd$$

$$T_{41} = i2kG^*(t^2-1)\cos ksd - i2kG^*(t^2-1)\cos ktd$$

$$T_{42} = -kG^*\frac{(1-t^2)^2}{t}\sin ksd - 4kG^*t\sin ktd$$

$$T_{43} = i\frac{1-t^2}{t}\sin ksd + 2it\sin ktd$$

$$T_{44} = (t^2-1)\cos ksd\ + 2\cos ktd$$

Performing a partial inversion on a transfer matrix will result in a stiffness matrix that is faster to solve and more stable than the transfer matrix.

$$\begin{Bmatrix} P_1 \\ iR_1 \\ P_2 \\ iR_2 \end{Bmatrix} = \frac{(1+t^2)kG^*}{D} \begin{bmatrix} S_{11} & S_{12} & S_{13} & S_{14} \\ S_{21} & S_{12} & S_{23} & S_{24} \\ S_{31} & S_{32} & S_{33} & S_{34} \\ S_{41} & S_{42} & S_{43} & S_{44} \end{bmatrix} \begin{Bmatrix} u_1 \\ iw_1 \\ u_2 \\ iw_2 \end{Bmatrix}$$

$$S_{11} = \frac{1}{t}\cos ksd \ \sin ktd + s \sin ksd \cos ktd$$

$$S_{12} = S_{21} = \frac{3-t^2}{1+t^2}(1 - \cos ksd \ \cos ktd) + \frac{1+2s^2t^2-t^2}{st(1+t^2)} \sin ksd \ \sin ktd$$

$$S_{13} = S_{31} = -s \sin ksd - \frac{1}{t} \sin ktd \qquad \text{Equation 2.61}$$

$$S_{14} = S_{41} = \cos ksd - \cos ktd$$

$$S_{22} = \frac{1}{s}\sin ksd \ \cos ktd + t \cos ksd \sin ktd$$

$$S_{23} = S_{32} = -\cos ksd + \cos ktd$$

$$S_{24} = S_{42} = -\frac{1}{s}\sin ksd - t \sin ktd$$

$$S_{33} = \frac{1}{t}\cos ksd \ \sin ktd + s \sin ksd \cos ktd$$

$$S_{34} = S_{43} = \frac{t^2 - 3}{1 + t^2}(1 - \cos ksd \ \cos ktd) + \frac{t^2 - 2s^2t^2 - 1}{st(1 + t^2)} \sin ksd \ \sin ktd$$

$$S_{44} = \frac{1}{s} \sin ksd \ \cos ktd + t \cos ksd \sin ktd$$

Where

$$D = 2(1 - \cos ksd \cos ktd) + (st + \frac{1}{st}) \sin ksd \sin ktd \qquad \text{Equation 2.62}$$

As a special case of out-of-plane motion, the dynamic stiffness matrix for half-space is derived by considering only the outgoing wave incident $A_P = A_{SV} = 0$. This leads to the following:

$$\begin{Bmatrix} P_0 \\ iR_0 \end{Bmatrix} = kG^* \begin{bmatrix} \frac{is(1 + t^2)}{1 + st} & 2 - \frac{1 + t^2}{1 + st} \\ 2 - \frac{1 + t^2}{1 + st} & \frac{it(1 + t^2)}{1 + st} \end{bmatrix} \begin{Bmatrix} u_0 \\ iw_0 \end{Bmatrix} \qquad \text{Equation 2.63}$$

The subscript 0 refers to the free surface of the half-space.

2.6.3.2 Out of Plane Wave Motion

The nomenclature of in-plane wave propagation is shown in Figure 2.9. Using the same procedure as in-plane motion for out-of-plane motion we have the following:

$$v(z,x) = v(z)\exp(-ikx) \qquad \text{Equation 2.64}$$

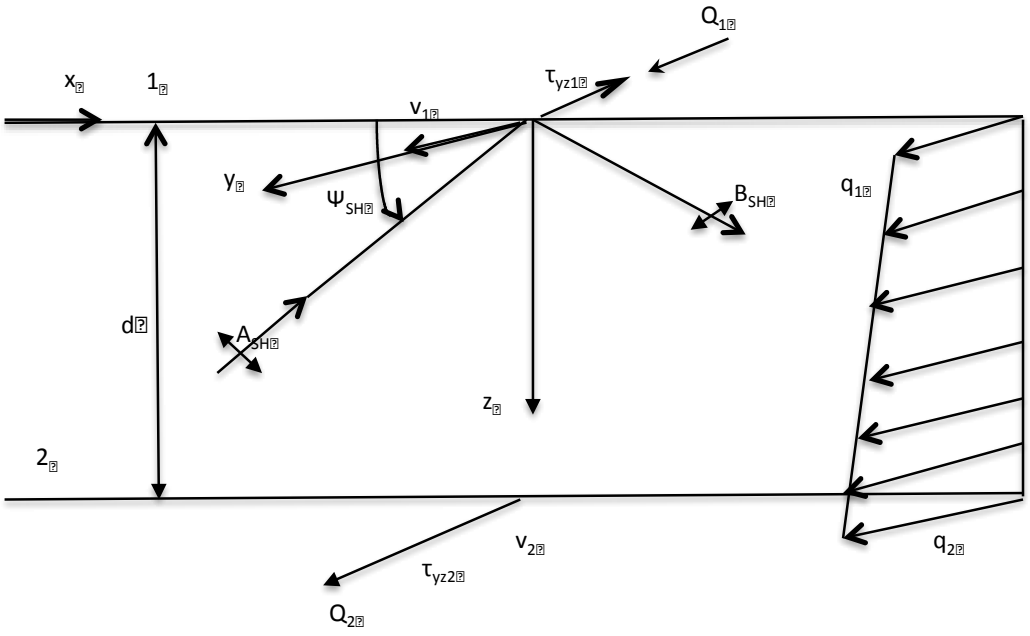

Figure 2.9 Nomenclature of wave propagation in a layer representing out of plane motion (Wolf, 1985)

The transfer matrix in this case is as follows:

$$\begin{Bmatrix} v_2 \\ \tau_{yz2} \end{Bmatrix} = kG^* \begin{bmatrix} \cos ktd & (ktG^*)^{-1} \sin ktd \\ -ktG^* \sin ktd & \cos ktd \end{bmatrix} \begin{Bmatrix} v_1 \\ \tau_{yz1} \end{Bmatrix} \quad \text{Equation 2.65}$$

And stiffness matrix is as follows:

$$\begin{Bmatrix} Q_1 \\ Q_2 \end{Bmatrix} = \frac{kG^*}{\sin ktd} \begin{bmatrix} \cos ktd & -1 \\ -1 & \cos ktd \end{bmatrix} \begin{Bmatrix} v_1 \\ v_2 \end{Bmatrix} \quad \text{Equation 2.66}$$

For half-space when there is no incoming wave incident, the force at the free surface equals the following:

$$Q_0 = iktG^* v_0 \quad \text{Equation 2.67}$$

For solving the stiffness matrix problem, one needs to take the following steps. First, the sources should be transformed from the space-time domain into the frequency-wavenumber domain. This step is done in closed-form solution for ideal load. Next, for each frequency and wavenumber, the stiffness matrix of each layer, and by superposition, the stiffness matrix of the whole layered system is formed (or assembled). By solving this matrix, the displacements are obtained in the frequency-wavenumber domain. Finally performing an inverse transform into the space-time domain will produce the desired results.

The next chapter discusses the basis for acoustic testing of concrete decks, including SASW and MASW.

3 Ultrasonic Seismic Methods for Concrete NDT

The material property of concrete is an essential parameter in bridge-deck evaluation. Several surface-wave seismic methods have been developed to enable in-situ evaluation of material properties. Ultrasonic seismic methods have gained popularity among the in-situ methods in the recent decade because of their accuracy in detecting certain types of defects (Gucunski N. , et al., 2013). They are also excellent candidates for post-construction quality control. They work by measuring the properties of the ultrasonic waves like velocity attenuation, and various wave propagation phenomena, like dispersion. Three ultrasonic seismic methods are commonly used: impact echo (IE), ultrasonic body-waves (UBW) and ultrasonic seismic waves (USW). IE is a reflection base method. It measures and characterizes reflections from internal flaws and external surfaces and can determine the extent and location of the internal flaws. UBW and USW work by measuring body wave and surface-wave velocities. Due to the relationships between velocity and elastic modulus of the material, USW and UBW results can be related to material properties. Figure 3.1 shows the schematic basics of USW, UBW and IE.

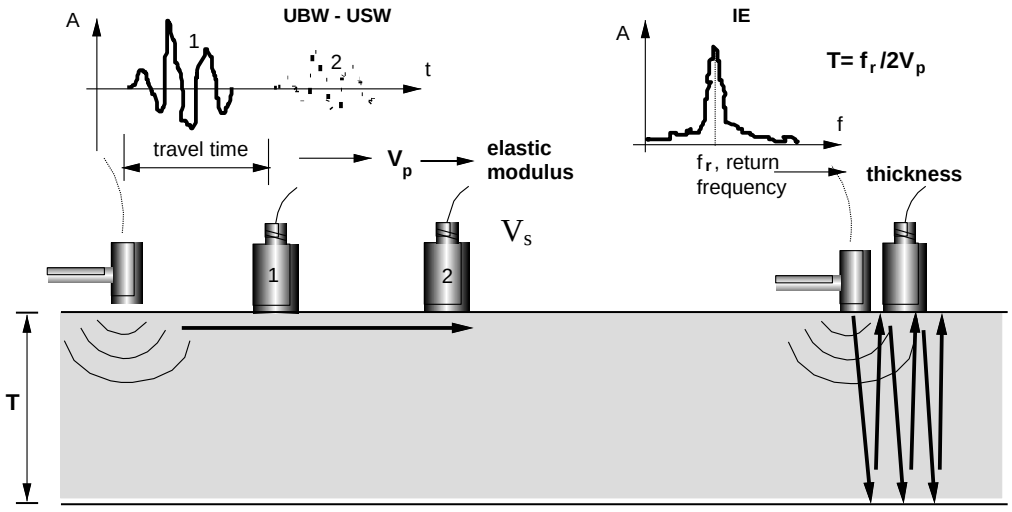

Figure 3.1 Basics of USW,UBW and IE (Gucunski, Consolazio, & Maher, 2000)

Evaluating material properties of concrete using nondestructive ultrasonic seismic methods is of primary interest for this research. Due to the higher amplitude of surface-waves, USW has an advantage over the other seismic methods in NDT testing of bridge-decks. In the following sections a brief introduction to commonly used surface-wave methods is presented.

3.1 Spectral Analysis of Surface-Waves (SASW)

The spectral analysis of surface-waves (SASW) method is a surface seismic method for measuring in-situ elastic modulus and thicknesses developed for soils and commonly used on pavements. The method was first introduced by Heisey et al (Heisey, Stokoe II, & Meyer, 1982) and then developed by other researchers at University of Austin (Nazarian, Stokoe II, & Hudson, 1983; Nazarian, Stokoe II, Briggs, & Rogers, 1987).

Several publications describe the SASW method in detail (Aoud, 1993; Stokoe II, Wright, Bay, & Roesset, 1994; Stokoe II & Santamarina, 2000; Sevensson, 2001). The method works based on measuring the surface-wave velocity (phase-velocity) between two sensors.

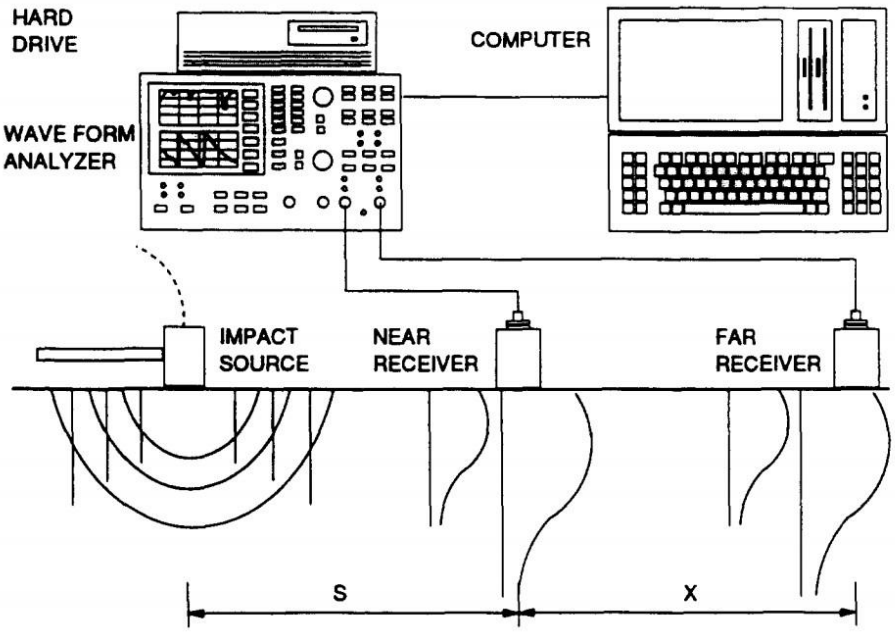

Figure 3.2 A Schematic procedure of SASW test (Gucunski & Woods, 1992)

The SASW testing is divided into three phases: 1) data collection in the field, 2) dispersion curve analysis, and 3) inversion process to obtain the shear-wave velocity profile. A schematic of the method is presented in Figure 3.2. Elastic waves are generated by an impact on the surface of the system. Two receivers are used to detect the wave signal at fixed locations. These signals are recorded and analyzed by the signal analyzer

to develop dispersion curve. To reduce the effect of noise the test is repeated multiple times.

In order to calculate the dispersion curve, the phase difference between the two recorded signals is computed using the phase of the cross power spectrum to obtain the phase velocity between the two time histories. The result is a wrapped phase angle within the limits of -180 and 180 degrees. After unwrapping the phase difference, phase-velocity is determined using Equation 3.1, where $\Delta x$is the distance between sensors, ω is the frequency, $\Delta\emptyset$ is the phase difference and V_{ph} is the phase-velocity. Phase-velocity is plotted against wavelength to better represent the wave propagation through the cross section of the medium. Figure 3.3 shows the steps for developing a dispersion curve for a 20cm concrete bridge-deck with a uniform thickness. The dashed line shows the unwrapped phase angle where the solid line is the wrapped version. The dispersion curve is plotted in both frequency and depth domains

$$V_{ph} = \frac{\omega \Delta x}{\Delta \emptyset} \qquad \text{Equation 3.1}$$

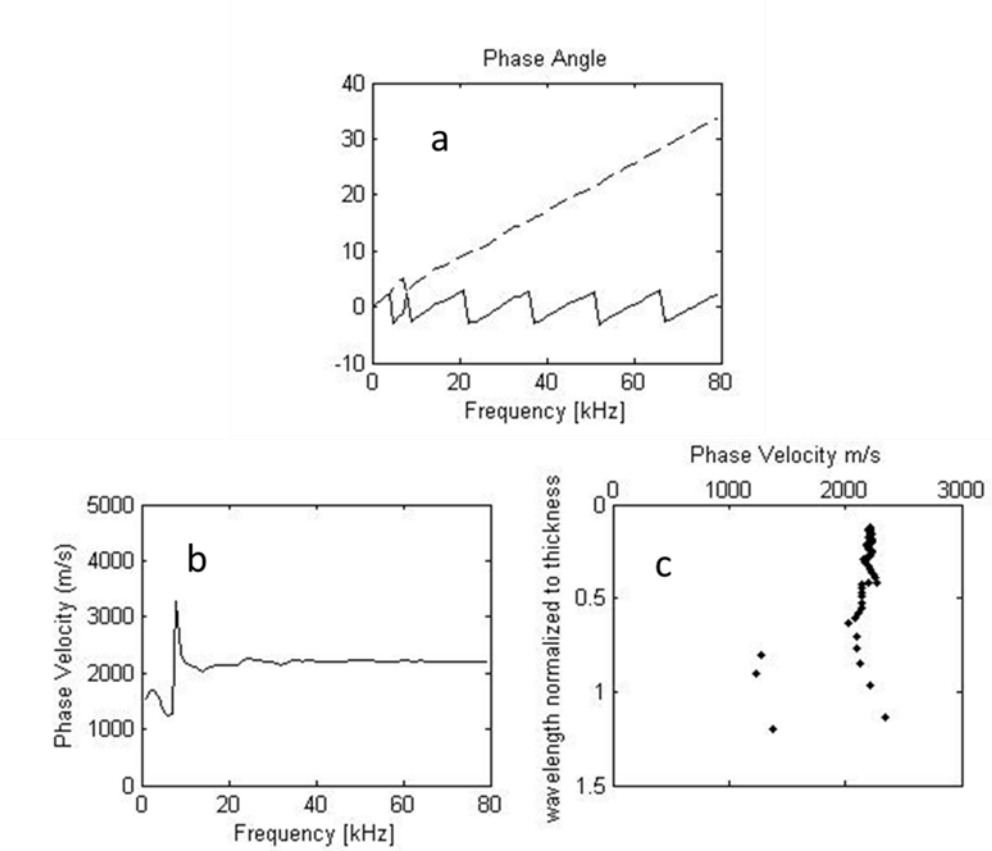

Figure 3.3 a) Unwrapped and rapped phase angle in the top left b) phase-velocity vs. frequency in the bottom left and c) phase-velocity vs. wavelength in the bottom right calculated for a 20cm solid concrete bridge-deck with a Rayleigh wave velocity of 2200m/s

After the experimental dispersion curve is established, the shear-wave velocity profile is obtained using the inversion process. This process has proven to be challenging. Earlier, Nazarian (Nazarian S. , 1984) modeled and compared all the possible scenarios to precisely match the measured dispersion curve with the theoretical curve This process

was time consuming and not accurate enough (Williams & Gucunski, 1995). Artificial Intelligence (AI) methods such as Neural Network (Williams & Gucunski, 1995; Wu, Wang, Abdallah, & Nazarian, 2002) and genetic algorithms (Al-Hunaidi, 1998) were then used to match the results. All these efforts have improved the overall performance of SASW method. However, the main limitation of this method is that only one phase-velocity can be evaluated at each frequency because just two sensors are used. The SASW method cannot detect different modes of propagation over a pavement system as described earlier in the Lamb wave discussion; it simply measures the superposition of all the propagating waves at the specific receiver location.

There have been multiple efforts to commercialize the use of seismic methods for the testing of pavements and bridge decks. Portable seismic property analyzer (PSPA) is one of these devices. While the description of the approach below is not used directly in this research, it is provided to give the reader necessary background on the topic.

3.2 Portable Seismic Property Analyzer (PSPA)

The PSPA was developed as a pavement-testing device, that integrates all three of the ultrasonic techniques previously described (UBW, USW, IE). It is an extension of the seismic pavement analyzer (SPA) at the University of Texas at El Paso and is produced by Geomedia Research and Development, Inc., EL Paso. As illustrated in Figure 3.4 a, the device consists of three main elements. The core of the system is a sensor box: a box that contains a solenoid-type impact hammer and two high-frequency accelerometers. All controls and data acquisition are in a computer that is connected by a serial cable to the sensor box.

In order to simplify the bridge-deck evaluation, information is collected at preset locations. In case of PSPA, these locations usually follow a 1X1 ft. to 2X2 ft. grid, depending on the needed spatial resolution of the concrete modulus (Figure 3.4 b). Testing via the PSPA is simple and relatively fast. A single point takes less than 30 seconds (Gucunski, Slabaugh, Wang, Fang, & Maher, 2007). The sensor box is placed at the test point and a series of impacts (6-10) of 50 μs duration are applied. The acceleration histories are recorded and analyzed. The frequency range of testing is between 2 and 30 kHz and it is fairly insensitive to traffic-induced vibrations.

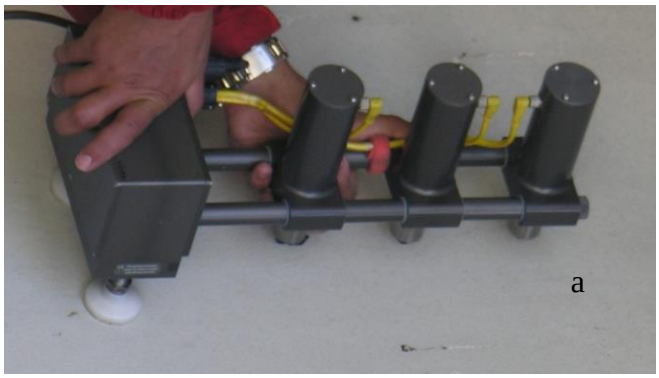

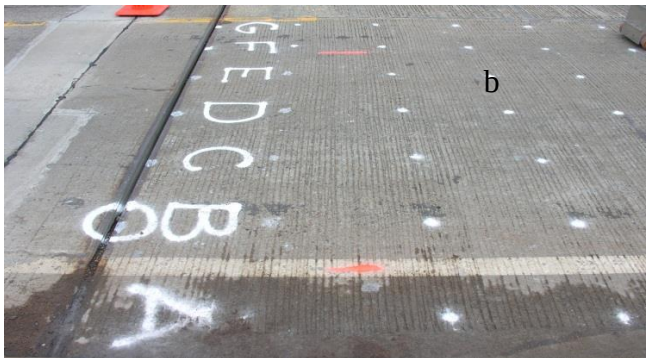

Figure 3.4 a) PSPA sensor box. b) The grid system used for PSPA for bridge-deck testing c) Testing with PSPA using grid system

A snapshot of PSPA program menu is presented in Figure 3.5. The frequency range that is used in the dispersion analysis is marked by a yellow bar. The dispersion curve for the test point is plotted across the thickness, and averaged for the test point.

3.2.1 Examples of Field Implementation of PSPA

PSPA testing results are commonly described in terms of shear and Young's moduli (or P- and S-wave velocity) distributions. A bridge-deck evaluation was conducted during September 17-22, 2009, in Haymarket, VA, on U.S. Route 15 (James Madison Highway) over Interstate 66 (I-66), approximately 38 miles west of Washington, DC. The elastic modulus distribution for the deck is shown in Figure 3.6. While in this particular case, variations in moduli are rather large; variation in concrete modulus along the deck does not necessarily indicate deterioration. Such variations can often be introduced at the time of construction as a result of material variation and placement procedures. Therefore, only periodic measurements to detect changes in the concrete modulus can be useful in identifying the deterioration processes (Gucunski & Nazarian, 2010).

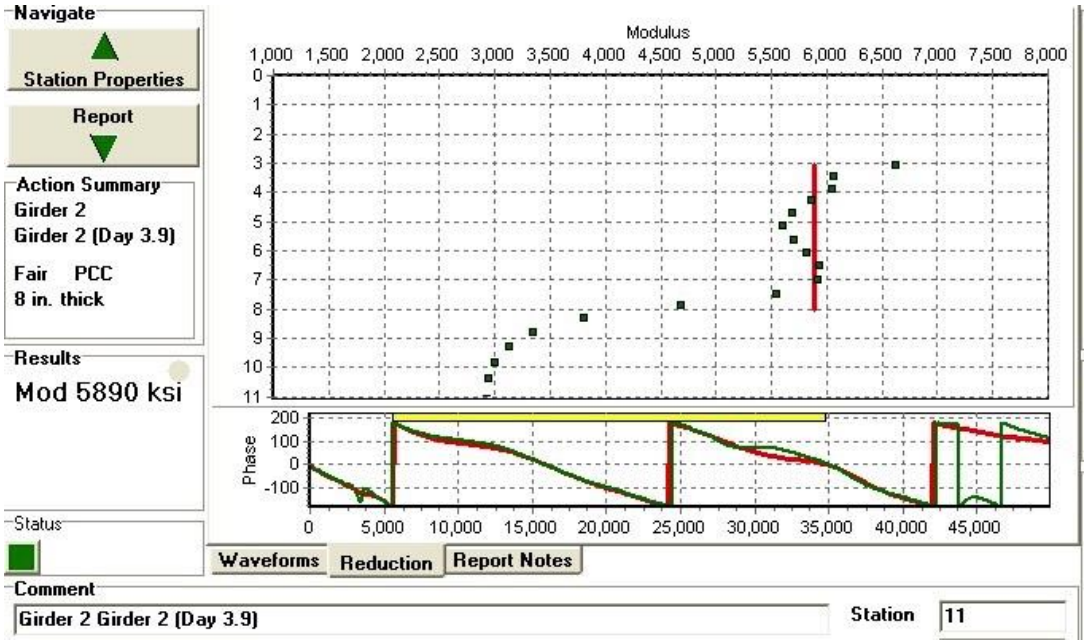

Figure 3.5 PSPA software program user interface

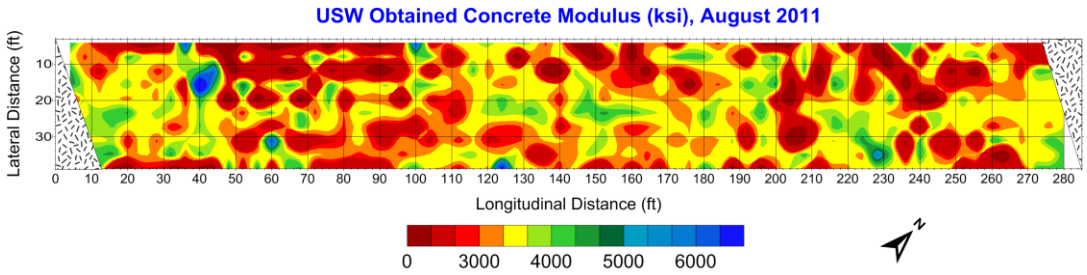

Figure 3.6 Modulus variation maps for the Virginia bridge survey 2011 from USW

As shown in Figure 3.5 the final results in PSPA testing for a specific point are given in the form of average modulus of concrete through the thickness. By using the average modulus for each test point one can get an estimate of the concrete quality (Figure 3.6).

In recent years a newer method of surface-wave testing, called multi-channel analysis of surface-waves (MASW), has been implemented in the assessment of concrete slabs (Ryden, Choon, & Miller, 2003). The basics of this method are similar to those of SASW. The major difference is in the number of sensors that are used to gather the information. The MASW method can facilitate a more accurate inversion process because of the extra available information. In the next section, the MASW method will be discussed.

3.3 Multichannel Analysis of Surface-waves (MASW)

The MASW method overcomes some of the common practical issues associated with using the SASW method. In general the advantages of using the MASW method can be summarized as following (Park, Miller, & Xia, 1998):

1. Multiple sensors enable us to be free of the effect of the sensor location on any specific Lamb wave mode of interest. Still, the receiver positioning still has to be taken into account during analysis.
2. It has the benefit of avoiding the data reduction and forming (or evaluating) the experimental dispersion curve
3. It is considerably faster, as it covers more area and takes less time to post process the data
4. The MASW method emphasizes the near-field and far-field effects whereas SASW is known to have problems with such effects.

When using only a pair of sensors, the source and receiver arrangement should be established based on the site properties (Roesset, Chang, Stokoe II, & Auoad, 1990); this can be challenging because of uniqueness of each site. The effect of the noise recorded in only one pair of receivers is another issue that makes it appealing to use more sensors. The dispersion analysis for the SASW method is complicated and needs the operator's best judgment. This is a common issue known as near-field and far field effects. There is also less need to repeat the test, because more sensors are recording at the same time (Ryden N. , 2004).

As mentioned earlier, the basics of the MASW are similar to those of the SASW except the number of sensors and the dispersion analysis. It is based on N equally spaced signals collected at the surface. Each sensor is connected to a multichannel recording device. The same impact source as in SASW method (i.e. a small ball or a solenoid) could be used. The frequency content of the generated wave is defined by the characteristics of the test site and impact source. Based on these characteristics a specific size of the actuator is chosen. For bridge decks because of similarity in site characteristics this is constant. The smaller the impact source is, the higher the frequency content of the generated wave become.

As in SASW, the testing procedure for MASW surveys usually consists of three steps: Data Acquisition, dispersion analysis and inversion analysis. Multichannel shot gatherers are used. The data is transformed into velocity-frequency domain. Despite the SASW method the multichannel approach does not attempt to calculate individual phase-velocity lines, but constructs an image-space plot in which dispersion trends are identified from the pattern of energy accumulation in this space (Park, Miller, & Xia, 1998). The detailed dispersion analysis of the MASW method will be discussed in chapter 5.

4 Dispersion Analysis for Wave Propagation in Layered Media

4.1 Dispersion Analysis

In order to study the dispersive characteristics of surface-waves, an appropriate imaging process is needed. Conventionally, this process was done by analyzing a pair of observations. SASW method is illustrated here using FEM simulation of the test. The first step is to transfer the recorded signals from the time domain into the frequency domain. Then the phase of cross-power spectrum and the coherence, between the two records are calculated. In areas of high coherence the phase-shift is unwrapped and used to calculate the phase-velocity from Equation 3.1:

$$V_{ph} = \frac{\omega \Delta x}{\Delta \emptyset}$$

Sometimes it is necessary to apply a window function on the recorded signal to reduce the effects of reflections and body-waves on the phase-velocity.

Figure 4.1 shows the accelerations recorded from a FEM model of a concrete specimen. The sensors are 5 cm apart, and the shear-wave velocity of the slab is 2500 m/s. The acceleration spectra of the records are represented in Figure 4.2. Using the records from locations at 10 cm and 25 cm, the SASW analysis was performed. Figure 4.3 shows the phase angle of cross-power spectrum. The dashed line shows the unwrapped phase angle where the solid line is the wrapped version. The dispersion curve is plotted in both frequency and depth domains. Since the signals are recorded synthetically, the coherence

is 1 in the absence of environmental noise. The dispersion curve approaches the Rayleigh wave velocity of the deck at higher frequencies. At lower frequencies at Figure 4.3-c the dispersion curve is branching. This phenomenon is caused by the existence of multiple modes with strong amplitudes. With just two sensors, the effect of multiple modes cannot be separated.

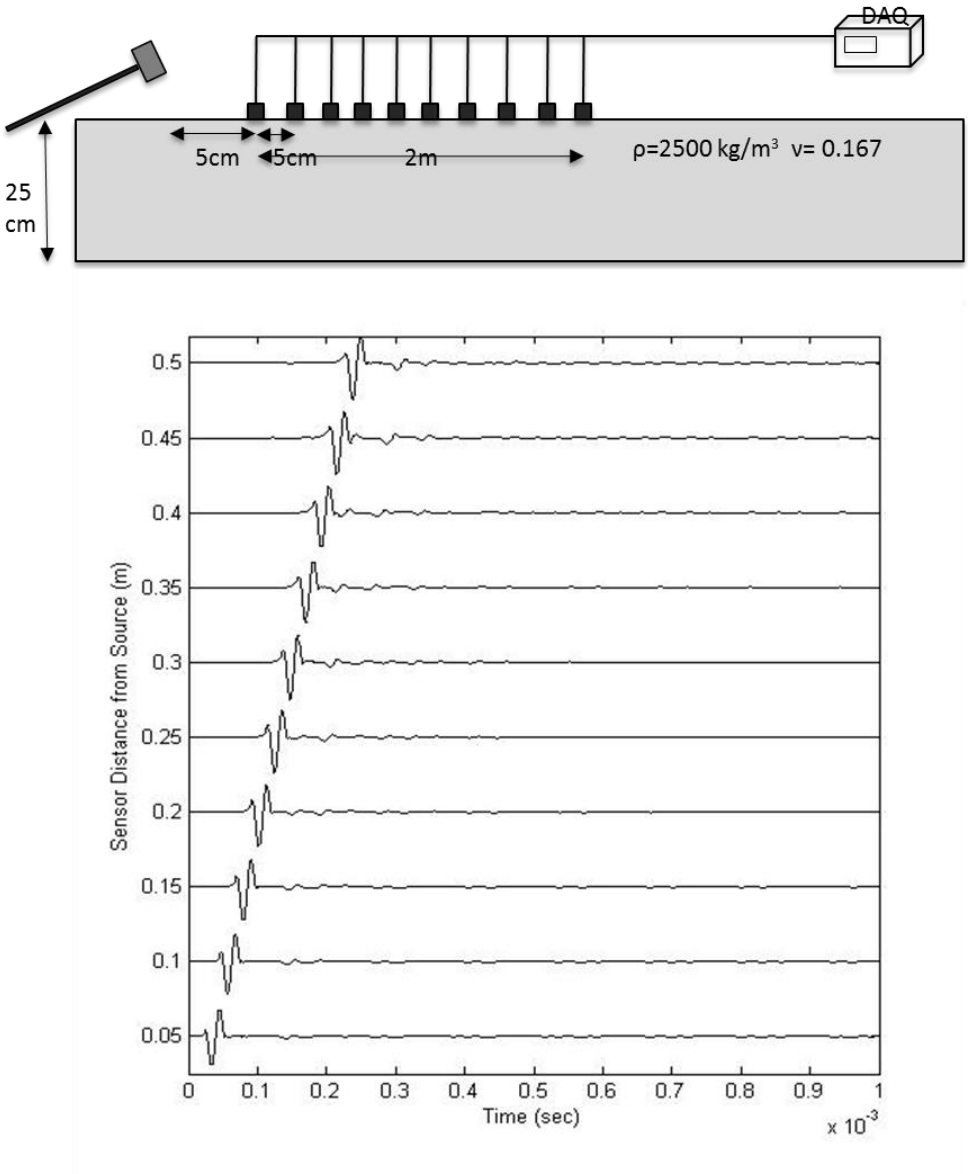

Figure 4.1 Recorded accelerations from FEM model of a concrete slab

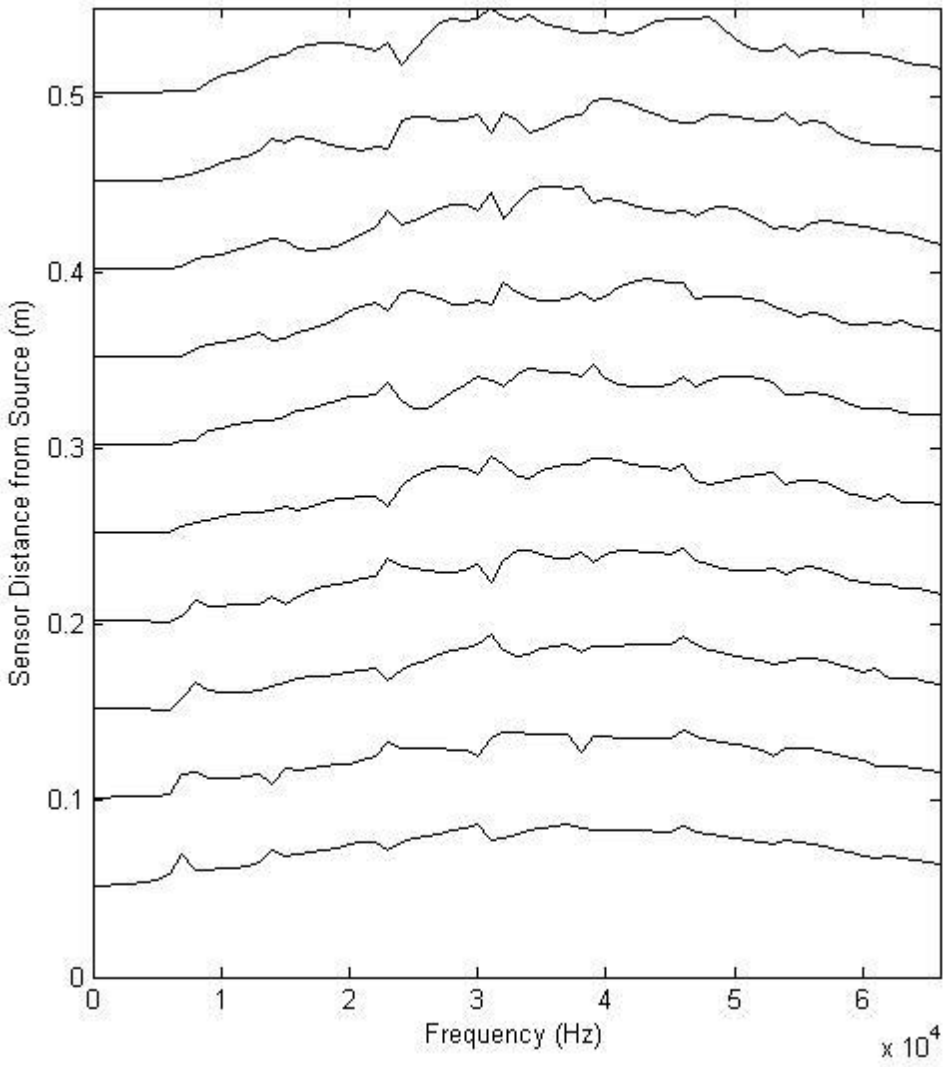

Figure 4.2 Acceleration spectra from FEM model

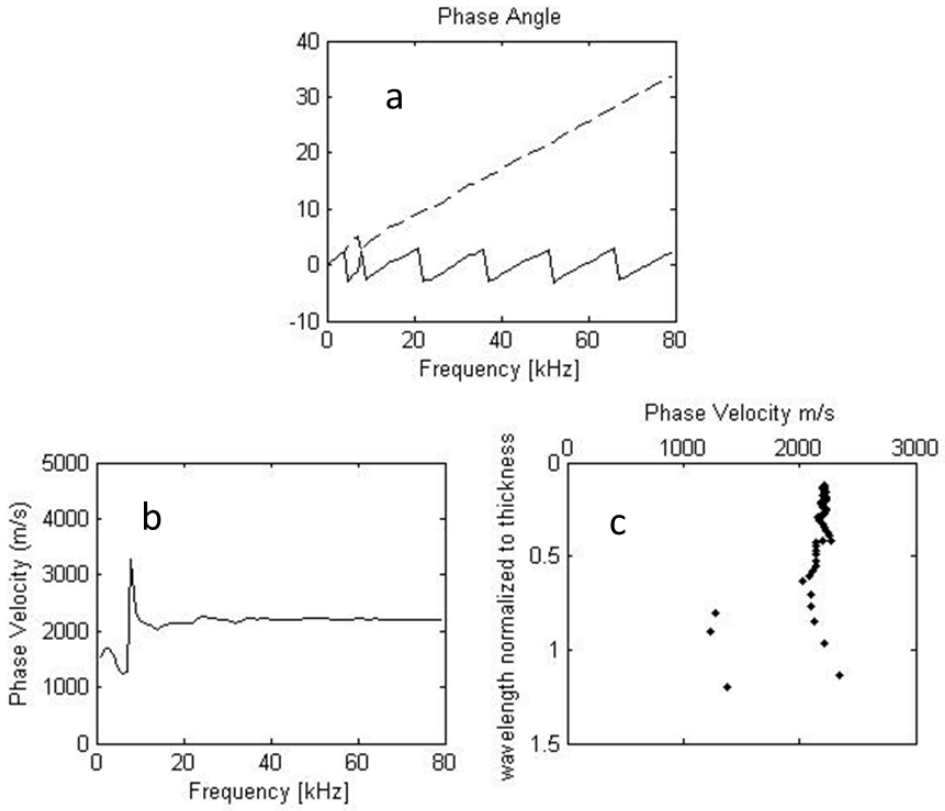

Figure 4.3 Typical SASW analysis on signals recorded at 10 cm and 25 cm from the source obtained from FEM of a concrete deck a) Phase of cross-power spectrum, b) Dispersion Curve vs. Frequency, c) Dispersion Curve vs. Depth

Using several records simultaneously, like in the MASW testing, offers some advantages over the conventional SASW method. The main advantage is that all of the data is used to construct the final dispersion surface. Therefore, there is no subjective selection of data, i.e. no time history windowing or filtering of low-coherence frequencies. Also multiple modes can be detected at each frequency that can be useful in the inversion process.

The MASW method takes advantage of this benefit. In the MASW method, the time-space domain is transformed into either the frequency-wavenumber or the frequency-phase-velocity domain. Several methods have been developed to extract the dispersion curve from the multichannel test data. The traditional f-k method (Gabriels, Snieder, & Nolet, 1987) is the former type, whereas the pi-omega transformation (McMechan & and Yedlin, 1981) and the phase-shift method (Park, Miller, & Xia, 1998) are two instances of the latter type. The phase-shift method achieves higher resolution than the pi-omega method (Park, Miller, & Xia, 1998; Moro, Pipan, Forte, & Finetti, 2003), and is used in this research.

A multi-channel recording set is illustrated in Figure 4.4. In the phase-shift method, a N-channel record mr_N is defined as an array of N traces collected: $mr_N = r_i$ (i=1, 2, …, N). And in the frequency domain as it is $MR_N(\omega) = R_i(\omega) = FFT[r_i]$. $R_i(\omega)$ can be decomposed into its amplitude $A_i(\omega)$ and phase $P_i(\omega)$.

$$R_i(\omega) = A_i(\omega)P_i(\omega) \qquad \text{i=1,2, …,N} \qquad \text{Equation 4.1}$$

Since the amplitude does not carry much information about the phase-velocity, $R_i(\omega)$ can be normalized without any significant loss of information.

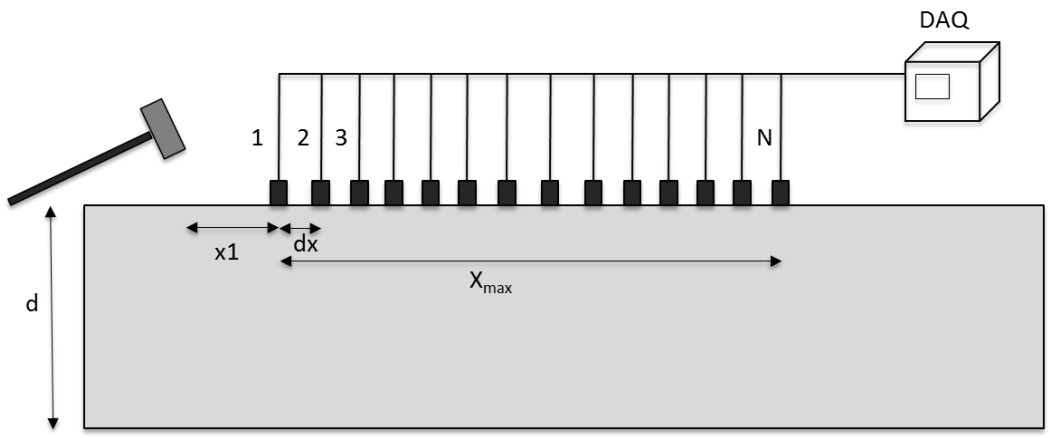

Figure 4.4 Multi-channel recording schematic

The phase-shift method can be divided into the following steps (Ólafsdóttir, 2014):

1. The first step is to transfer all the data into the frequency domain by performing a fast Fourier transform (FFT). The data is thus decomposed into individual frequency steps.

$$R_i(\omega) = FFT(r_i) \qquad \text{i=1,2, …,N} \qquad \text{Equation 4.2}$$

2. Then second step is to normalize the data by dividing the complex value by its amplitude (Figure 4.5 a and b).

$$R_{i,norm}(\omega) = \frac{R_i(\omega)}{|R_i(\omega)|} = P_i(\omega) \qquad \text{Equation 4.3}$$

3. In the third step, for a given testing phase-velocity and frequency in the range of interest, a number of phase-shifts are calculated to compensate for the time delay that corresponds with a specific offset.

$$\delta_{i,\tau} = \omega \, {(x_1 + (i-1)dx)}/{C_T} \qquad \text{Equation 4.4}$$

4. The phase-shifts are then applied to individual components of each trace, and summed together (Equation 4.5). $C_T$is phase-velocity and $A_s(\omega, C_T)$ is the energy.

$$A_s(\omega, C_T) = e^{-i\delta_{1,\tau}} R_{i,norm}(\omega) + e^{-i\delta_{2,\tau}} R_{2,norm}(\omega) + \cdots + e^{-i\delta_{N,\tau}} R_{N,norm}(\omega) \qquad \text{Equation 4.5}$$

5. Steps 3 and 4 are then repeated for all of the frequency steps using the varying phase-velocity steps.
6. The summed amplitude of the transformed energy is then plotted in the frequency-phase-velocity domain.

Figure 4.5 illustrates 40 synthetic sinusoidal signals that were collected at 5cm steps. The frequency of the propagation is 10 kHz and the phase-velocity is 1000 m/s. Each line is showing one sinusoidal signal in time domain. Using the phase-shift to calculate the amplitude of the summed sinusoid curves, the 2D scanned curve is plotted in Figure 4.6 across the different phase velocities. This plot has one main lope that the peak

corresponds to the designated phase-velocity. The sharpness affects the resolution of the dispersion curve. Figure 4.6 shows the effect of the number of the traces on the sharpness of the main lope. The solid line represents using 40 traces. In case of a dashed line, only 4 traces are used to calculate the summed amplitude. A parametric study is performed in chapter 5 to determine the optimal sensor arrangement.

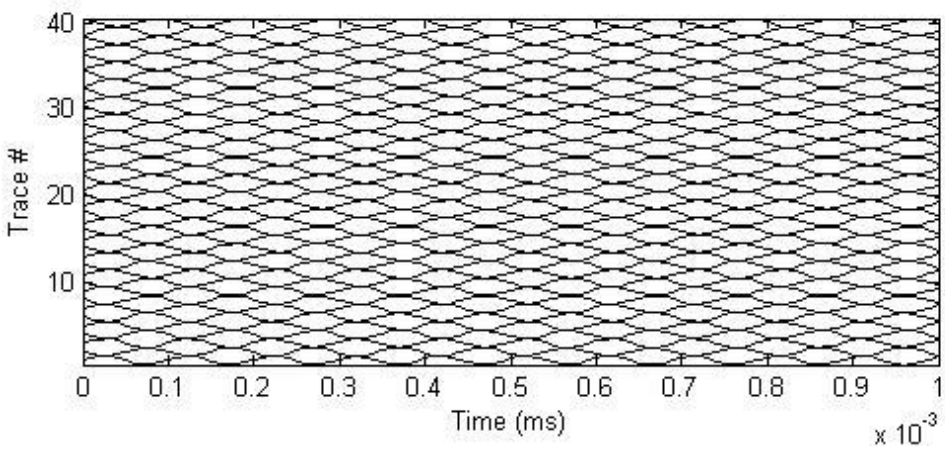

Figure 4.5 Synthetic record in which a sinusoidal trace with single frequency (10 kHz) and phase-velocity (1000 m/s) are displayed

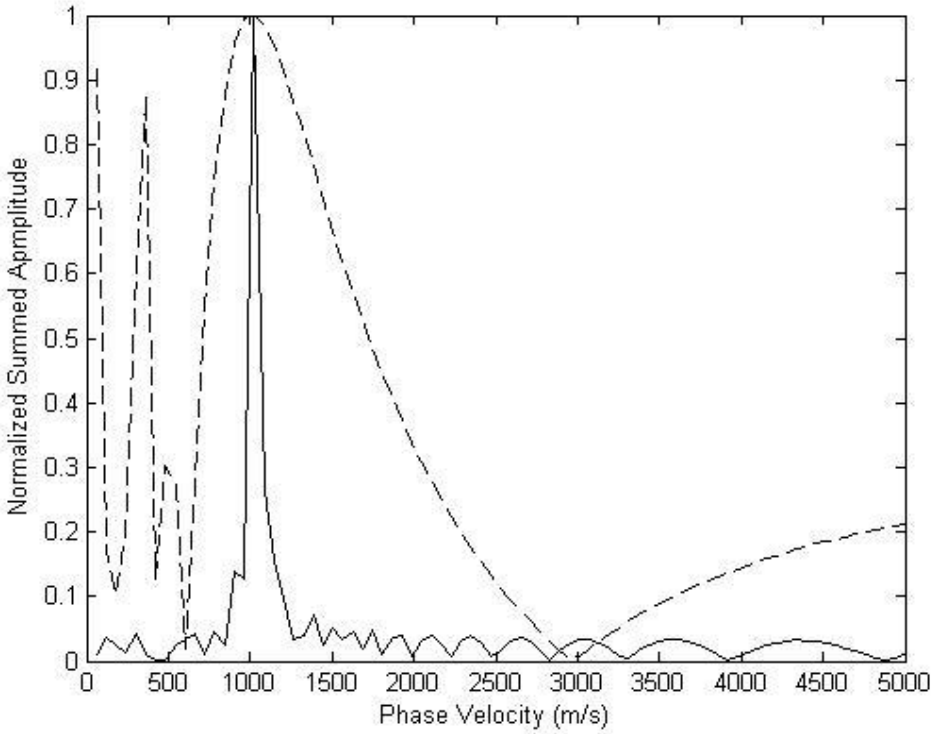

Figure 4.6 Normalized summed amplitudes for different number of traces. Solid line represents N=40 and dashed line is for N=4.

To identify the dispersion curve, the above process is repeated for all the different frequency components. The 2D curves for summed amplitudes are gathered and plotted as a 3D image that is a function of frequency and phase-velocity. Display of all summed energy in frequency-phase-velocity space shows a pattern of energy accumulation that represents the dispersion curve.

4.2 Wave Propagation in a Uniform plate

Wave propagation in a uniform plate is discussed here. Lamb theory discussed in chapter 2 is used to for this analysis. A root-finding algorithm called LAMBDISPERSE is developed in MATLAB to solve Equation 2.37 and Equation 2.38 . Figure 4.7 shows the Lamb modes in wave propagation in a uniform plate along with the plate specifics.

The two fundamental modes, A_0 and S_0, are the only modes that exist at the very low frequency. S_0 starts at a quasi-longitudinal wave velocity that is the same as P-wave velocity. On the other hand, both of these modes approach the Rayleigh wave velocity at the higher frequencies. In this example, Rayleigh wave motion develops at around 20 kHz. It can be shown analytically that Equation 4.2 and Equation 4.3 reduce to the Rayleigh wave dispersion equation at the infinity frequency. This is because, at these high frequencies, the plate with finite thickness can be considered as a semi-infinite medium for the propagating wave. All of the other higher modes approach to the shear-wave velocity at higher frequencies. Another fact about wave propagation in uniform plates is that all the symmetric modes have a straight segment in which the phase-velocity is equal to the quasi-longitudinal wave velocity.

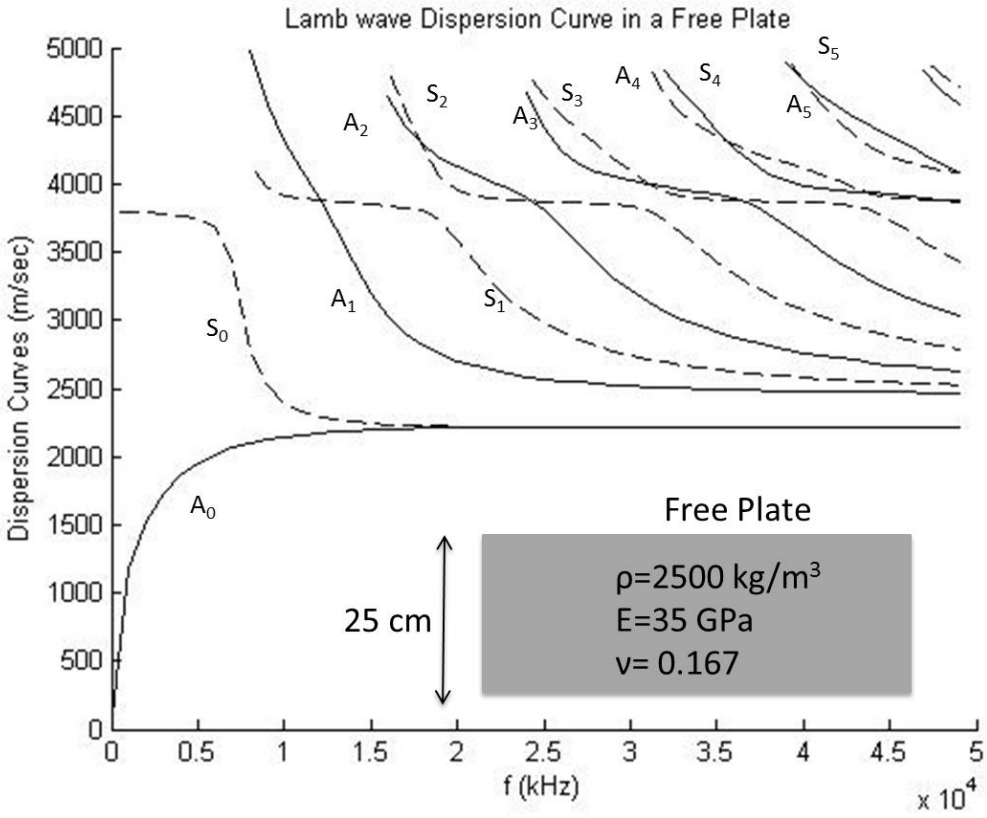

Figure 4.7 Lamb wave dispersion curve for a free concrete plate. Solid line represents the antisymmetric modes and dashed line is for symmetric modes.

A sensitivity analysis was performed to determine the effect of plate properties on Lamb wave modes. Figure 4.8 shows the effect of 10% increase in elastic modulus, density, Poisson's ratio, and plate thickness on Lamb wave modes (shown as a dashed line). This result is then compared to the reference model (which is shown as a solid line). A_0 mode is widely used in bridge-deck evaluations. From Figure 4.8 it is clear that this mode is not very sensitive to the plate properties. In order to increase the sensitivity of the testing information gathered from higher modes should be utilized. Also the Poisson's ratio has the least effect on the Lamb modes, especially in a higher frequency range. At higher

Poisson's ratios, this affect is more visible (Ryden, Choon, & Miller, 2003).

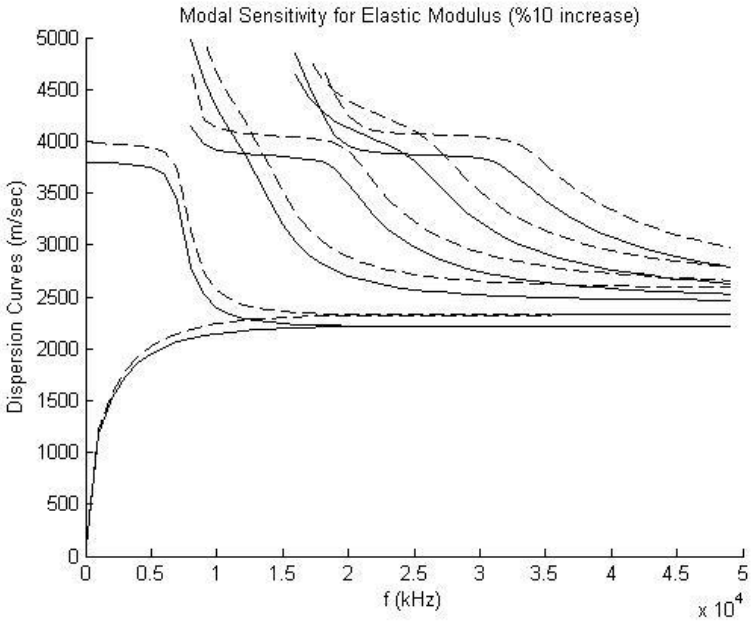

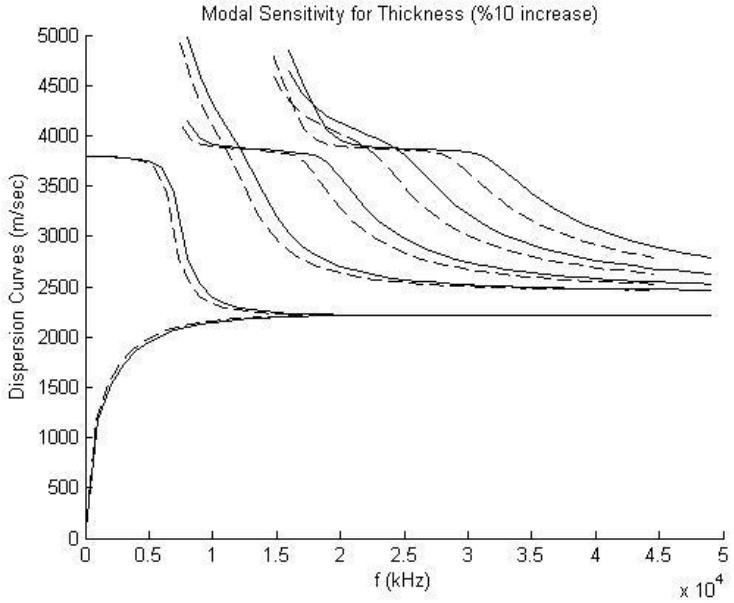

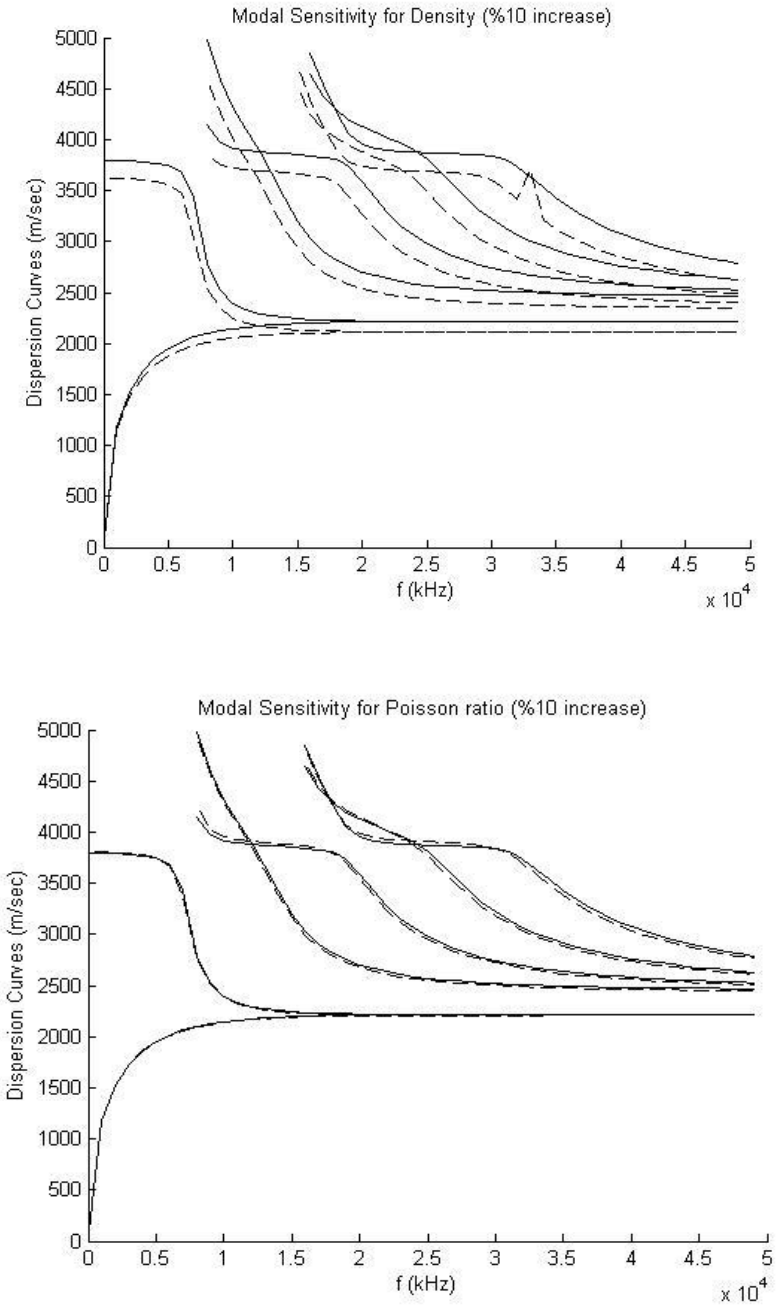

Figure 4.8 Effect of 10% increase in plate properties on the Lamb wave modes.

Solid line represents the base model.

Lamb wave propagation in plates is similar to ripples cause by a splash (Graff, 1975).

The velocity of individual ripples is just like phase-velocity. They can travel faster than the group, and in effect originate at the end of the group and die out at front. The in-plane velocity of energy propagation is called group velocity and is defined by the slope of dispersion curve.

$$C_G = \frac{d\omega}{dk} \qquad \text{Equation 4.6}$$

4.3 Wave Propagation in a Layered Medium

When waves propagate through a layered medium, the theoretical dispersion can be calculated using matrix techniques that are based on wave propagation theory. Surface wave test can be described as an axisymmetric problem with circular loading at the middle. This study uses the stiffness matrix technique proposed by Kausel and Roesset (Kausel & Roesset, 1981). The formulation for this method is presented in chapter 2. The stiffness matrix of a layer relates forces and displacements at the top and the bottom of a layer. In case of a half-space, the boundary conditions are met only for the top. In a layered medium a global matrix is built by combining the layer matrices for different layers that overlap at their interfaces. This matrix is then called a global stiffness matrix or system stiffness matrix. Figure 4.9 shows the schematic assembly process for a 3-layer system.

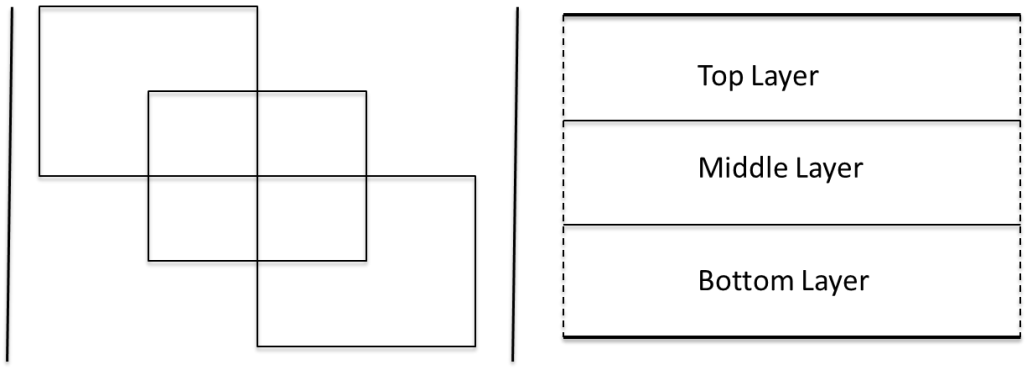

Figure 4.9 Schematic representation of 3-layer matrix assembly for the global stiffness matrix.

The following system of equations governs the dynamic response in layered media.

$$\boldsymbol{Su} = \boldsymbol{q} \qquad \text{Equation 4.7}$$

$\boldsymbol{S}$ represents the stiffness matrix, $\boldsymbol{u}$ represents the vector of displacement at layer interfaces and $\boldsymbol{q}$ is the external loading vector. Each point of the dispersion curve represents a solution to $\boldsymbol{S}$ that satisfies all the boundary conditions. To acquire Rayleigh-Lamb modes, the external load should be zero. The dispersion equation then becomes:

$$f(f,k) = det[\boldsymbol{S}] = 0 \qquad \text{Equation 4.8}$$

This equation can also be considered as an eigenvalue problem where eigenvalues are the phase velocities and the displacement vector is the mode shape as a function of depth.

Using the cylindrical coordination, the source is represented as a circular loading with intensity p and radius R_0 at the surface. It will be transformed from the spatial domain

into the frequency wave-number domain by using Fourier and Henkel's transformation. Equation 4.9 represents this transformation (Wolf, 1985).

$$\mathbf{q}(k,n) = a_n \int_{r=0}^{\infty} \mathbf{C}_n(k,r) \int_{\theta=0}^{2\pi} \mathbf{D}(n\theta)\mathbf{P}(r,\theta)\, d\theta\, dr$$

$$a_n = \begin{cases} \dfrac{1}{2\pi} & for\ \ n = 0 \\ \dfrac{1}{\pi} & for\ n \neq 0 \end{cases}$$

For a symmetric case

$$\mathbf{D}(n\theta) = \begin{bmatrix} |\cos n\theta| & & \\ & |-\sin n\theta| & \\ & & |\cos n\theta| \end{bmatrix} \qquad \text{Equation 4.9}$$

For an anti-symmetric case

$$\mathbf{D}(n\theta) = \begin{bmatrix} |\sin n\theta| & & \\ & |\cos n\theta| & \\ & & |\sin n\theta| \end{bmatrix}$$

$$\mathbf{C}_n(k,r) = \begin{bmatrix} \dfrac{\partial J_n(kr)}{k\partial R} & \dfrac{n}{kr}J_n(kr) & 0 \\ \dfrac{n}{kr}J_n(kr) & \dfrac{\partial J_n(kr)}{k\partial r} & 0 \\ 0 & 0 & -J_n(kr) \end{bmatrix}$$

For this study only the symmetric case is of interest. $\mathbf{q}(k,n)$ and $\mathbf{P}(r,\theta)$ are the loading vectors in frequency wave number domain and spatial domain respectively. $J_n(kr)$is the Bessel function of the first kind and n order. In an axisymmetric case with uniform loading with intensity of p_0 and radius of R_0 Equation 4.9 is simplified to the following:

$$q_0(k) = -\frac{p_0 R_0}{k} J_1(kR_0) \qquad \text{Equation 4.10}$$

By solving the matrix equation (Equation 4.7) the displacement components in the axisymmetric case $(w(k), u(k))$ will be obtained. The next step is to transform the displacement components from the frequency wavenumber domain back into the spatial domain. This is achieved by using the inverse Hankel's transform. The general equation is as follows:

$$\mathbf{u_s}(r,\theta) = \sum_{n=0}^{\infty} \mathbf{D}(n\theta) \int_{k=0}^{\infty} k\mathbf{C}_n(k,r)\, \mathbf{u}(k,n)dk \qquad \text{Equation 4.11}$$

Here, $\mathbf{u_s}$ and $\mathbf{u}$ represent the displacement vector in the spatial and frequency wave-number domains, respectively. For the case of surface displacements in an axisymmetric model surface Equation 4.11 will be simplified into the following:

$$\begin{bmatrix} u_{s0}(r) \\ w_{s0}(r) \end{bmatrix} = \int_{k=0}^{\infty} \begin{bmatrix} \frac{\partial J_0(kr)}{\partial r} & \\ & -kJ_0(kr) \end{bmatrix} \begin{bmatrix} u_0(r) \\ w_0(r) \end{bmatrix} dk \qquad \text{Equation 4.12}$$

By combining Equation 4.12 with Equation 4.10 in the case of unit vertical loading, vertical displacement can be written as follows:

$$w_{s0}(r) = -p_0 R_0 \int_{k=0}^{\infty} J_1(kR_0) J_0(kr) w_0^1(k) dk \qquad \text{Equation 4.13}$$

The algorithm used to solve the wave equation using stiffness matrix method was the program DISPER developed by Gucunski & Woods (Gucunski & Woods, 1991). This algorithm uses the stiffness matrix approach to evaluate the response of a layered medium to unit loading in the frequency-phase velocity domain.

Figure 4.10 shows Lamb wave dispersion curves for a three-layer system with air as half-space using the stiffness matrix method. Uniform plate dispersion curves are plotted as a dotted line for comparison purposes. The Lamb modes in the uniform plate match with the high-amplitude areas of dispersion surface. In the case of a layered system, most of the energy is concentrated in the fundamental modes, A_0 and S_0. There are traces of A_1 and S_1 modes in the dispersion curve, but the amplitudes decrease as the number of higher modes increases. Next, the shear wave velocity of each of the three layers is reduced to one half of the other two layers to study the effects of layer shear wave velocity on Lamb modes.

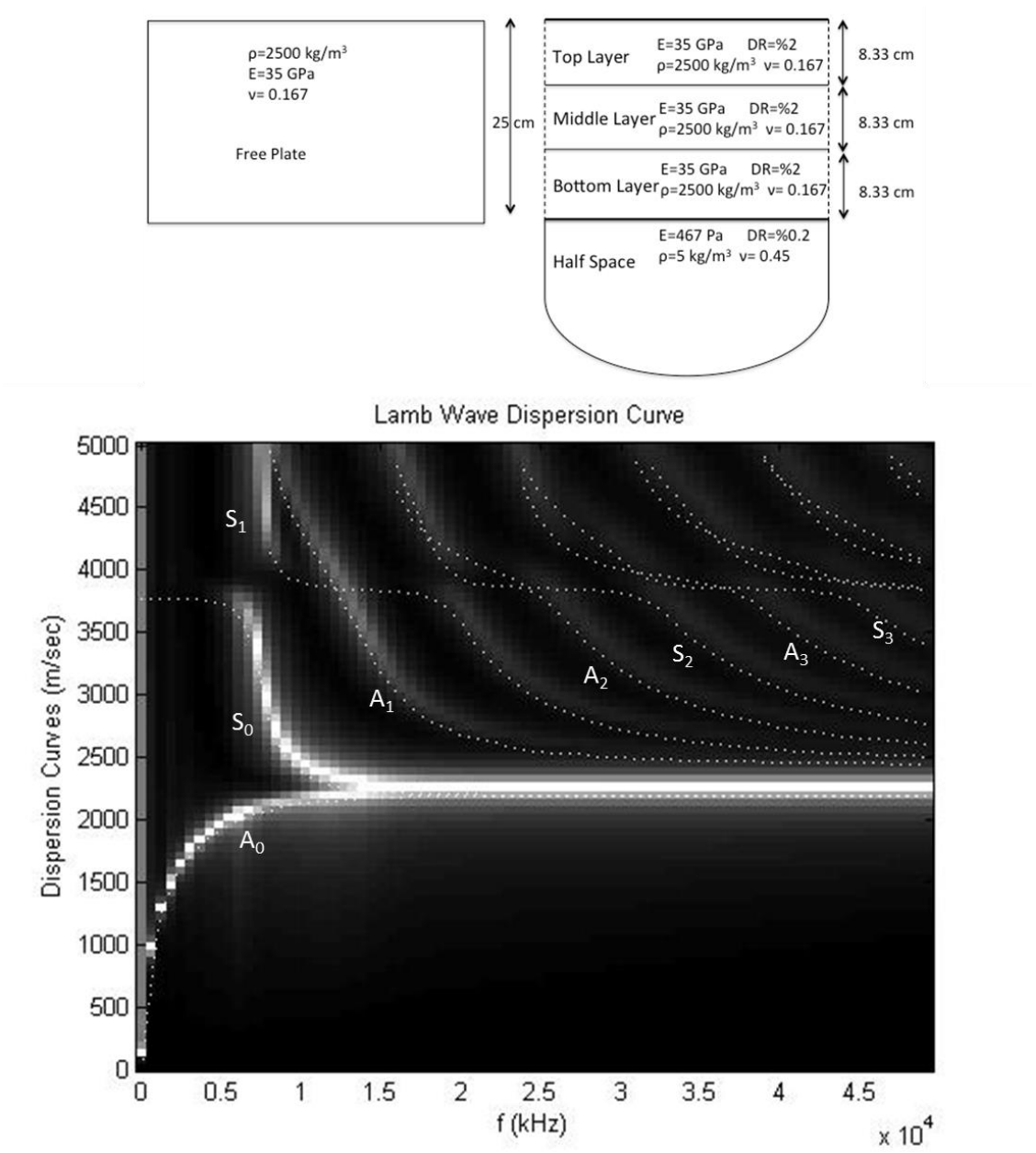

Figure 4.10 Lamb wave modes in case of a uniform plate shown as dotted lines, and a 3-layer homogenous system with half-space using matrix techniques

Figure 4.11 represents the Lamb dispersion curve for a 3-layer system with a soft top layer. Most of the energy is concentrated in the fundamental modes. Comparing this case to the uniform plate case, it can be observed that almost all of the Lamb modes have a

different trend. The fundamental modes converge to the top layer's Rayleigh wave velocity. This velocity is less than the uniform case. It should be noted that the anti-symmetric mode in the frequency range of 0 to 5 kHz follows a similar to that of the uniform plate case. Also the fundamental symmetric mode converges to the original P-wave velocity that is the same as lower and middle layer P-wave velocity. This can be used as the signature feature of this case.

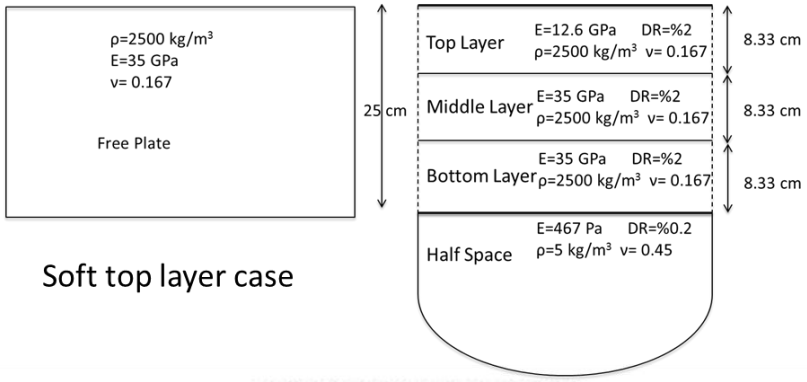

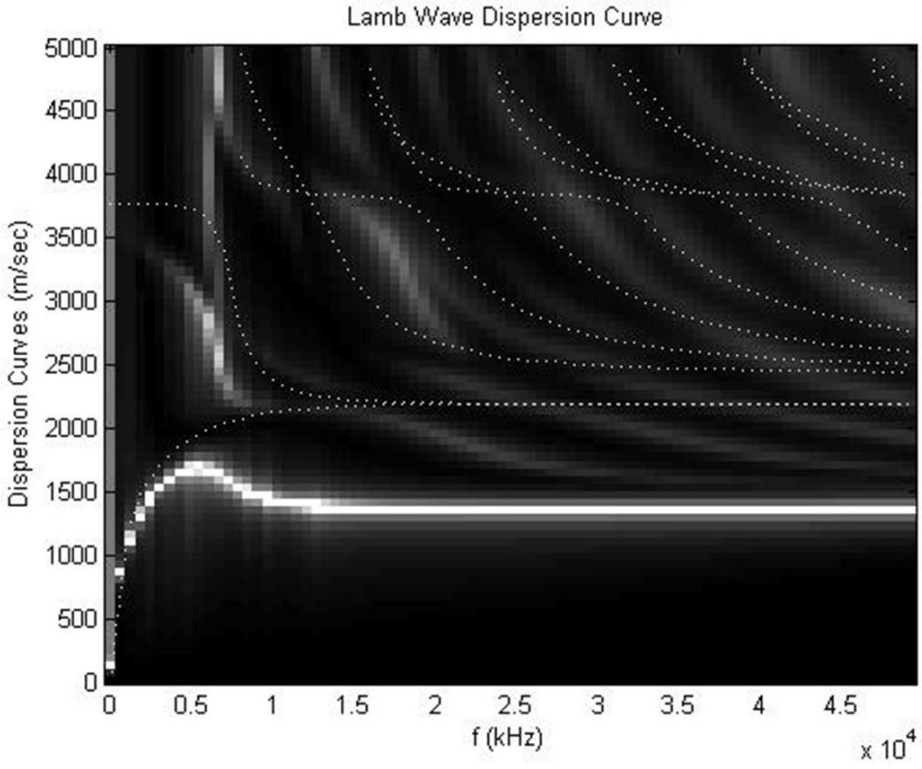

Figure 4.11 Lamb wave modes in case of a uniform plate shown as dotted lines and a 3-layer system with softer top layer and air as half-space using matrix techniques

Figure 4.12 represents a 3-layer system with a soft layer in the middle. In this case we see more of the higher modes having brighter spots that indicate higher dispersion curve amplitudes. The modal amplitudes in the lowest and highest frequencies are similar to the uniform case. So a soft layer trapped in between hard layers excites the Lamb modes in the middle frequency range (i.e. 10 kHz to 30 kHz). The only mode that can be directly compared to the uniform plate case is the fundamental anti-symmetric mode.

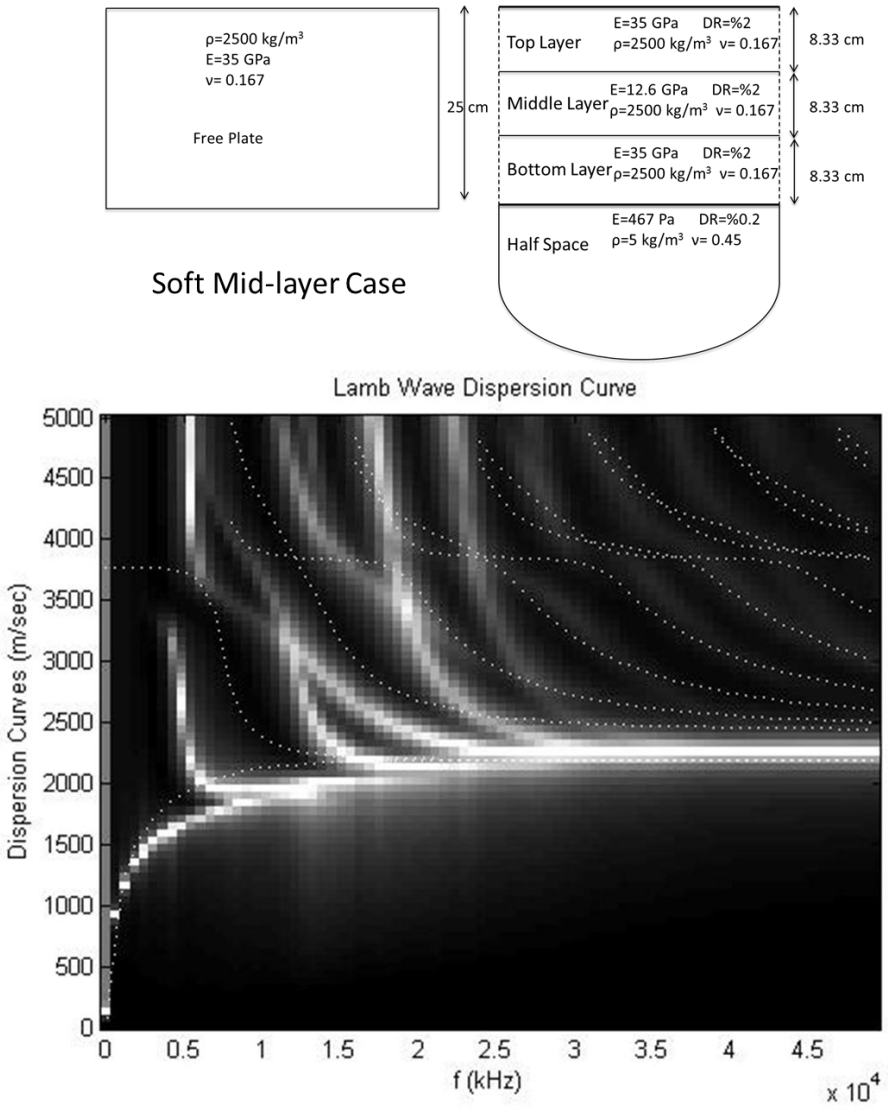

Figure 4.12 Lamb wave modes in case of a uniform plate shown as dotted lines and a 3-layer system with softer middle layer and air as half-space using matrix techniques

Figure 4.13 represents a 3-layer system with a soft bottom layer. In terms of the modal amplitudes, it is similar to the 3-layer uniform case. The first few modes have high

amplitudes and higher modes are hard to notice. Compared to the uniform plate case, the S_0 and A_0 have similar trends to the dotted lines, which represent the uniform plate case. However, the S_1 and A_1 modes have high amplitudes and different frequency-velocity content. This feature can be used as additional beneficial information in the inversion process.

As it is shown in Figure 4.13 the change in the properties of the bottom layer is reflected in S_1 and A_1 modes. Since they have high amplitude and are detectable on the surface using the full dispersion surface of Lamb modes can help to identify defects in such cases.

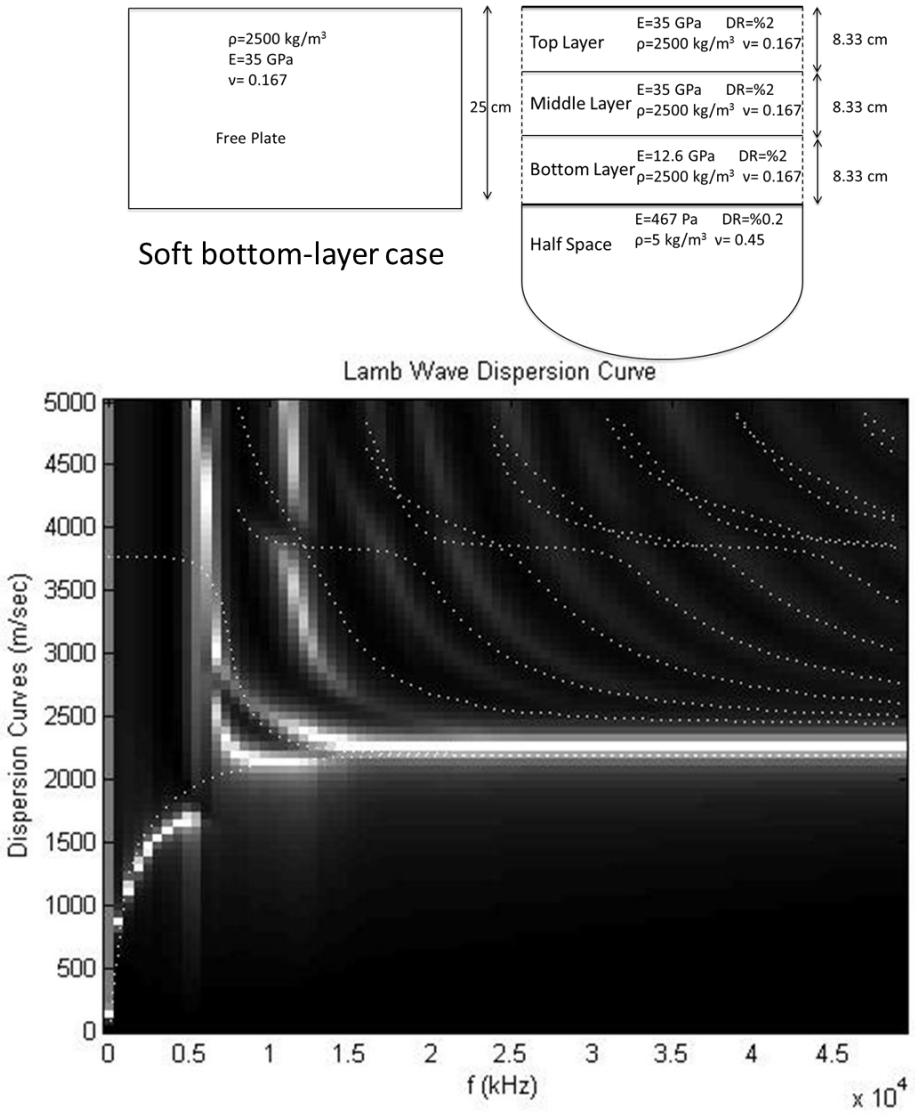

Figure 4.13 Lamb wave modes in case of a uniform plate shown as dotted lines and a 3-layer system with softer bottom layer and air as half-space using matrix techniques

4.4 Parametric Study

In order to better understand the effect of layer parameters on the Lamb wave dispersion surface, a series of parametric studies was performed. Equation 4.14 shows the parameters involved in calculating the dispersion surface for multi-layer media. Next, each of these variables is examined for a 3-layer system with a very low velocity half-space.

$$f(Vs_i, d_i, \rho_i, \upsilon_i) \qquad \text{i=1, 2, 3…} \qquad \text{Equation 4.14}$$

4.4.1 Shear-wave Velocity

Shear-wave velocity is the main variable of interest for NDE of bridge decks. The effects of each layer's shear-wave velocity on dispersion curve are discussed here. The medium to investigate is three-layered system profiles. The layered systems consist of three equally thick layers with material properties in a range typically found for sound to deteriorated concrete, and a half-space with air-like properties.

Table 4.1 Fixed layer parameters for layer shear velocity parametric study

Layer	**V_s (m/s)**	**ρ (kg/m^3)**	**d /T**	**ν**
1	Variable	2500	1/3	0.167
2	2500	2500	1/3	0.167
3	2500	2500	1/3	0.167

Figure 4.14 shows the dispersion surface for the first set of three-layered systems in this section. This set is for studying the change in the top layer's shear-wave velocity. It is the 2500 m/s case in the top plot, 2000m/s in the middle plot, and 1250 m/s in the bottom plot. Other than the parameter of the interest, all the parameters are kept identical to those presented in Table 4.1. The most significant effect of this parameter is on the phase-velocity at high frequencies. At higher frequencies, the phase-velocity represents the Rayleigh wave velocity of the close to surface material, which is the top layer. So, the Rayleigh wave velocity of the top layer can be directly calculated from this feature and then converted into the shear-wave velocity. This feature is used later in the inversion algorithim. From the top to bottom, the phase-velocity decreases in the high-frequency section of plots. This is directly correlated with the decrease of the parameter of interest.

The second observation to make from Figure 4.14 is that the frequency content of the modes shift slightly toward lower frequencies.

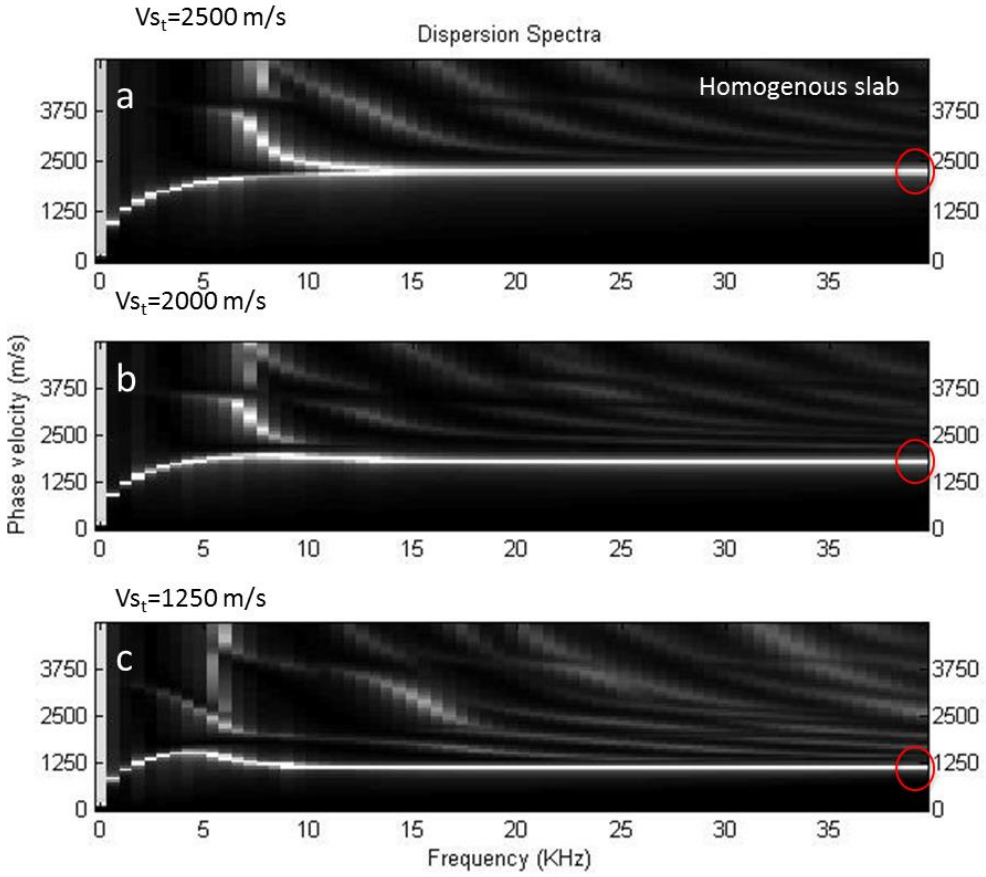

Figure 4.14 The variation in dispersion surface caused by changing the top layer's shear-wave velocity

Figure 4.15 shows the dispersion surface for the second set of three-layered systems. This set is prepared to study the effect of change of the middle layer's shear-wave velocity. All of the parameters are kept identical (Table 4.1) except the shear-wave velocity of the middle layer. It is 2500 m/s in the top plot, 2000m/s in the middle plot and 1250 m/s in the bottom plot. The most significant effect of this parameter is on the participation of higher modes. In Figure 4.15-a only the A_0 and S_0 modes are fully present. However, in

Figure 4.15-c the first 8 modes can be observed well. The same frequency content shift can be seen as in the previous case, which is slightly towards lower frequencies.

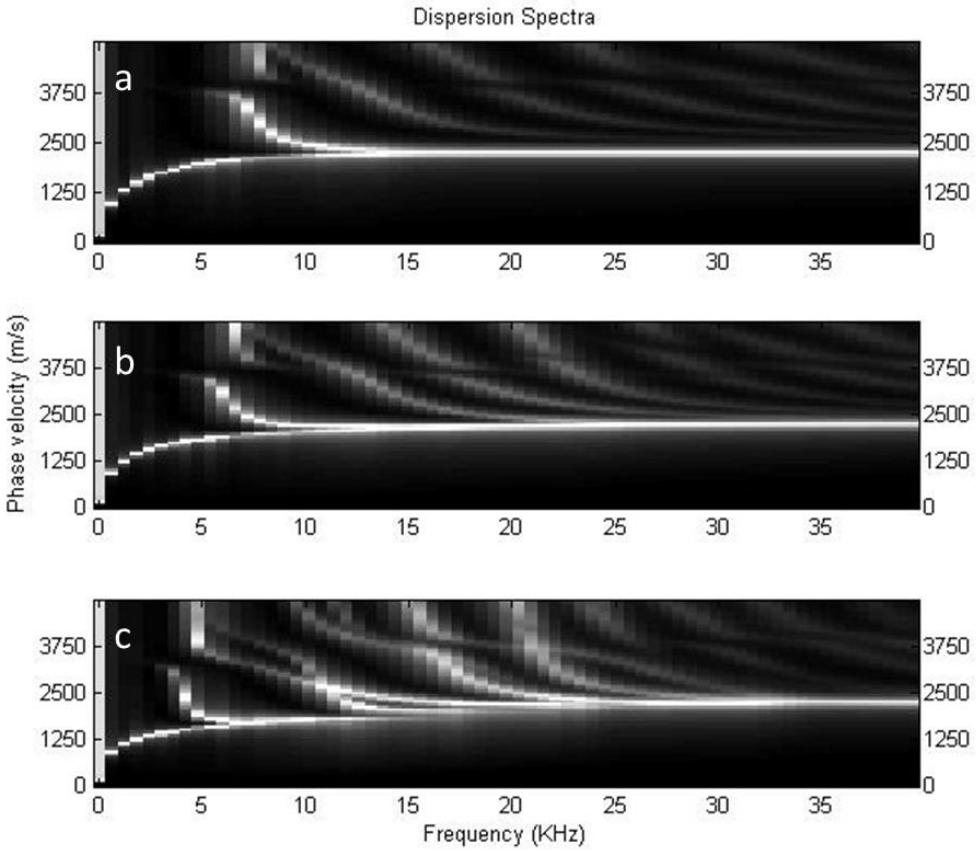

Figure 4.15 The variation in dispersion surface caused by changing the middle layer's shear-wave velocity

Figure 4.16 shows the dispersion surface for the third set of three-layered systems in this section. This set is for studying the change in the shear-wave velocity of the bottom layer. All the parameters are kept identical except the shear-wave velocity at the bottom layer.

This variable is 2500 m/s in plot a, 2000m/s in plot b and 1250 m/s in plot c. In general, the shear-wave velocity of the bottom layer has less effect on the dispersion surface than the other two layers. The biggest impact is on the lower frequency content of the A_0 mode. The amplitudes are lower reflecting the lower mode participation. The next few modes also have higher amplitudes, relative to the identical layer case.

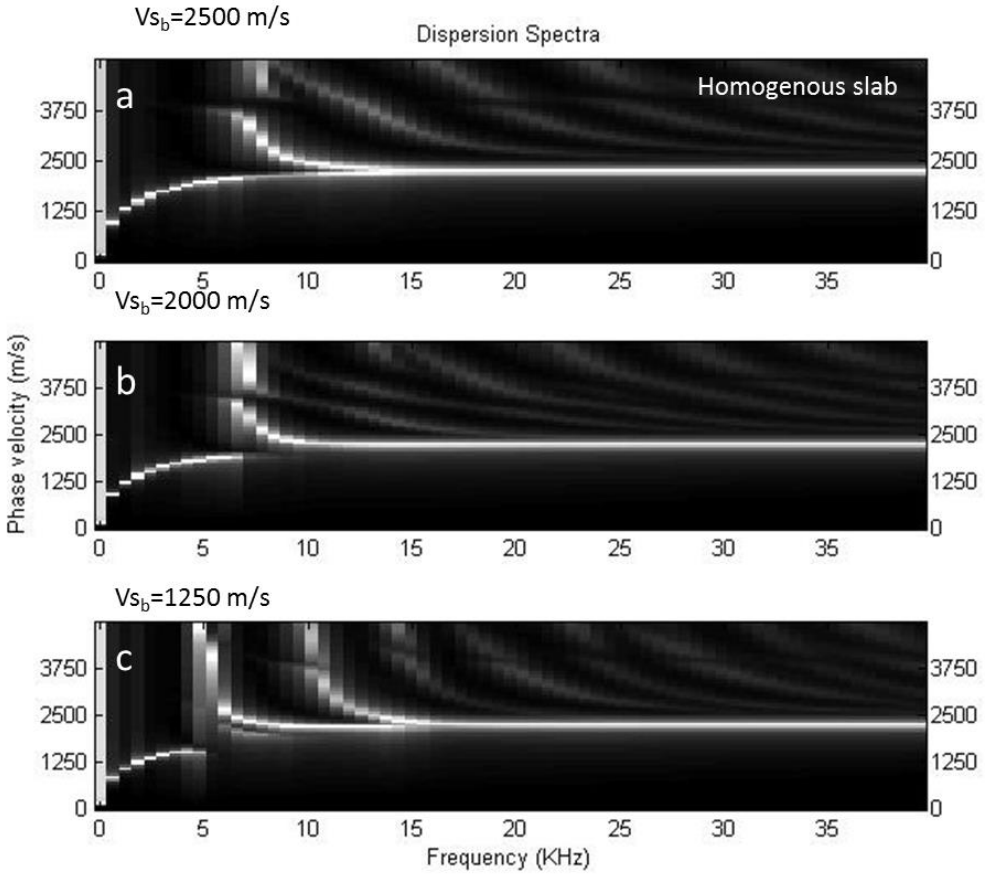

Figure 4.16 The variation in dispersion surface caused by changing the bottom layer's shear-wave velocity

4.4.2 Thickness of Weak Layer

In this section, the effects of the layer's thickness variation on the dispersion surface are discussed. The layer of interest has a lower shear-wave velocity than the rest of the layers (about half). The layer thickness will vary from 1/6 to 2/3 of the total thickness. Other than the variable of interest, all the other parameters are identical and described in Table 4.2. This analysis can provide an understanding of how the dispersion surface is affected during the progressive stages of any defect that can result in the modulus decrease in a section of a bridge-deck.

Table 4.2 Fixed layer parameters for thickness of weak layer parametric study

Layer	ρ (kg/m^3)	V_s (m/s)	ν
1,2,3	2500	2500	0.167

Figure 4.17 shows the dispersion surface for the first set of three-layered systems in this section. This set is for studying the change in the thickness of the top layer. This variable is 1/6 in plot a, 1/3 in plot b and 2/3 in plot c. As the weak layer extends from the top, the number of modes involved in the frequency/velocity range of interest increases. The first few dominant modes also shift toward lower frequencies.

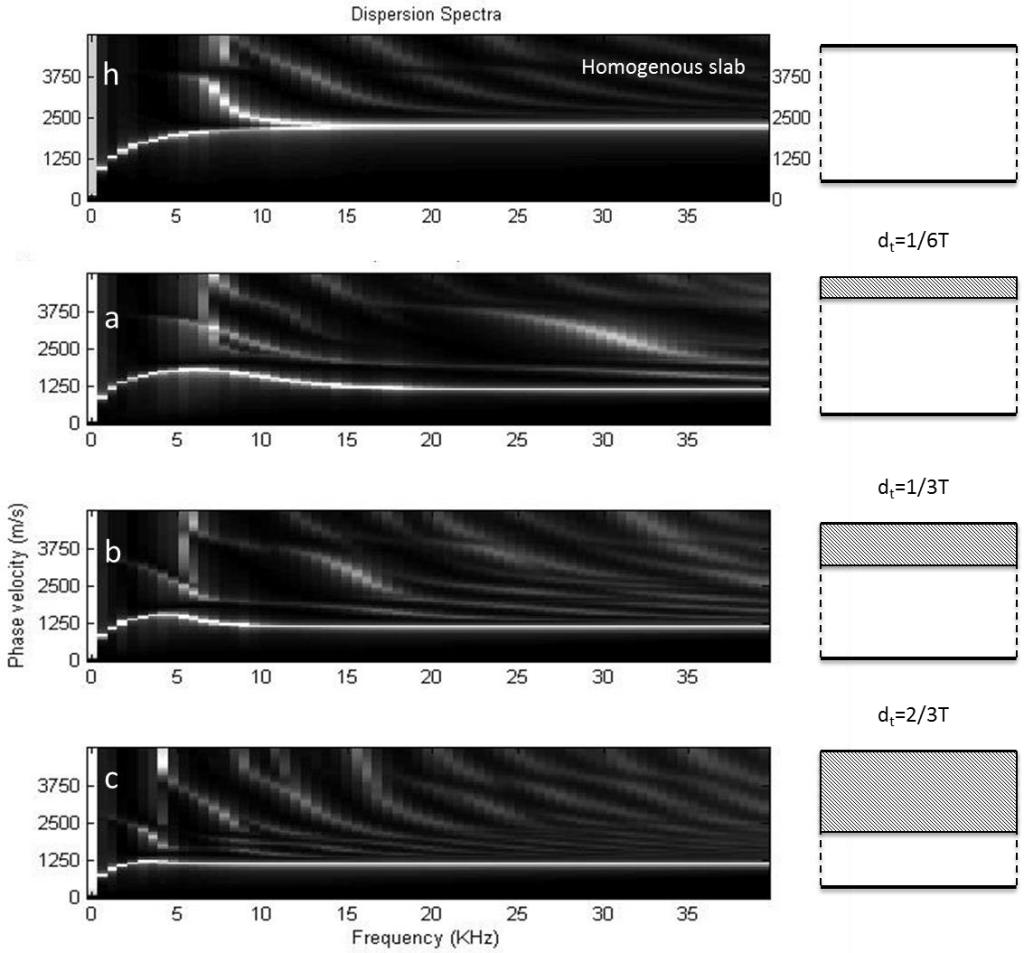

Figure 4.17 The variation in dispersion surface caused by changing the weak top layer's thickness

Figure 4.18 shows the dispersion surface for the second set of three-layered systems in this section. This set is for studying the change in the thickness of the middle layer. The variable of interest is 1/6 of the deck thickness in plot a, 1/3 in plot b and 2/3 in plot c. Other than the variable of the interest, all the other parameters are identical and described in Table 4.2. As in the previous case the increase in the thickness of the weak layer increases the number of mode shapes in the dispersion surface. The difference is that here

the higher modes have higher amplitudes, especially in the extreme case represented in Figure 4.18-c.

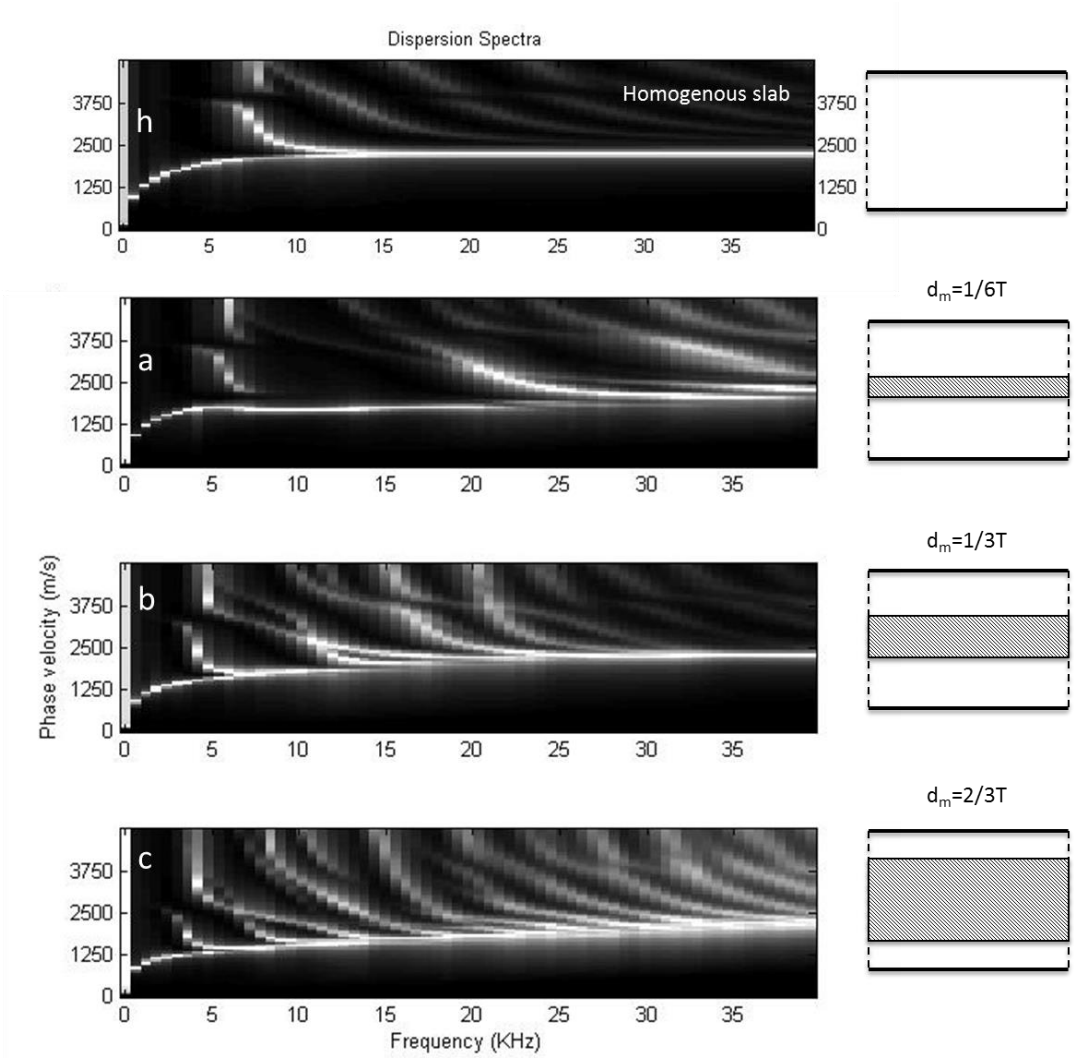

Figure 4.18 The variation in dispersion surface caused by changing the weak middle layer's thickness

Figure 4.19 shows the dispersion surface for the third set of three-layered systems. This set is for studying the change in the thickness of the bottom layer. The variable of interest is 1/6 of the deck thickness in plot, 1/3 in plot b, and 2/3 in plot c. Other than the variable

of the interest all the other parameters are identical and described in Table 4.2. As the weak layer extends from the bottom of the layer higher modes are amplified. The higher frequency content remains the same. This is because the top layer's properties are not changed in this case.

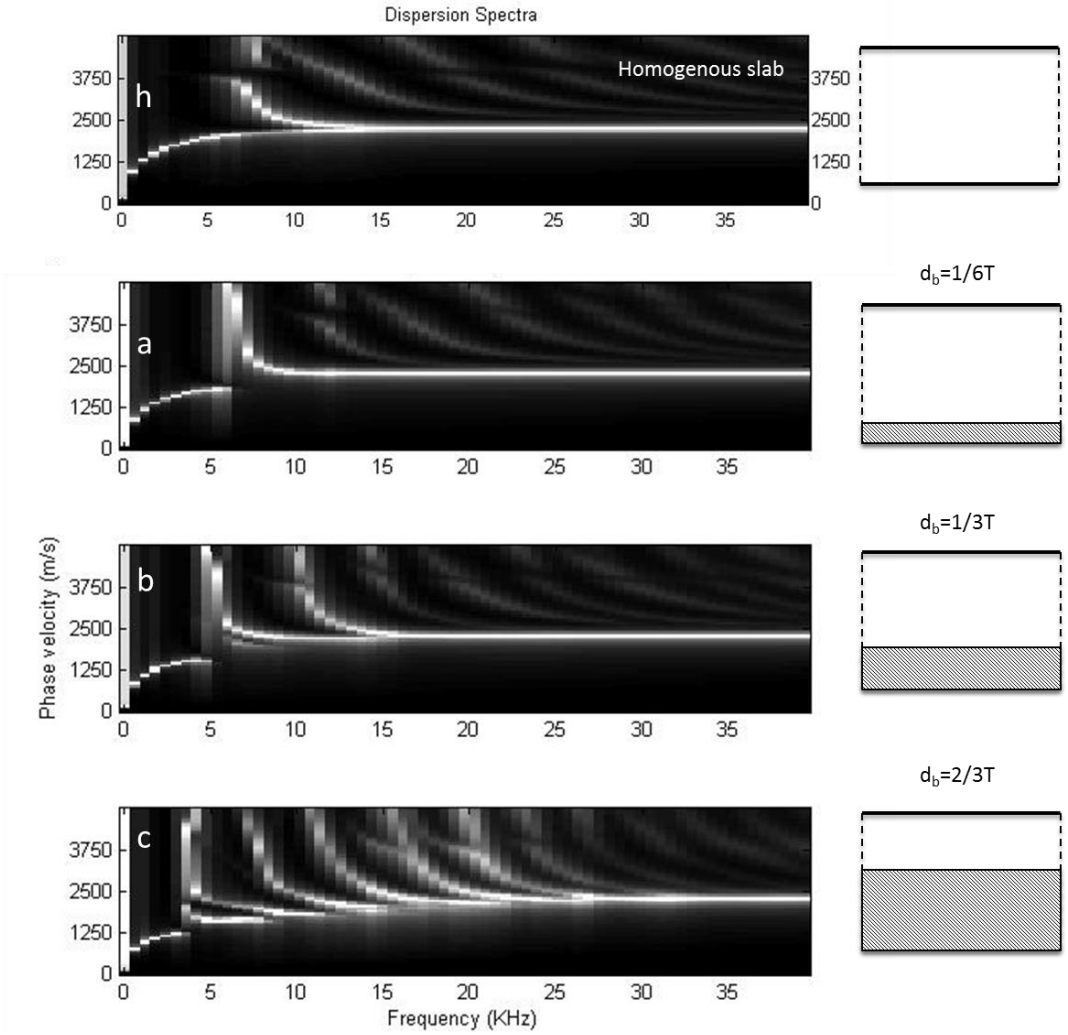

Figure 4.19 The variation in dispersion surface caused by changing the weak bottom layer's thickness

4.4.3 Location of the Weak Layer

In this section, the effects of the location of the weak layer on the dispersion surface are discussed. The thickness of the weak layer is constant and its location is moved from the top to the bottom of the deck to study the changes in the dispersion surface. All the other layer parameters, including the layer thickness, remain constant. Considering .the weak layer as the representative of flaw, one use of this analysis is to develop understanding of how the dispersion surface is affected by the location of a flaw in the bridge-deck.

Figure 4.20 shows the dispersion surface for the first set of three-layered systems in this section. This set is for studying the dispersion surface caused by changing the location of a hypothetical weak layer. In this case the weak layer thickness is 1/6 of total thickness. The other two layers have thicknesses) of 1/3T and 1/2T. Other than the variable of the interest all the other parameters are identical and described in Table 4.2. At the right hand side of each plot, there is a schematic figure to show the size and location of the weak layer. As the weak layer changes its location from the top to the bottom, the mode amplitudes and frequency content change throughout the dispersion surface.

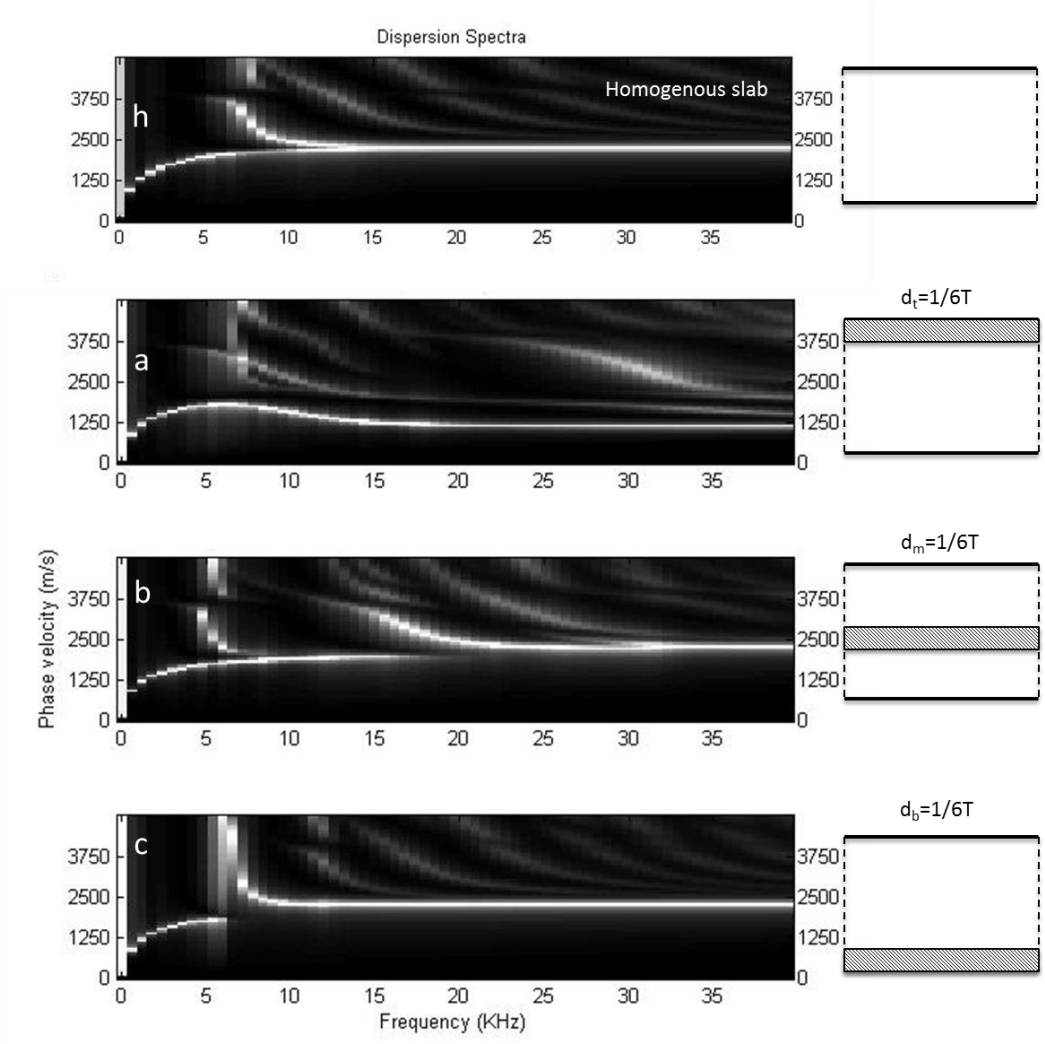

Figure 4.20 The variation in dispersion surface caused by changing the location of the weak layer with thickness of 1/6T

Figure 4.21 shows the dispersion surface for the second set of three-layered systems in this section. This set is for studying the dispersion surface caused by changing the location of a hypothetical weak layer. In this case, the weak layer thickness is 1/3 of total thickness. The other two layers have thicknesses of 1/3T. Other than the variable of interest, all the other parameters are identical and described in Table 4.2. At the right

hand side of each plot there is a schematic showing the size and location of the weak layer. More dispersion modes are involved in this case with 1/3 weak layer than in the previous case with thinner weak layer.

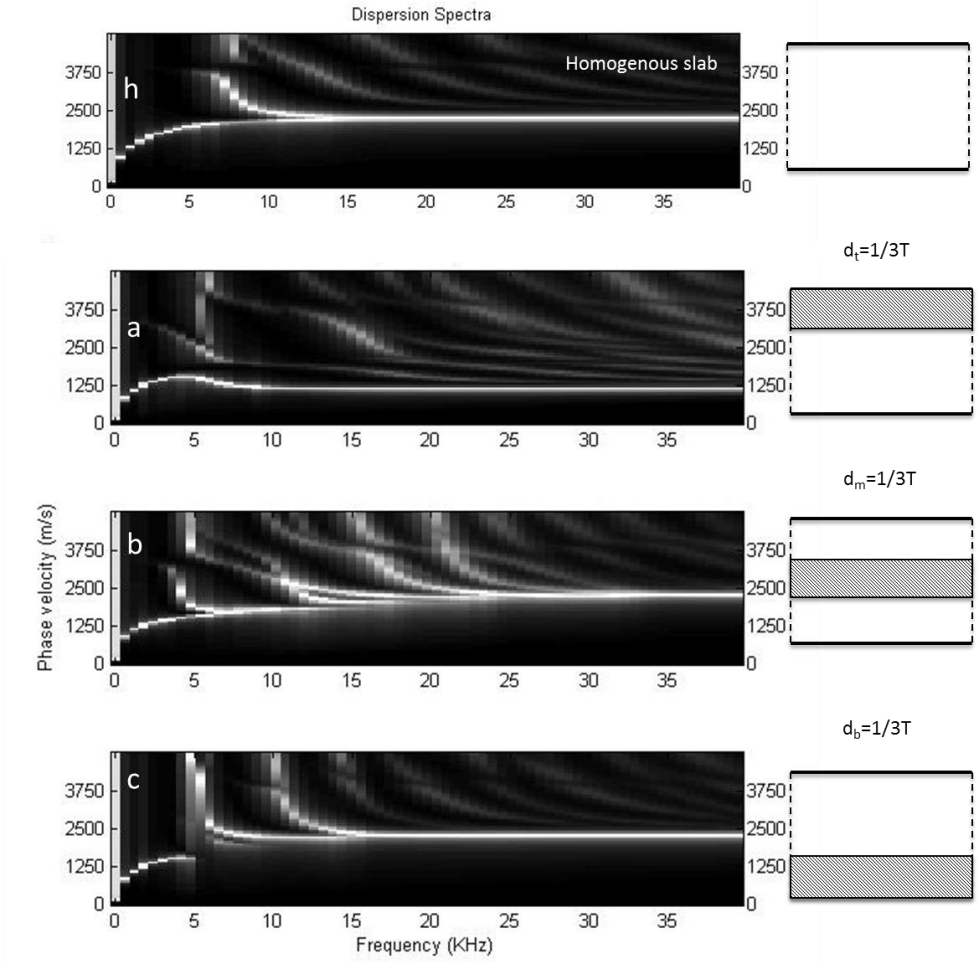

Figure 4.21 The variation in dispersion surface caused by changing the location of the weak layer with thickness of 1/3T

Figure 4.22 shows the dispersion surface for the third set of three-layered systems in this section In this case the weak layer thickness is 2/3 of total thickness. The other two layers have thicknesses of 1/6T. Again, all the other parameters are identical and described in

Table 4.2. At the right hand side of each plot there is a schematic figure to show the size and location of the weak layer. The same trend continues here. As the weak layer's thickness increase, more modes are present in the dispersion surface.

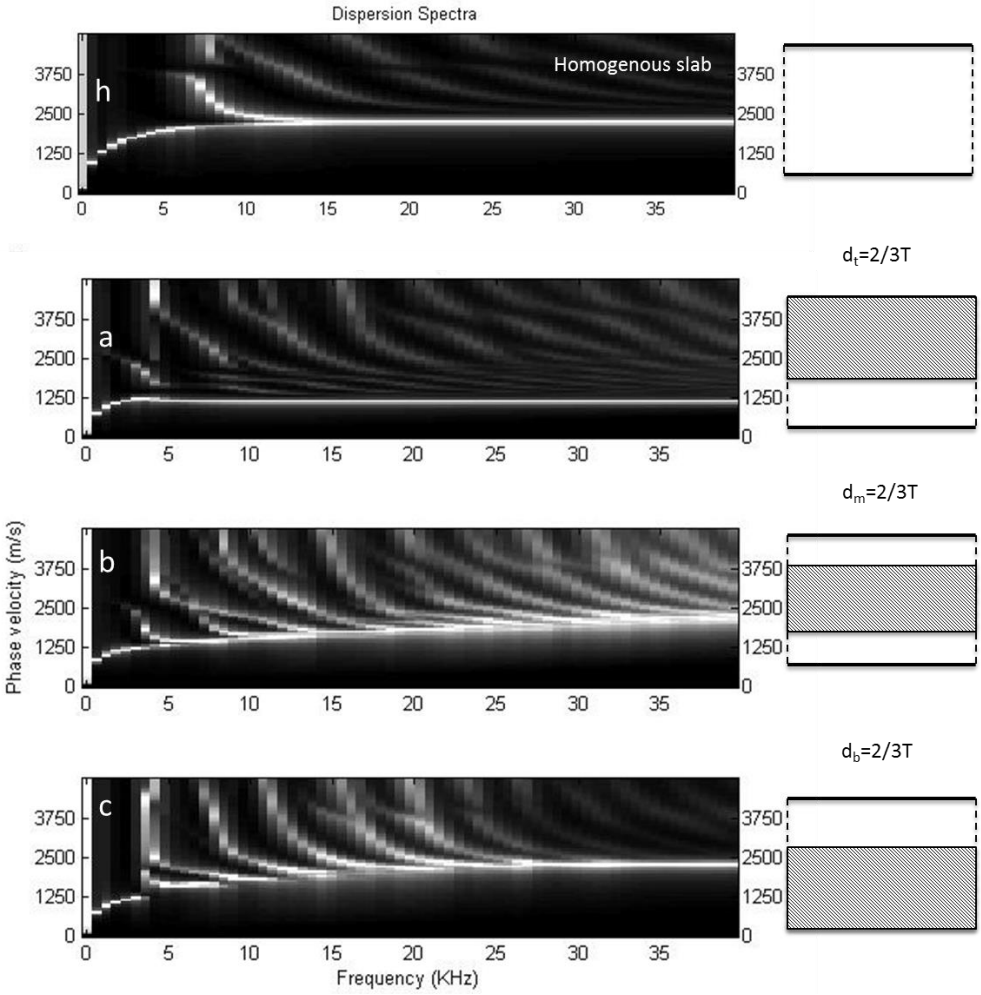

Figure 4.22 The variation in dispersion surface caused by changing the location of the weak layer with thickness of 2/3T

4.4.4 Layer Density

In this section the effects of the density of each layer on the dispersion surface are discussed. The density of the layer of interest varies from 833 kg/m^3 to 2500 kg/m^3. Other than the parameter of the interest, all the parameters are kept identical and are presented in Table 4.3.

Figure 4.23 shows the dispersion surface for the first set of three-layered systems,. This set is for studying the effects of the top layer's density. The variable of interest is 2500 kg/m^3 in plot a, 1666 kg/m^{3}in plot b and 833 kg/m^{3}in plot c. The phase-velocity amplitudes in the frequency range of 5-10 kHz show higher amplitudes than the rest of the plot. This can be due to the lower density of the deck at this frequency range which is related to the top.

Table 4.3 Fixed layer parameters for layer density parametric study

Layer	Vs (m/s)	d /T	ν
1,2,3	2500	1/3	0.167

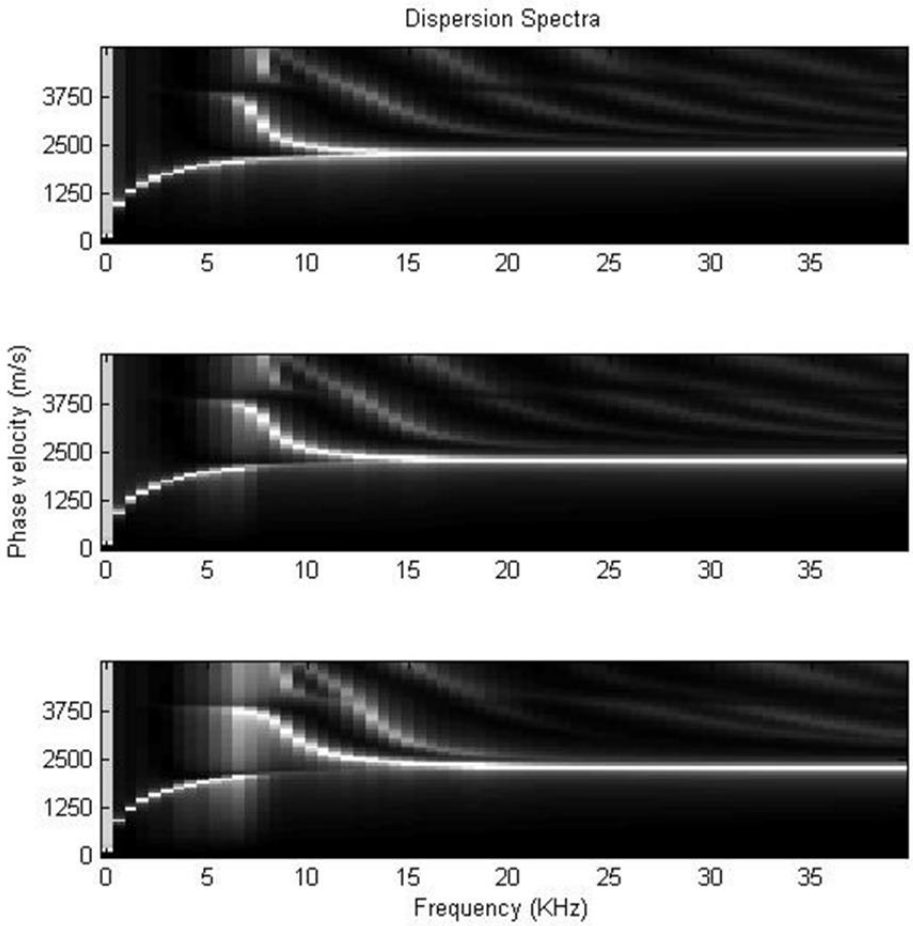

Figure 4.23 The variation in dispersion surface caused by changing the density of the top layer

Figure 4.24 shows the dispersion surface for the second set of three-layered systems in this section. This set is for studying the effects of the middle layer's density. The variable of interest is 2500 kg/m^3 in plot a, 1666 kg/m^{3}in plot b and 833 kg/m^{3}in plot c. The gap between the first mode (A_0) and the rest of the modes increases as the density of the second layer decreases.

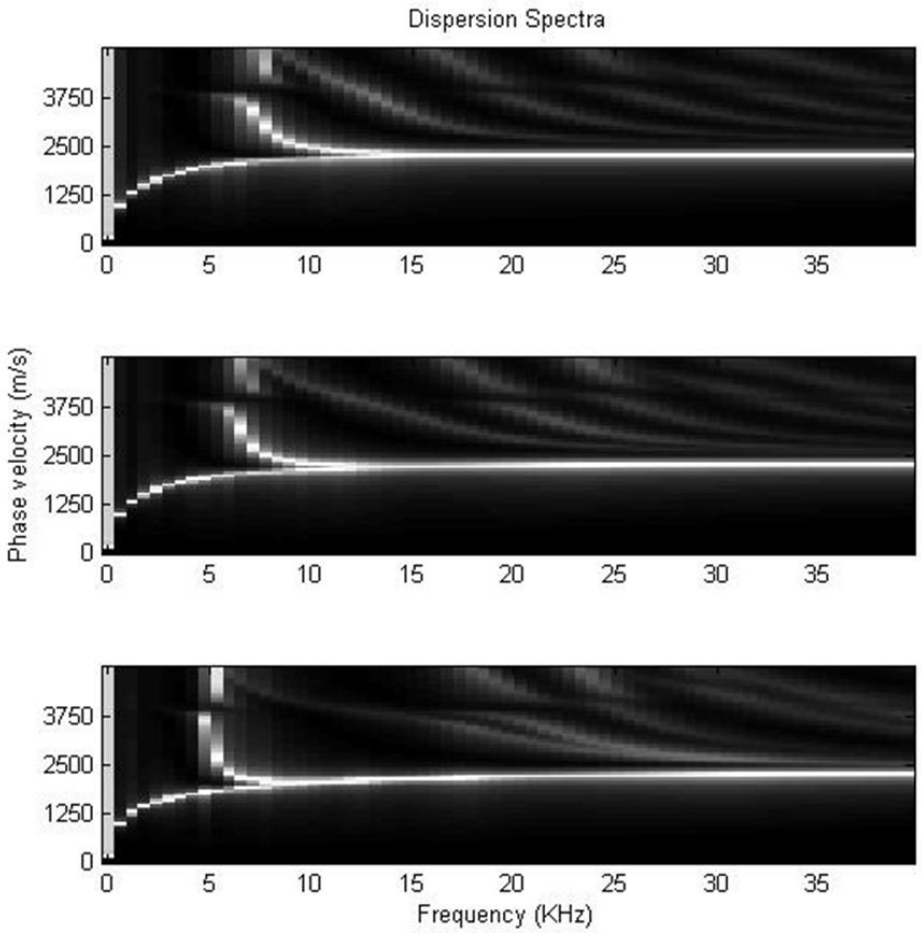

Figure 4.24 The variation in dispersion surface caused by changing the density of the middle layer

Figure 4.25 shows the dispersion surface for the third set of three-layered systems in this section. This set is for studying the effects of the bottom layer's density. The variable of interest is 2500 kg/m^3 in plot a, 1666 kg/m^{3}in plot b and 833 kg/m^{3}in plot c. There is not much observable change in the dispersion surface following the effects of the bottom layer's density.

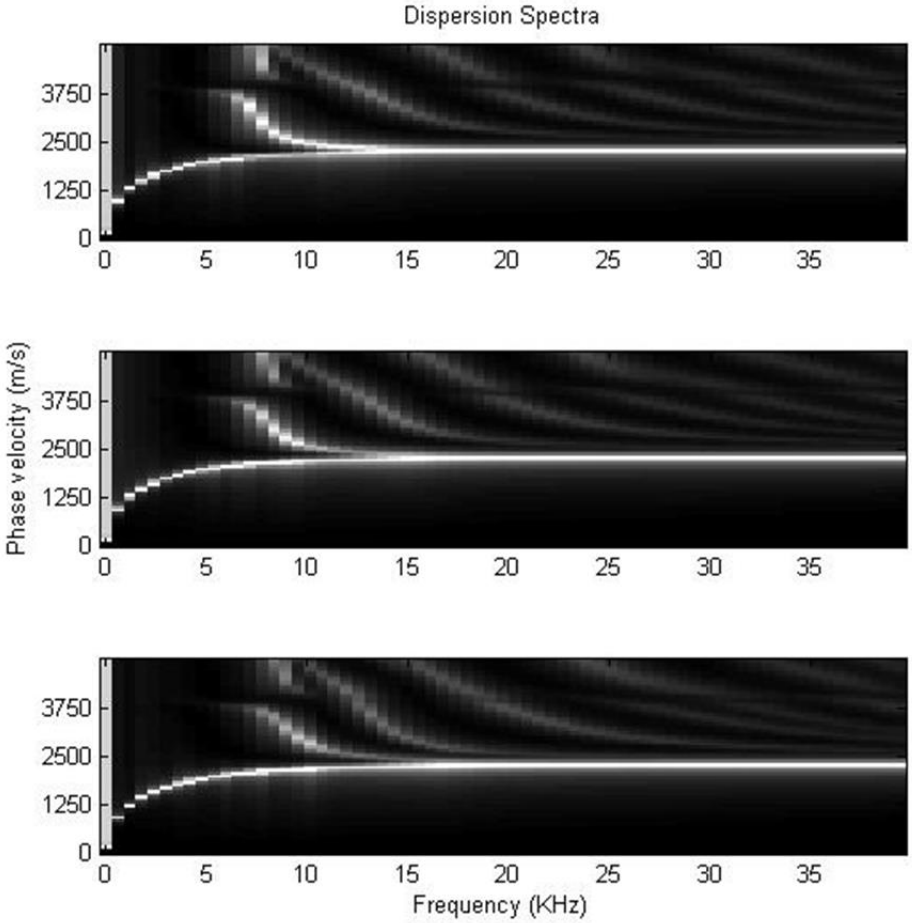

Figure 4.25 The variation in dispersion surface caused by changing the density of the bottom layer

4.4.5 Layer Poisson's ratio

In this section the effects of the density of each layer on the dispersion surface are discussed. The Poisson's ratio of the layer of interest varies from 0.0835 to 0.25. Other than the parameter of the interest all the parameters are kept identical as presented in Table 4.4.

Figure 4.26 shows the dispersion surface for the first set of three-layered systems in this section. This set is for studying the effects of the top layer's Poisson's ratio. The variable of interest is 0.25 in plot a, 0.167 in plot b and 0.0835 in plot c. The Poisson's ratio of the top layer does not have a major impact on the dispersion surface. All the symmetric modes have an almost flat portion that is representative of the longitudinal wave velocity in the plate. As the Poisson's ratio of the top layer decreases the corresponding speed also decreases and the flat portion moves towards lower phase-velocity.

Table 4.4 Fixed layer parameters for layer Poisson's ratio parametric study

Layer	Vs (m/s)	d /T	ρ (kg/m^3)
1,2,3	2500	1/3	2500

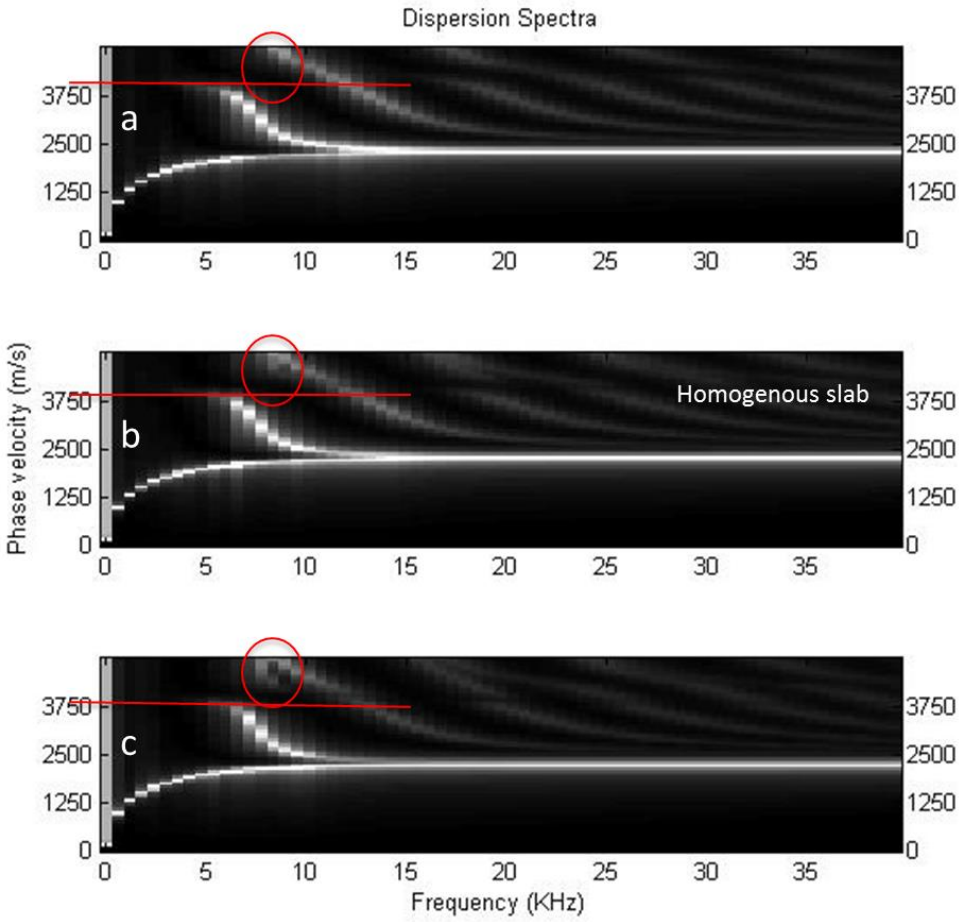

Figure 4.26 The variation in dispersion surface caused by changing the Poisson's ratio of the top layer

Figure 4.27 shows the dispersion surface for the second set of three-layered systems in this section. This set is for studying the effects of the middle layer's Poisson's ratio. The variable of interest is 0.25 in plot a, 0.167 in plot b, and 0.0835 in plot c. As the Poisson's ratio of the middle layer decreases the corresponding quasi-longitudinal wave speed also decreases and the flat part moves towards lower phase-velocity.

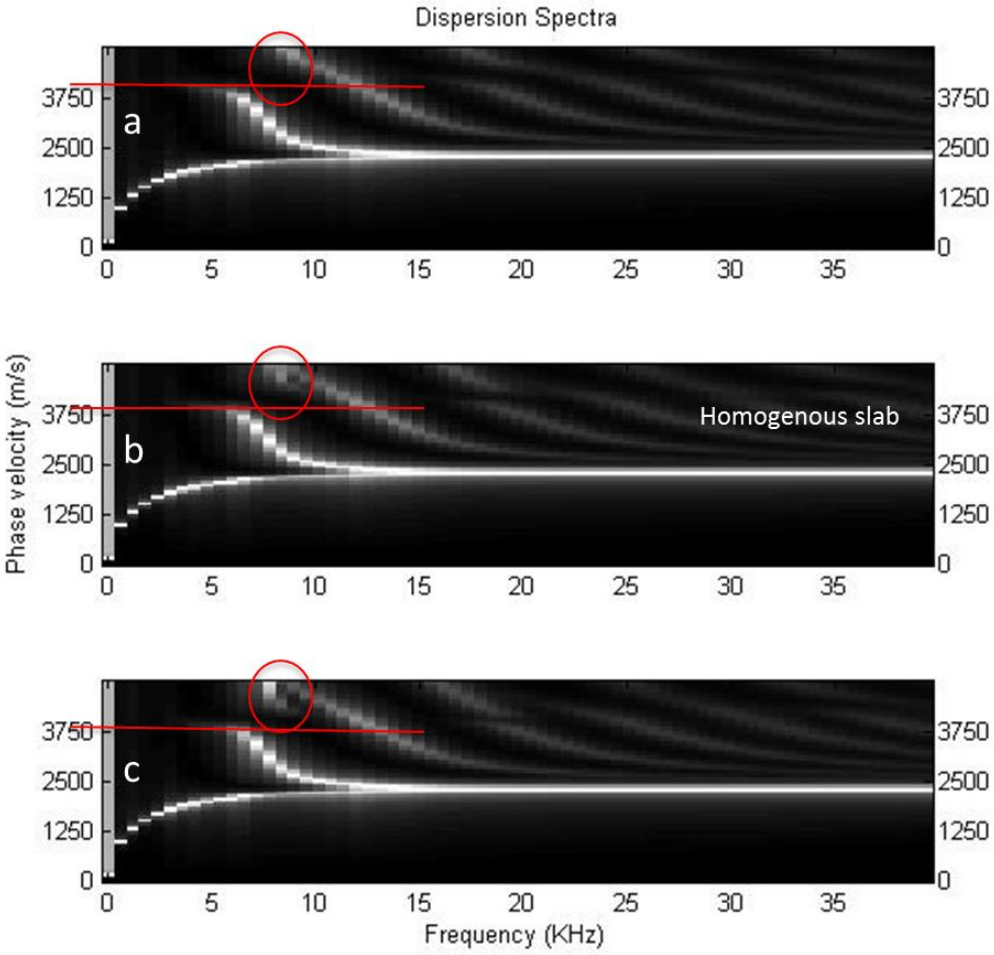

Figure 4.27 The variation in dispersion surface caused by changing the density of the middle layer

Figure 4.28 shows the dispersion surface for the third set of three-layered systems in this section. This set is for studying the effects of the bottom layer's Poisson's ratio. The variable of interest is 0.25 in plot a, 0.167 in plot b, and 0.0835 in plot c. As the Poisson's ratio of the bottom layer decreases the corresponding quasi-longitudinal wave speed also decreases and the flat part moves towards lower phase-velocity.

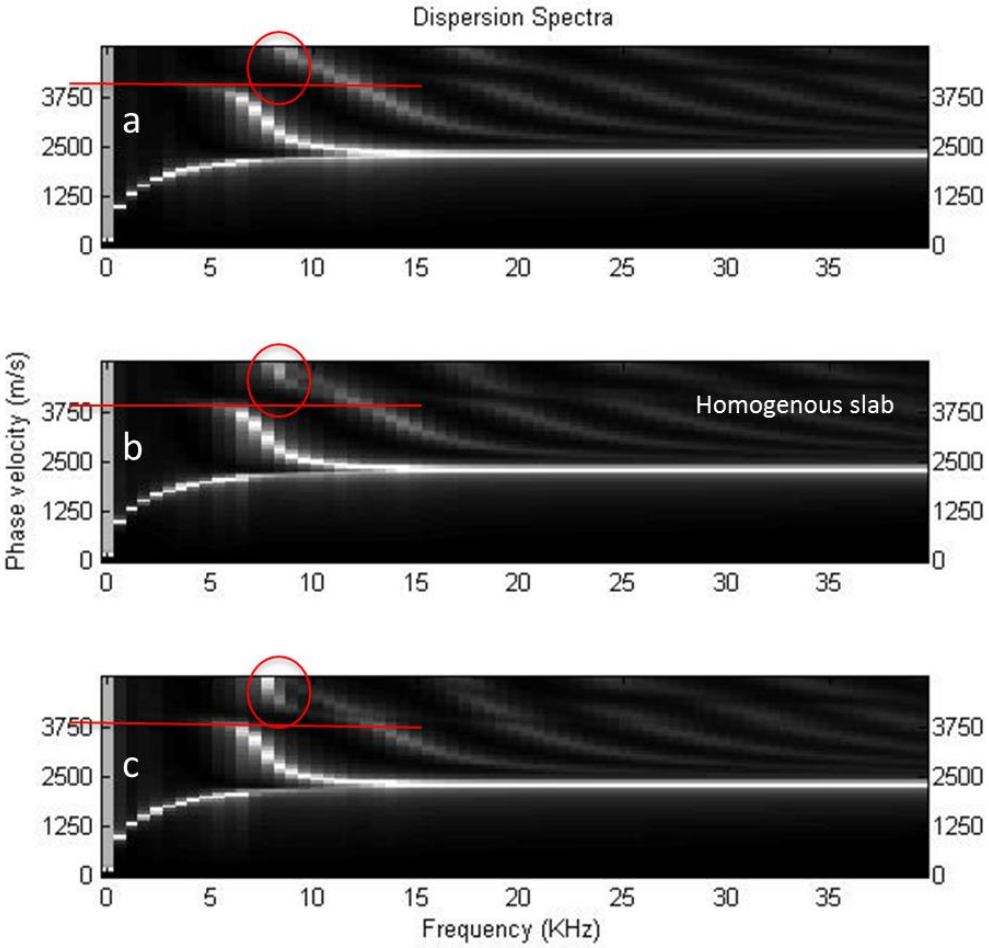

Figure 4.28 The variation in dispersion surface caused by changing the density of the bottom layer

The difference between the three sets is minor. Different frequency ranges get amplified under closer investigation under the influence of the corresponding layer with variable Poisson's ratio.

4.4.6 Conclusion

The parametric study shows that different model parameters each contribute to certain signatures in the dispersion surface. An intelligent inversion algorithm can utilize these signatures for a faster and more accurate inversion. The most significant signature is the effect of top layer's shear-wave velocity, which will be directly implemented into the inversion process later in chapter 6.

5 Finite-element Analysis

A numerical study is conducted to investigate the complex pattern of transient seismic wave propagation within layered concrete bridge deck. As mentioned earlier, there is no analytical solution for the Rayleigh-Lamb equation. Therefore, there are two ways to study the interaction of propagating waves within a layered concrete media: 1) solve the wave propagation equation numerically using the stiffness matrix method, and 2) perform a finite-element analysis (FEA) for numerical estimation, which will be discussed here.

FEA, also called the finite-element method (FEM), is used in this chapter to study the interaction of propagating seismic waves with idealized layers in concrete bridge decks. It is a numerical procedure for obtaining approximate solutions to differential equations governing idealized physical problems. The continuum is first divided into a finite number of discrete parts: finite elements. This discretized representation of the continuum is referred to as a finite-element model (mesh). For applications involving stress and displacement analysis, variation of stresses or displacements within each element in the model is described by a set of assumed functions, called shape functions. Energy principles are used to formulate force-displacement equations for each element. These element equations are then combined to construct global equations that describe the behavior of the entire model. Solutions of these global equations are used to approximate displacements or stresses at any point within the continuum. (Cook R. D., 2002; Sansalone, Carino, & Hsu, 1987)

The results obtained from a finite-element analysis are approximations to the desired exact solutions. It is important to evaluate the accuracy of the numerical simulation results. Performing a preliminary FEA on a simplified model and comparing the obtained numerical solution to available analytical or experimental results can achieve this purpose. Such analysis parameters should be selected with extra care when FEM is applied to obtain the solution of dynamic problems involving wave propagation (Sansalone M. C., 1987; Sansalone, Carino, & Hsu, 1987; Ganji, Gucunski, & Maher, 1997; Bathe, 1996; Zerwer, 2002). FEA has been proven to be successful in studying the stress-wave propagation in layered concrete plates when the required accuracy of the parameters is satisfied (Sansalone M. C., 1987; Sansalone, Carino, & Hsu, 1987).

In this study, surface-waves are numerically modeled using commercially available ABAQUS Standard, CAE and Explicit 6.13-3 package (ABAQUS, 2013). The numerical study here was conducted on two-dimensional (2D) finite-element axisymmetric models. According to Sansalone et al. (Sansalone, Carino, & Hsu, 1987) a 2D finite-element model provides a considerably fast and sufficiently accurate way to investigate wave propagation in in-plain cases.

To investigate the effectiveness and limitation of surface-wave testing and to come up with an optimal sensor and actuator setting, a number of two-dimensional analyses on simplified finite-element models are performed. For the axisymmetric simulation, four-node axisymmetric elements (CAX4) are selected. CINAX4 elements are applied at the simulation model boundary, at the far edge of the zone, to simulate an infinite energy-absorbing boundary. Material properties are assumed to be homogeneous. Because a low

strain level is induced in the medium by applying the simulated impact, concrete is modeled as a linearly elastic material with Poisson's ratio $n = 0.167$, density $r = 2500 kg/m^3$ and elastic modulus $E = 35 \times 10^9 \frac{N}{m^2}$. The shear-wave velocity in concrete for the given parameters is

$$Cs = \sqrt{\frac{E}{2(1+\nu)\rho}} = 2449 \text{ m/s} \qquad \text{Equation 5.1}$$

while the compression wave velocity is

$$Cp = \sqrt{\frac{E(1-\nu)}{(1+\nu)(1-2\nu)\rho}} = 3873 \text{ m/s} \qquad \text{Equation 5.2}$$

and Rayleigh wave velocity is

$$C_R = \frac{0.862 + 1.14\nu}{1+\nu} C_s = 2208\, m/s \qquad \text{Equation 5.3}$$

Rayleigh damping is considered in the governing equation of motion.

$$[C] = \alpha[K] + \beta[M] \qquad \text{Equation 5.4}$$

To introduce material Rayleigh damping, the stiffness matrix multiplier α is set to 0.4 and β the mass matrix multiplier is set to 1.085×10^{-10}. This choice was made after

performing a series of analyses of wave propagation in sound decks with varying values of β and α and comparing the attenuation levels to those from available field records.

The controlling parameters for the FEM analysis are the following: element size, time step, size of the model and impact duration. The effect of these parameters and acceptable ranges needed to ensure the accuracy of the numerical results are also discussed here.

5.1 Element Size

In wave propagation applications, the element size depends on the highest frequency of interest and the lowest velocity wave (V_R). Very large elements will filter higher frequencies while very small elements can introduce numerical stability. An approximate element size (g) can be estimated from the following relationship according to Zerwer (Zerwer, 2002):

$$g \leq \chi \lambda_{min} \qquad \text{Equation 5.5}$$

$$\lambda_{min} = \frac{C_R}{f_{max}} \qquad \text{Equation 5.6}$$

The constant χ must be less than 0.5 because of the Nyquist limit (Zerwer, 2002) , and depending on the mass matrices it could be taken as 0.25 or 0.2 for consistent or lumped mass matrices. It is assumed that elements have square dimensions in this formulation. However, this article adopts the value suggested by Moser et al. (Moser, Jacobs, & Qu,

1999), which is the most conservative resolution, utilizing 20 elements to describe the minimum wavelength.

Assuming the maximum frequency of interest $f_{max} = 50KHz$, the minimum wavelength for surface-wave components is obtained.

$$\lambda_{min} = \frac{2208}{50000} = 0.04\ m \qquad \text{Equation 5.7}$$

So the element size is set to 1mm to satisfy the following condition:

$$g \leq \frac{40}{20} = 2\ mm \qquad \text{Equation 5.8}$$

Figure 5.1 shows the schematic of the element size in a 2mX0.2m FEM model.

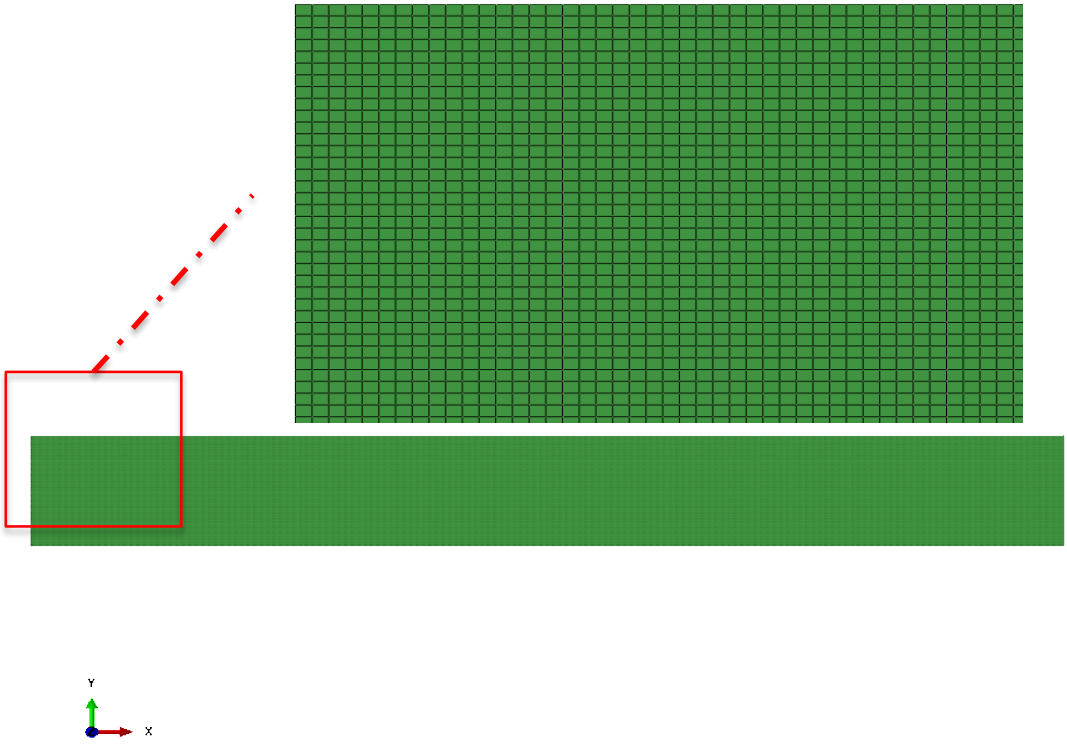

Figure 5.1 Schematic of element size for a 2mX0.2m FEM model

5.2 Overall dimensions of the model:

5.2.1 Absorbing Boundaries

Lysmer-Kuhlemeyer (LK) boundaries are often used as infinite boundaries in FEM analysis. The basis is a simple viscous damper that has appropriate damping constants and is connected to the boundary node to absorb wave energy. LK boundaries apply distributed damping to absorb the incident wave energy.

$$\sigma_{xx} = -d_p \dot{u}_x \qquad \text{Equation 5.9}$$

$$\sigma_{xy} = -d_s \dot{u}_y \qquad \text{Equation 5.10}$$

$$\sigma_{xz} = -d_s \dot{u}_x \qquad \text{Equation 5.11}$$

σ_{xx} is the axial stress and σ_{xy}&σ_{xz} are shear stress. The $\dot{u}_x$& $\dot{u}_y$ are the derivative of the displacement in x and y direction. d_s and d_p are constants for damping applied to attenuate longitudinal and shear-wave energy respectively (Lysmer, 1969). The LK boundary is available in the ABAQUS FE software package where it is named "infinite-element". The values of damping coefficient are embedded in the software formulations and do not need to be defined by the user. The LK boundaries have some limitations, but work quite well when the dominant direction of propagation is orthogonal to the boundaries (Cohen, 1983).

5.2.2 Model Size

The model should be large enough so that the reflected waves from the artificial model boundaries do not contaminate records obtained at desired locations during the prescribed recording time. Even though absorbent boundaries will be used in this model, the behavior of such elements in ABAQUS has been questioned by many researchers (Liu, 2003; Kausel E. , 1998). So, first the dimension of the model is calculated by ignoring the absorbing boundaries. Then these boundaries are factored in. In reference to the parameters shown in Figure 5.2, these criteria can be summarized in the following equation:

$$t_{max} < \frac{\min(2d - x)}{V_R} \qquad \text{Equation 5.12}$$

$$\mathrm{d} > \frac{1}{2}(C_R t_{max} + x_{max}) \qquad \text{Equation 5.13}$$

where t_{max}= duration of the time record, d= the shortest distance between the impact source and the artificial boundary of the model, $x1$= distance between the impact source and any receiving transducer, x_{max}= the distance between the impact source and the furthest receiving transducer.

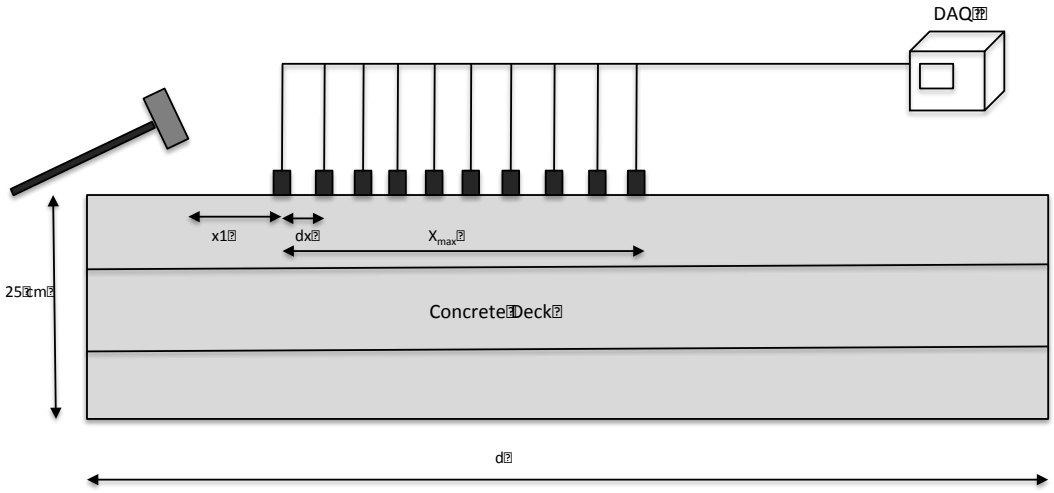

Figure 5.2 Source and the sensor arrangement on a concrete bridge-deck

The duration of the records is set to 1 millisecond. So using Equation 5.13:

$$d > \frac{1}{2}(2208 \times 0.001 + 1) = 1.6m \qquad \text{Equation 5.14}$$

Figure 5.3 show the normalized acceleration recoded at 20 cm from the source in different model sizes. It is obvious that, despite using infinite boundary elements, there is still a slight reflection affecting the record. For this reason, the size of the element is set to 2m.

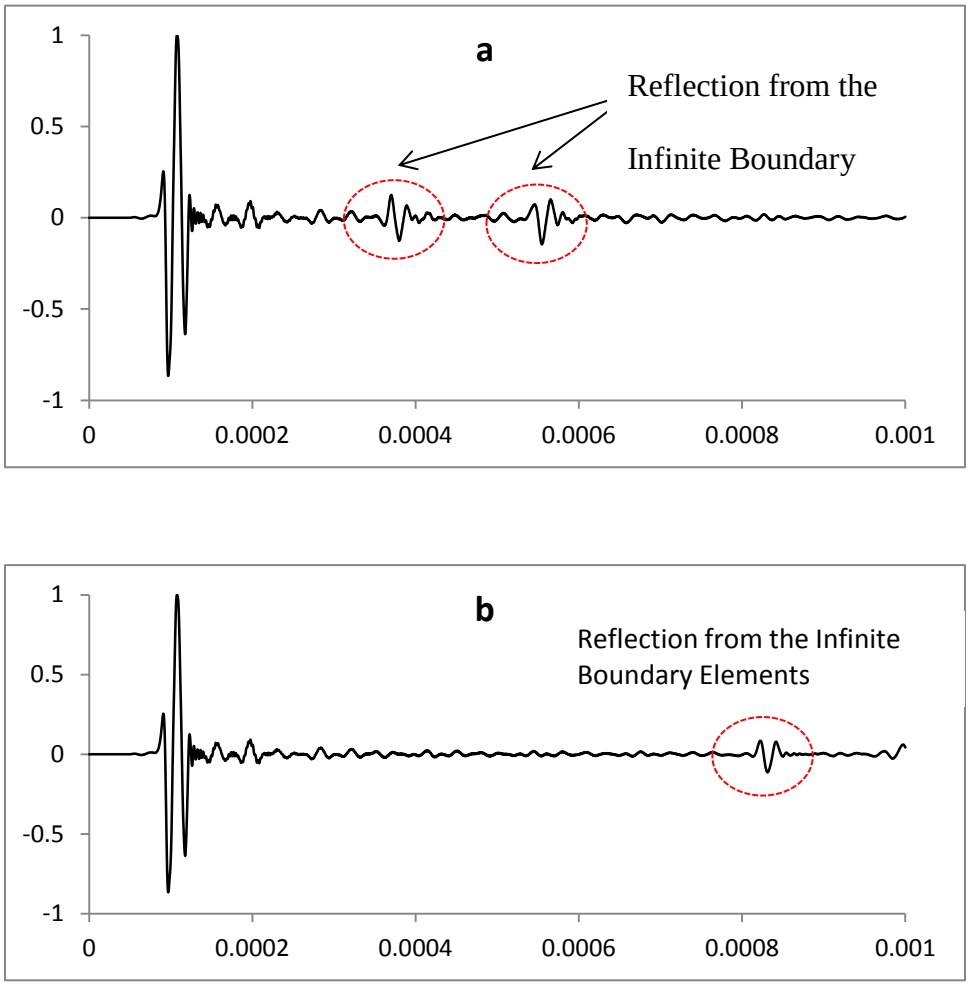

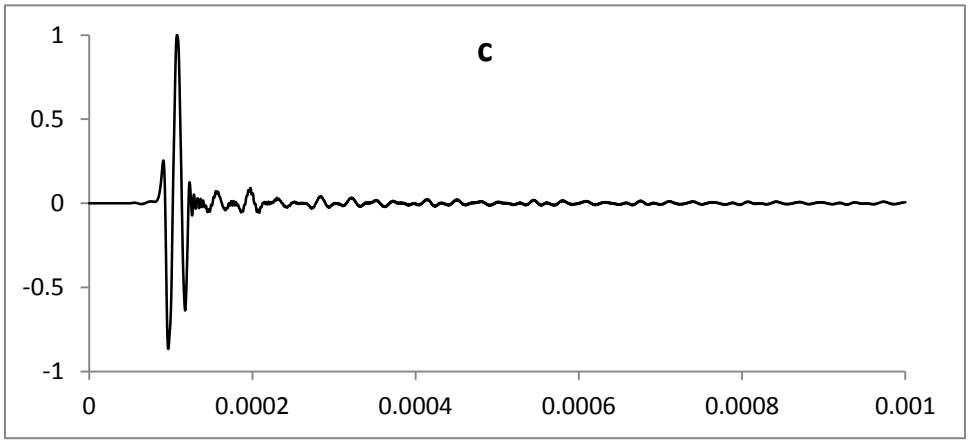

Figure 5.3 Normalized acceleration at 20 cm from the source using a) 0.5m b) 1m c) 2m axisymmetric FEM model.

Also the thickness of the deck is set to 25 cm to represent the majority of the concrete bridge decks in practice.

5.3 Time step:

In simple terms, the time step used in the analysis should be small enough to prevent the compression wave from "jumping over" the smallest element in the model. At the same time, using a very small time step will result in spurious oscillations (Gibb's phenomenon) in the numerical results.

If $L_e$represents the "effective length" of a finite-element, then

$$\Delta t = \frac{L_e}{V_p} \qquad \text{Equation 5.15}$$

The effective length and corresponding time step must be able to represent the complete wave propagation accurately. They are chosen depending on the characteristics of the finite-elements used.

To simulate the surface-wave test and find the acceleration field due to a short duration impact, an explicit transient dynamic analysis was performed. The ABAQUS program uses the explicit dynamic integration method, which is also known as the forward Euler or central difference algorithm (ABAQUS, 2013), to solve the equations of motion in transient dynamic analysis. An integration time step $\Delta t = 0.1\ \mu s$ was used in this study. This time step satisfies the criteria stated in Equation (3-5) when $L_e = 0.001m$ (the smallest element size in the mesh)

$$\Delta t \leq \frac{L_e}{C_p} = \frac{0.001}{3873} \approx 0.26\ \mu s \qquad \text{Equation 5.16}$$

5.4 Impact duration:

In practice, acoustic waves are generated by a short mechanical impact, usually by tapping a steel sphere or a hammer with a metal tip on the surface of the structure to be examined. To simulate this in FEM, the input pulse can be approximated by a half-sine curve, whereas its contact time or duration depends primarily on the size of the impact source used and the stiffness and roughness of the concrete surface. The effective use of sinusoidal function in simulating the transient contact force has been studied by the previous researchers (Hughes, 1987; Kim JH, 2008).

The impact point source was applied on the free surface of half-space at the axis of symmetry (i.e., r=0) (see Figure 5.2). The force function of the transient impact source is as follows:

$$f(t) = sin^{n}\left(\frac{\pi t}{T}\right) \qquad 0 \leqq t \leqq T \qquad \text{Equation 5.17}$$

$$f(t) = 0 \qquad t > T \qquad \text{Equation 5.18}$$

Figure 5.4 shows normalized acceleration at 20 cm from the source for a solid 2m concrete slab using different sin shape functions simulated in ABAQUS. Gibbs phenomenon appears in numerical solutions, as shown by the finite-element analysis results. This is a numerical error that occurs at simple discontinuities. Applying numerical damping or using a higher order shape function will avoid this phenomenon (Cook R. D., 2002; Kim & Kwak, 2008). The above sin function is not differentiable at t=0 and t=T if n=1 and spurious oscillations occur when simulating the behavior of discontinuous function. Given that displacement, velocity and acceleration needing 1st, 2nd and 3rd order differentiability n=3 is the minimum order required to be used if acceleration is the desired response. All the analyses are done using a third order sin impact function.

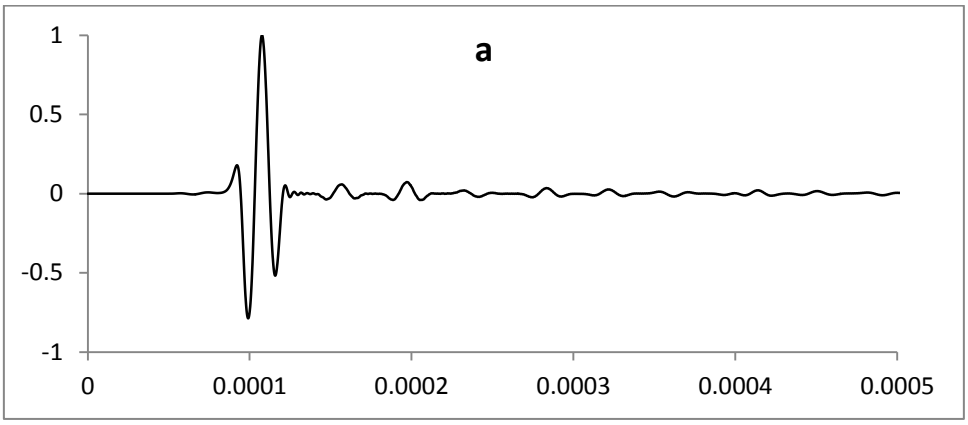
a
1
0.5
0
-0.5
-1
0
0.0001
0.0002
0.0003
0.0004
0.0005

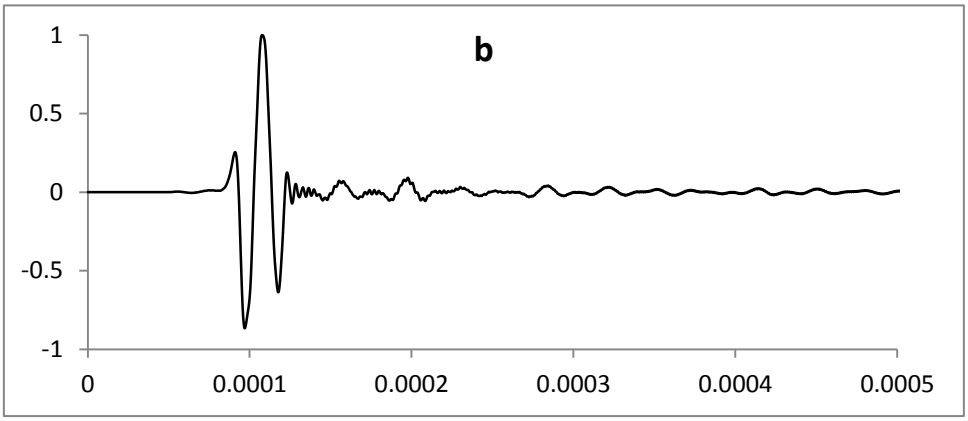
b
1
0.5
0
-0.5
-1
0
0.0001
0.0002
0.0003
0.0004
0.0005

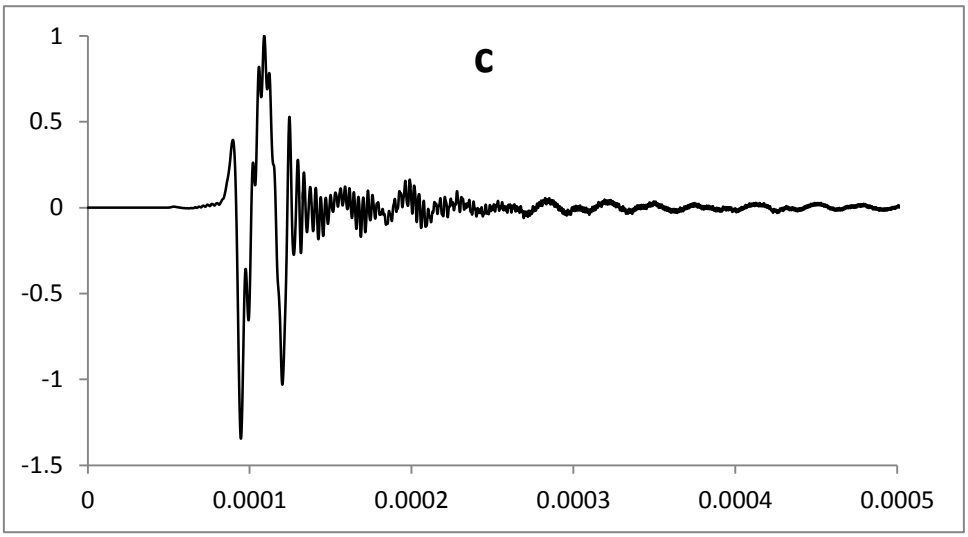
c
1
0.5
0
-0.5
-1
-1.5
0
0.0001
0.0002
0.0003
0.0004
0.0005

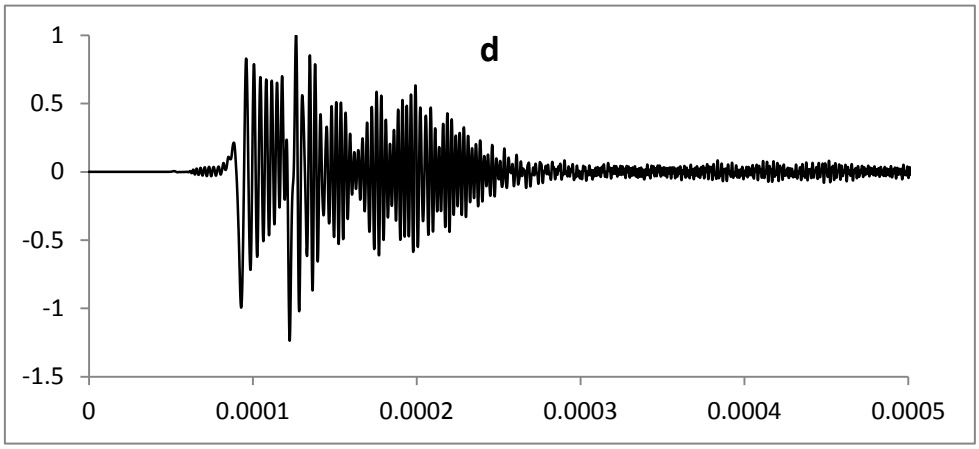

Figure 5.4 Normalized acceleration at 20 cm from the source in 2m concrete slab using a)n=4 b)n=3 c)n=2 d)n=1 sin shape functions

The duration of impact is an important impact characteristic, as it determines the frequency content of the generated stress waves and may also introduce Gibbs phenomenon if not chosen wisely. Figure 5.5 illustrates how choosing an impact too short can cause numerical instability and lead to the Gibbs phenomenon. By using impact duration of 10μs in Figure 5.5-c the results exhibit spurious oscillations.

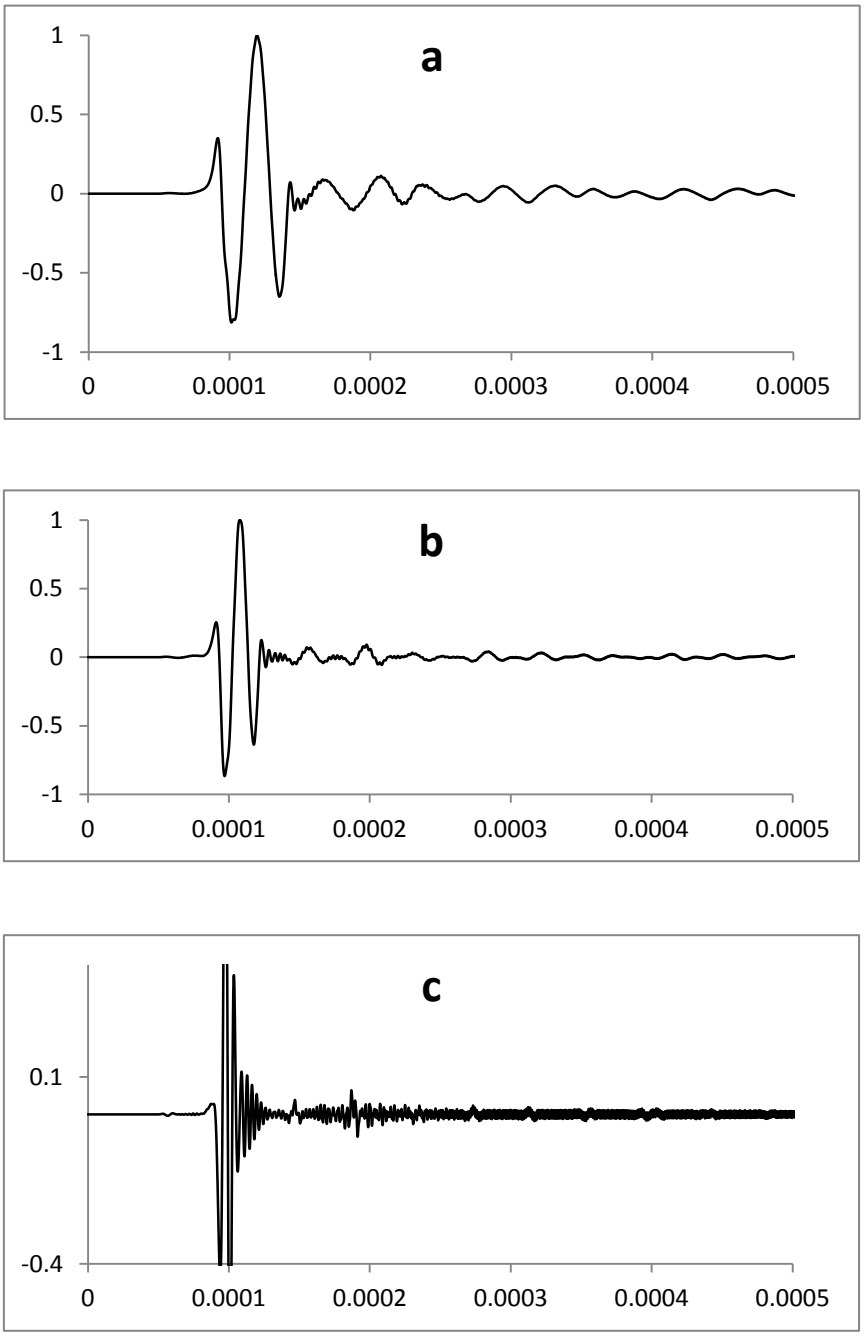

Figure 5.5 Normalized acceleration recorded at 20 cm from the source using 3rd order sin impact function and a) T=50μs b) T=30μs c) T=10μs

Generally the duration of the impact (T) should be less than following:

$$T \leq \frac{1}{f_c} \qquad \text{Equation 5.19}$$

where f_c is the central frequency of the interest. For practical purposes this frequency is assumed to be 30 KHz. This is considering the range of central frequency for accelerometers in the market.

$$T \leq \frac{1}{30000} = 33.3\ \mu s \qquad \text{Equation 5.20}$$

The default duration of impact in this study is 30 μs. Figure 5.6 shows the spectral magnitude of this function. For the frequency range of interest (i.e. less than 40 kHz) this function generates decent amount of energy.

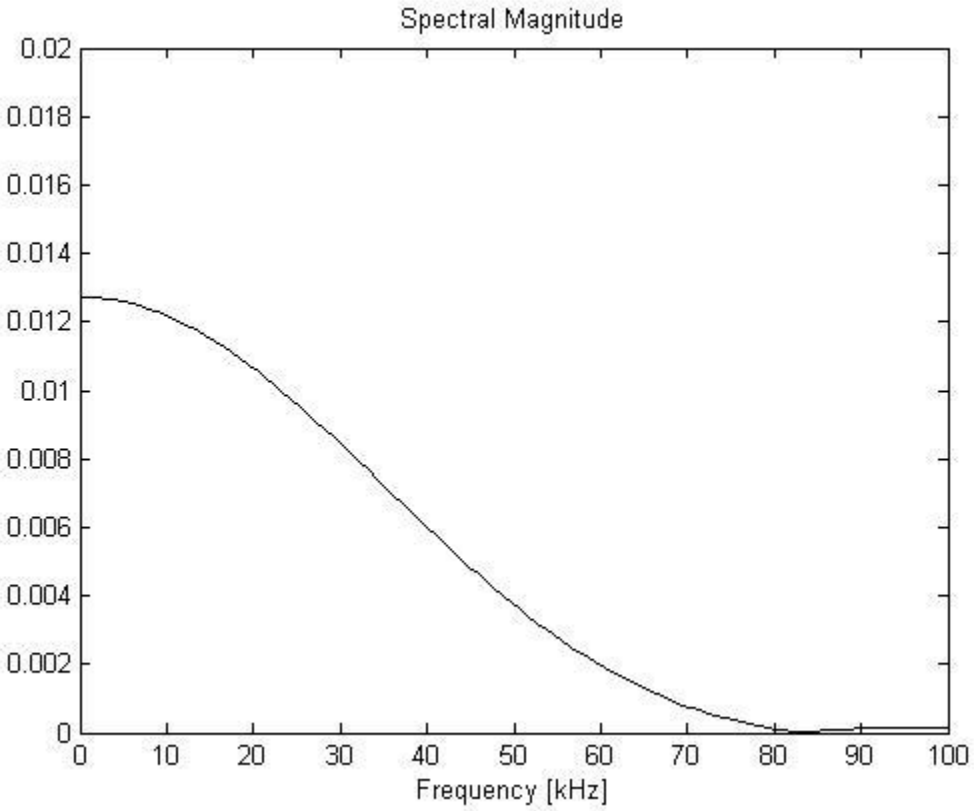

Figure 5.6 Spectral magnitude of a 3rd order sin function with impact duration of 30μs

5.5 Visual Examination of Wave Propagation in Layered Media

One way to investigate the phenomena of wave propagation in layered media is by visual examination. The ABAQUS visualization module allows for step-by-step contoured field outputs for any variable of interest. Using this feature a number of cases are examined.

The location of the impact is the upper left corner of each time step contour. All the model parameters are kept identical except for the layer shear wave velocity. The fixed

parameters are the same as previously discussed optimized values and are presented at Table 5.2.

The following cases of layer shear-wave velocities are examined (Table 5.1).

Table 5.1 The shear-wave velocity of each layer for visualization cases

Case Name	**Vs_1 (m/s)**	**Vs_2 (m/s)**	**Vs_3 (m/s)**	**Purpose**
V01	2500	2500	2500	Reference Model – Uniform case
V02	1250	2500	2500	Weak Top Layer
V03	2500	1250	2500	Weak Middle Layer
V04	2500	2500	1250	Weak Bottom Layer
V05	2500	1250	1250	Hard Top Layer
V06	1250	2500	1250	Hard Middle Layer
V07	1250	1250	2500	Hard Bottom Layer

Table 5.2 Finite Element Model Parameters

Dimension	2mX0.2M
Element Size	1mm
Time Steps	0.1μs
Impact Duration	30 μs

5.5.1 Case V01

Figure 5.7 shows the progressive snapshots of contoured velocity magnitude in the solid concrete deck FEM model. The wavefront is continuous throughout the layers as expected. From time step 90μs onwards the reflections from the bottom of the model reflections affect the wavefront.

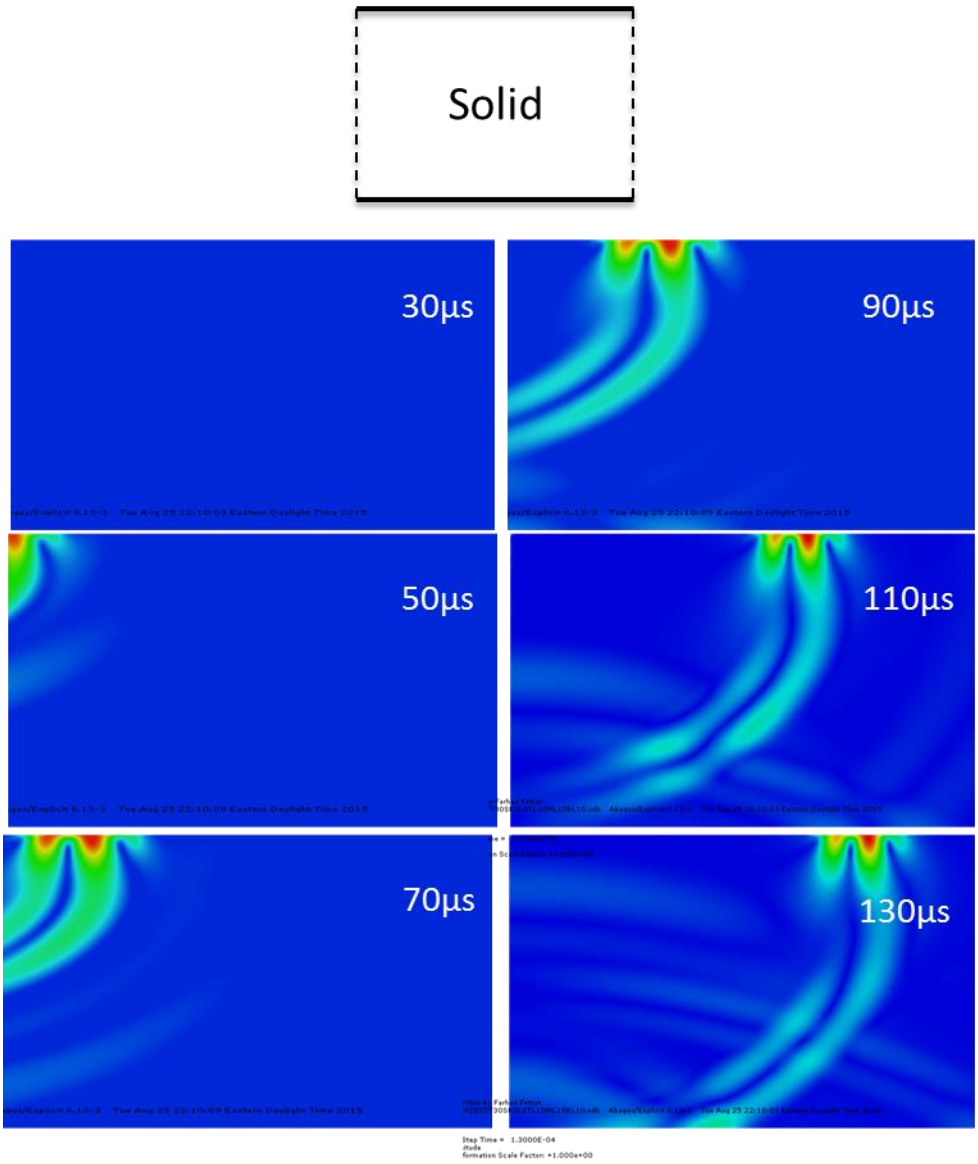

Figure 5.7 Snapshots of velocity magnitude in case V01, a solid concrete specimen, impacted at time 0. The step time is shown on each snapshot.

5.5.2 Case V02

Figure 5.8 shows the progressive snapshots of contoured velocity magnitude in the layered concrete deck FEM model with a weak top layer. The speed of propagation is

slower due to the lower shear-wave velocity of the top layer. Figure 5.9 compares the current case with case V01. Aside from the lower propagation speed, the wavefront fades away in the middle and bottom layer. This is because a considerable amount of energy is reflected before entering the lower velocity medium and the amplitude of the acceleration in the lower layers is relatively less than the top layer.

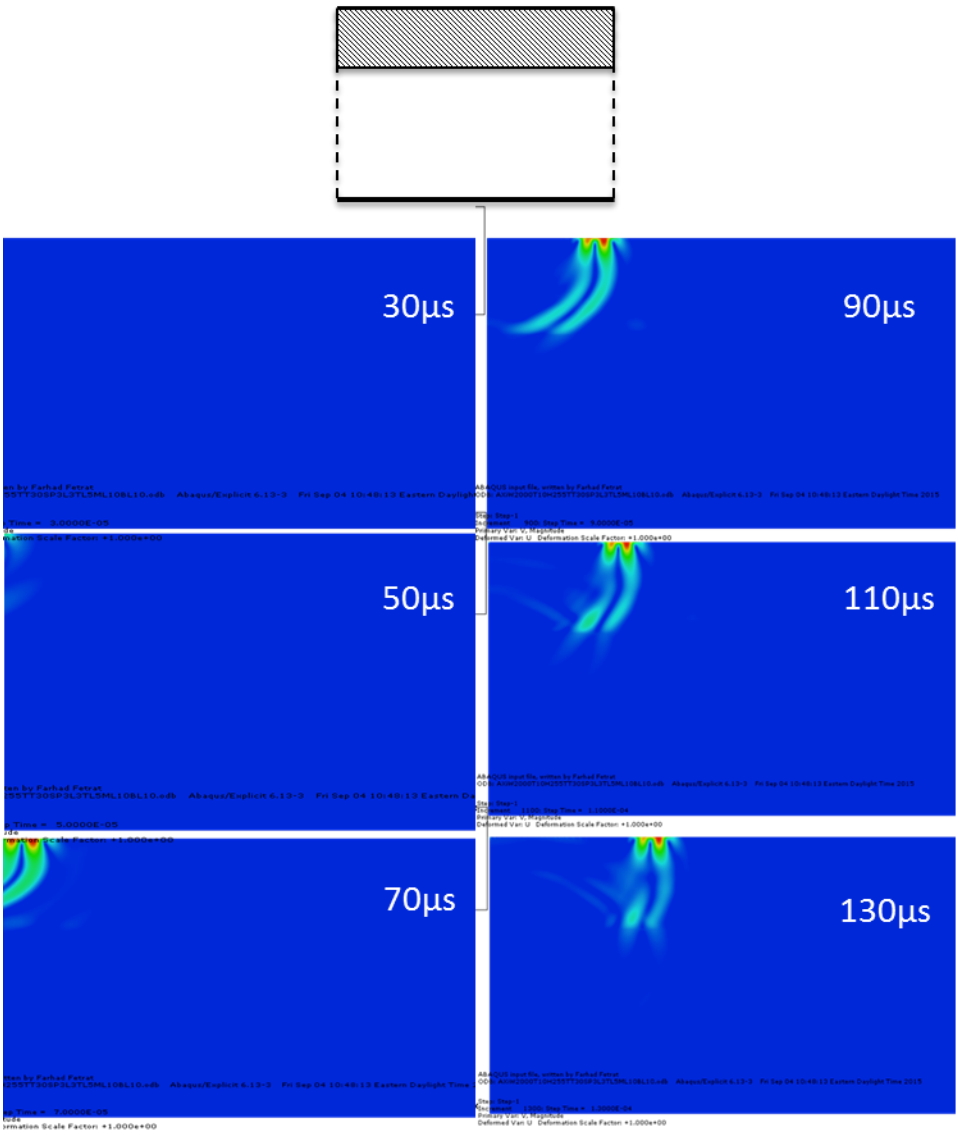

Figure 5.8 Snapshots of velocity magnitude in case V02 , a three-layer concrete specimen with weak top layer, impacted at time 0. The step time is shown on each snapshot.

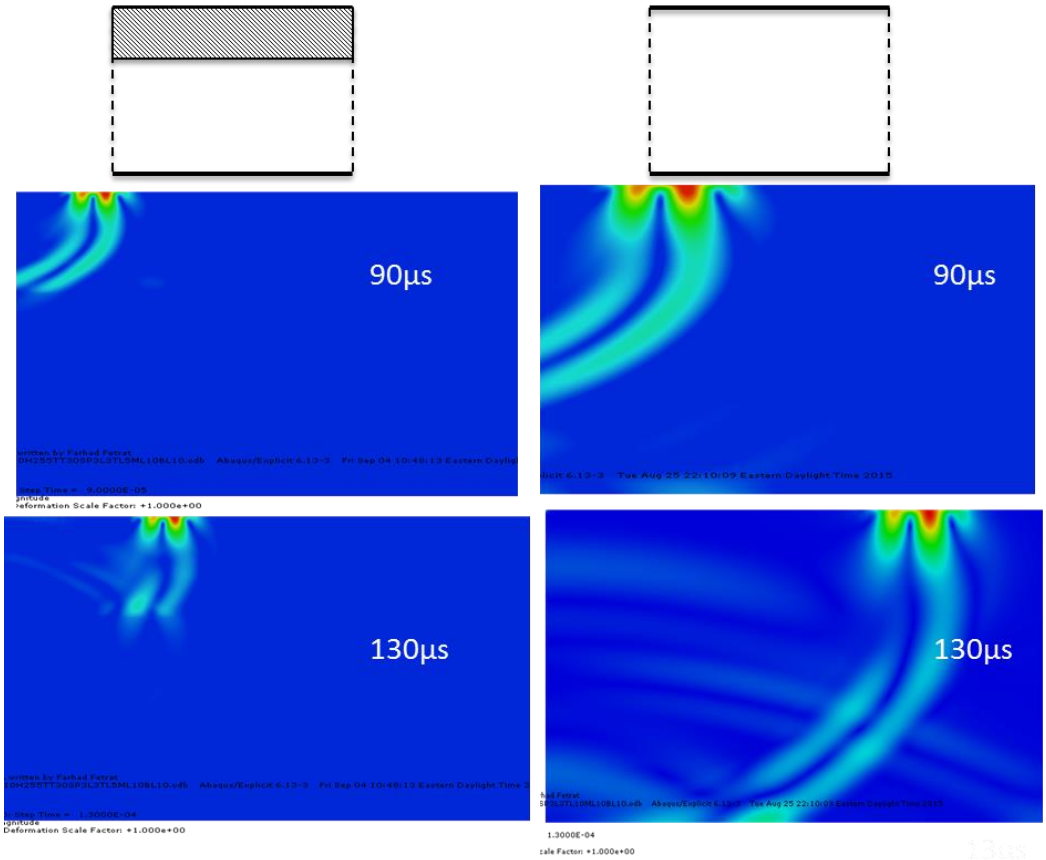

Figure 5.9 Snapshots of velocity magnitude in a three-layer concrete specimen with identical layers at right and with weak top layer at left at 90µs and 130µs.

5.5.3 Case V03

Figure 5.10 shows the progressive snapshots of contoured velocity magnitude in a layered concrete deck FEM model with a weak middle layer. The wavefront flattens towards the horizontal axis after entering the middle layer. This is due to the lower shear-wave velocity of this layer. After exiting the middle layer the propagation angle changes again. There are more wavefronts in the middle layer when compared to the uniform case in Figure 5.11.

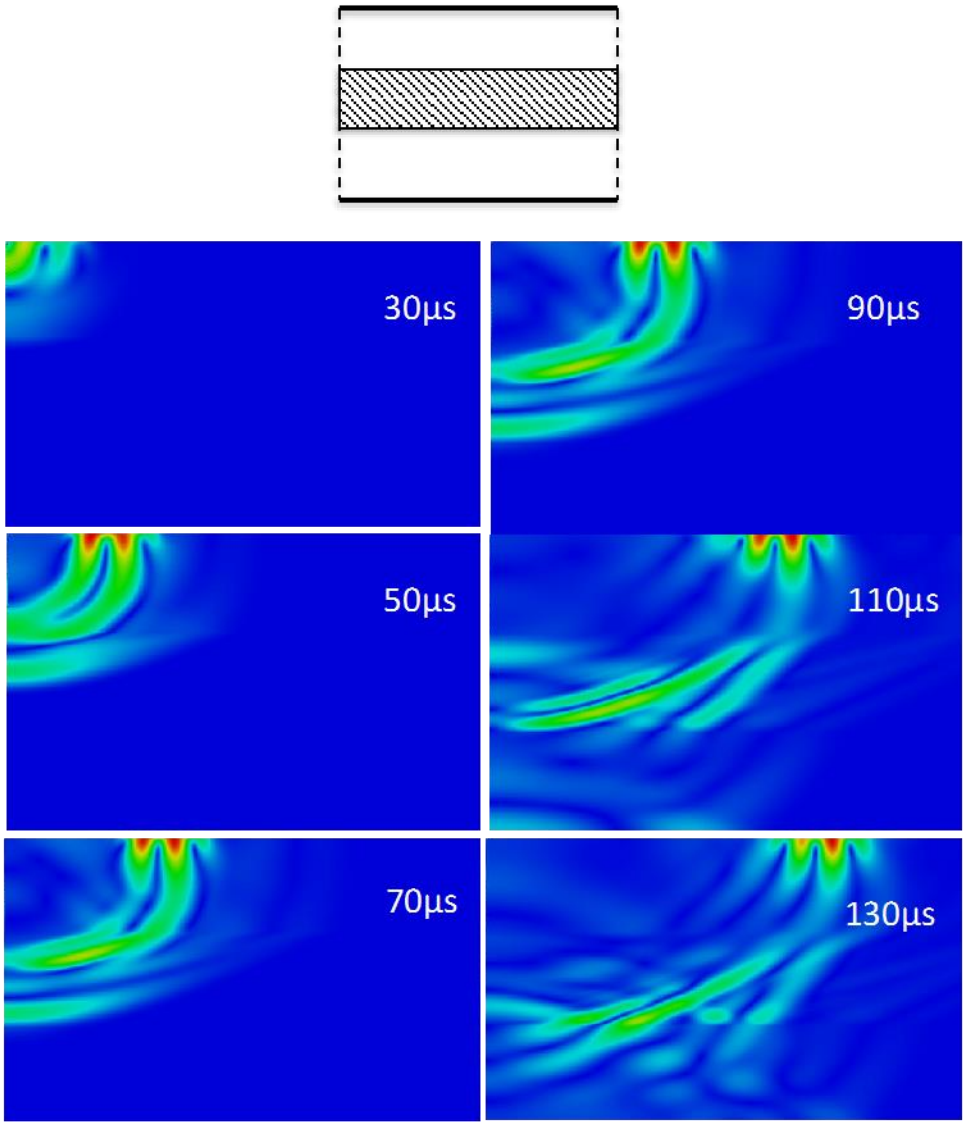

Figure 5.10 Snapshots of velocity magnitude in case V03 ,a three-layer concrete specimen with weak middle layer, impacted at time 0. The step time is shown on each snapshot.

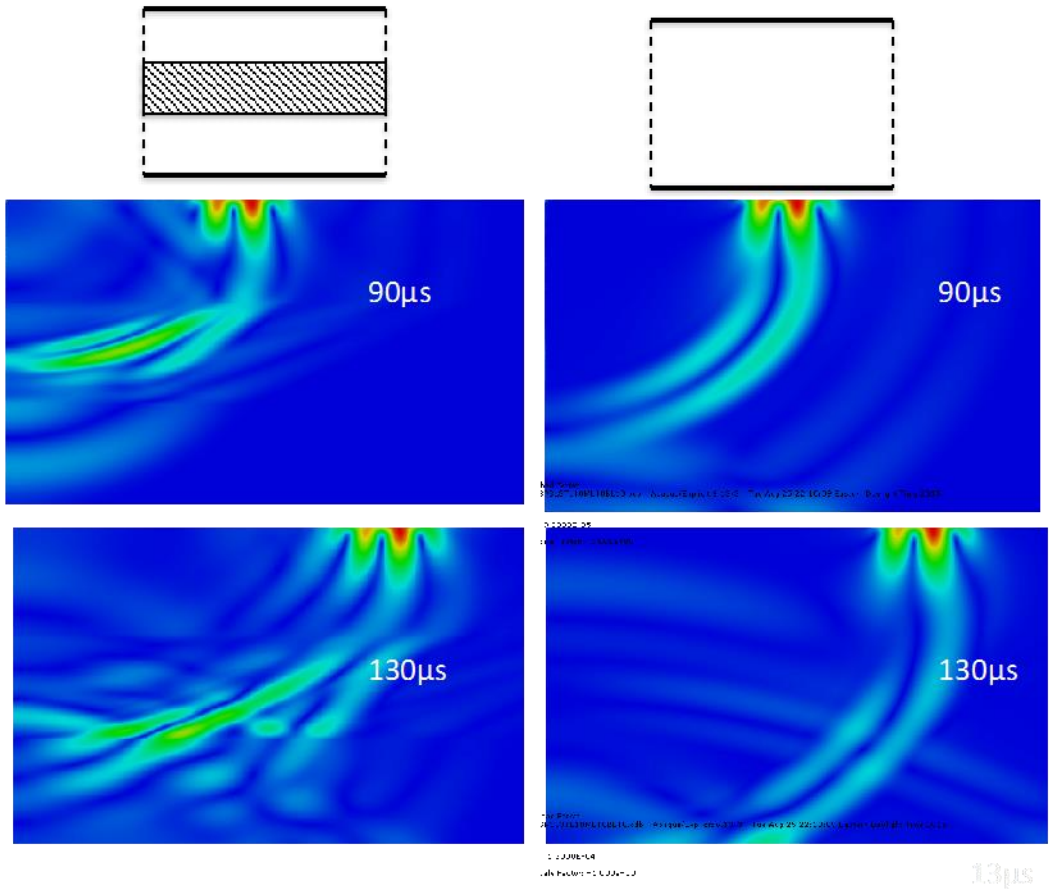

Figure 5.11 Snapshots of velocity magnitude in a three-layer concrete specimen with identical layers at right and with weak middle layer at left at 90µs and 130µs.

5.5.4 Case V04

Figure 5.12 shows the progressive snapshots of contoured velocity magnitude in the layered concrete deck FEM model with a weak bottom layer. The wavefront flattens towards the horizontal axis after entering the bottom layer. This is due to the lower shear-wave velocity of this layer. There are more wavefronts in the bottom layer than in the uniform case depicted in Figure 5.13.

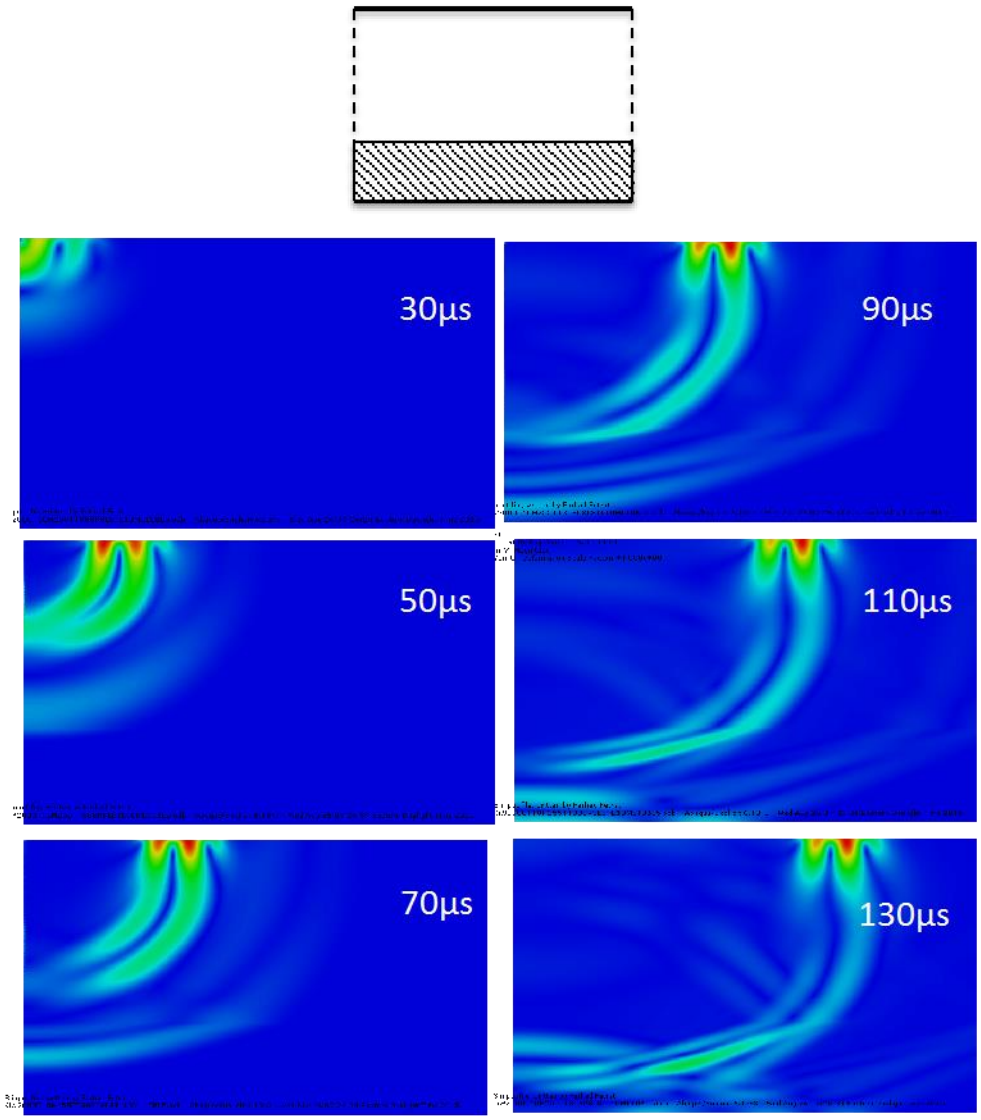

Figure 5.12 Snapshots of velocity magnitude in a three-layer concrete specimen with weak bottom layer impacted at time 0. The step time is shown on each snapshot.

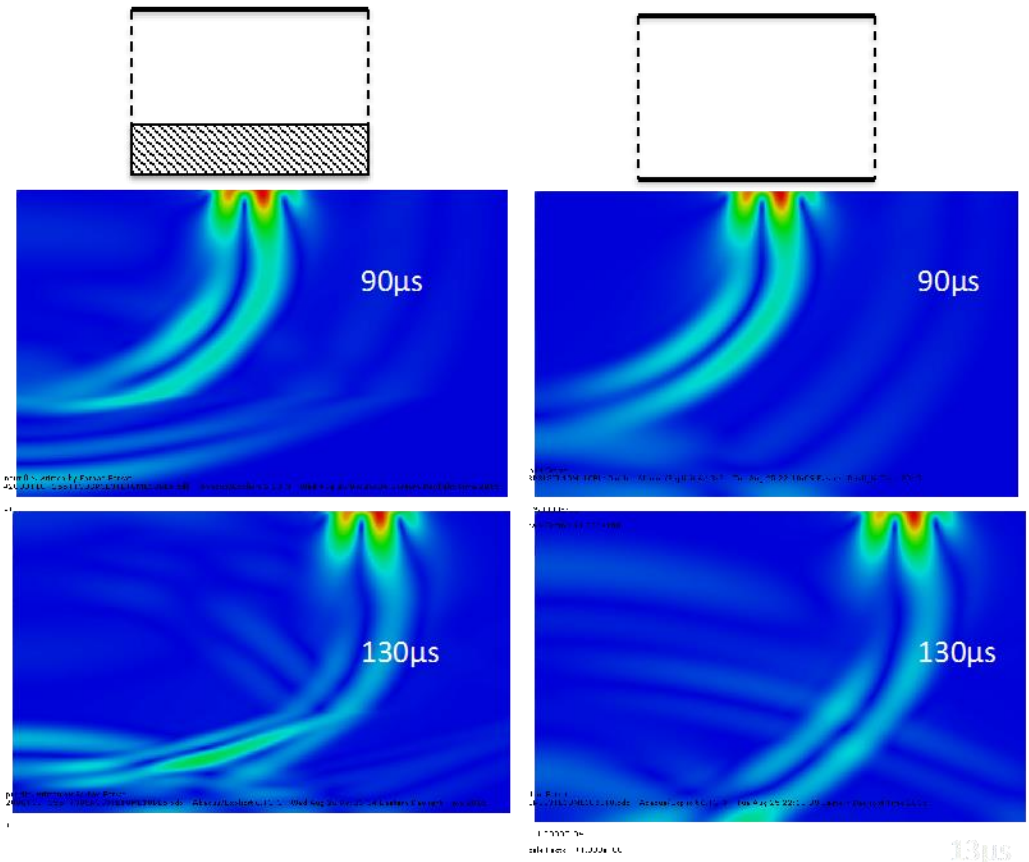

Figure 5.13 Snapshots of velocity magnitude in a three-layer concrete specimen with identical layers at right and with weak bottom layer at left at 90µs and 130µs.

5.5.5 Case V05

Figure 5.14 shows the progressive snapshots of contoured velocity magnitude in the layered concrete deck FEM model with a hard top layer. This case is similar to case V03 except the weak layer is extended to the bottom of the specimen. The wavefront flattens towards the horizontal axis after entering the middle layer and continues to propagate with this angle until it reaches the bottom. There are more wavefronts in the middle layer when compared to the uniform case in Figure 5.15.

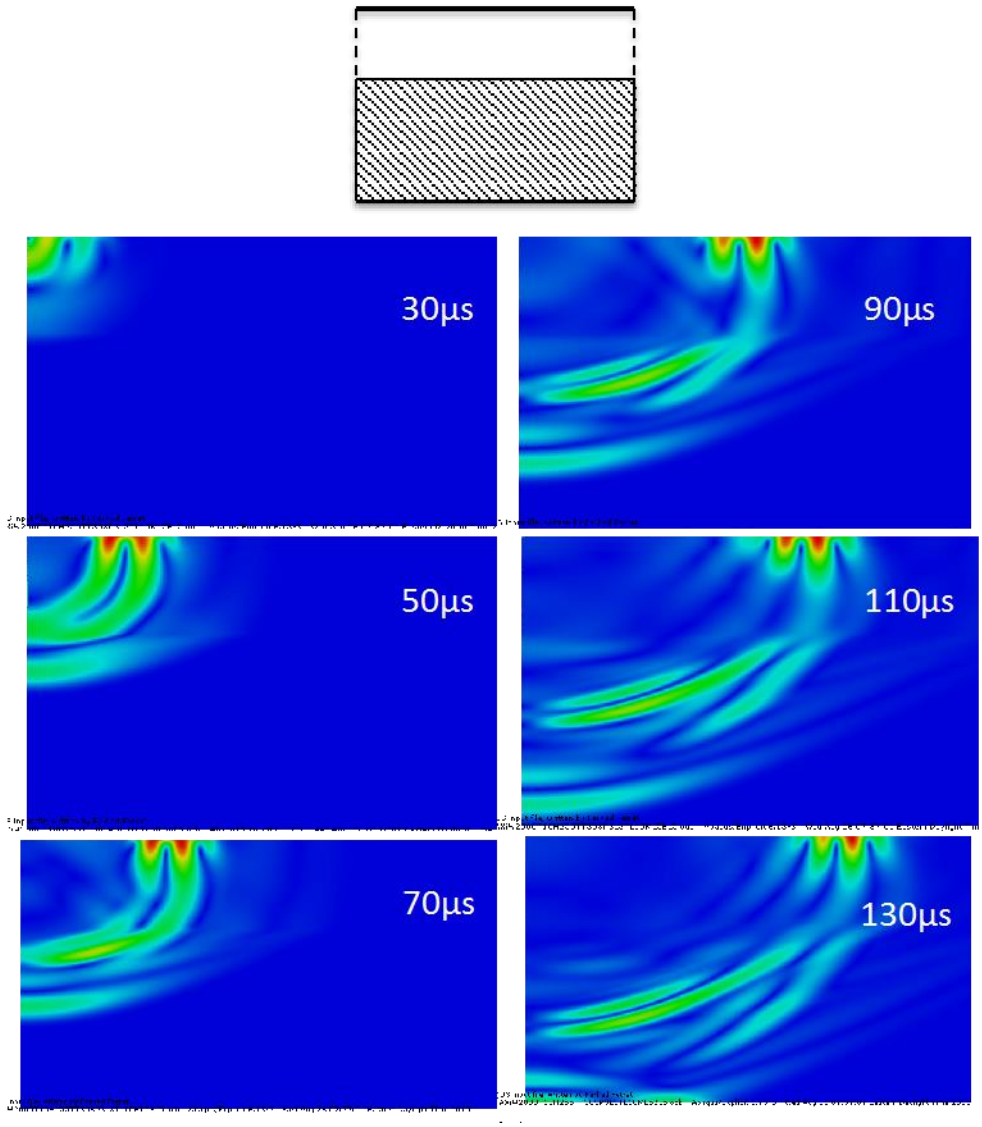

Figure 5.14 Snapshots of velocity magnitude in a three-layer concrete specimen with hard top layer impacted at time 0. The step time is shown on each snapshot.

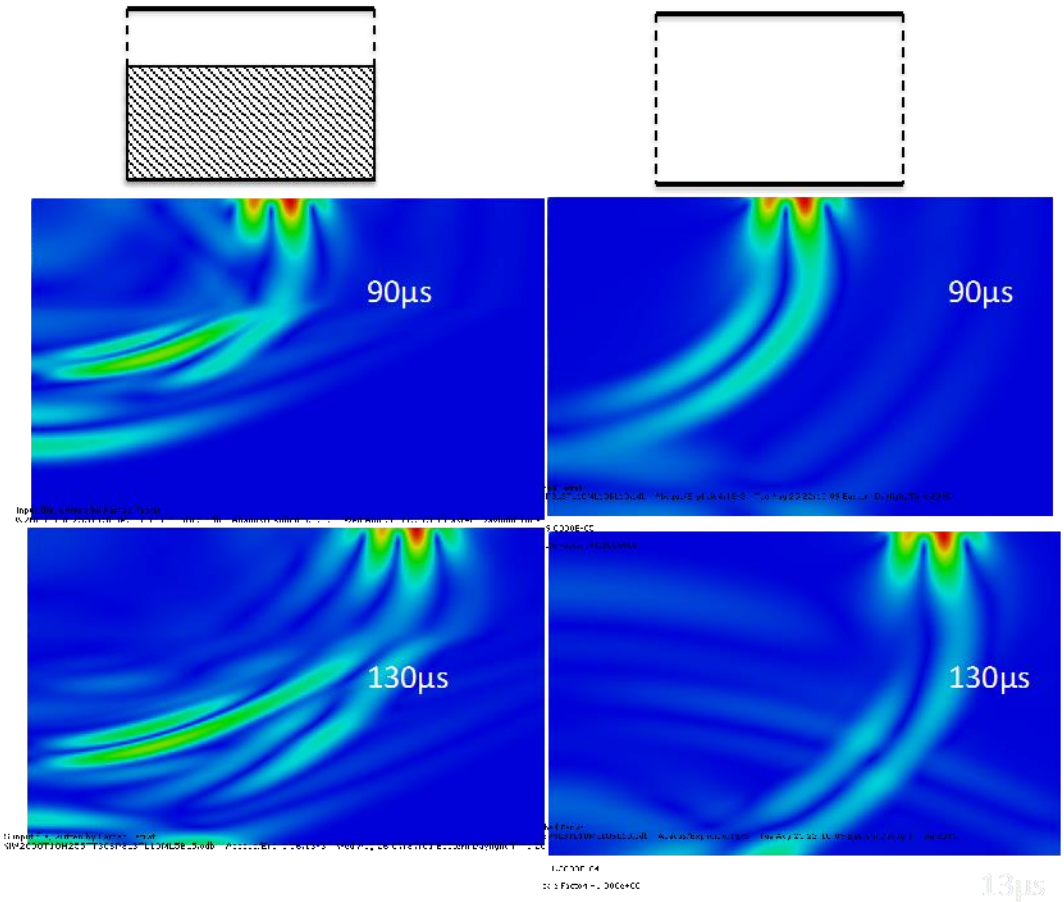

Figure 5.15 Snapshots of velocity magnitude in a three-layer concrete specimen with identical layers at right and with hard top layer at left at 90µs and 130µs

5.5.6 Case V06

Figure 5.16 shows the progressive snapshots of contoured velocity magnitude in a layered concrete deck FEM model with a hard middle layer. The speed of propagation is slower due to the lower shear-wave velocity of the top layer. Figure 5.17 compares the current case with case V01. Aside from a lower propagation speed, the wavefront fades away in the middle and bottom layer.

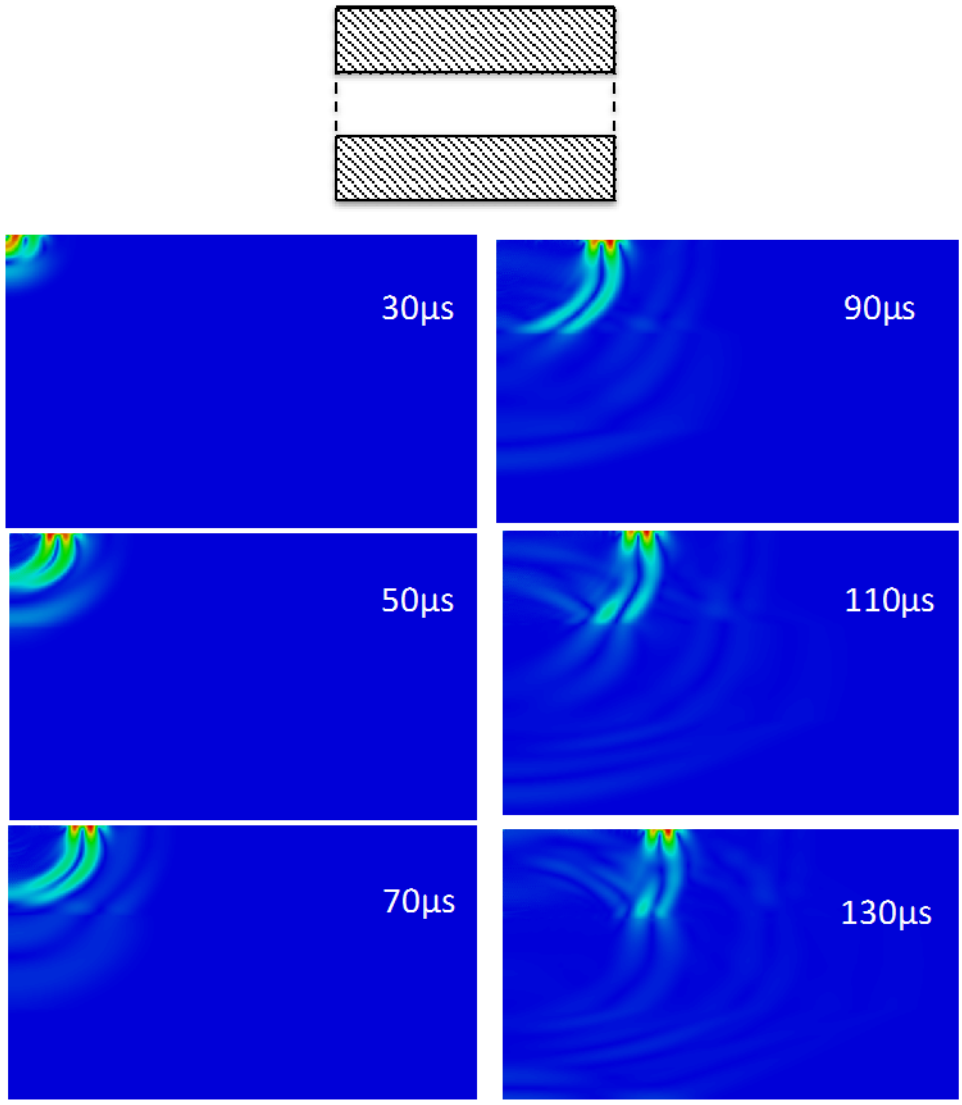

Figure 5.16 Snapshots of velocity magnitude in a three-layer concrete specimen with hard middle layer impacted at time 0. The step time is shown on each snapshot.

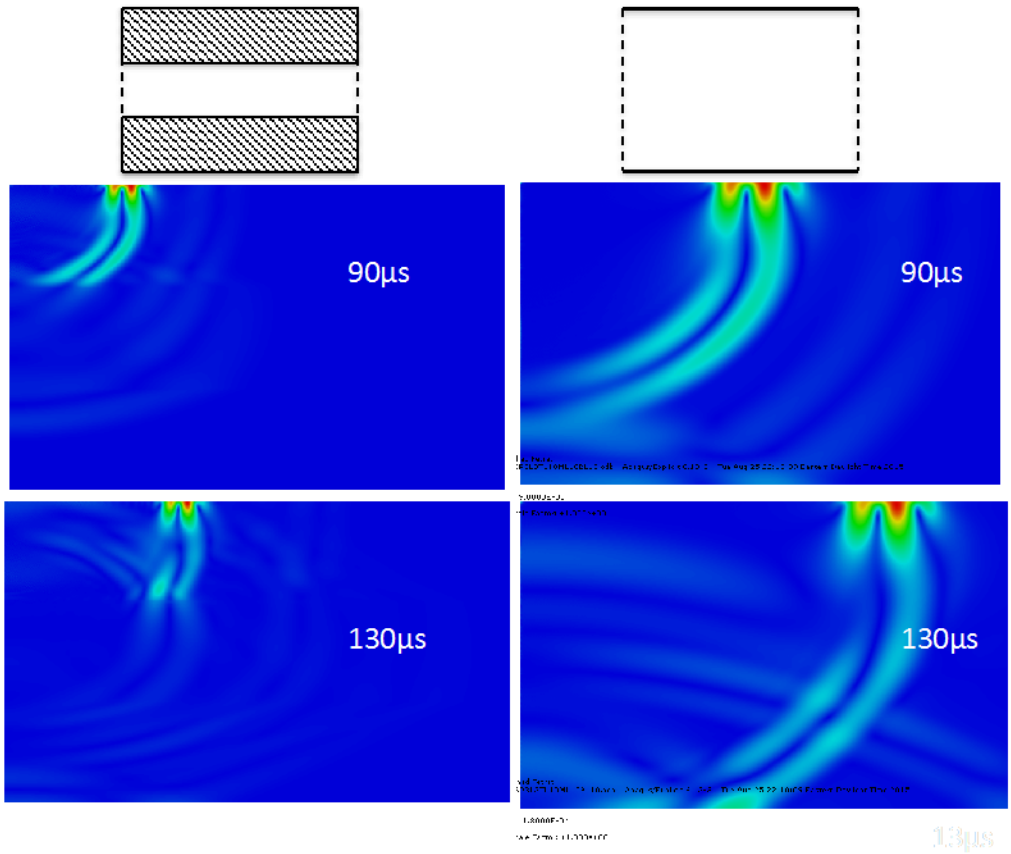

Figure 5.17 Snapshots of velocity magnitude in a three-layer concrete specimen with identical layers at right and with hard middle layer at left at 90µs and 130µs.

5.5.7 Case V07

Figure 5.18 shows the progressive snapshots of contoured velocity magnitude in the layered concrete deck FEM model with a hard bottom layer. The speed of propagation is slower due to the lower shear-wave velocity of the top layer. Figure 5.19 compares the current case with case V01. Aside from lower propagation speed, the wavefront fades away in the bottom.

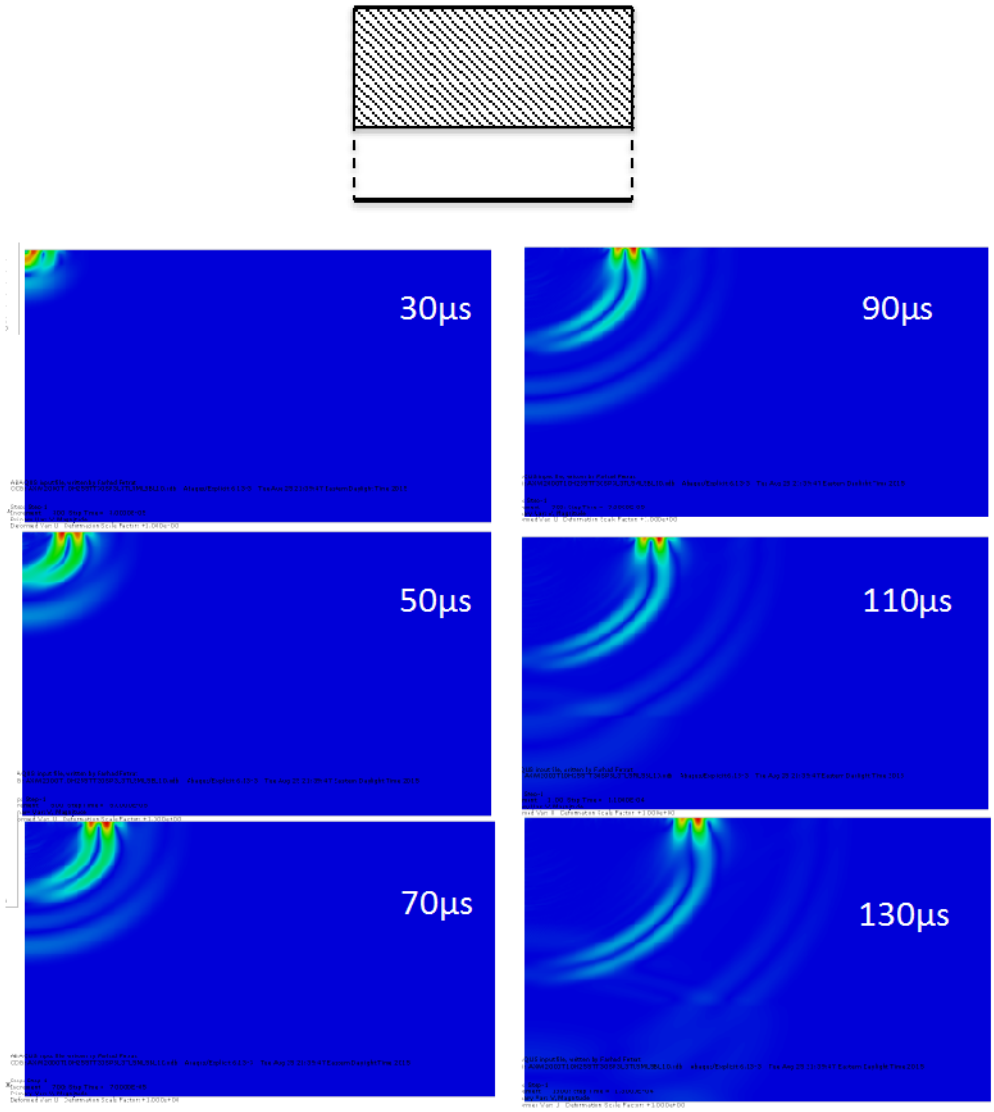

Figure 5.18 Snapshots of velocity magnitude in a three-layer concrete specimen with hard middle layer impacted at time 0. The step time is shown on each snapshot.

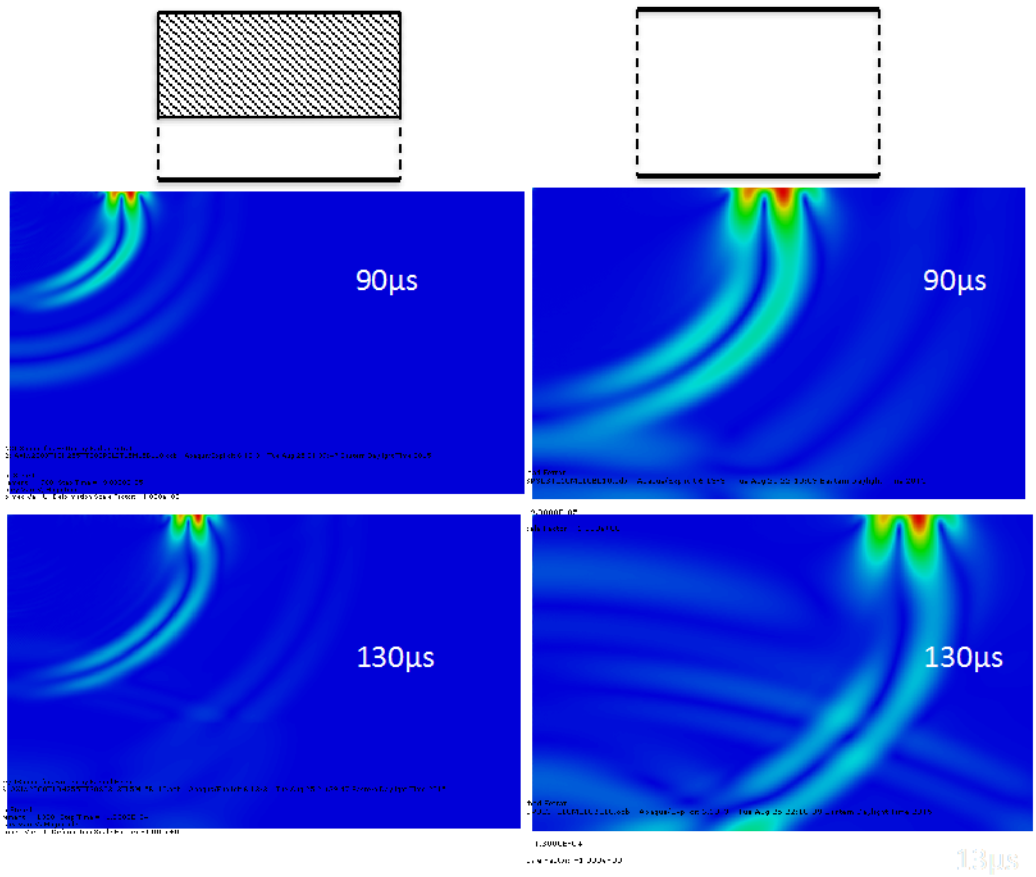

Figure 5.19 Snapshots of velocity magnitude in a three-layer concrete specimen with identical layers at right and with hard bottom layer at left at 90µs and 130µs.

5.5.8 Visualization Conclusions

After examining the visualization cases the following conclusions are reached:

1. In almost all the cases with soft top-layer, the wavefront amplitude disappears after entering the lower layer with higher shear-wave velocity.
2. In cases of harder top layer once the wavefront enter the softer lower layer, it flattens out and divides into more ripples.

3. The speed of wave propagation along the surface depends only on the shear-wave velocity of the top layer.

5.6 Source and Sensor Arrangement

In order to come up with an efficient source and sensor set up, a series of parameter studies has been carried over. The examined parameters will include the total number of sensors, the distance between the source and first sensor, and the spacing between the sensors.

In MASW method the dispersion curve is obtained by transforming the surface-wave fields from the offset-time domain into the phase-frequency domain by using a phase-shift method (Park, Miller, & Xia, 1998). This method is described in details in section 4.1. The governing equations are repeated here. A N-channel record mr_N is defined as an array of N traces collected: $mr_N = r_i$ (i=1, 2, …,N). And in the frequency domain as it is $MR_N(\omega) = R_i(\omega) = FFT[r_i]$. $R_i(\omega)$ can be decomposed into its amplitude $A_i(\omega)$ and phase $P_i(\omega)$.

$$A_s(C_T) = e^{-i\delta_{1,\tau}}R_{i,norm}(\omega) + e^{-i\delta_{2,\tau}}R_{2,norm}(\omega) + \cdots + e^{-i\delta_{N,\tau}}R_{N,norm}(\omega) \quad \text{Equation 5.21}$$

$$\delta_{i,\tau} = \omega\,{(x_1 + (i-1)dx)}/{C_T} \quad \text{Equation 5.22}$$

Where

$$R_{i,norm}(\omega) = \frac{R_i(\omega)}{|R_i(\omega)|} \qquad \text{Equation 5.23}$$

A_s is the summed amplitude of *N* traces. R is the Fourier transform of source wave at each sensor location. Since A_s is a complex number, to evaluate the resolution of dispersion curve there are two approaches: 1-to use the absolute form of the complex number 2-to use the real part of the complex number. For the sake of simplicity of the analysis, the absolute form is used in this research. Also, it has been shown that *x1*,the factor for general closeness of the sensor array, does not cause a significant change in the resolution (Park, Miller, & Xia, 2001). For this reason, it is assumed that *x1* is the same as *dx*.

Figure 5.20 shows the changing trend of the normalized absolute value with a different number of sensors. The data is extracted from numerical simulation of a 3-layer system with soft middle layer (case V03) using ABAQUS. For the full dispersion surface refer to Figure 5.26. The frequency and array length are kept constant at 8 kHz and 2m respectively. The number of receivers is changing from 100 to 10. Here it is expected to see dominant peak between 1500m/s and 2000 m/s. It is clear that increasing the number of sensor increases the resolution of the amplitude at different velocities. An excessively coarse spacing increases the spatial aliasing problem, which becomes problematic at lower phase-velocities.

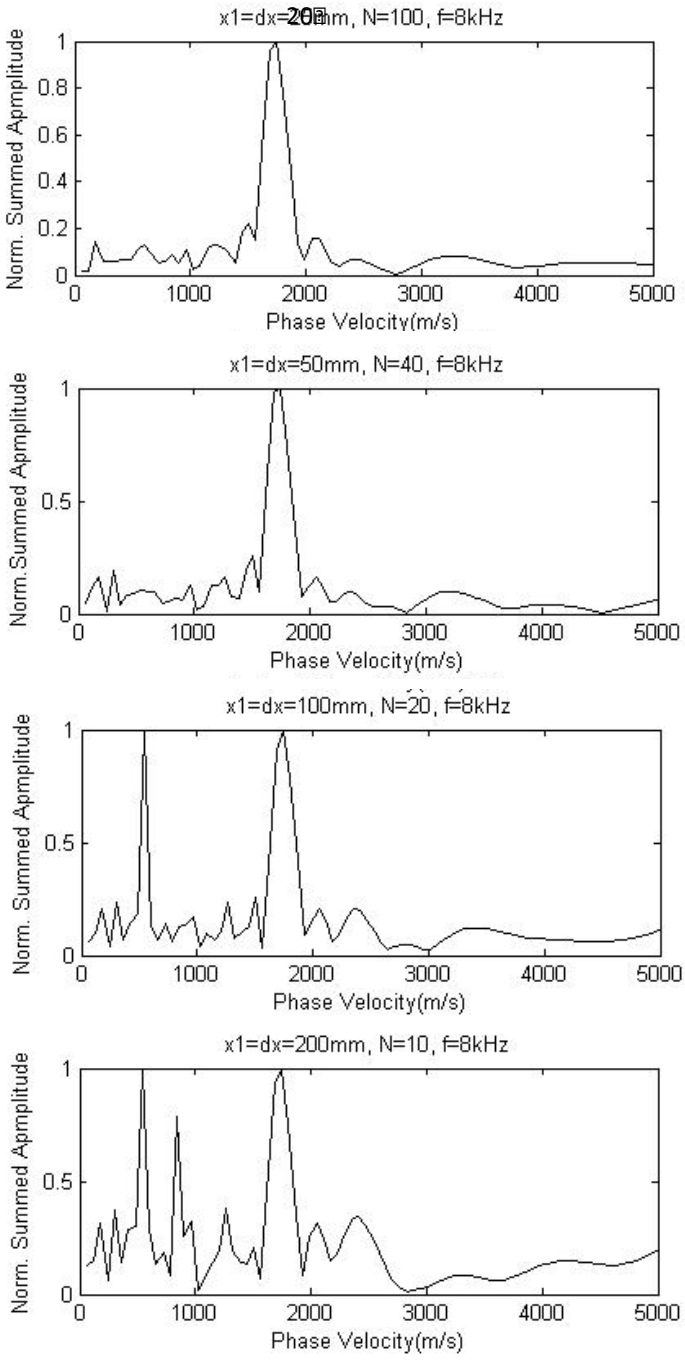

Figure 5.20 Changing trend of the normalized absolute value showing how the resolution of dispersion curve changes with the number of sensors assuming a constant array size (X_{max})

Figure 5.21 shows the effect of the array size (X_{max}) in the resolution of the amplitude assuming a constant number of sensors. The same numerical simulation is used here as in previous case. The sharper the peak at the expected frequency will result in a higher resolution dispersion surface. It is shown that spreading the sensors out further can increase the resolution and decrease the aliasing noise issues. It should also be noted that, even though the longer array seems to increase the signal quality; it is in reality limited because of the material damping. When doing field experiments, the near-field and far-field effects should also be taken into account.

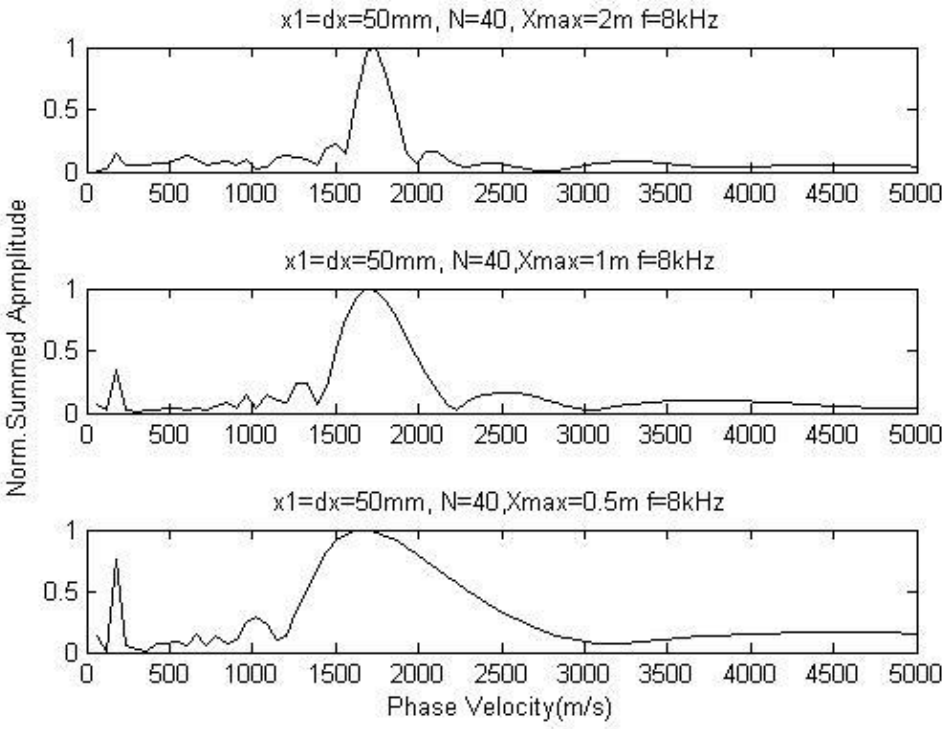

Figure 5.21 Changing trend of the normalized absolute value showing how the resolution increases by spreading the sensors apart

5.7 Finite-element Model Validation

In order to verify the accuracy of the results from the FEM model, a number of dispersion surface are compared to the results from the forward problem discussed in the previous chapter. All the sensor locations in the original FEM model are considered for this analysis. The sensors are 1mm apart in this case. The forward problem results are obtained from DISPER program. The dispersion surface consists of 67X67 elements. This matrix represents 67 phase-velocity amplitudes in the range of 0 to 5000 m/s in 67 frequency steps in the range of 0 to 40 kHz.

Since the shear-wave velocity of the each layer is the most important variable affecting the dispersion curve, the validation is done for three different values of each layer's shear-wave velocity. The values are the minimum, median and maximum of the range of values considered for the inversion analysis, as shown in Table 5.3. All the other model parameters are kept identical to the values discussed earlier in this chapter and are the same for all three layers. Figure 5.22 Figure 5.28 compare the dispersion surface from the FEM to the forward model for different layer shear velocities.

Table 5.3 Shear-wave velocity values used to validate the FEM Model

Minimum (m/s)	Median (m/s)	Maximum (m/s)
1250	1750	2500

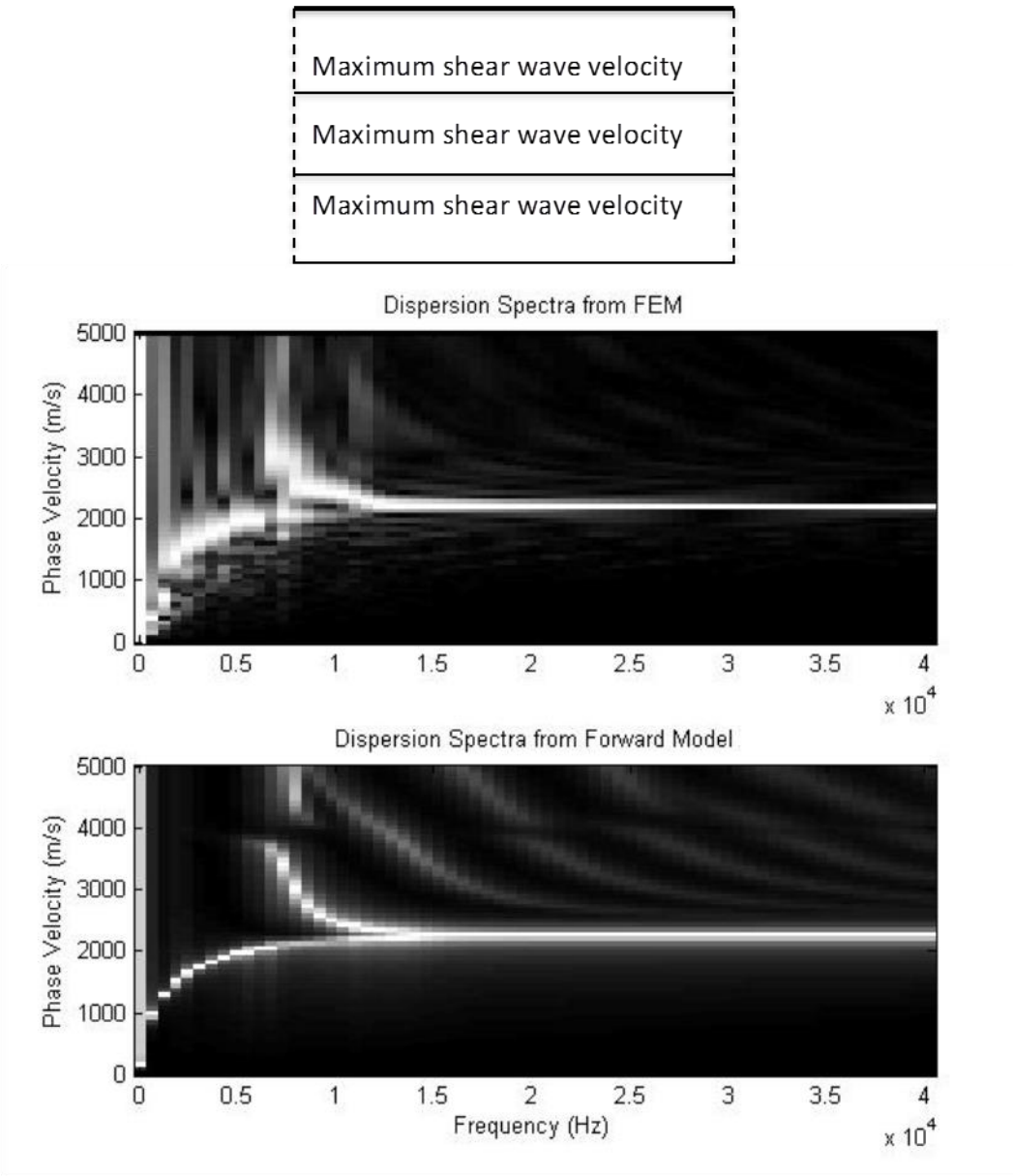

Figure 5.22 Dispersion surface from FEM model at the top compared to the forward model for the uniform case.

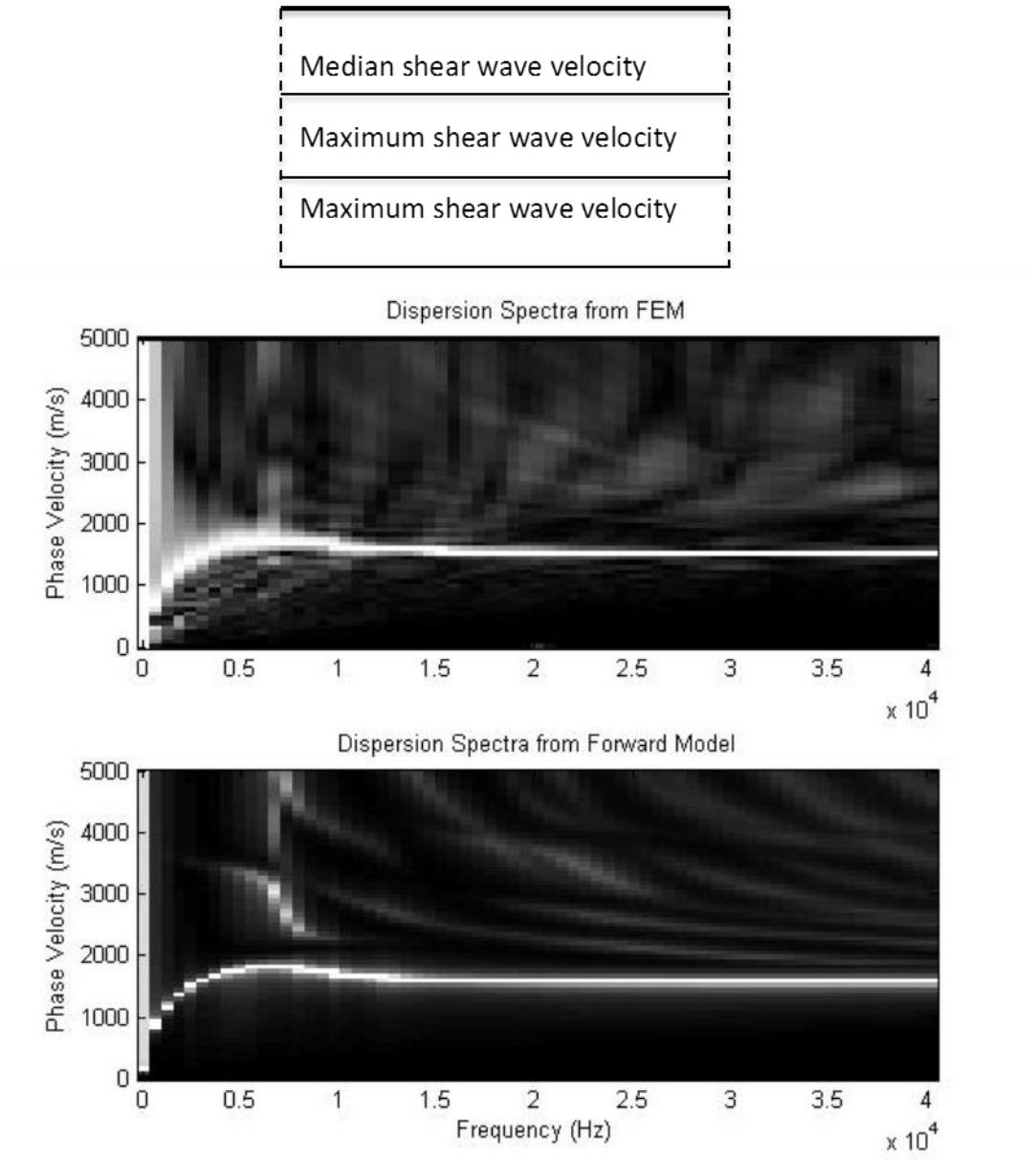

Figure 5.23 Dispersion surface from FEM model at the top compared to the forward model for case with median shear-wave velocity for top layer.

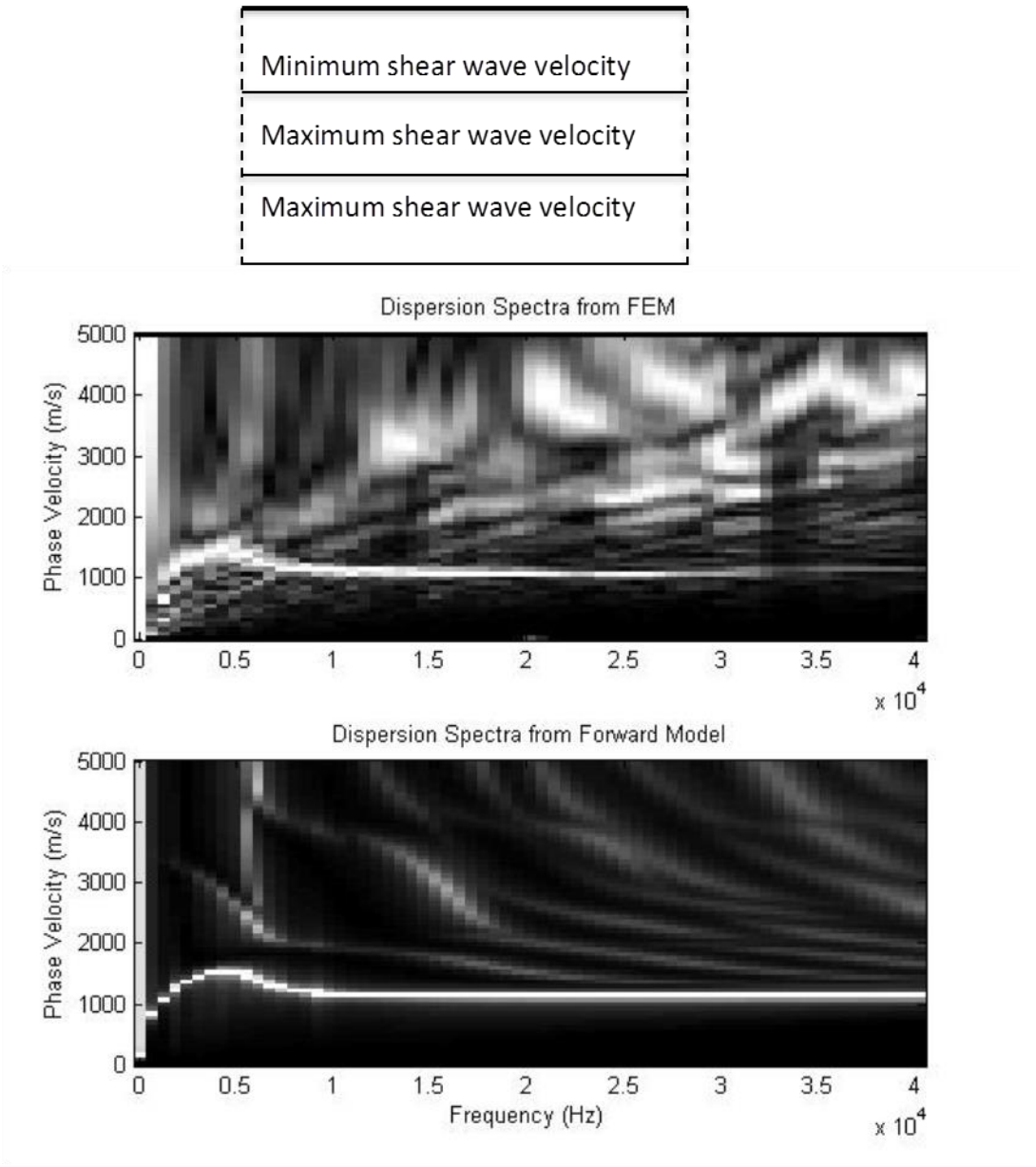

Figure 5.24 Dispersion surface from FEM model at the top compared to the forward model for case with minimum shear-wave velocity for top layer.

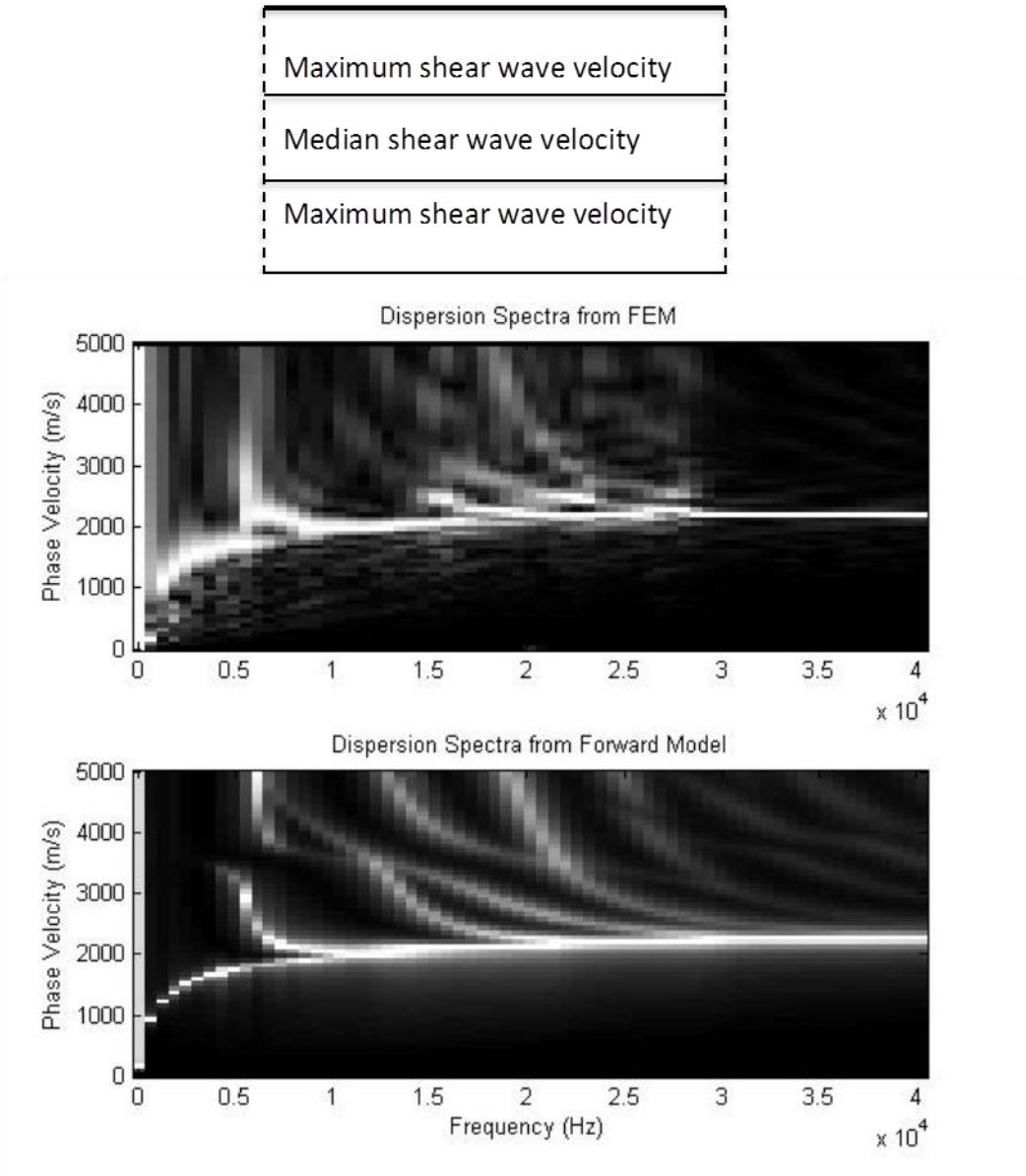

Figure 5.25 Dispersion surface from FEM model at the top compared to the forward model for case with median shear-wave velocity for middle layer.

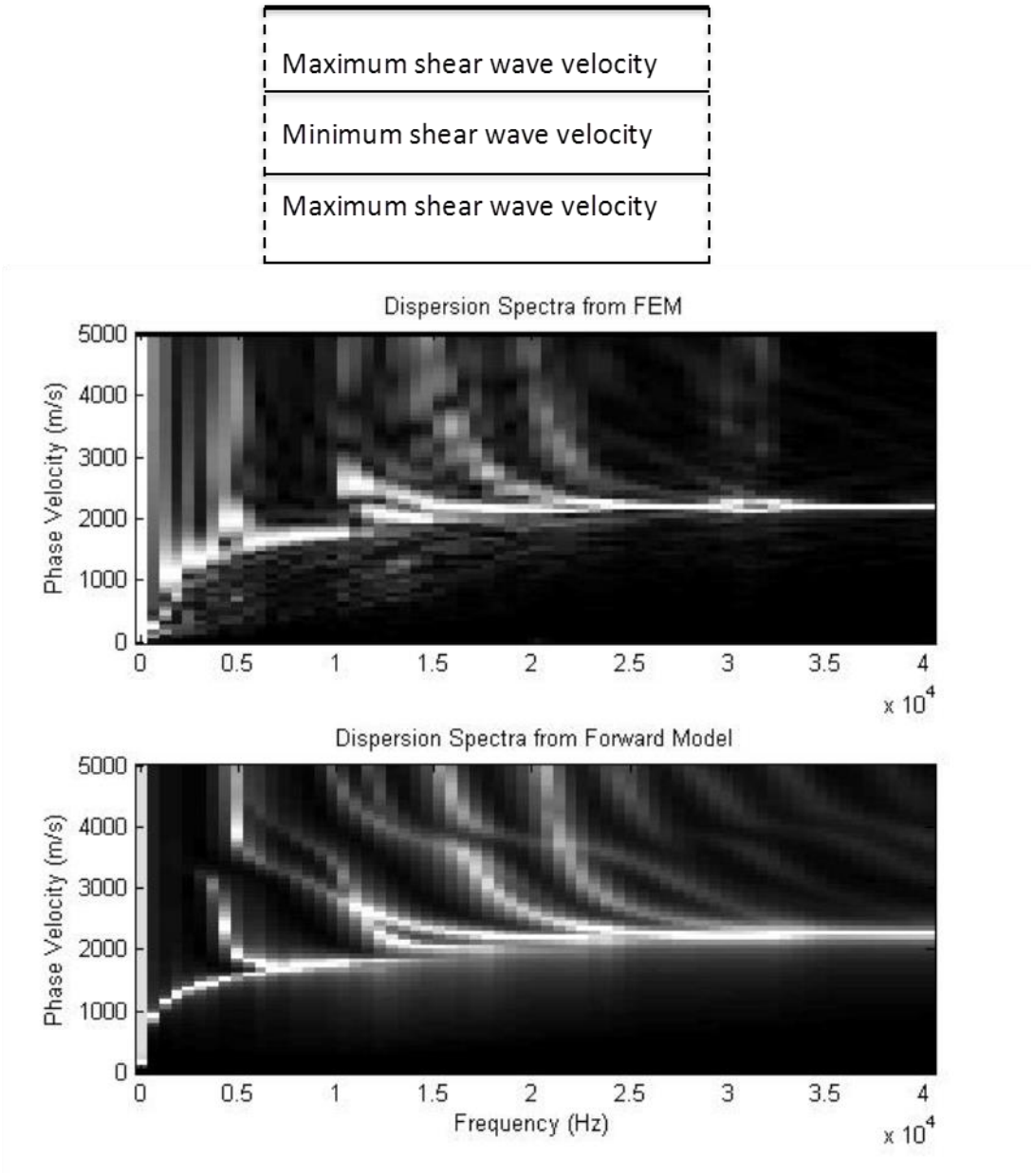

Figure 5.26 Dispersion surface from FEM model at the top compared to the forward model for case with minimum shear-wave velocity for top layer.

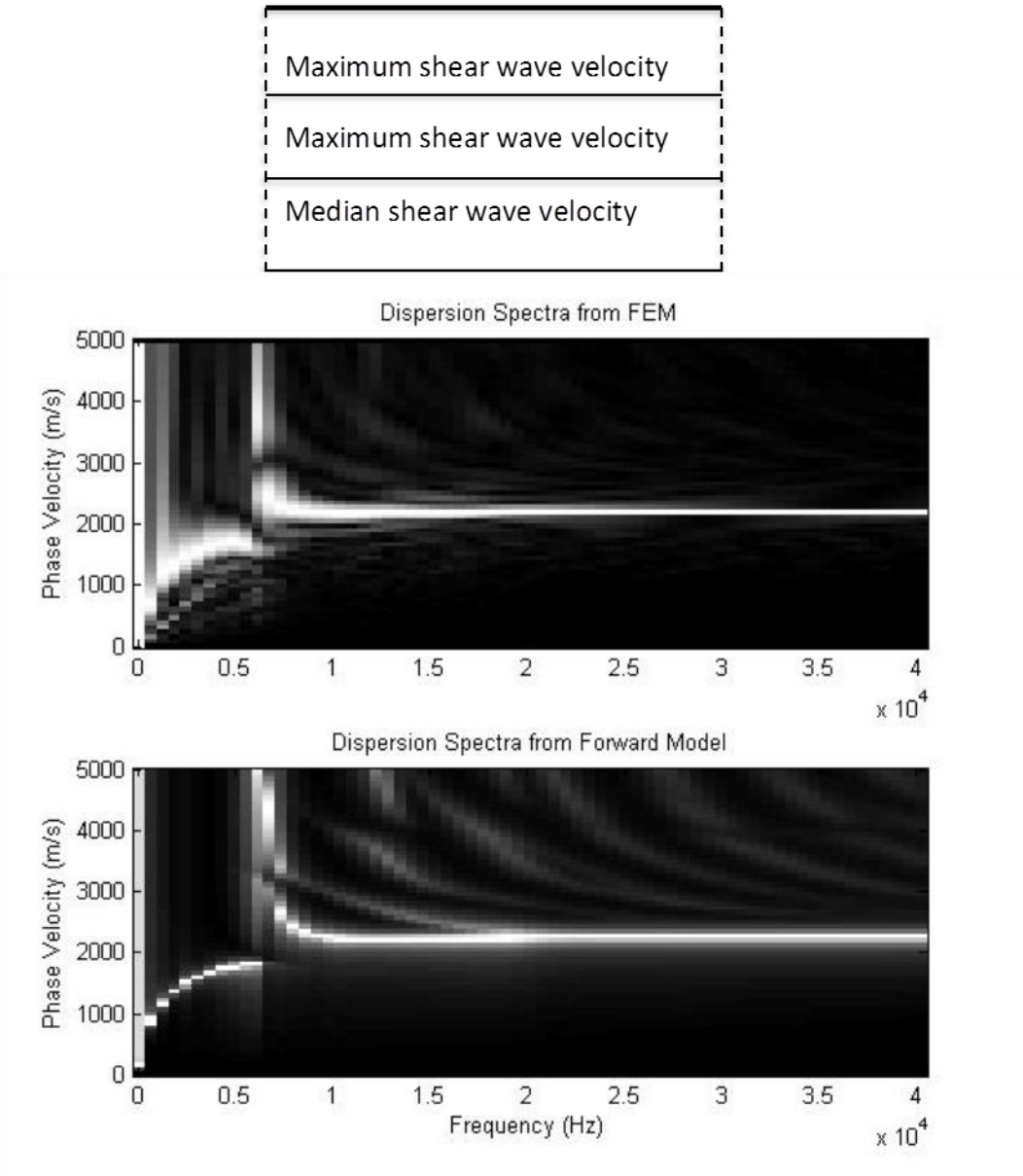

Figure 5.27 Dispersion surface from FEM model at the top compared to the forward model for case with median shear-wave velocity for bottom layer

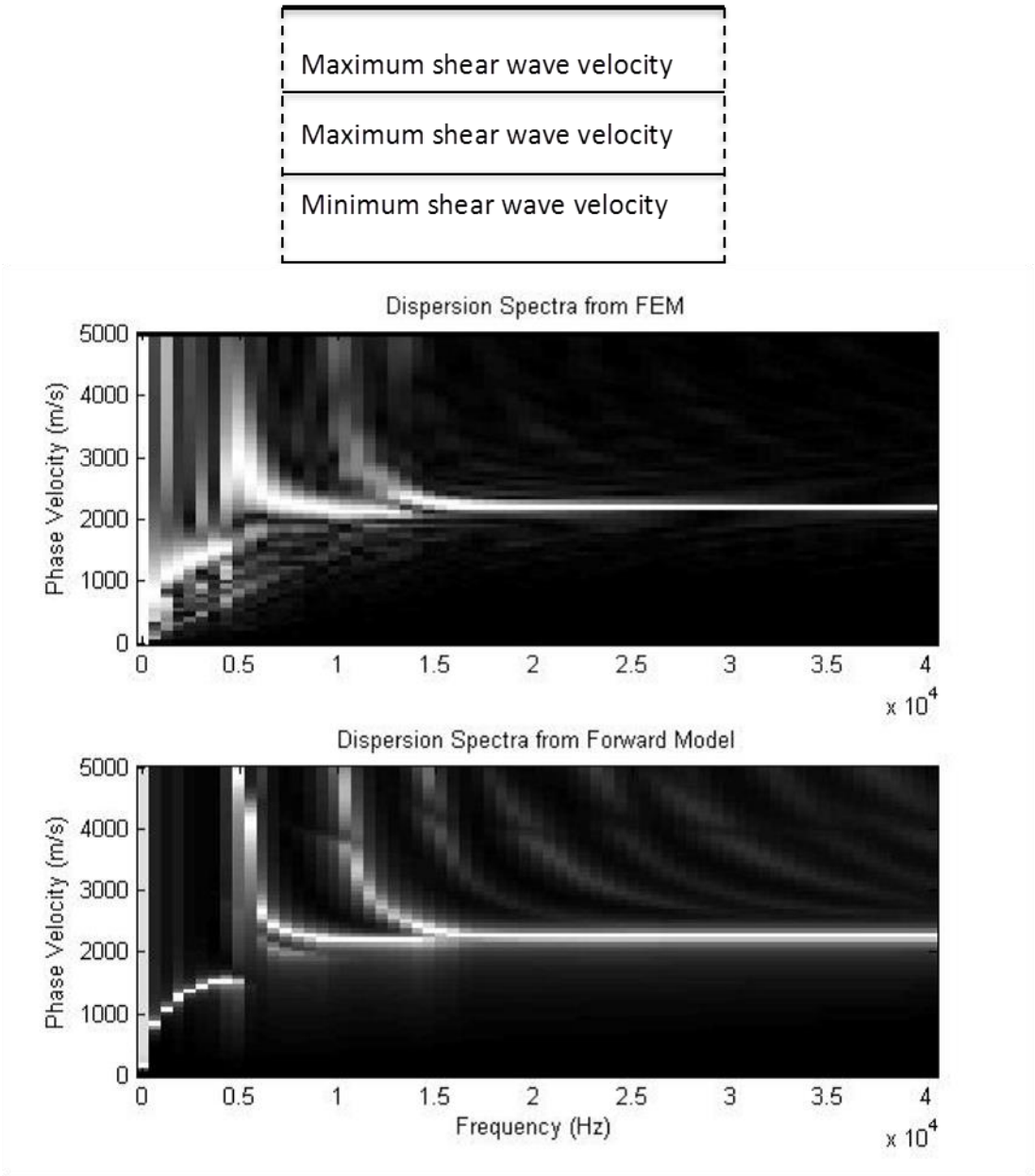

Figure 5.28 Dispersion surface from FEM model at the top compared to the forward model for case with minimum shear-wave velocity for bottom layer.

5.7.1 Conclusion

Based on the comparisons between the dispersion surface from the FEM model and DISPER, the results from the FEM model are consistent with DISPER results. However there are few differences:

1. The lower frequency content of the dispersion surface is significantly noisier than DISPER results.
2. In the case with minimum phase velocity at the top layer, there is a significant energy in the higher modes. This is due to the reflection from the interface of harder layer. This can make the inversion process challenging.
3. In the case with the median phase velocity at the top layer, the asymmetric 0^{th} mode is dominating the FEM results. The symmetric 0^{th} mode is not observable in FEM results despite being present in DISPER dispersion surface.
4. In the uniform case and the cases with soft bottom layer the higher modes are not visible in the FEM results.

6 Inversion Analysis

6.1 Introduction (Background)

In the context of bridge-deck testing, the inversion of the surface-wave testing means the estimation of bridge-deck's properties from the measured surface-wave data. Researchers have used various types of surface-wave data for the purpose of estimation. Several authors (Nazarian & Stokoe II, 1984; Gucunski & Woods, 1991; Ganji, Gucunski, & Nazarian, 1998; Nazarian S. , 1984) used the dispersion curve(s), (Hadidi & Gucunski, 2003) used the raw field record and (Ryden & Park, 2006) used the dispersion surface. Regardless of the input data, the inversion process cannot be solved directly, as it is non-unique and nonlinear. It is nonlinear because a small change in layer properties can result in big changes in the surface-wave data, and vice versa. It is non-unique because multiple profiles can exist for one set of surface-wave data. An optimization technique must be used to find the most probable solution. Two approaches can be utilized for this solution. The first are deterministic approaches, in which the objective is to find a model that its theoretical response best fits the observed data. The second are probabilistic approaches, which offer statistical techniques to include a priori information about the solution and to evaluate uncertainty measures.

When using discrete dispersion curves in inversion, the detection of correct mode numbers becomes a difficult task (Zhang & Chan, 2003). The proposed method is based on a full dispersion surface. The first advantage of using the dispersion surface is that it involves using the maximum amount of information available. Therefore, the problems

with mode jumps and misidentification are avoided. The second advantage is in the speed of the process. There is no need for data reduction and extraction of an experimental dispersion curve. The full process from data collection to layer identification is automated.

The procedure for the study of any physical inversion problem can be divided into the following steps (Tarantola, 2005):

1. Parameterization of the system: In this process, as minimum number of model parameters that can completely describe the system are selected.
2. Forward Modeling: Discovery of the governing physical laws needed to express the observable values from a gives set of model parameters values.
3. Inverse Modeling: Use of the results of measurements to form observable variables from which to infer model parameter values.

6.2 Forward Modeling (Theoretical Dispersion Surface)

The forward model is calculated from an assumed layer model. The stiffness-matrix technique described in chapters 2 and 3 is used. This method relates the displacements and the forces at the layer intervals. Then these matrices are assembled to form the global stiffness matrix. Each layer is assumed to be homogenous with respect to density, layer thickness, phase wave velocity and Poisson's ratio. The vertical displacement at the surface is calculated as a function of phase-velocity and frequency. The phase velocities of interest are considered to be less than 5000 m/s for concrete. Also, considering the

modal contents of the dispersion surface and the sensitivity of the available accelerometers, the upper frequency boundary is defined as 40 kHz.

6.3 Error Function

Once the theoretical multimodal dispersion surface is obtained, the next step is to compare it with the experimental dispersion surface. In order to compare the results from the forward model with the observation an appropriate error function is needed:

$$\mathbf{C}_{obs} - \mathbf{C}_{frw} = \Delta\mathbf{C} \qquad \text{Equation 6.1}$$

The frequency range and the frequency sampling have the largest influence on the error function. In practice the DAQ system and the sensors in use dictate these parameters. In FEM simulations, the time steps and the duration of the record define the frequency parameters. The frequency steps for the forward problem here are set to match those of the FEM model. The dispersion surface consists of 67X67 elements. This matrix represents 4489 amplitudes at 67 phase-velocity steps in the range of 0 to 5000 m/s across 67 frequency steps in the range of 0 to 40 kHz. For each frequency the maximum phase-velocity amplitude is normalized to 1. As mentioned in chapter 4, the bright lines are representative of Lamb modes. Since there is no mode selection process, all the modes in this frequency range are considered in the error function regardless of their amplitudes. The brighter the lines are the more these Lamb modes participate in the dispersion surface. The strength and weakness of the modes affect the error function. The

minimum error function will search for the closest amplitude and frequency content of each mode.

Figure 6.1 shows the element by element comparison between the observed dispersion surface and the forward problem. The ΔC matrix contains the difference between the 4489 elements.

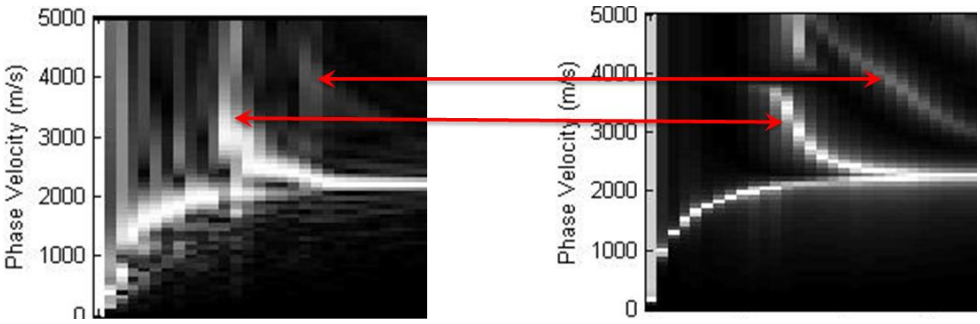

Figure 6.1 Observed dispersion surface is compared to the forward problem element by element for the entire 67X67 elements in the dispersion surface matrix

Generally, the difference between the theoretical and experimental dispersion curves is measured using the Root Mean Squares (RMS) error:

$$\mathrm{RMS}_e = \sqrt{\frac{\sum_1^N \Delta C_i^{\,2}}{N}} \qquad \text{Equation 6.2}$$

where, ΔC_i is the differences between the amplitude of the experimental and theoretical phase velocities at each frequency, and N is the number of elements in matrix $\Delta\mathbf{C}$. All the modes are treated equally and are included in the procedure. The dispersion surface elements are calculated by transferring the time history records at different sensor

locations, into frequency-phase velocity domain using phase-shift method described in the previous chapter.

Different error functions have been used in the past for inversion of surface-waves. In order to gauge the performance of the error function in bridge-deck testing applications, an experimental study is performed using the following error functions.

$$\mathrm{MEAN}(\Delta \mathrm{C}) = \overline{\Delta \mathrm{C}} = \frac{\sum_1^N \Delta C_i}{N} \qquad \text{Equation 6.3}$$

$$\mathrm{Stdv}(\Delta \mathrm{C}) = \sqrt{\frac{\sum_1^N (\Delta C_i - \overline{\Delta \mathrm{C}})^2}{N-1}} \qquad \text{Equation 6.4}$$

$$\mathrm{MEAN}\left(\frac{\mathrm{C}_{obs}}{\mathrm{C}_{frw}}\right) = \frac{\sum_1^N \frac{\mathrm{C}_{obs_i}}{\mathrm{C}_{frw}}}{N} \qquad \text{Equation 6.5}$$

It is assumed that adding to the sensor spacing will increase the amount of noise in the system. So error functions are ranked in terms of their response to the added noise. The changes in these error functions are compared to the RMSe function in Figure 6.2. RMSe function has the sharpest reaction to the variation in the sensor spacing and will be used for the inversion calculations in this research.

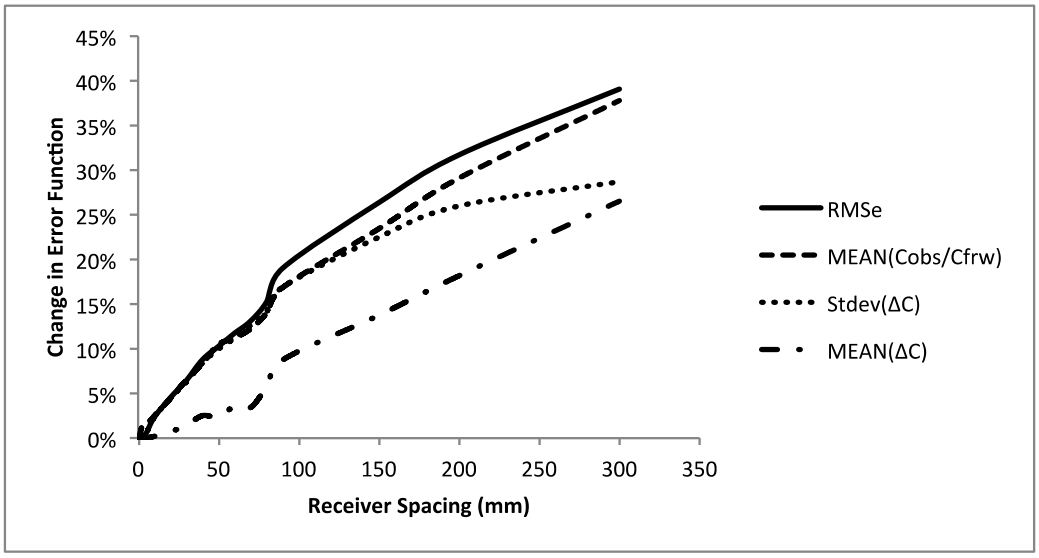

Figure 6.2 Comparing the change in different error functions by changing the receiver spacing in a 3-layer FEM model

6.4 Sensitivity Analysis (Parameterization of the System)

It is important to find out which parameters in the layer model have a noticeable influence on the dispersion surface. To understand this, sensitivity analysis needs to be performed on all the layer model parameters. First, the layer model parameters are introduced in Figure 6.3. Then a layer model is chosen as a reference to compare with the new models. The properties of this reference layer model are presented in Table 6.1

Top Layer	$\rho_1, V_{s1}, d_1, \nu_1$
Middle Layer	$\rho_2, V_{s2}, d_2, \nu_2$
Bottom Layer	$\rho_3, V_{s3}, d_3, \nu_3$

Figure 6.3 Model parameters for a 3-layer bridge-deck system

Table 6.1 Reference layer model for sensitivity analysis

Layer	Vs (m/s)	d (m)	ν	ρ (kg/m^3)
1	2500	0.083	0.167	2500
2	2500	0.083	0.167	2500
3	2500	0.083	0.167	2500

Figure 6.4 shows the effect of a $\pm$%10 change of each layer parameter on the error function using the reference model in Table 6.1. The first layer's shear-wave velocity has the highest influence on the dispersion surface. Other important factors are the second and third shear-wave velocity and layer thicknesses. Poisson's ratio and density have the least effect in this case.

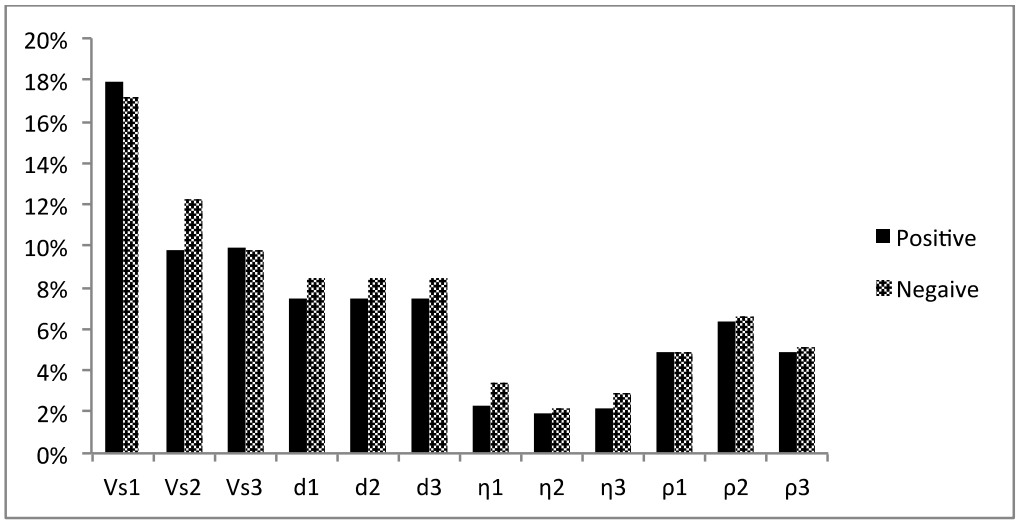

Figure 6.4 The effect of a ±%10 change in the error function using the layer model in Figure 6.3

Next, a one-dimensional sensitivity analysis for each parameter in the reference layer model is performed. In order to better understand the effect of each parameter on the error function, its variation is plotted for the parameter value changing from -%50 to +%50 compared to the reference model. All of the other layer parameters are kept identical to the reference model. Figure 6.5 shows the effect of the shear-wave velocity of each layer on the error function. The first layer's phase-velocity has the strongest effect on the error function in the variation range. The other shear wave velocities have a similar, but still weaker effect.

The effect of thickness of different layers is shown in Figure 6.6 followed by the effects of density and Poisson's ratio in Figure 6.7 and Figure 6.8.

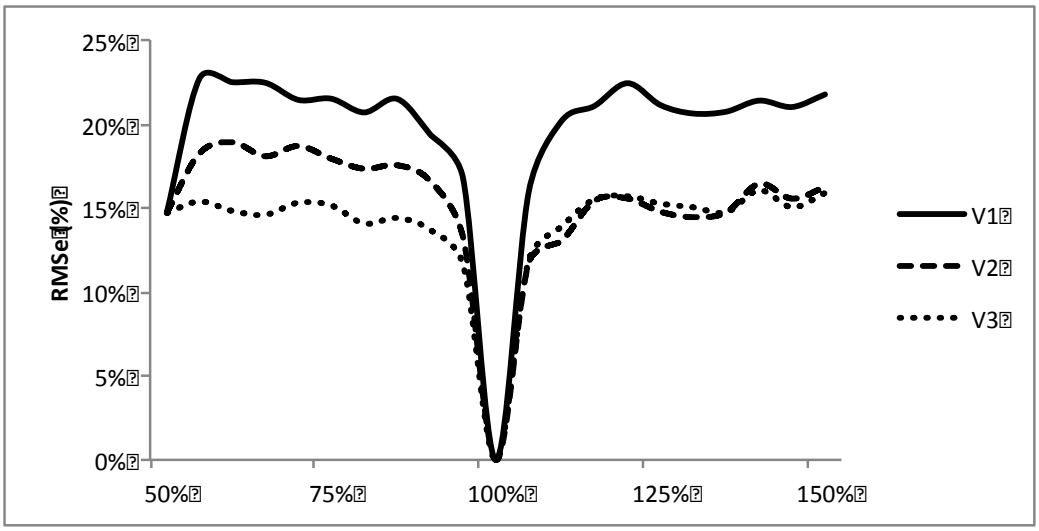

Figure 6.5 RMSe variation with change in shear-wave velocity of each layer.

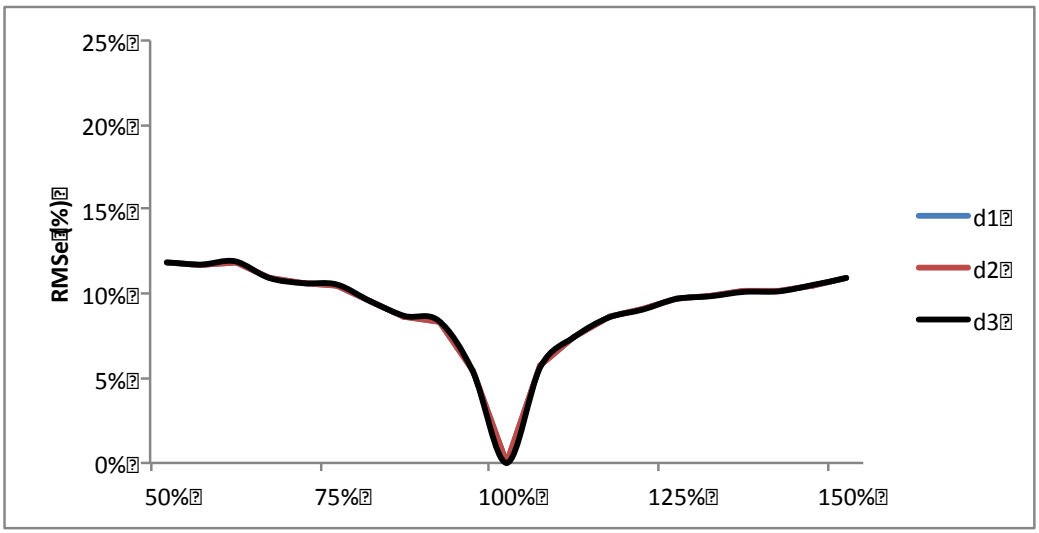

Figure 6.6 RMSe variation with change in thickness of each layer

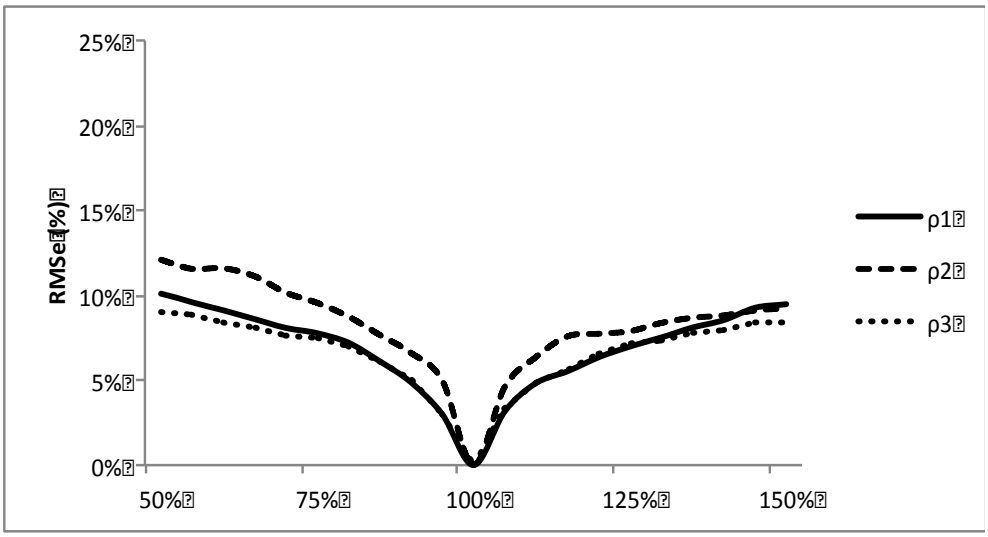

Figure 6.7 RMSe variation with change in density of each layer

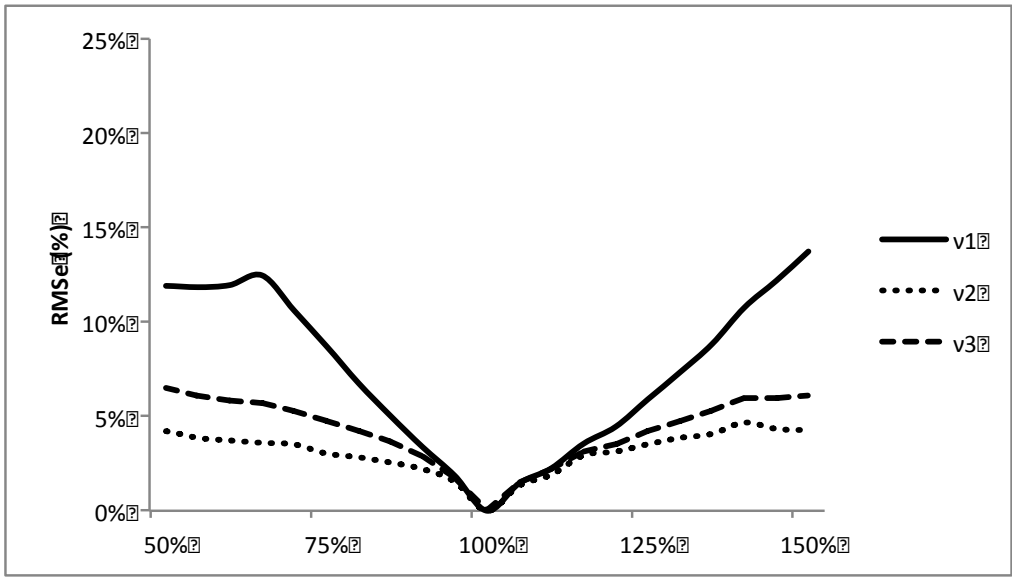

Figure 6.8 RMSe variation with change in Poison ratio of each layer

The one-dimensional sections of parameter space can give a good estimate of RMSe function behavior. However, further difficulties can arise from correlated parameters and local minima in the parameter space. In order to gauge the effect of the parameter

correlation in the error minimization process, two-dimensional plots of the model space are presented in Figure 6.9 to Figure 6.13. Each plot is describing the error function by changing the values of two of the model parameters in the range of $\pm\%50$ of their original value. Five pairs of parameters are selected for this analysis based on the results in the one dimensional sensitivity analysis. The darker locations are representative of error function minima and vice versa. It can be observed that the change in the error function is not necessarily linear with the underlying parameter and there are local minima and maxima in each set.

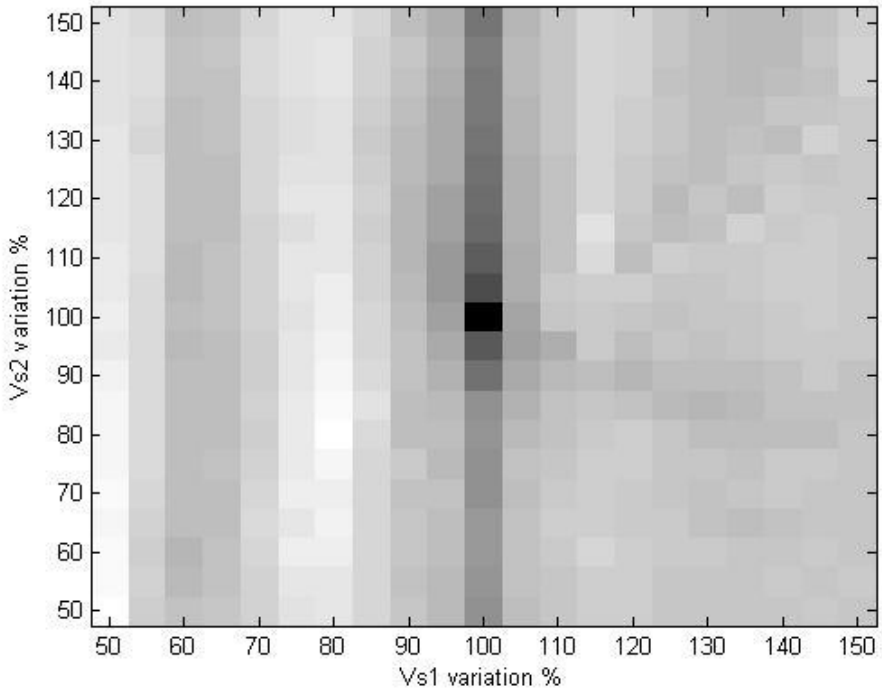

Figure 6.9 Two-dimensional variation of error function by changing the shear-wave velocity of the top layer and middle layer .The darker points are indicators of lower errors.

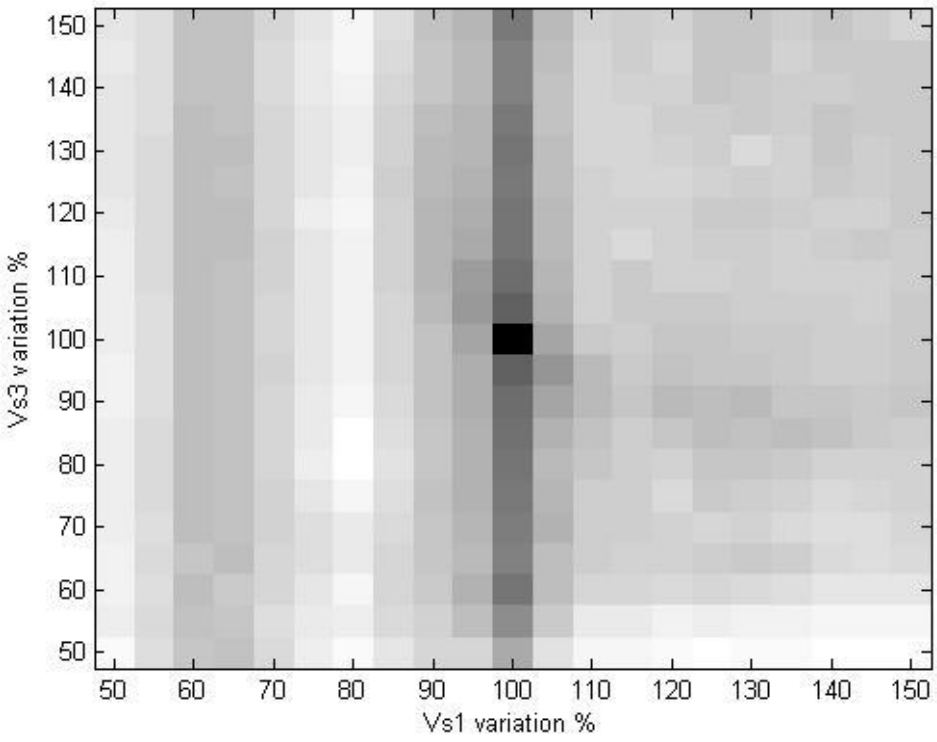

Figure 6.10 Two-dimensional variation of error function by changing the shear-wave velocity of the top layer and bottom layer .The darker points are indicators of lower errors.

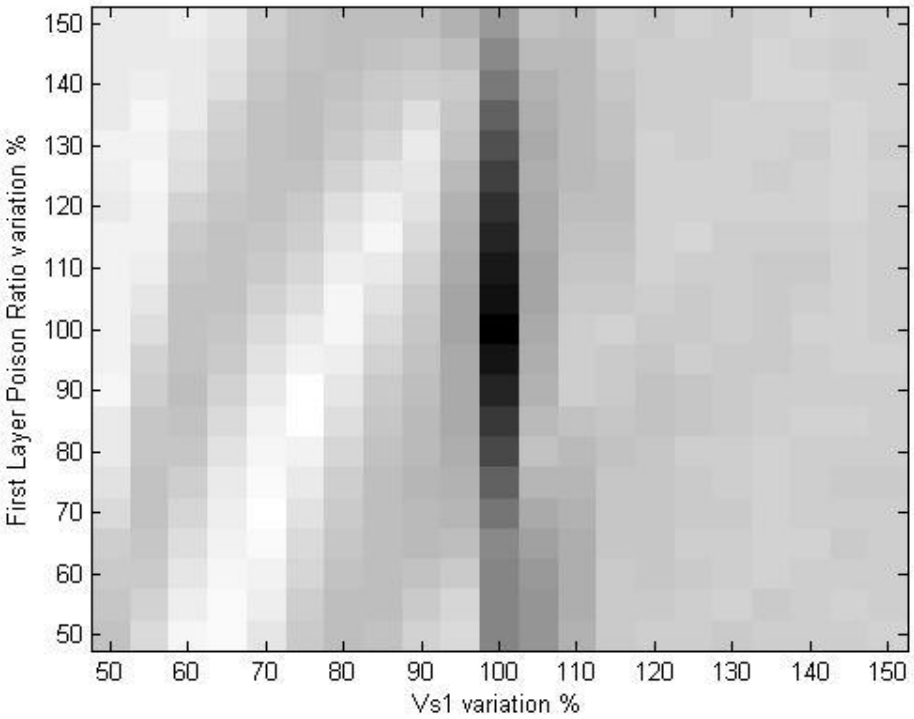

Figure 6.11 Two-dimensional variation of error function by changing the Poisson's ratio of the top layer and shear-wave velocity of top layer .The darker points are indicators of lower errors.

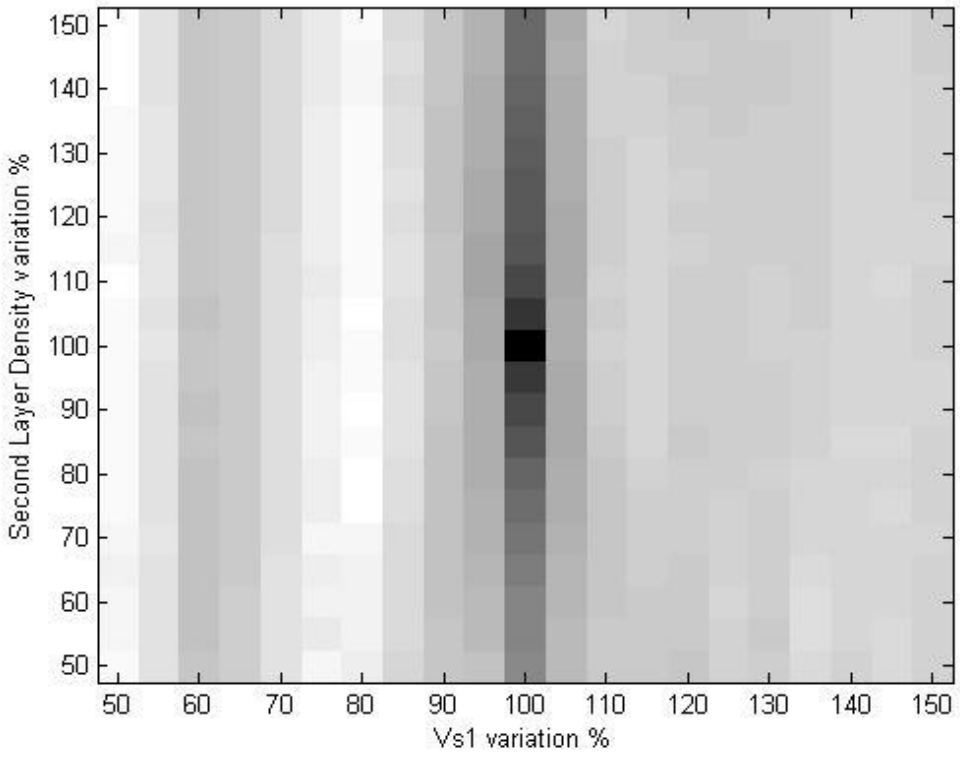

Figure 6.12 Two-dimensional variation of error function by changing the density of the middle layer and shear-wave velocity of top layer .The darker points are indicators of lower errors.

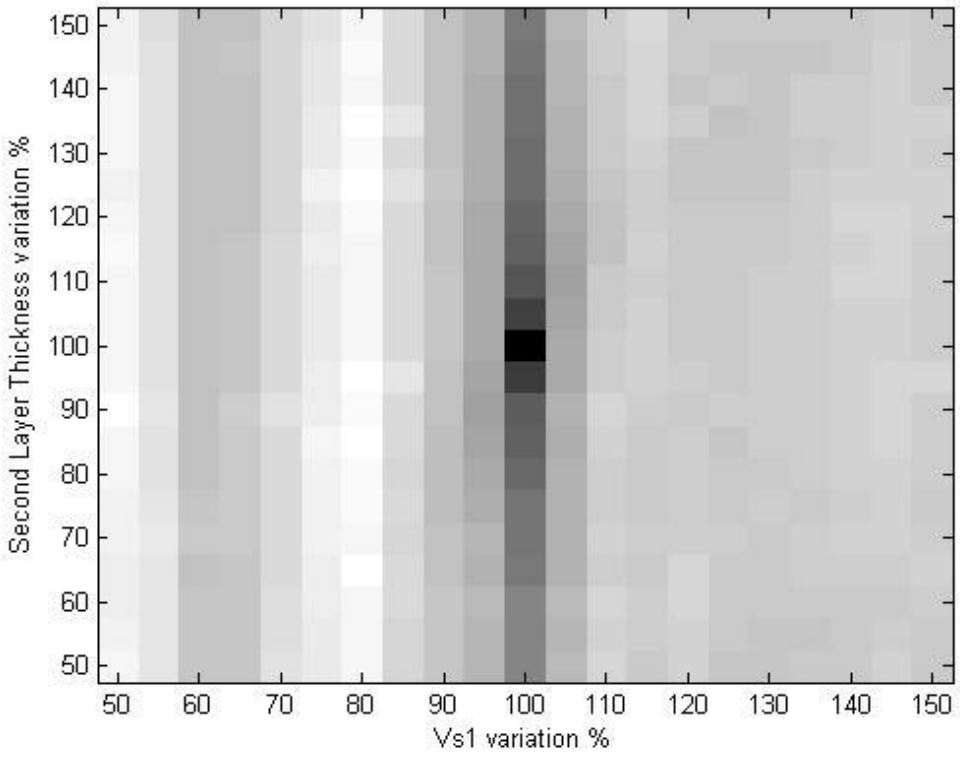

Figure 6.13 Two-dimensional variation of error function by changing the thickness of the middle layer and shear-wave velocity of top layer .The darker points are indicators of lower errors.

The local minima and parameter correlations can make the inversion of the concrete decks a challenging task. In order to overcome these difficulties an efficient global search method is necessary.

6.5 Inversion Algorithm

The objective of inversion algorithm is to find a phase-velocity dispersion surface from a profile that matches with the measured dispersion surface. This is achieved by using the error function described earlier. Each inversion problem is unique because of the number of influential model parameters and the lower and upper boundaries for each value. On the other hand the inversion process cannot be solved directly and needs an optimization technique to find the most suitable answers. The optimization technique can be deterministic, probabilistic, or a combination of both (Park C. B.). The benefit of the deterministic technique is in finding the global minimum, but the drawback is the speed when dealing with a large number of parameters. There are two probabilistic approaches to perform inversion: a local search method and a global search method. The local search method is performed by an iterative search for the minimum error in the vicinity of the starting point. In the global method, however, a stochastic procedure is performed over the solution space to find the global minimum. The main advantage of the global method is that the local minimums are avoided. Also, the problem can be solved in a non-linear form. The disadvantage of this method is that it can be slow, if the number of the model parameters is large. The global search is performed in the following steps:

1. The model values are chosen.
2. The forward model is solved based on the chosen values.
3. The error is calculated based on comparing the forward model to the observation.

4. If the error is in the acceptable range, the model parameters are saved and the process is stopped.
5. Steps 1-4 are repeated either for all the points in the solution space or for a randomly selected subset of this universe.

By taking advantage of the information about the model space, the inversion search can be limited. In bridge decks we deal with plate like concrete structures. Dividing the deck profile into three layers with variable thicknesses can provide the required accuracy for practical bridge deck inversion problems. The rest of the influential parameters are chosen based on the results of sensitivity analyses on all the model parameters. For further simplification the axes of dispersion surface could be normalized for any given Poisson's ratio. This can be achieved by dividing the phase-velocity axis to the shear velocity and multiplying the frequency axis by the thickness of the bridge-deck.

The boundary limits of each of the material property parameters are limited to certain physical boundaries. In concrete bridge decks, the physical boundaries are set by the upper and lower values of each variable found in existing bridges. The model parameter boundaries used in this research are shown in Table 6.2.

Table 6.2 Limits for model parameters considering bridge-deck material

Model Parameter	Limits
Shear-wave Velocity	1250-2500 m/s
Layer thickness	(1/6 -2/3) of deck thickness

Table 6.3 Parameters of the database for a concrete bridge-deck

d_1/d	d_2/d	d_3/d	V_{S1}/V_{s0}	V_{S2}/V_{s01}	V_{S3}/V_{s0}
1/6	1/6	1/6	0.5	0.5	0.5
1/3	1/3	1/3	0.6	0.6	0.6
1/2	1/2	1/2	0.7	0.7	0.7
2/3	2/3	2/3	0.8	0.8	0.8
			0.9	0.9	0.9
			1	1	1

To further reduce the search time, a search grid is developed. Each model parameter range is divided into practically important intervals. Table 6.3 shows the grid used for

layer parameters in the inversion algorithm. The parameters are defined in terms of the dimensionless layer thickness d_i/d and dimensionless shear phase-velocity V_{Si}/V_{s0}.. d is the deck thickness, ρ_0 is the reference density and V_{s0} is the reference shear-wave velocity. The reference values are from Table 6.1.

Each of the three layers can have the thickness from 1/6 to 2/3 of the total thickness. The sum of the three layers should add up to the deck thickness. With this constraint in mind, the list of iteration cases involving the layer thicknesses are shown in Table 6.4.

Table 6.4 Layer thickness cases

Top Layer Thickness/ Total Thickness	**Middle Layer Thickness/ Total Thickness**	**Bottom Layer Thickness/ Total Thickness**
1/6	1/6	2/3
1/6	2/3	1/6
1/6	1/2	1/3
1/6	1/3	1/2
1/3	1/6	1/2
1/3	1/2	1/6
1/3	1/3	1/3
1/2	1/3	1/6
1/2	1/6	1/3
2/3	1/6	1/6

The total number of solution grid size is:

$$Grid\ size = Layer\ Cases \times Shear\ wave\ velocity\ Cases = 10 \times 6^3 = 2160 \quad \text{Equation 6.6}$$

The phase-velocity at the high end of the dispersion curve can be directly correlated to the shear-wave velocity of the top layer (Xia, Miller, & Park, 1999). The shear-wave of the top layer is calculated from the average phase-velocity between 30kHz to 40kHz and from the Poisson's ratio:

$$C_R = \frac{0.862 + 1.14\nu}{1 + \nu} C_s = 0.91 C_s \quad \text{Equation 6.7}$$

A combination of the deterministic and the probabilistic approach is used in this research with a global optimization technique. This is because of the dimensions of the inverse problem and the computational power available at the time of the research.

In order to further accelerate the process, a database of dispersion surface is generated from the numerical simulation of MASW test using the DISPER Program (Gucunski & Woods, 1991). This database is stored as part of the inversion package.

The required capacity to store this database is follows:

$$Required\ Memory = forward\ problem\ dispesion\ curve\ file\ size \times Grid\ Size$$

$$= 46kb \times 2160 = 97\ Mb$$

A MATLAB program DECKINVERSE is generated to implement the inversion algorithm discussed here. A summary of the required steps for the inversion algorithm is shown in Figure 6.14.

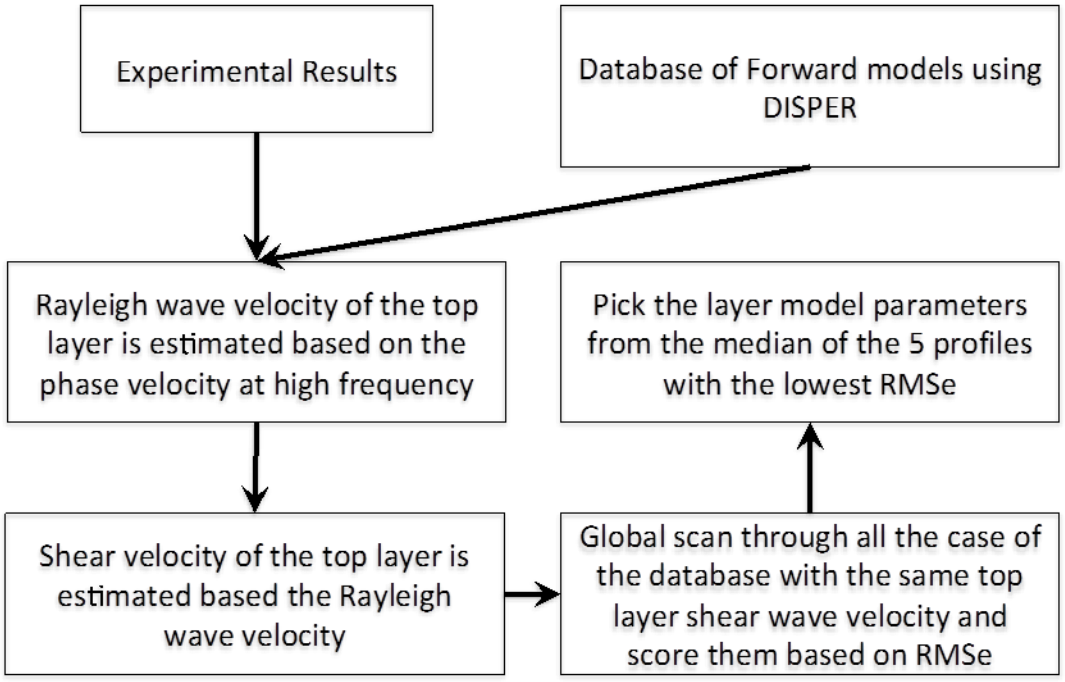

Figure 6.14 Inversion algorithm

6.6 Inversion Examples Using Finite-element Models

In order to evaluate the performance of the inversion algorithm a series of finite-element examples are inverted. These examples are in two categories. In the first category, all the model parameters of the FEM are identical to one of the forward models in the database. On the other hand, category two contains examples in which there is at least one parameter that does not match exactly with the database.

To simulate a real case, testing environment acceleration time histories were collected with 0.05 m steps over the range of 0.05–2.00 m using a cubic sine function as the trigger. The fixed model parameters are described in Figure 6.15.

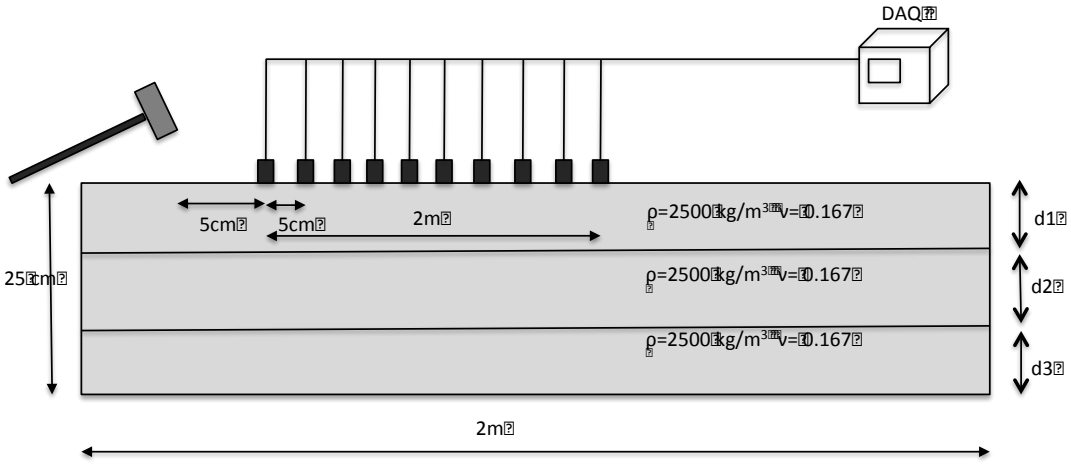

Figure 6.15 Model parameters of FEM model used for inversion process

6.6.1 Examples with the Same Parameters as the Database

The inverted and reference layer parameters are presented in Table 6.5 and Table 6.6 for all the cases in this section. The dispersion surface for the reference model is calculated

by using DISPER program (Gucunski & Woods, 1991) using the same model parameters as the FEM model.

Figure 6.16 to Figure 6.23 show a schematic of layer structures and the dispersion surface for both finite-element and inverted models. The shear-wave velocity of the top layer is inverted accurately in almost all cases except case IN05. As described in Figure 6.20, the FEM dispersion surface for this case is very noisy. Because of the high velocity noise present in the higher frequency range, the algorithm cannot locate the correct Rayleigh wave velocity. This might be because of a numerical error due to high contrast between the shear-wave velocity of the top and middle layer. Case IN06, which exhibits less contrast, is inverted properly and exhibits less noisy FEM dispersion surface.

The second case in which the algorithm has difficulty finding the right match is case IN03. Both the layer thicknesses and the shear-wave velocity of the middle layer are misinterpreted. The results are better when there is less contrast of shear-wave velocity between the middle layer and the bottom layer in case IN04. However, it is still not ideal due to misinterpretation of layer thicknesses. This is mainly because surface-wave is carrying less information about the deeper layers compared to the shallower ones. So, the inversion results become less accurate for the deeper layers. That being said, compared to the traditional SASW method, using multiple modes of dispersion spectra, MASW based inversion methods still provided better inversion results.

Table 6.5 Shear-wave velocity for the inverted models vs. their reference.

Case Number	Figure number	Shear-wave Velocity TL (m/s)		Shear-wave Velocity ML (m/s)		Shear-wave Velocity BL (m/s)	
		Reference	Inverted	Reference	Inverted	Reference	Inverted
IN01	Figure 6.16	2500	2500	1250	1250	2500	2250
IN02	Figure 6.17	2500	2500	1750	1750	2500	2250
IN03	Figure 6.18	2500	2500	2500	1250	1250	1250
IN04	Figure 6.19	2500	2500	2500	2250	1750	1500
IN05	Figure 6.20	1250	2500	2500	1250	2500	2250
IN06	Figure 6.21	1750	1750	2500	2250	2500	2500
IN07	Figure 6.22	2500	2500	1750	1750	2500	2500
IN08	Figure 6.23	2500	2500	2500	2250	1750	1750

Table 6.6 Layer thicknesses for the inverted models vs. their reference.

Case Number	TL Thickness (cm)		ML Thickness (cm)		BL Thickness (cm)	
	Reference	Inverted	Reference	Inverted	Reference	Inverted
IN01	8.33	8.33	8.33	8.33	8.33	8.33
IN02	8.33	8.33	8.33	8.33	8.33	8.33
IN03	8.33	4.2	8.33	4.2	8.33	16.7
IN04	8.33	4.2	8.33	16.7	8.33	4.2
IN05	8.33	8.33	8.33	8.33	8.33	8.33
IN06	8.33	8.33	8.33	8.33	8.33	8.33
IN07	4.2	4.2	4.2	4.2	16.7	16.7
IN08	16.7	16.7	4.2	4.2	4.2	4.2

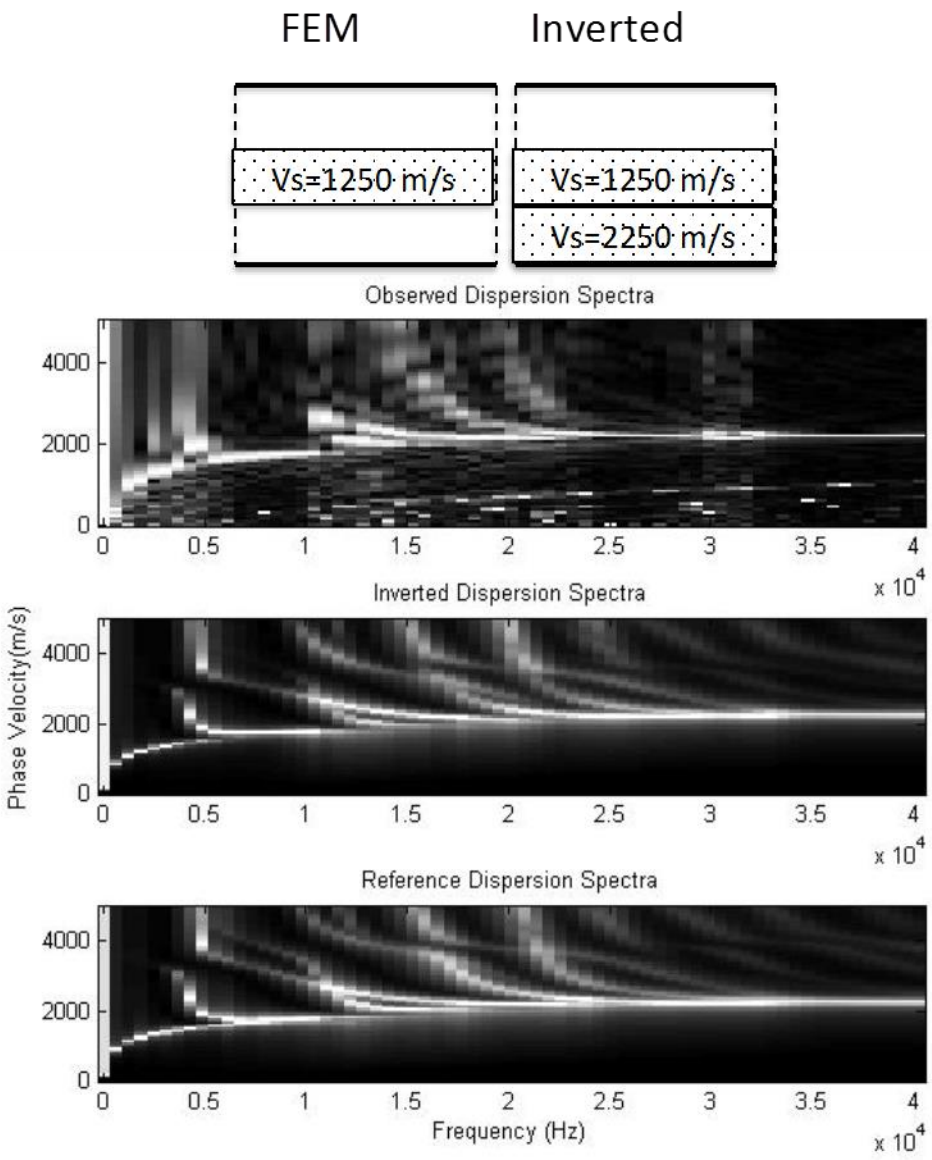

Figure 6.16 Comparison between the dispersion surface from FEM at the top, the inverted profile at the middle and the reference database model at the bottom for Case IN01.

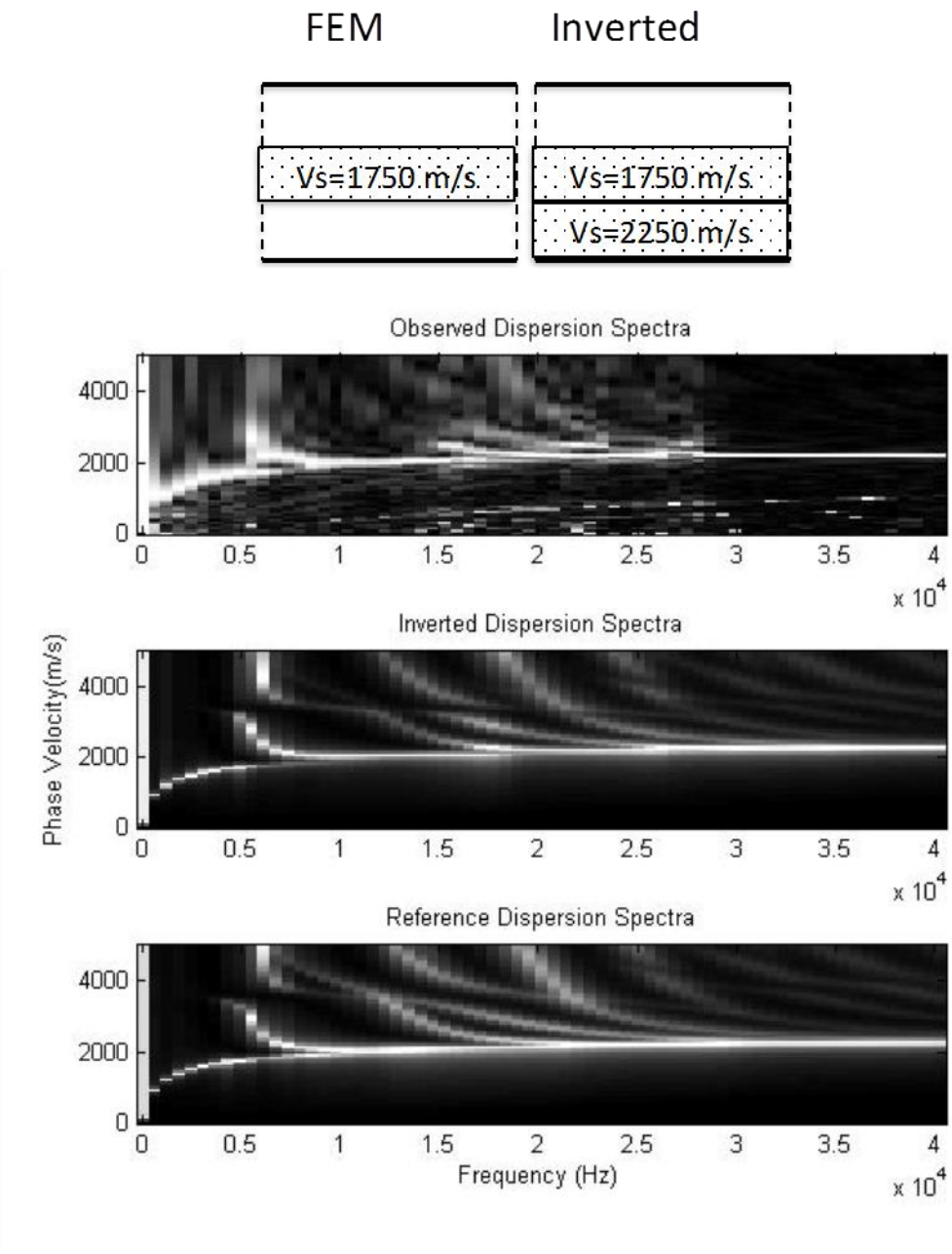

Figure 6.17 Comparison between the dispersion surface from FEM at the top, the inverted profile at the middle and the reference database model at the bottom for Case IN02.

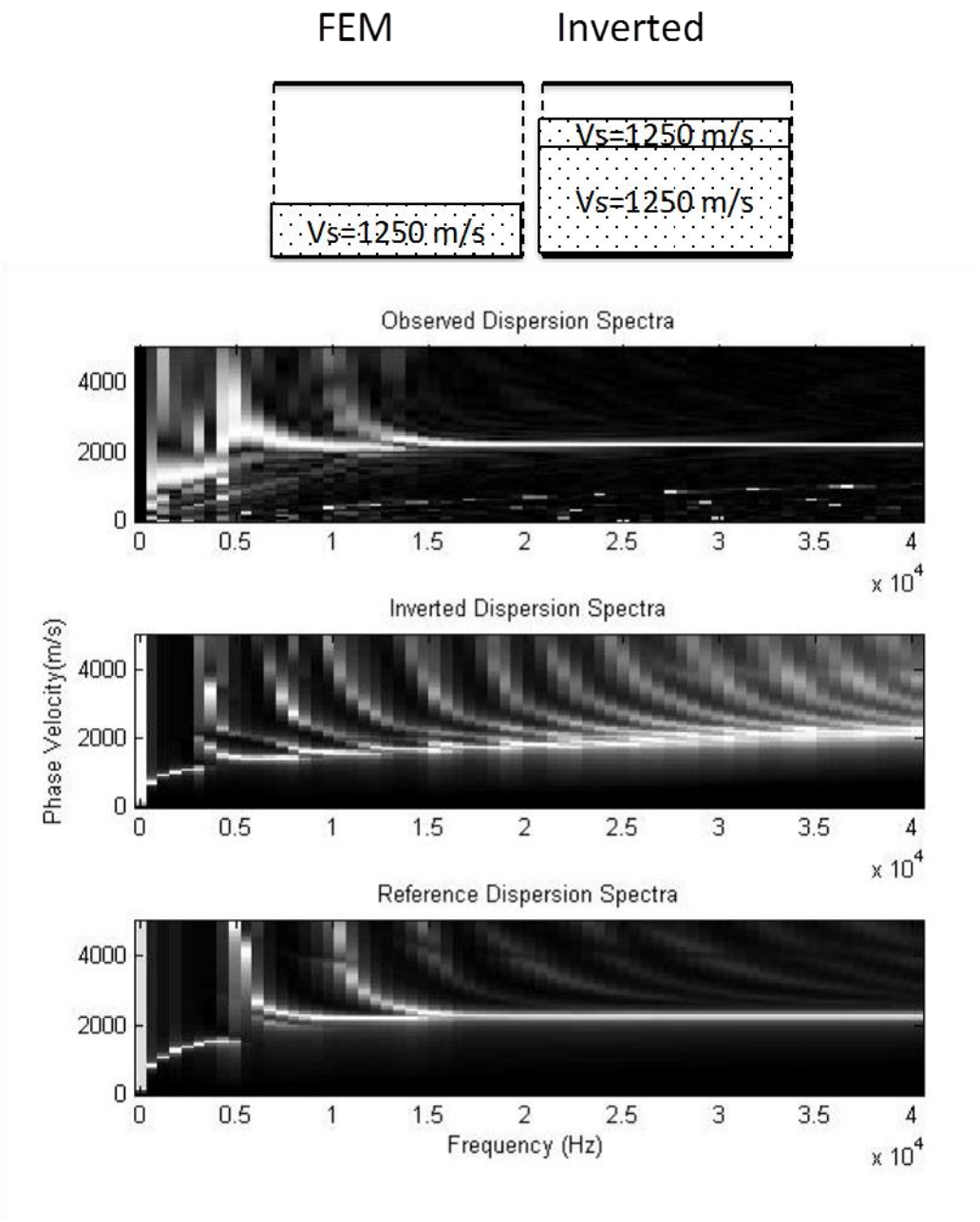

Figure 6.18 Comparison between the dispersion surface from FEM at the top, the inverted profile at the middle and the reference database model at the bottom for Case IN03.

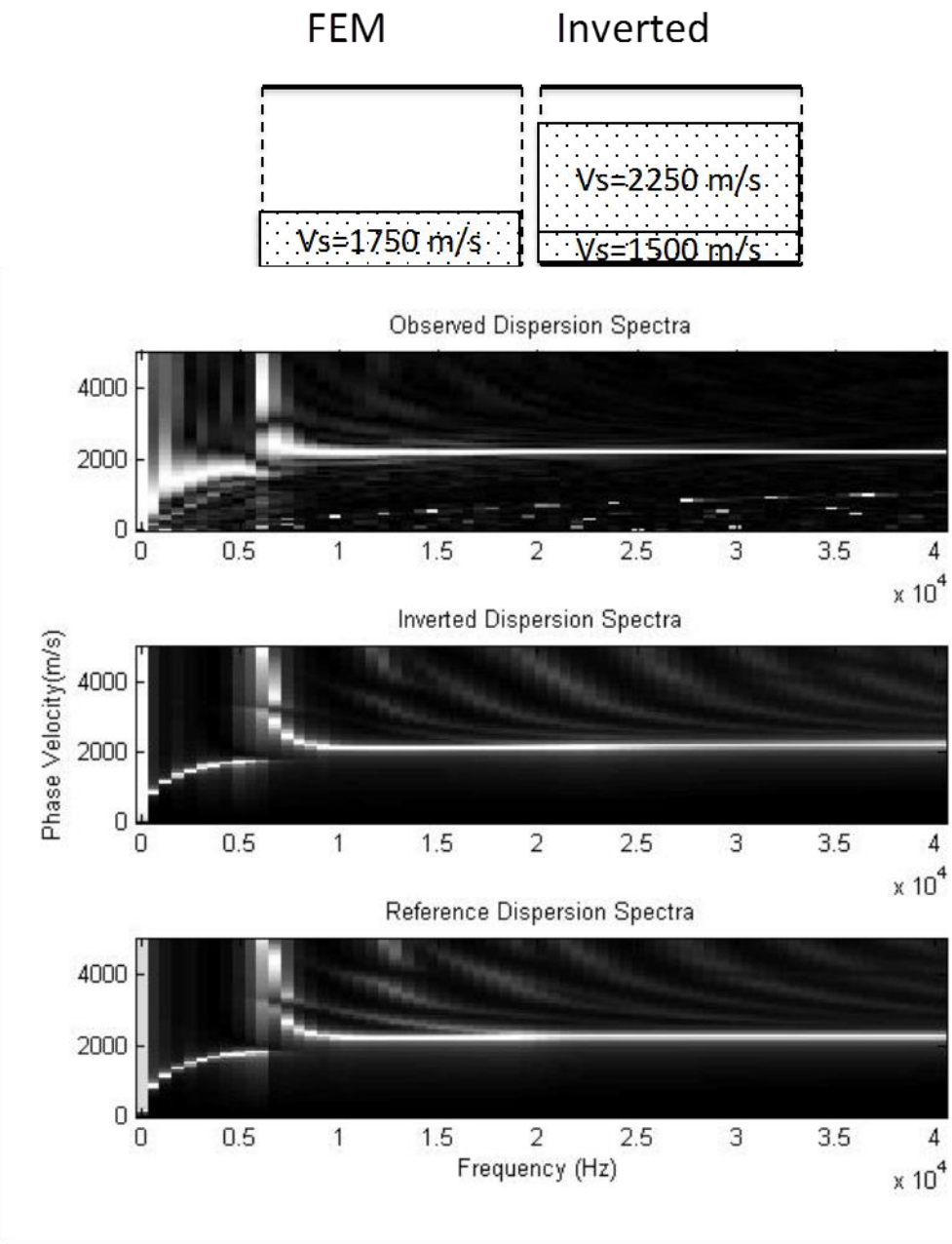

Figure 6.19 Comparison between the dispersion surface from FEM at the top, the inverted profile at the middle and the reference database model at the bottom for Case IN04.

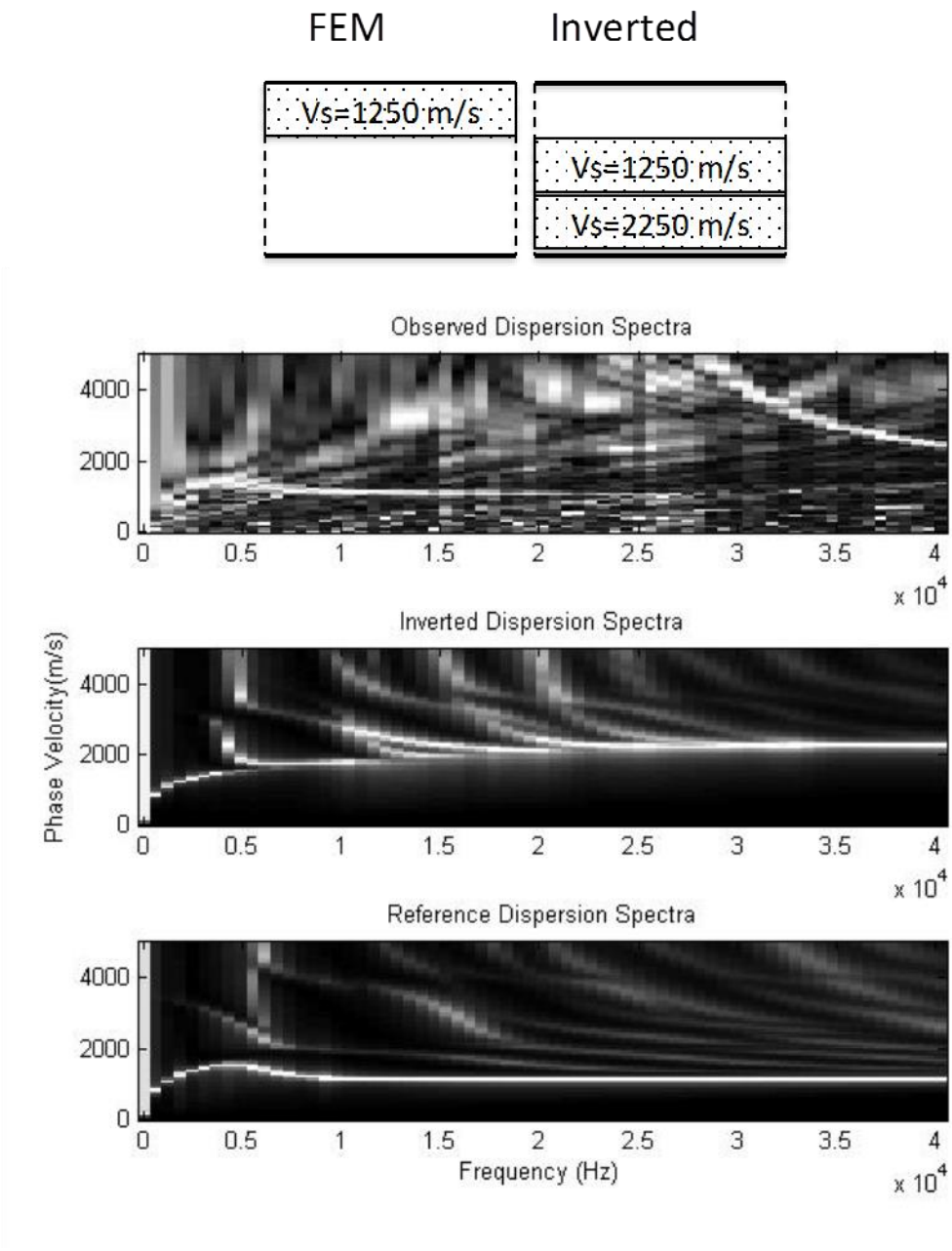

Figure 6.20 Comparison between the dispersion surface from FEM at the top, the inverted profile at the middle and the reference database model at the bottom for Case IN05.

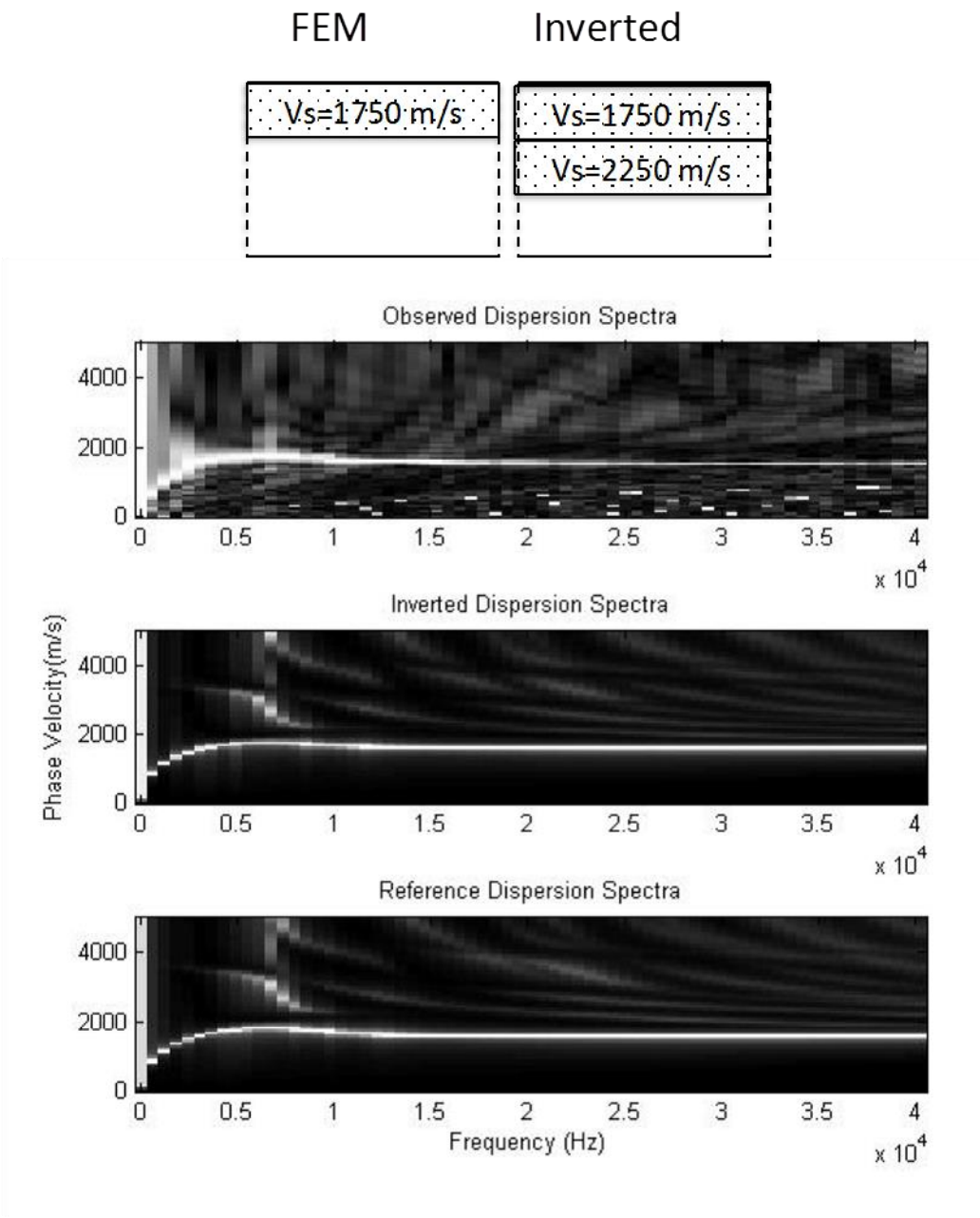

Figure 6.21 Comparison between the dispersion surface from FEM at the top, the inverted profile at the middle and the reference database model at the bottom for Case IN06.

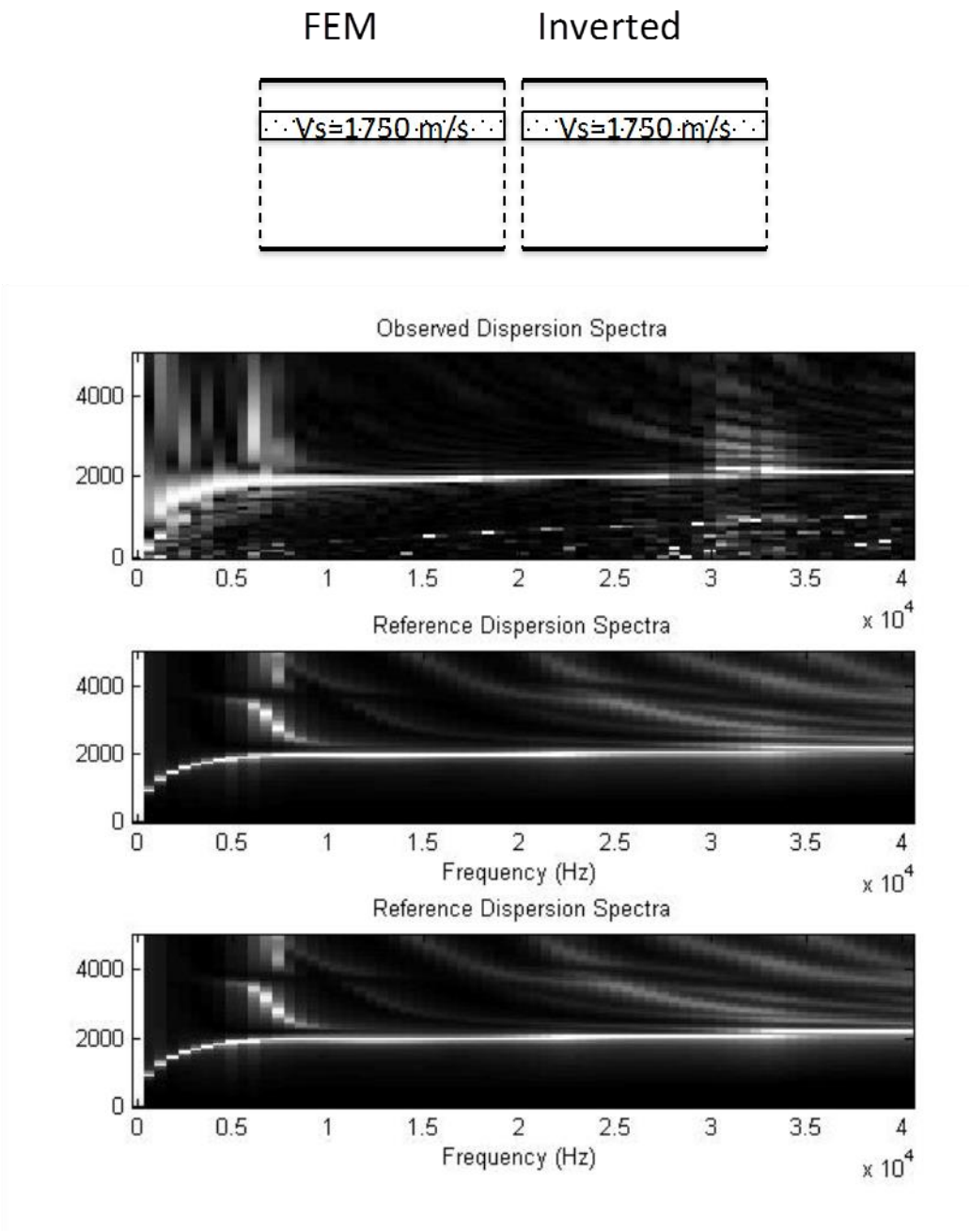

Figure 6.22 Comparison between the dispersion surface from FEM at the top, the inverted profile at the middle and the reference database model at the bottom for Case IN07.

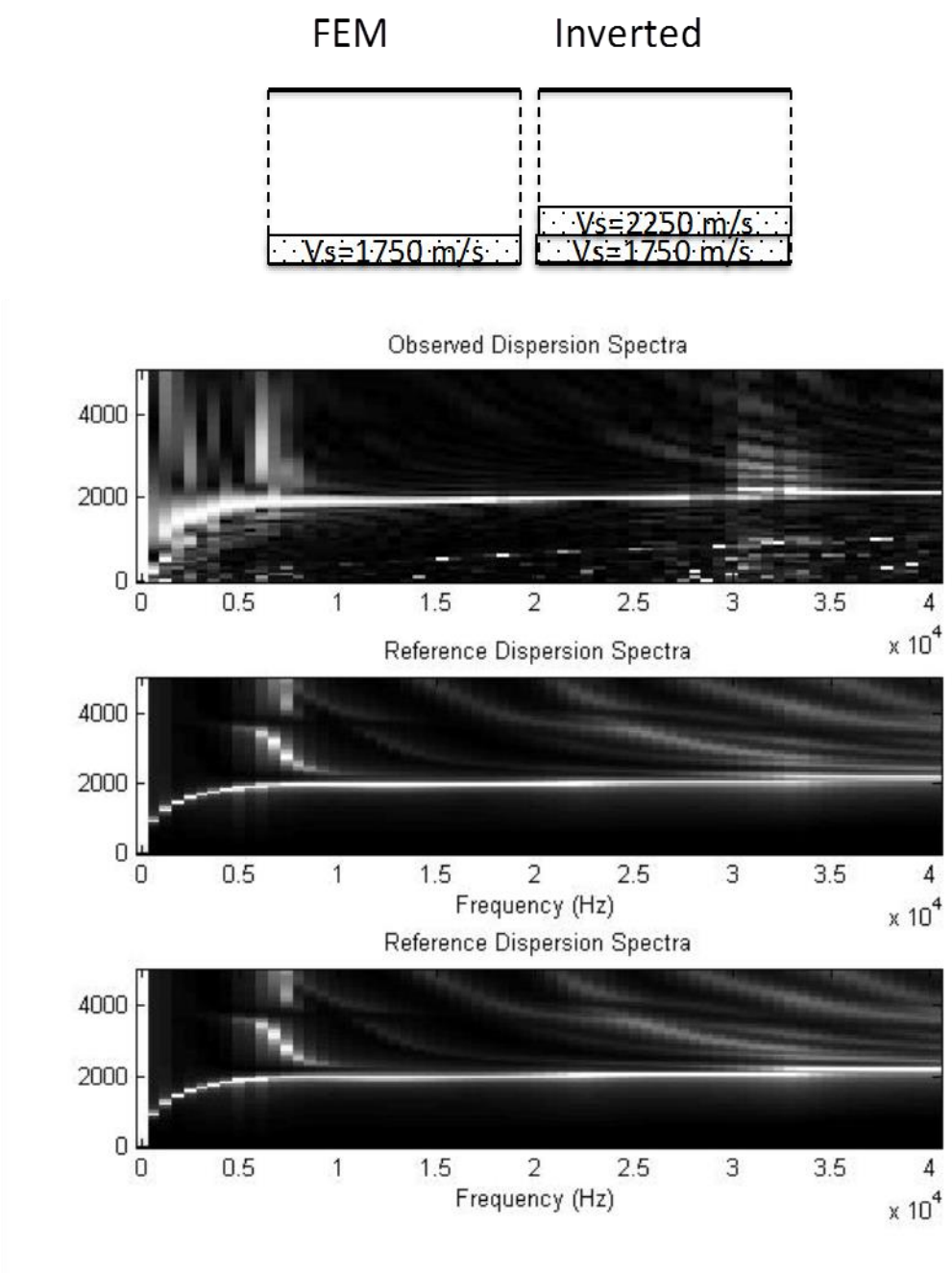

Figure 6.23 Comparison between the dispersion surface from FEM at the top, the inverted profile at the middle and the reference database model at the bottom for Case IN08.

In an attempt to increase the accuracy of the inversion algorithm a number of thresholds were applied to the dispersion surface prior to the error function calculation. The objective was to reduce the effect of low amplitude noise on the inversion results. Despite reducing the effect of the low amplitude content in the dispersion surface, the inversion results did not change. Figure 6.24 and Figure 6.25 show a schematic of layer structures and the dispersion surface for both finite-element and inverted models using threshold values of 0.1 and 0.5 respectively for case IN03. As shown in the figures the inverted profiles are identical to no threshold one in Figure 6.18.

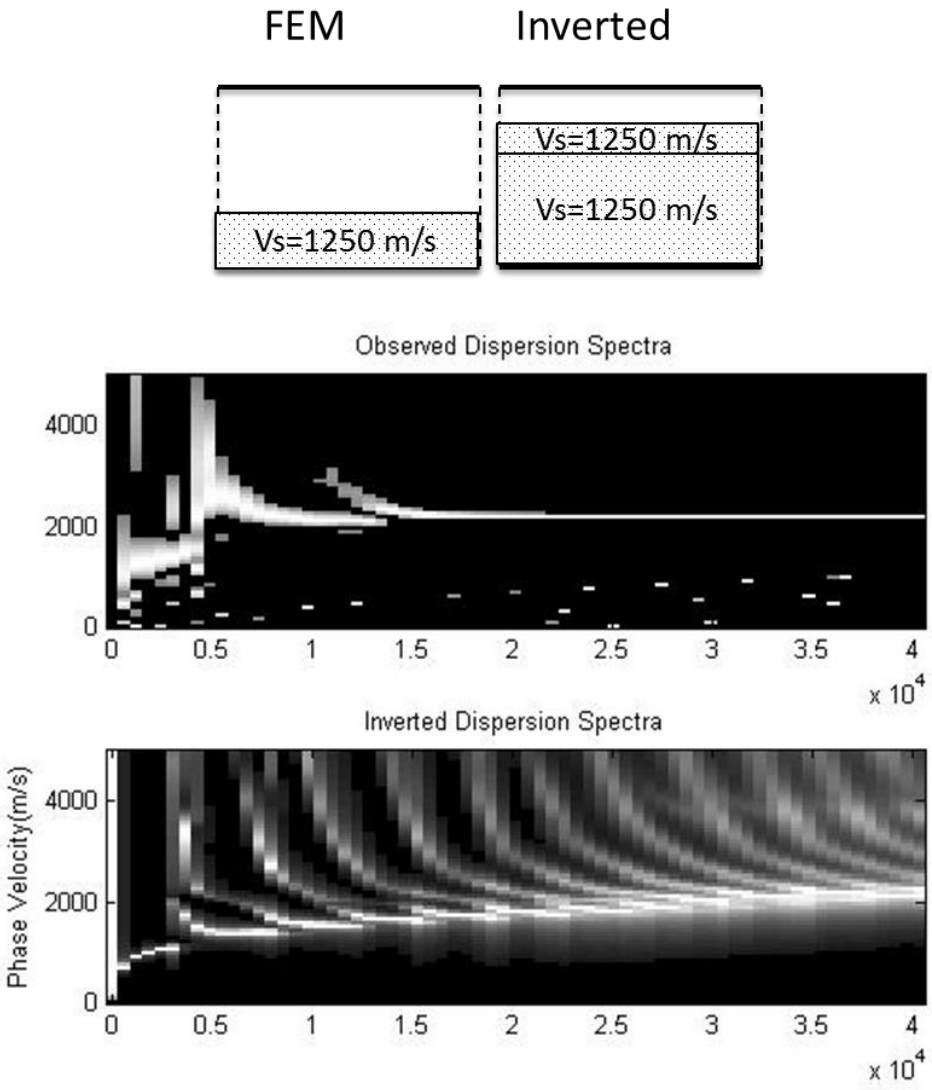

Figure 6.24 Comparison between the dispersion surface from FEM at the top, the inverted profile at the middle using threshold value of 0.1 for Case IN03

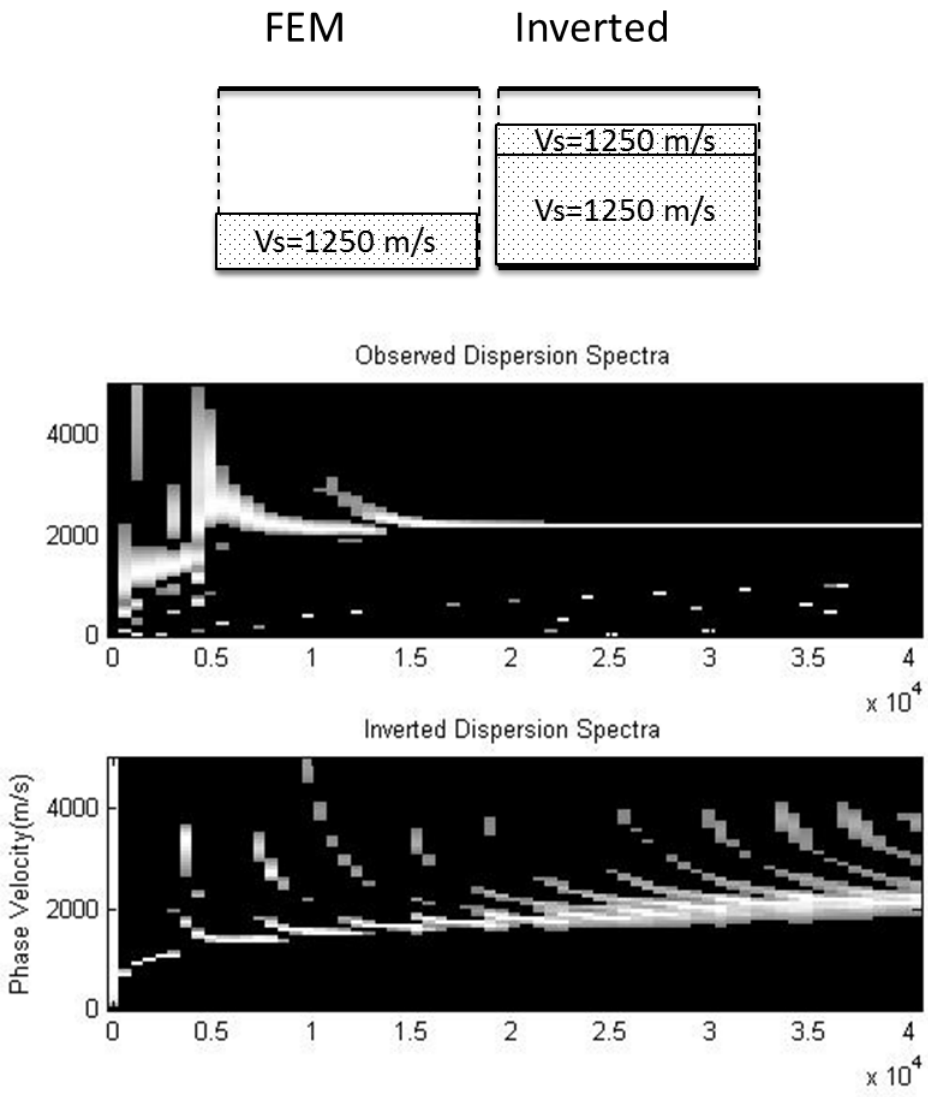

Figure 6.25 Comparison between the dispersion surface from FEM at the top, the inverted profile at the middle using threshold value of 0.5 for Case IN03

6.6.2 Examples with Parameters different than those in the Database

In order to test the inversion algorithm outside of the database models, a series of examples with different parameters than the models in the database are considered. Since the layer shear-wave velocity has the biggest impact on the dispersion spectra, the examples in the category have the values for shear-wave velocity different from those in the database. The density and the Poisson's ratio for all the layers in FEM models have fixed values. These values are represented in Table 6.7. The inverted and reference layer parameters are compared based on the shear-wave velocity of each layer in Table 6.8 and the thickness of each layer in Table 6.9 for all the cases in this section.

Table 6.7 Fixed layer parameters for the FEM models

Layer	**ρ (kg/m^3)**	**ν**
1,2,3	2500	0.167

Figure 6.26 to Figure 6.28 show a schematic of layer structures and the dispersion surface for both finite-element and inverted models. Except for the middle layer in cases IN10 and IN11, the shear-wave velocities of all the layers are inverted with less than 10% errors. The errors for those two cases are 25% and 18% respectively.

Table 6.8 Shear-wave velocity for the out of database inverted models vs. their closest reference.

Case Number	Figure number	Shear-wave Velocity TL (m/s)		Shear-wave Velocity ML (m/s)		Shear-wave Velocity BL (m/s)	
		Reference	Inverted	Reference	Inverted	Reference	Inverted
IN10	Figure 6.26	1875	1750	2375	2000	2375	2500
IN11	Figure 6.27	2375	2250	1875	1500	2375	2500
IN12	Figure 6.28	2375	2250	2375	2500	1875	2000

Table 6.9 Layer thicknesses for the out of database inverted models vs. their closest reference.

Case Number	TL Thickness (cm)		ML Thickness (cm)		BL Thickness (cm)	
	Reference	Inverted	Reference	Inverted	Reference	Inverted
IN01	8.33	4.2	8.33	8.33	8.33	12.5
IN02	8.33	16.7	8.33	4.2	8.33	4.2
IN03	8.33	4.2	8.33	8.3	8.33	12.5

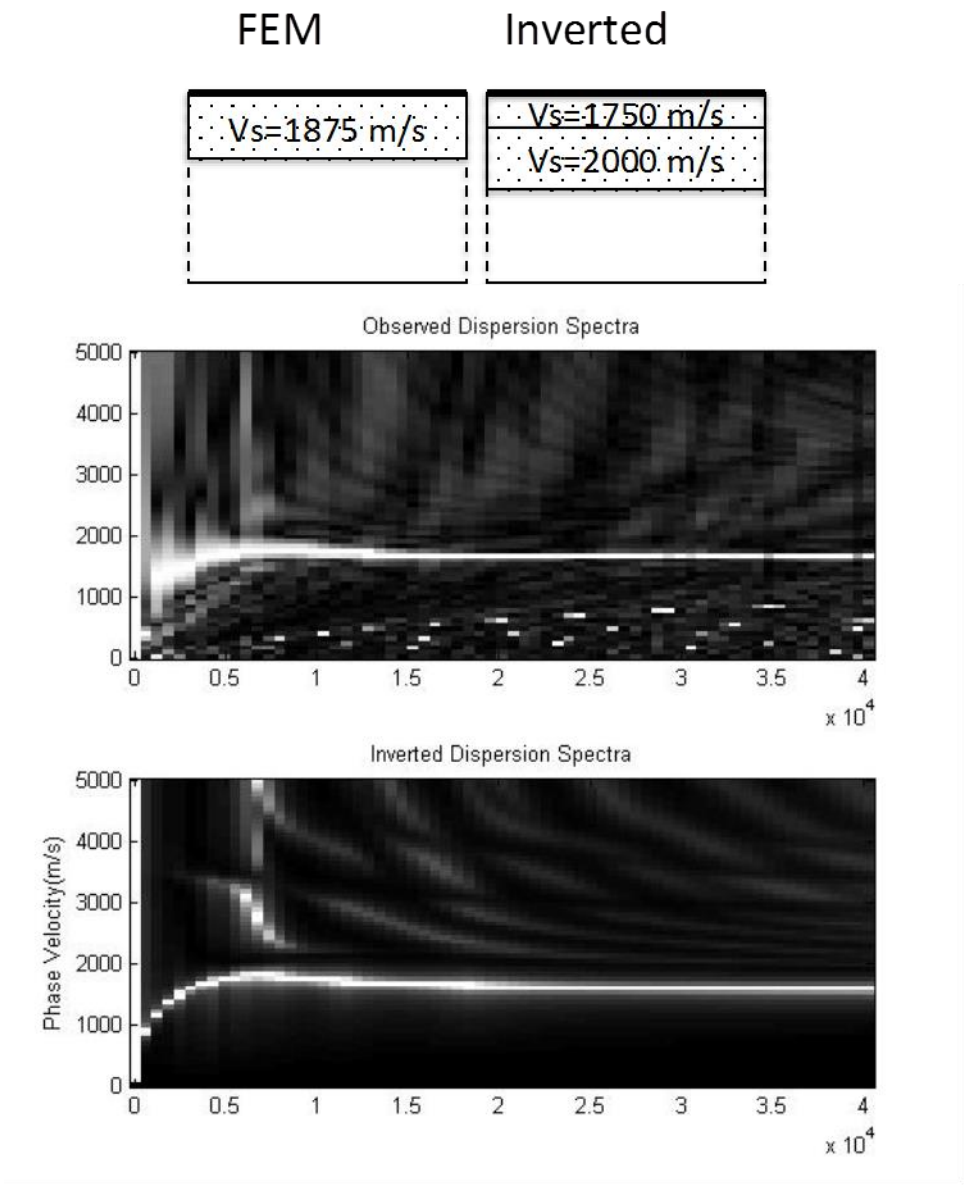

Figure 6.26 Comparison between the dispersion surface from FEM at the top and the inverted profile at the bottom for Case IN10.

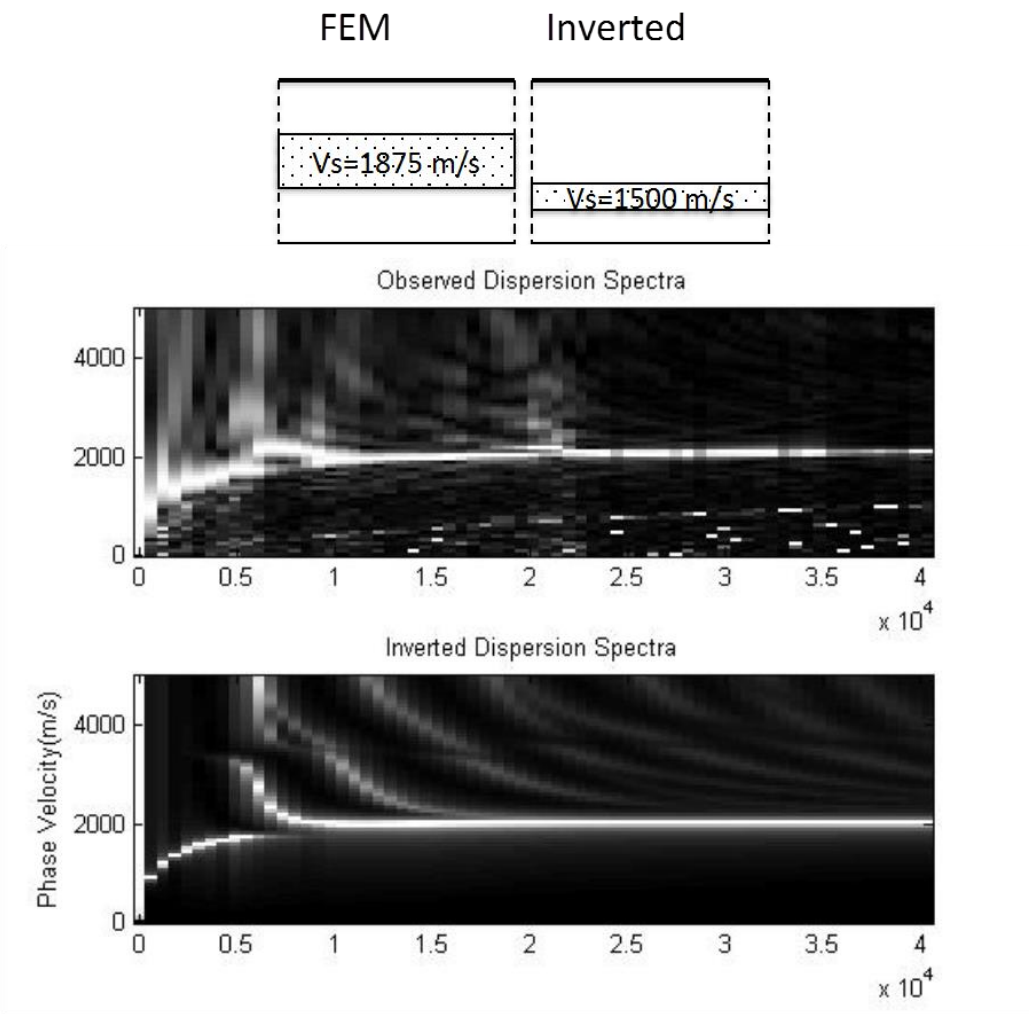

Figure 6.27 Comparison between the dispersion surface from FEM at the top and the inverted profile at the bottom for Case IN11.

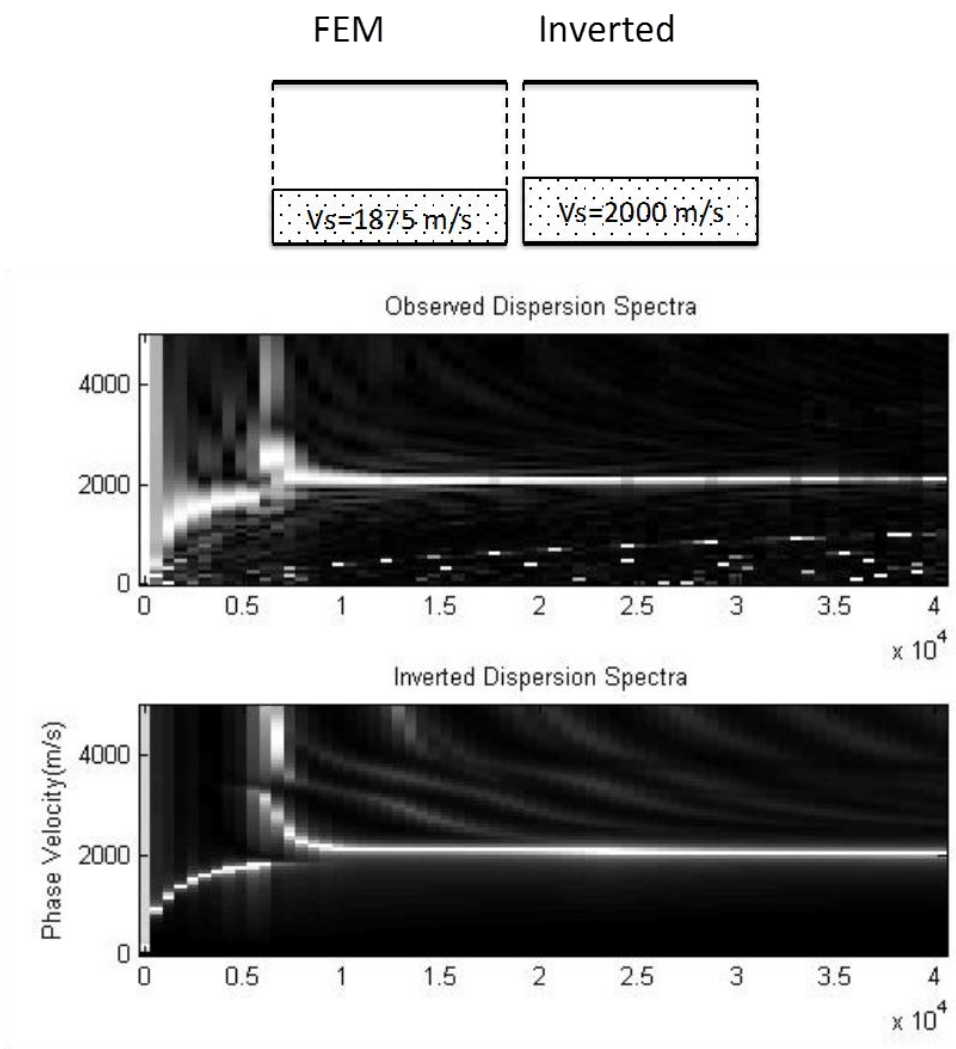

Figure 6.28 Comparison between the dispersion surface from FEM at the top and the inverted profile at the bottom for Case IN12.

7 Experimental Study

7.1 Design of Experiment

In order to evaluate and validate the results obtained from the recently developed inversion algorithm, an experimental test is performed. A three-layer slab is designed to represent the properties of an actual bridge-deck with different layer properties. Three control specimens from the material used in each layer are built to act as control specimens for each layer. The dimension of the main specimen is chosen based on the wave propagation speed in concrete to reduce the effects of boundary reflections. Another factor used in choosing the dimension of the slabs was budget limitation. Table 7.1 gives a description of the test slabs.

Table 7.1 Concrete specimens used in the experimental study

Slab #	Width and Length (feet)	# of Layers	Type of Material	Thickness (inches)
S01	4X6	3	Regular Concrete	3
			Light weight Concrete	3
			Regular Concrete	3
LC01	4X4	1	Regular Concrete	9
LC02	4X4	1	Light weight Concrete	9
LC03	4X4	1	Regular Concrete	9

These specimens are designed and built in the asphalt laboratory of Rutgers University located at Livingstone campus, Edison, NJ. S01 is the main three-layer specimen built to study the wave propagation in layered media using he DECKINVERSE inversion algorithm.

To make lightweight concrete, special expanded glass aggregates are used in the design mix. The technical data sheet for this material is shown in Table 7.2.

Table 7.2 Technical fact sheet for Poraver expanded glass aggregates

(Poraver.com, 2015)

PROPERTIES		STANDARD	PORAVER® STANDARD GRAIN SIZES					PORAVER® SPECIAL GRAIN SIZES	
Grain size	[mm]	ASTM C136	0.1-0.3	0.25-0.5	0.5-1	1-2	2-4	0.04-0.125	4-8
Particle size	[mesh #]		140-50	60-35	35-18	18-10	10-5	400-120	5-5/16"
Fineness modulus			0.66	1.92	2.72	3.81	4.7	*on request*	5.73
Dry loose bulk density	[kg/m³]	ASTM C9/C29M	400 ± 60	340 ± 30	270 ± 30	230 ± 30	190 ± 20	530 ± 70	180 ± 20
	[lb/ft³]		25 ± 3.8	21.2 ± 3.2	16.9 ± 3	14.4 ± 2.1	11.9 ± 1.8	33.1 ± 4.4	11.2 ± 1.7
Apparent density	[kg/m³]	ASTM C128	850 ± 120	680 ± 50	450 ± 50	410 ± 50	350 ± 40	*on request*	300 ± 40
	[lb/ft³]		53.1 ± 8.4	42.5 ± 5.6	28.1 ± 4.4	25.6 ± 3.6	21.8 ± 3	*on request*	18.7 ± 2.7
Compressive strength	[MPa]	EN 13055-1	2.8	2.6	2	1.6	1.4	*on request*	1.2
	[PSI]		406	377	290	232	203	*on request*	174
Water absorption by mass [1]	[Mass. %]	ASTM C128	35	28	20	20	23	*on request*	20
Water absorption by volume [1]	[Vol. %]	ASTM C128	22	15	9	7	7	*on request*	5
Organic impurities		ASTM C40	no injurious compounds					no injurious compounds	
Staining index (index number)		ASTM C641	0					0	
Loss on ignition	[%]	ASTM C114	~1					~1	
Clay lumps and friable particles	[%]	ASTM C142	-	-	-	< 2	< 2	-	< 2
Oversize		EN 13055-1	≤ 10% by mass					≤ 10% by mass	
Undersize			≤ 15% by mass					≤ 15% by mass	

[1] *% absorption determined after 5 minutes submerged in water*

The following data are valid for all grain sizes:									
pH value			9-12					9-12	
Moisture content on delivery			≤ 0.5 %					≤ 0.5 %	
Softening point			approx. 700°C / 1300°F					approx. 700°C / 1300°F	
Color			creamy white					creamy white	
Thermal conductivity	[W/m·K]		-	-	-	-	0.07 [2]	-	0.07 [2]
	[BTU-in/hr-ft²-°F]		-	-	-	-	0.486 [2]	-	0.486 [2]

The strength grades may vary within the tolerance range of bulk densities.
The availability and delivery conditions for special grain sizes will be agreed on an individual basis.

[2] *calculated values DIBt according to approval Z-23.11-114*

PORAVER NORTH AMERICA INC. · 2429 Bowman Street · Innisfil, Ontario, L9S 3V6, Canada
Phone +1 705 431 0022 · Fax +1 705 431 2701 · info@poraver.com · www.poraver.com

Also the design mix suggested by the manufacturer is represented in Table 7.3. For this study 800 kg/m3 density is chosen (the last row in Table 7.3). Other than Poraver

aggregates (1-2mm and 4-8mm), DaraFill air-entraining agent (Figure 7.1) and fly ash are used to obtain the desired lightweight concrete.

Figure 7.1 DaraFill air entertainer agent

The addition of DaraFill generates stable air contents of 15 to 30%, and significantly reduces mix water, and improves flow ability (grace.com, 2015). This also helps to reduce the concrete density by 15- 30%.

Table 7.3 Suggested design mix for Poraver aggregates (Poraver.com, 2015)

poraver by Dennert

* The product information is given in good faith, but without warranty. This also applies to proprietary rights of third parties. The above information does not release from own tests of the products as to their suitability for the intended purpose and procedures. The application, use and processing of our products and the products manufactured by you on the basis of our technical advice are beyond our control and, therefore, entirely your own responsibility.

Lightweight concrete with Poraver® expanded glass

Non-binding guide formulations*

density	guide formulations								characteristics				
	Poraver [5]				cement	water	fillers [1]	additives [3]	density		compressive strength	strength class	thermal conductivity λ
kg/m³	0.5 - 1 mm dm³	1 - 2 mm dm³	2 - 4 mm dm³	4 - 8 mm dm³	CEM I 42.5 R kg	kg	kg	g	wet kg/dm³	105° C kg/dm³	28 d N/mm²		W/(m*K)
300	–	–	875 (166 kg)	–	110	80	–	550	0.6	0.31	0.4		0.08
	–	–	–	800 (136 kg)	125	80	–	500	0.5	0.30	0.8		
400	–	–	820 (156 kg)	–	200	155	–	470	0.49	0.41	2.2		0.11
	–	–	–	800 (136 kg)	225	130	–	500	0.49	0.40	2.0		
	480 (125 kg)	–	480 (91 kg)	–	130	120	–	480	0.48	0.39	2.5		
450 [4]	–	**435 (100 kg)**	–	**620 (111 kg)**	**200**	**125**	–	**250**	**0.51**	**0.44**	**4.4**	**LAC 2**	**0.11** [2]
500	–	–	800 (152 kg)	–	285	160	–	500	060	0.51	4.9		0.13 [2]
	–	–	–	800 (136 kg)	300	160	–	500	0.61	0.50	4.0		
	470 (122 kg)	–	470 (89 kg)	–	195	150	–	470	0.58	0.50	4.8		
600	–	–	800 (152 kg)	–	360	180	–	500	0.70	0.60	6.4		0.16 [2]
	450 (117 kg)	–	450 (86 kg)	–	290	165	–	490	0.67	0.56	7.8		
	–	–	–	800 (136 kg)	400	200	–	500	0.72	0.60	7.0		
700	–	–	800 (152 kg)	–	380	220	60	500	0.81	0.68	11.0		0.18 [2]
	–	–	–	800 (136 kg)	425	230	100	500	0.84	0.70	7.0		
700 [4]	–	**452 (118 kg)**	–	**627 (113 kg)**	**325**	**190**	**60**	**510**	**0.79**	**0.66**	**10.0**	**LAC 5**	**0.18** [2]
800	–	–	800 (152 kg)	–	425	225	95	480	0.90	0.76	11.2		0.21 [2]
	–	200 (46 kg)	200 (38 kg)	400 (68 kg)	425	260	175	500	0.98	0.80	10.0		
800 [4]	–	**452 (104 kg)**	–	**630 (113 kg)**	**360**	**205**	**120**	**500**	**0.91**	**0.78**	**13.0**	**LAC 8**	**0.21** [2]

[1] e. g. fly ash
[2] calclated values DIBt according to technical approval Z. 3.42 - 44
>> thermal conductivities beyond the technical approval are determined DIN 4108
[3] air-entraining agent
[4] formulations ***poraFORM according to technical approval
[5] the bulk density may vary within the tolerance range

:ditor SIK / Author DM

7.2 Construction of Validation Slabs

In order to cast the specimens, a plywood mold was designed and built to house the fresh concrete. Figure 7.2 depicts the molds built for the 4 validation specimens. The molds consist of 5/8” plywood. The walls are supported by pieces of 2X4 at each foot to withstand the forces applied during the casting process. The floor sits on 2X4s spaced one foot apart to act as beams. These beams create a 4-inches gap between the specimen and the ground. This gap is helpful for transporting the slabs with a forklift. Two layers

of mesh reinforcement are used at 2.5” from the top and the bottom of the specimens. In order to keep this mesh in place while pouring, it sits on small pieces of #4 rebar drilled through the plywood.

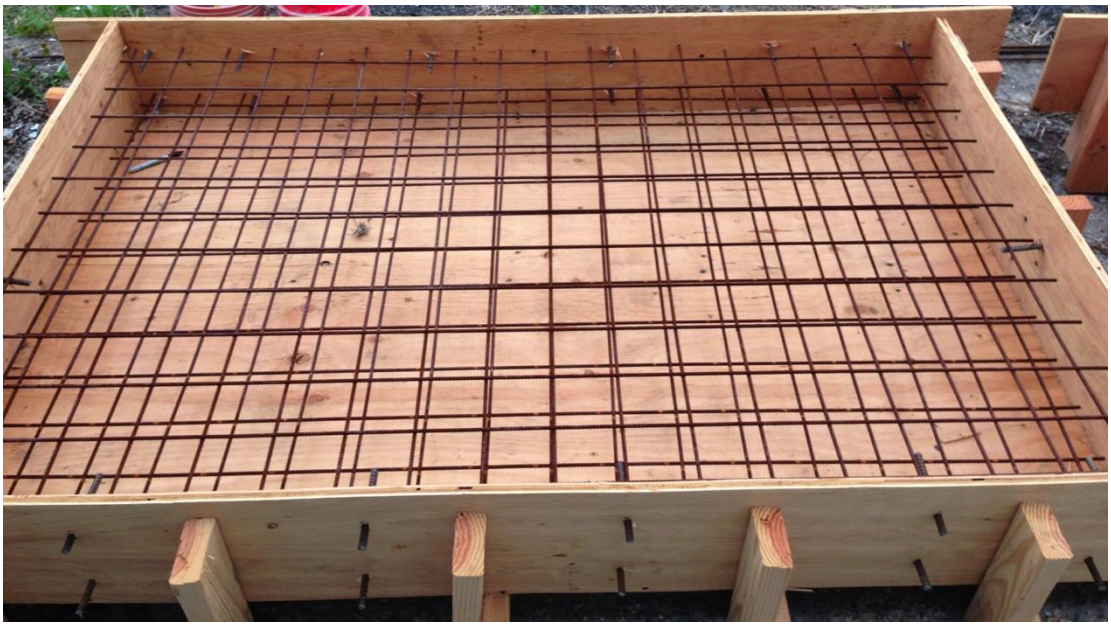

Figure 7.2 Plywood molds for validation specimens

For the layered specimen (S01), the time of casting each layer is an important factor. There should be enough time between each cast so that each layer gains enough strength to withstand pressure from the layer above. On the other hand, if the concrete sits for too long, the new layer cannot properly bond with the old one. To satisfy these conditions S01 was cast over three consecutive days, thus giving approximately one day for each layer to harden. The casting procedure for each layer along and the control specimen is discussed next.

7.2.1 Day 1-Premixed Concrete Delivery

Premixed concrete was delivered from Clayton Concrete, Edison, NJ. The nominal compression strength of the batch was stated as 4000-psi (27.5 MPa). This concrete was used in specimen LC01 and the bottom layer of the S01 specimen. Figure 7.3 shows the casting process for this phase. A hand-held needle vibrator was used for concrete compaction. After the pouring was complete, the surface was smoothed with a 2X4 piece.

Figure 7.3 Casting Process - Day 1

7.2.2 Day 2- Light Weight Concrete Casting

Lightweight concrete was mixed at the Rutgers asphalt laboratory located in Livingstone campus, NJ. As shown in Figure 7.4 the concrete mix consists of two sizes of aggregates (1-2mm and 4-8mm), water, air entertainer, fly ash as filler and cement (fly ash and cement not shown in the picture). These elements were measured and then hand mixed in plastic trays as shown in Figure 7.5. Because of the lightweight aggregates, a power mixer was not used. The higher speed of the power mixer causes the lighter material to float and thereby segregate from the rest of the mix. Specimen LC02 and the second layer of specimen S01 were filled using the design mix mentioned earlier for 800 kg/m^3 density in the manual for Poraver materials.

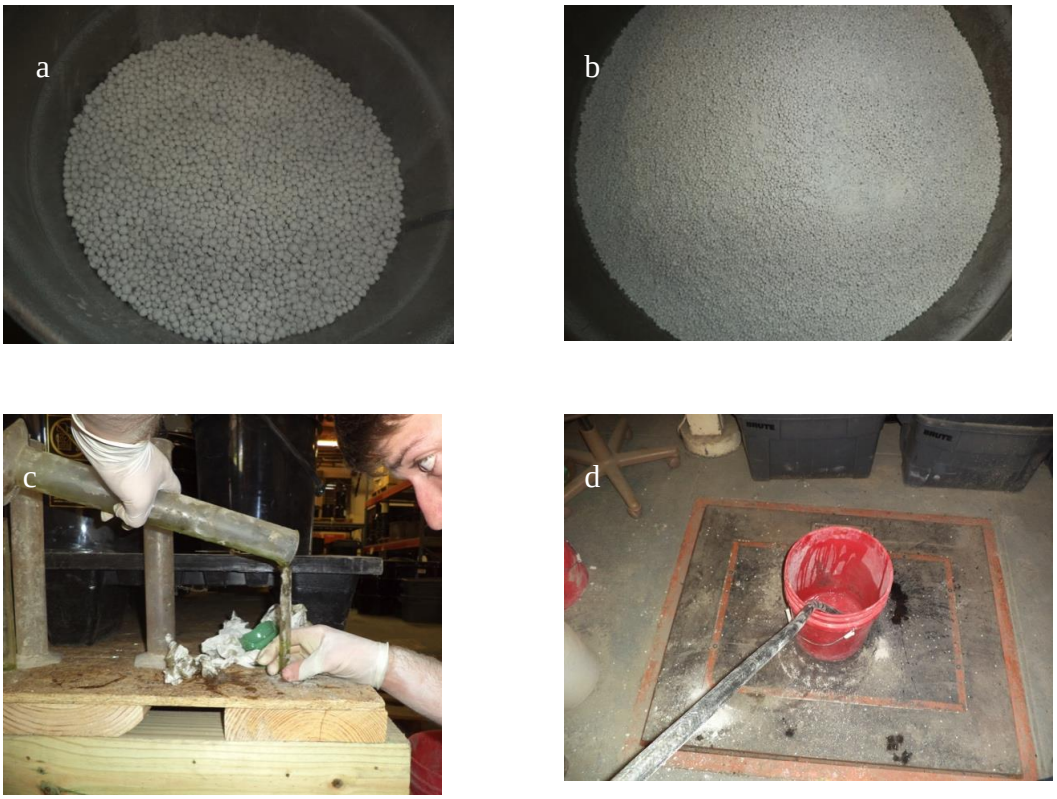

Figure 7.4 a) Coarse aggregate b) Fine aggregate c) Air-entertainer c) water

Figure 7.5 Light weight concrete mixing procedure-Day 2

7.2.3 Day 3- Premixed Concrete Delivery

In day 3 the premixed concrete was delivered from the same vendor, with the same nominal compression strength (27.5 MPa). This concrete was used in specimen LC03 and the top layer of the S01 specimen. Figure 7.6 shows the casting process for this phase.

Figure 7.6 Casting Process – Day 3

7.3 Experimental Test Setup

The down side of using the MASW method is that the testing procedure is lengthier and the testing setup is more expensive because of the number of sensors. In order to overcome the cost issue for this test, only 2 sensors and one impact source, were used. Experimental tests were performed using Agilent DAQ model 35670A (Figure 7.7). The Key specifications of this device are as follows (keysight.com):

Figure 7.7 Agilent DAQ Model 35670A (keysight.com)

- 102.4 kHz at 1 channel, 51.2 kHz at 2 channel, 25.6 kHz at 4 channel
- 100, 200, 400, 800 and 1600 lines of resolution
- 90 dB dynamic range, 130 dB in swept-sine mode

Since 2 channels were utilized the highest frequency range would be 51.2 kHz. The two channels are filled with PCB 352A60 sensors. The specifications of these sensors are illustrated in Table 7.4. The sensors are very sensitive and can pick up anything between the ranges of 5-60 kHz. Because of the relatively rough surface in concrete, the ideal

bounding between the surface and the sensor cannot be achieved. The highest recorded frequency is therefore expected to be lower than the sensors range.

Table 7.4 PCB 352A60 Specifications (PCB.com, 2014)

	ENGLISH	SI
Performance		
Sensitivity (±15 %)	10 mV/g	1.02 mV/(m/s²)
Measurement Range	±500 g pk	±4905 m/s² pk
Frequency Range (±3 dB)	5 to 60000 Hz	5 to 60000 Hz
Electrical Filter Corner Frequency	45 kHz	45 kHz
Electrical Filter Roll-off	10 dB/decade	10 dB/decade
Resonant Frequency	≥95 kHz	≥95 kHz
Broadband Resolution (1 to 10000	0.002 g rms	0.02 m/s² rms
Non-Linearity	≤1 %	≤1 %
Transverse Sensitivity	≤5 %	≤5 %
Environmental		
Overload Limit	±5000 g pk	±49050 m/s² pk
Temperature Range	-65 to 250 °F	-54 to +121 °C
Base Strain Sensitivity	≤0.05 g/με	≤0.49 (m/s²)/με
Electrical		
Excitation Voltage	18 to 30 VDC	18 to 30 VDC
Constant Current Excitation	2 to 20 mA	2 to 20 mA
Output Impedance	≤100 Ohm	≤100 Ohm
Output Bias Voltage	8 to 12 VDC	8 to 12 VDC

Discharge Time Constant	0.02 to 0.06 sec	0.02 to 0.06 sec
Spectral Noise (10 Hz)	160 µg/√Hz	1570
Spectral Noise (100 Hz)	40 µg/√Hz	390 (µm/sec2)/√Hz
Spectral Noise (1 kHz)	15 µg/√Hz	147 (µm/sec2)/√Hz
Spectral Noise (10 kHz)	10 µg/√Hz	98 (µm/sec2)/√Hz
Physical		
Size - Height	0.81 in	21.6 mm
Weight	0.21 oz	6.0 gm
Sensing Element	Ceramic	Ceramic
Size - Hex	3/8 in	3/8 in
Sensing Geometry	Shear	Shear
Housing Material	Stainless Steel	Stainless Steel
Sealing	Welded	Welded Hermetic
Electrical Connector	5-44 Coaxial	5-44 Coaxial
Electrical Connection Position	Top	Top
Mounting	Integral Stud	Integral Stud
Mounting Thread	10-32 Male	10-32 Male

There are two ways to simulate the true multi-channel results using only two sensors:

1. In one method the source location is fixed along with one of the sensors. The other sensor is moved step by step to the specific sensor locations. At each location the hammer is triggered and the results are recoded. The fixed sensor is used as a reference. The DAQ starts recording once the fixed sensor reaches

a certain level of amplitude. Each record is normalized to the maximum amplitude.

2. In the second method the source is moved along with the control sensor. The down side of this method is that it takes longer and is not as accurate as the previous method. Every time the source is moved, a number of initial triggers are needed to stabilize the results. The dust and loose particles at the impact location are the reason for the impact calibration. Calibration significantly decreases the speed of the testing.

Sensors are fixed using petroleum wax or super glue. Both methods were tested for this study. The fixed source method was chosen, as it had more consistent records at each try. Figure 7.8 shows the experimental test setup in the top, a step of recording in fixed source method in the middle and a step of fixed sensor method at the bottom. As seen in the pictures, the PSPA device is used as the impact source. The signal is recorded when the control sensor detects a certain level of amplitude.

a

b

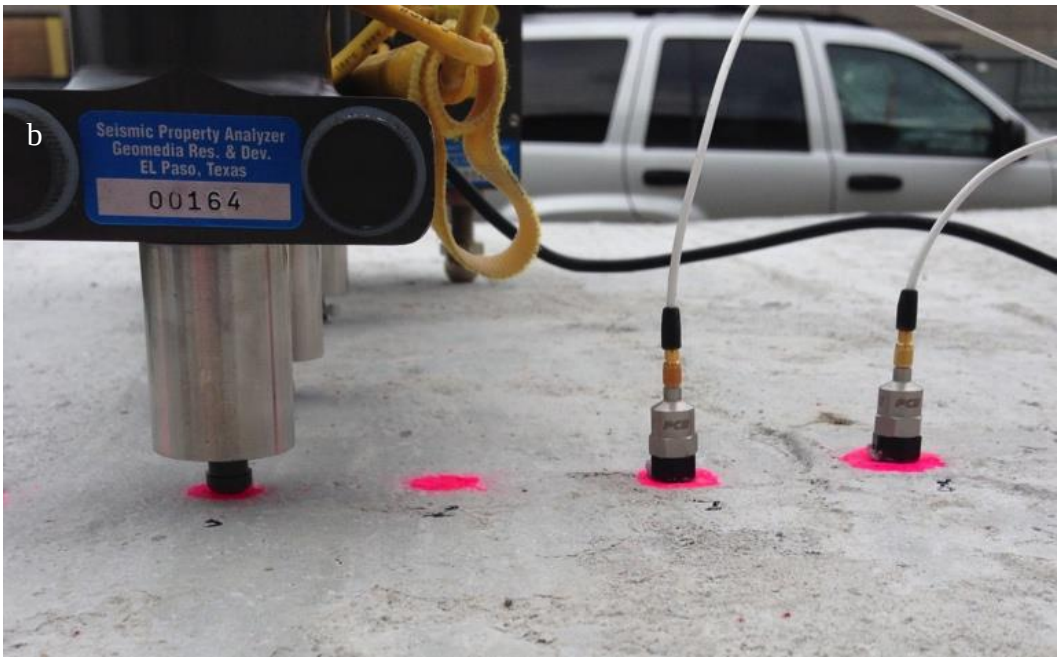
Seismic Property Analyzer
Geomedia Res. & Dev.
EL Paso, Texas
00164

Figure 7.8 a)Experimental test setup b)Recording with fixed source c) Recording with fixed sensor.

Figure 7.9 shows the time histories recorded at 32 sensor locations, each of which was placed 5 cm apart using the fixed source method.

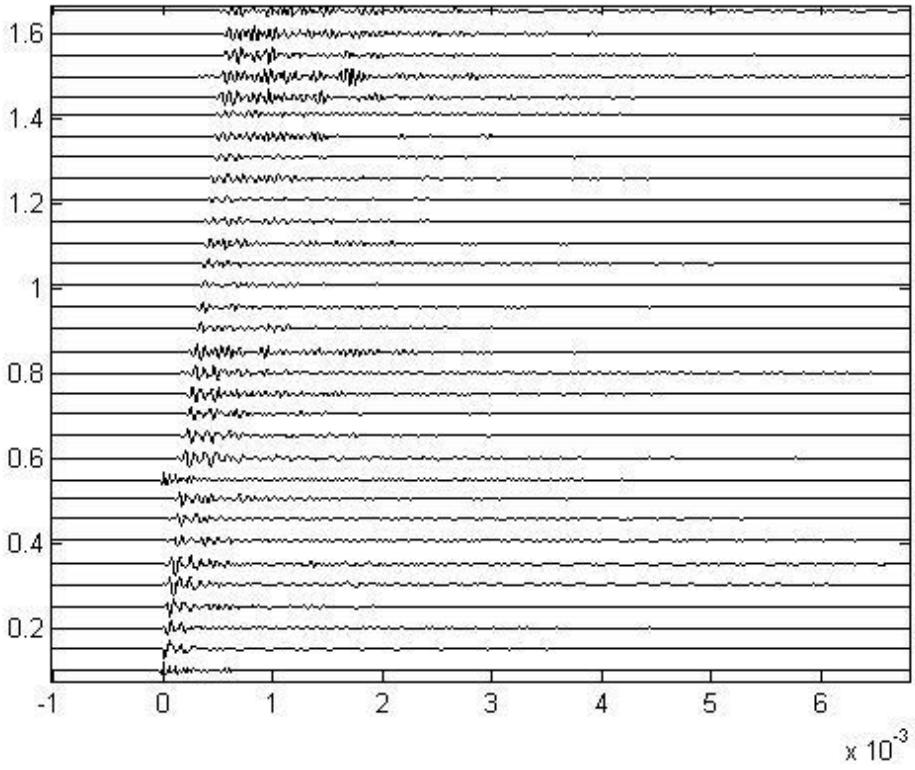

Figure 7.9 Time histories at each sensor location by using the fixed sensor method. The Y-axis shows the distance from the source in meters where the X-axis represents time in seconds

Figure 7.10 shows the normalized spectra of the 32 time histories in a stacked format. The frequency content of the records seems similar except for locations at 10 cm and 55cm apart from the source. This could be either because of the loose material at the impact location or because of insufficient bonding between the sensors and the concrete surface. These two records were excluded from the analysis.

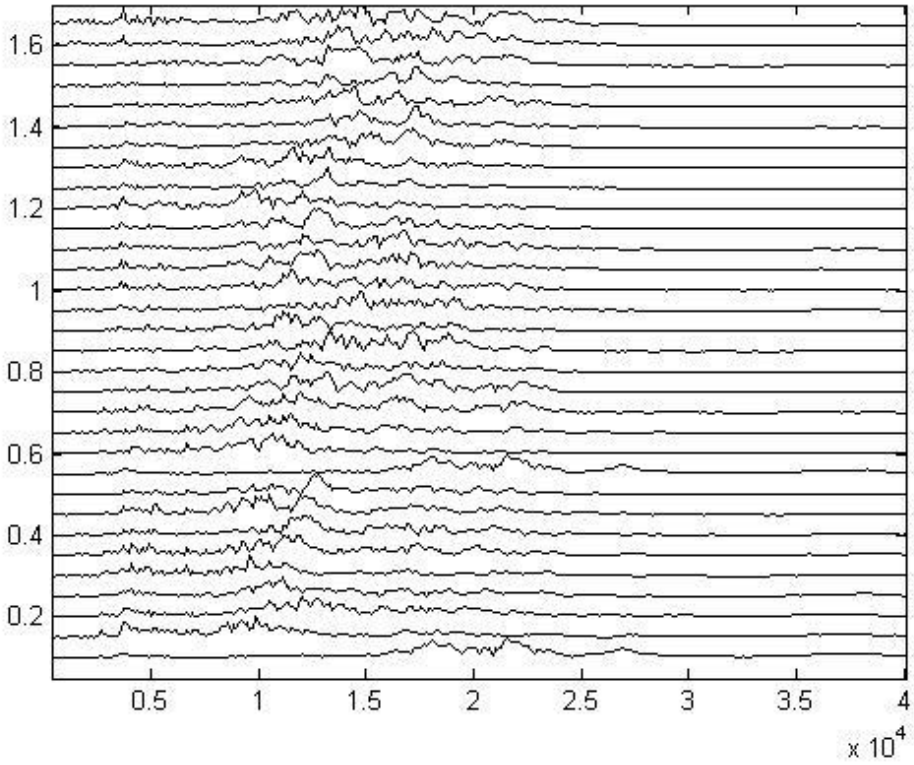

Figure 7.10 Normalized spectra of the time histories at different sensor locations

7.4 Results and Discussion

Using the SASW method on the control specimens, the surface-wave velocity of each layer is calculated. Using the PSPA the control specimens are measured for the elastic modulus. Table 7.5 shows modulus measurement results on the control specimens along with the standard deviation, mean and median for each specimen. Median results are chosen as reference points for to compare with the inversion results. Also Figure 7.11 to Figure 7.13 show the screen shots of PSPA software for the median measurement in each specimen.

Table 7.5 PSPA measurements on the control specimens

Test #	Bottom Layer (Ksi)	Middle Layer(ksi)	Top Layer (ksi)
1	4040	890	5320
2	4670	760	5520
3	3700	560	5170
4	4120	1050	5010
5	4001	930	4980
6	3670	850	5150
7	4820	910	5290
Std	411	143	174
Mean	4145	850	5205
Median	4040	890	5170

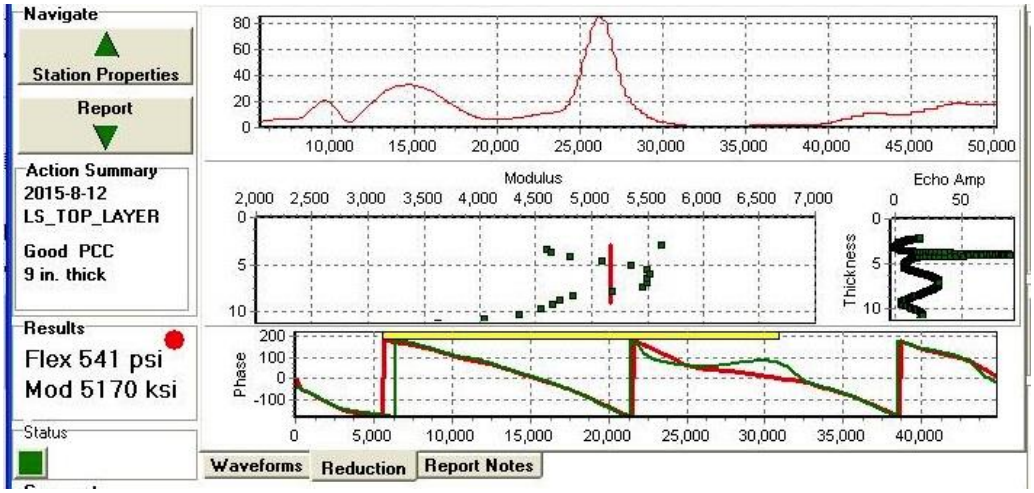

Figure 7.11 Median of modulus measurements for LC01 Specimen

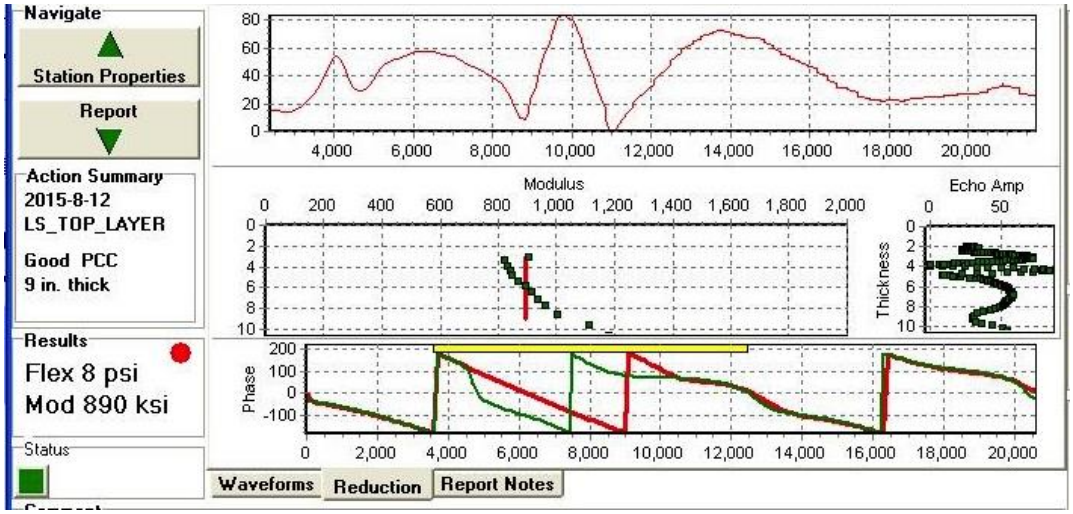

Figure 7.12 Median of modulus measurements for LC02 Specimen

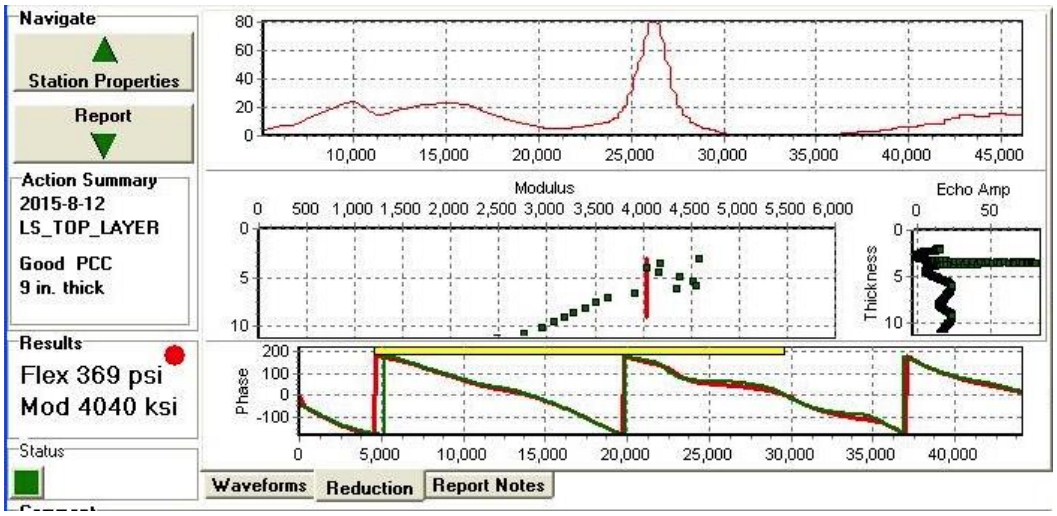

Figure 7.13 Median of modulus measurements for LC03 Specimen

Based on these results and density measurements from cylindrical specimens, the layer parameters are presented in Figure 7.14. The measured density of the middle layer is close to the design mix specification used, which is almost one third of regular concrete.

Table 7.6 The Specimen Layer Properties Based on the Measured Results

Layer	Type of Material	Layer Thickness/ Total Thickness	Measured Modulus (ksi)	Measured Modulus (MPa)	Measured Density ($1/m^3$)	Measured shear-wave velocity (m/s)
Top	Premixed Concrete (f_c =4000psi)	1/3	5170	35,655	2,330	2,525
Middle	Light weight Concrete	1/3	890	6,138	854	1,731
Bottom	Premixed Concrete (f_c =4000psi)	1/3	4040	27,862	2,258	2,268

Using the phase-shift method the dispersion surface is plotted in Figure 7.14. The overall dispersion surface seems noisier than FEM results due to the environmental and instrumental noise introduced in experimental tests.

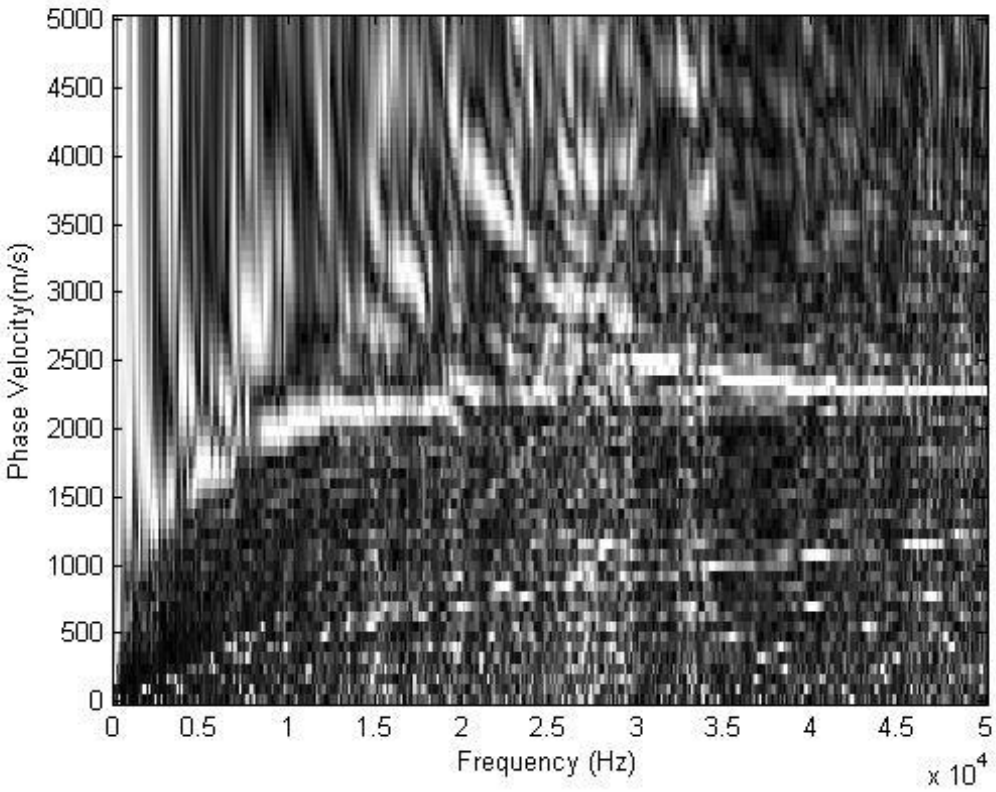

Figure 7.14 Dispersion surface of the fixed source experiment

Next in Figure 7.15 the dispersion surface is compared to the inverted and the reference dispersion surface. In the lower frequency range the experimental result is very noisy. This area is marked with red on the left side of Figure 7.15. Since the bottom layer properties are directly related to this frequency range this can affect the accuracy of the results for this layer. The overall trend of the dominant mode is clear in the results and so is the higher frequency content. These areas are related to the top and middle layers properties. There is also moderate amount of noise present in the mid-frequency range.

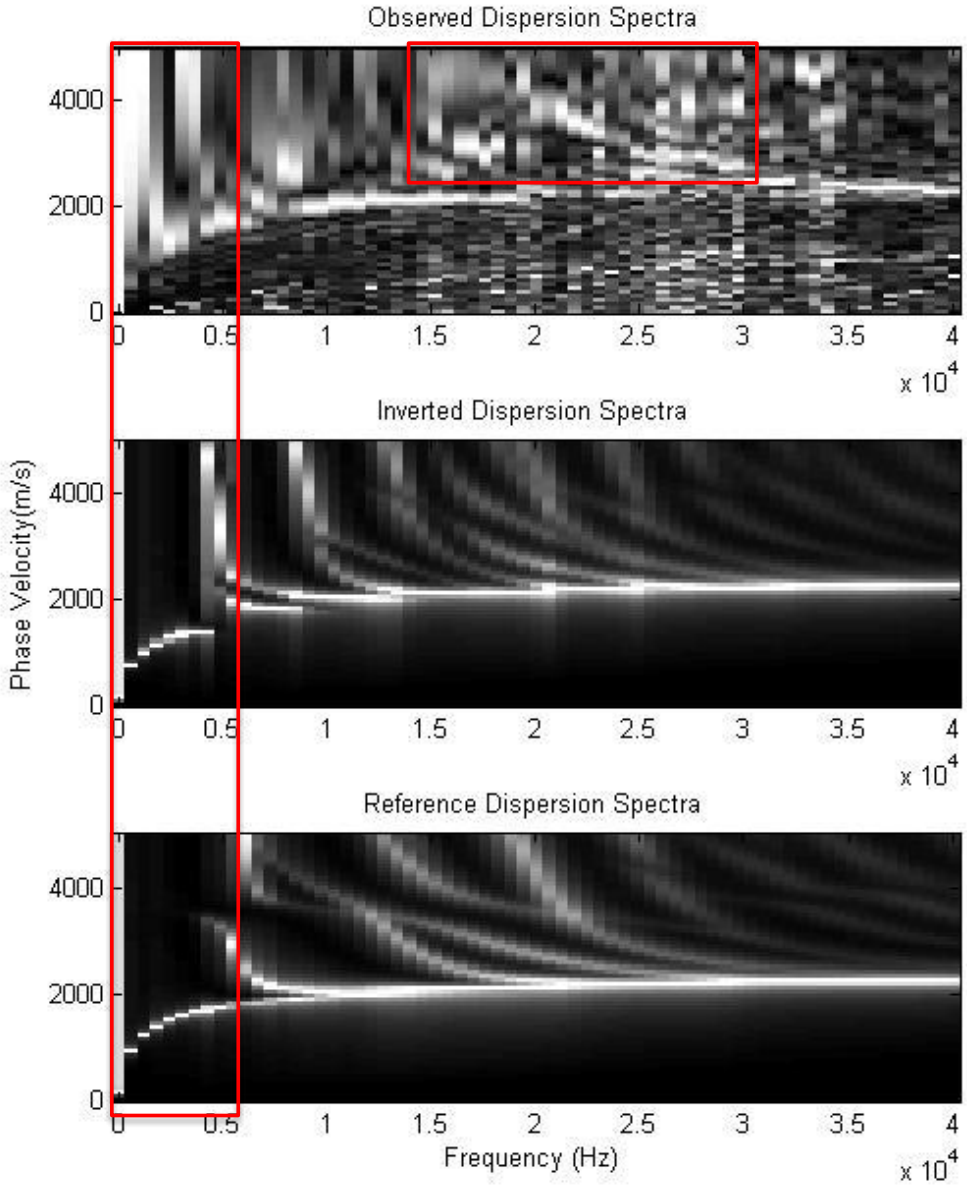

Figure 7.15 Comparison between the observed, inverted and the reference dispersion spectra

Table 7.7 shows the results from DECKINVERSE algorithm compared to the measured values.

Table 7.7 Inverted Layer parameters vs the expected results

Expected shear-wave velocity (m/s)	Inverted shear-wave velocity (m/s)	Inverted Thickness ratio
2,525	2500	1/3
1,731	1750	1/3
2,268	1250	1/3

The top and middle layer's velocity is inverted accurately, however the bottom layer configuration still proves to be challenging. Compared to the traditional method this method provides more details for layer properties. Using the PSPA the average modulus is calculated for each test location. No information is given regarding the change of modulus throughout the thickness. This method divides the thickness into three hypothetical layers with variable thicknesses and calculates the shear-wave velocity for each one.

8 Closure

8.1 Conclusion

Based on the results obtained from this research the following can be concluded:

1. Compared to SASW method use of multiple sensors results in presentation of results in terms of the dispersion surface instead of dispersion curve. This leads to the separation of Lamb modes in the dispersion surface. Use of dispersion surface provides more for the inversion process.
2. MASW dispersion analysis methods enable the automation of data analysis after data acquisition. The field data can be processed without any user input. This is particularly important when multiple dominant modes of propagation are present.
3. The use of full dispersion surface allows for the inversion process to be more accurate and sensitive to model parameters. Based on the parametric study each model parameter has a distinct effect on the dispersion surface. This allows for identification of more model parameters though the inversion process.
4. The proposed inversion algorithm is fast and accurate enough for practical purposes. In the past, the main concern regarding the use of multiple sensors has been the computational time for the inversion process (Ryden & Park, 2006). With this method the inversion simultaneously with the data collection. This is mainly due to the segmentation of the data space in the database and

pre-calculation of dispersion surfaces. At every run the algorithm minimizes the error function without the lengthy solution for the forward problem. Further optimization is done by utilizing the signatures present in the dispersion surface.

8.2 Recommendation for Future Work

The following describes the author's recommendation for further improvement of multi sensor surface-wave based testing methods in bridge decks:

1. Improvement of the inversion algorithm: As shown in the inversion example IN05, when there is high concentration of noise present in the dispersion surface, the result of inversion algorithm is not accurate. One solution to this problem is to develop smart pre-filtering of the dispersion surface prior the inversion process. This filter would exclude specific areas of noise and artifacts from the error function. Figure 8.1 shows the high noise and artifacts areas in the observed dispersion surfaces, marked by red boxes, for example IN05.By removing all or parts of these areas the inversion results should be improved.

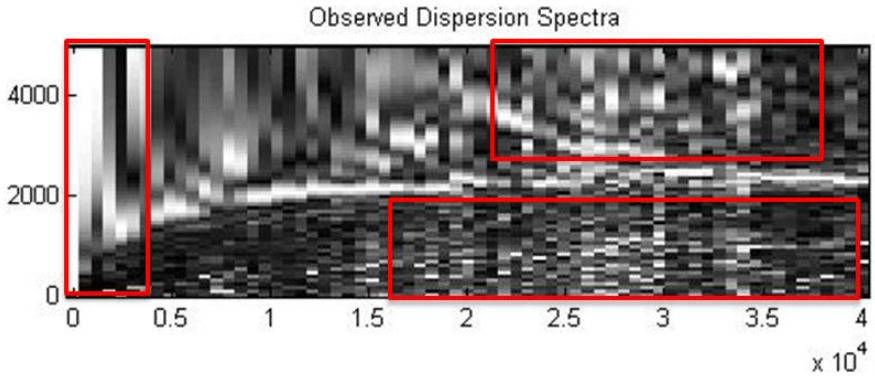

Figure 8.1 Potential high noise areas to be excluded in the inversion process marked with red on dispersion surface

2. Construction of a full-scale multi sensor array for a more comprehensive study of the DECKINVERSE algorithm: Using an array of sensors to gather the information at once for all sensor locations is expected to reduce noise in the dispersion surface. It will also increase the speed of data collection. Recording the time histories at once can potentially improve the accuracy of the inversion process.
3. An experimental study on actual bridge decks: The testing condition on different bridge decks can introduce unforeseen practical issues in the testing procedure. Therefore, the proposed method should be implemented on a variety of concrete bridge decks and the inversion process adjusted for those.

9 Bibliography

ABAQUS. (2013). Abaqus analysis user's manual. *Version 6.13-3*. Providence, RI, USA.

Achenbach, J. D. (1973). *Wave propagation in elastic solids.* Amesterdam: North Holland.

Al-Hunaidi, M. O. (1998). Evaludation-based genetic algorithms for analysis of nondestructive surface wave tests on pavements. *NDT&E International, 31*(4), 273-280.

Aoud, M. (1993). *Evaluation of flexible pavements and subgrades using the spectral analysis of surface waves (SASW) method.* Austin, Texas: Uinversity of Texas.

Bathe, K. J. (1996). *Filnite elemet procedures.* Englewood, NJ: Prentice-Hall, Inc.

Bolt, D. A. (1976). *Nuclear explosions and earthquakes.* San Francisco, CA: W. H. Freeman and Co.

Cohen, M. J. (1983). Silent boundary methods for transient analysis. *Computational Methods for Transient Analysis*, 301-360.

Cook, R. D. (2002). *Concepts and applications of finite element analysis.* John Wiley & Sons, Inc.

Cook, R. D. (2002). *Concepts and applications of finite elements.* Hoboken, NJ: John Wiley & sons Inc.

Elmore, C. E., & Heald, M. A. (1969). *Physics of waves.* McGraw-Hill Book Company.

Gabriels, P., Snieder, R., & Nolet, G. (1987). In situ measurements of shear-wave velocity in sediments. *Geophysical Prospecting*, 187-196.

Ganji, V., Gucunski, N., & Maher, A. (1997). Detection of underground obstacles by SASW method: numerical aspects. *Journal of Geotechnical and Geoenviromental Engineering, ASCE,* 212-219.

Ganji, V., Gucunski, N., & Nazarian, S. (1998). Automated inversion procedure for spectral analysis of surface waves. *Journal of Geotechnical Engineering, ASCE, 124*(8), 757-770.

grace.com. (2015). *DaraFill*. Retrieved August 2, 2015, from https://grace.com/construction/en-my/Documents/DaraFill.pdf

Graff, K. F. (1975). *Wave motion in elastic solids.* London: Oxford University Press.

Gucunski, N., & Nazarian, S. (2010). Material Characterization and Condition Assessment of Reinforced Concrete. *Structures Congress* (pp. 429-439). Orlando, Florida: ASCE.

Gucunski, N., & Woods, R. (1991). Inversion of Rayleigh wave dispersion curve for SASW test. *5th International Conference in Soild Dynamics and Earthquake Engineering*, (pp. 127-138). Karlsruhe, Germany.

Gucunski, N., & Woods, R. (1992, January). Numerical simulation of SASW test. *Soil Dynamics and Earthquake Engineering*, 213-227.

Gucunski, N., & Woods, R. D. (1991). Use of Rayleigh modes in interpretation of SASW test. *Second International Conference on Recent Advances in Geotechnical Earthquake Engineering and Soil Dynamics*,, (pp. 1399-1408). St. Louis, Missouri.

Gucunski, N., Consolazio, G., & Maher, A. (2000). *Concrete bridge deck delamination detection by integrated ultrasonic methods.* Toronto: ACI Meeting.

Gucunski, N., Nazarian, S., Wiggenhauser, H., Kutrubes, D., Imani, A., Romero, F., et al. (2013). *Nondestructive testing to indentify concerte bridge deck deterioration.* Washington, D.C.: TRB (Transportation Research Borad of National Academy).

Gucunski, N., Slabaugh, G., Wang, Z., Fang, T., & Maher, A. (2007). Visualization and interpretation of impact echo data from bridge. *Journal of Transportation Research*.

Hadidi, R., & Gucunski, N. (2003). Inversion of SASW dispersion curve using numerical simulation. *Symposium on the application of Geophysics to Engineering and Enviromental Problems* (pp. SUR-01). San Antonio, Texas: SAGEEP.

Hanskell, N. A. (1953). Dispersion of surface waves on multilayered media. *Bulletein of Seismic Scociety of America, 43*, 17-34.

Heisey, J., Stokoe II, K. H., & Meyer, A. H. (1982). Moduli of pavement systems from spectral analysis of surface waves. (pp. 22-31). Washington D.C.: Transportation Research Board (TRB).

Hughes, T. J. (1987). Finite element method- linear static and dynamic finite eLement analysis. Engleweed, NJ, USA.

Kausel, E. (1998). Local transmitting boundaries. *Journal of Engineering Mechanics*, 1011-1027.

Kausel, E. (2006). *Funamental soutions in elastodynamics.* New York: Cambridge University Press.

Kausel, E., & Roesset, J. M. (1981). Stiffness matrices for layered soils. *Bull. of Seismological Society of America*, 1743-1741.

keysight.com. (n.d.). *35670A FFT Dynamic Signal Analyzer, DC-102.4 kHz*. Retrieved August 1, 2015, from http://www.keysight.com/en/pd-1000001335:epsg:pro-pn-35670A/fft-dynamic-signal-analyzer-dc-1024-khz?&cc=US&lc=eng

Kim JH, K. H.-G. (2008). Nondestructive evaluation of elastic properties of concrete using simulation of surface waves. *Computer-aided Civil and Infrastructure Engineering, 23*(8), 611-24.

Kim, J. H., & Kwak, H.-G. (2008). Nondestructive evaluation of elastic properties of concrete using simulation of surface waves. *Computer-Aided Civil and Infrastructure Engineering, 23,* 611-624.

Knopoff, L. (1964). A matrix method for elastic wave problems. *Bulletin of Seismological Society of America*, 431-438.

Kolsky, H. (1963). *Stress waves in solids.* New York: Dover Publications.

Lamb, H. (1917). On waves in an elastic plate. *Proceeding of Royal Society of London, 93*, 114-128.

Liu, G. Q. (2003). A non-reflecting boundary for analyzing wave propagation using the finite element method . *Finite Element Analysis and Design, 39*, 403-417.

Lowe, M. (1995). Matrix techniques for modeling ultrasonic waves in multilayered media. *IEEE Transactions on Ultrasonics, Ferroelectrics, and Frequency Control*, 525-542.

Lysmer, J. K. (1969). Finite dynamic model for infinite media. *Journal of Engineering Mechanics*, 859–877.

McMechan, G., & and Yedlin, M. (1981). Analysisof dispersion waves by wave field transformation. *Geophysics, 46*(6), 869-874.

Moro, G. D., Pipan, M., Forte, E., & Finetti, I. (2003). Determination of Rayleigh wave dispersion curves for near surface application in unconsolidated sediments. *Society of Exploration Geopgysicsts*, 1247-50.

Moser, F., Jacobs, L. J., & Qu, J. (1999). Modeling elastic wave propagation in waveguides with the finite element method. *NDT&E International, 32*, 225–34 .

Nazarian, S. (1984). *In situ determination of soil deposits and pavement systems by spectral analysis of surface waves method.* Austin, Texas: University of Texas.

Nazarian, S., & Stokoe II, K. H. (1984). In-Situe shear wave velocityfrom spectral analysis of surface waves. *8th world Conference on Earthquake Engineering, 3*, pp. 31-38. San Francisco, CA.

Nazarian, S., Baker, M., & Crain, K. (1997). Assessing quality of concrete with wave propagation techniques. *Materials Journal, 94*(4), 296-306.

Nazarian, S., Stokoe II, K. H., & Hudson, W. R. (1983). Use of spectral analysis of surface waves method for determination of moduli and thicknesses of pavement

systems. *Transportation Research Record* (pp. 38-45). Washington D.C.: TRB 930.

Nazarian, Stokoe II, K. H., Briggs, R. C., & Rogers, R. (1987). Determination of pavement layer thickness and moduli by SASW method. *Transportation Research Record* (pp. 133-150). Washington D.C.: 1196.

Ólafsdóttir, A. E. (2014). *Multichannel analysis of surface waves: methods for dispersion analysis of surface wave data.* Reykjavík, Iceland: University of Icland.

Park, C. B. (n.d.). *Inversion analysis*. Retrieved from masw: http://www.masw.com

Park, C. B., Miller, R. D., & Xia, J. (1998). Ground roll as a tool to image near-surface anomoly. *Kansas Geological Survey.* 68th Anual Interanet Mtg. Soc. Expl. Gephys.

Park, C. B., Miller, R. D., & Xia, J. (1998). Imaging dispersion curves of surface waves on multi-channel record. *Kansas Geological Survey*, 1377-1380.

Park, C. B., Miller, R. D., & Xia, J. (2001). Offset and resolution of dispersion curve in multichannel analysis of surface waves (MASW). *Proceedings of SAPEEG*, (p. SSM$). Denver, colorado.

PCB.com. (2014). *PCB Electronics*. Retrieved May 15, 2014, from http://www.pcb.com/products.aspx?m=352A60

Poraver.com. (2015). *Poraver Expanded Glass*. Retrieved from http://www.poraver.com/us/products/technical-data/

Press, W. H., Flannery, B. P., Teukolsky, S. A., & Vetterling, W. T. (1986). *Numerical receips- the art of sceintific computing.* Cambridge , MA: Cambrige Univeristy Press.

Richart, F. H. (1970). *Vibrations of soils and foundations* . Englewood Cliffs, New Jersey: Prentice-Hall Inc .

Roesset, J. M., Chang, D. W., Stokoe II, K. H., & Auoad, M. (1990). Modulus and thikcness of the pavement surface layer from SASW tests. *Transportation Research Records*, 53-63.

Rose, L. J. (2004). *Ultrasonic waves in solid media.* Cambridge University Press.

Ryden, N. (2004). *Surface wave testing of pavement.* Lund: Lund University.

Ryden, N., & Park, C. B. (2006). Fast simulated anealing inversion of surface waves on pavement using phase velocity spectra. *Geophysics, 71*(4), 49-58.

Ryden, N., Choon, P. B., & Miller, R. D. (2003). Lamb wave analysis for non-destructive testing of concrete plate structures. *Symposium on the Application of Geophysics to Engineering and Environmental Problems* (p. INF03). San Antonio,Tx: SAGEEP.

Ryden, N., Park, C. B., & Miller, R. D. (2003). Lamb wave analysis for non-destructive testing of concrete plate structures. *Symposium on the Application of Geophysics to Engineering and Environmental Problems* (p. INF03). San Antonio,Tx: SAGEEP.

Ryden, N., Park, C. B., Ulriksen, P., & Miller, R. D. (2004). Multimodal approach to seismic pavement testing. *Journal of Geotechnical and Geoenvironmental Engineering, ASCE, 130*(6), 636-645.

Sansalone, M. C. (1987). A finite element study of the interaction of transient stress waves with planar flaws. *Journal of Research of the National Bureau of Standards, 92*(4), 279-290.

Sansalone, M., Carino, N. J., & Hsu, N. N. (1987, July-August). A finite element study of transient wave propagation in plates. *Journal of Research of the National Bureau of Standards, 92*(4), 267-278.

Sevensson, M. (2001). *Application of SASW technique in geotechnical in-situ testing.* Lund, Sweden: LTH, Lund University.

SHRP 2 Renewal Research S2-R06A-RR-1. (2013). *Nondestructive testing to indentify concerte bridge deck deterioration.* Washington D.C: TRB (Transportation Research Borad of National Academy).

Stokoe II, K. H., & Santamarina, J. C. (2000). Seismic wave based testing in geotechnical engineering. *GeoEng 2000.* Melbourne, Australia.

Stokoe II, K. H., Wright, S. G., Bay, J. A., & Roesset, J. M. (1994). Characterization of geotechnical sites by SASW method in geophysical characterization of sites. *ISSMFE Technical Commitee #10*.

Tarantola, A. (2005). *Inverse problem theory and methods for model parameter estimation.* Paris, France: Society for Industarial and Applied Mathematics.

Thomson, W. T. (1950). Transmission of elastic waves thorugh a stratified medium. *Journal of Applied Physics, 21,* 89-93.

Williams, T. P., & Gucunski, N. (1995). Neural networks for backcalculation of moduli from SASW test. *J. Comp. In Civ. Engrg., 9*(1), 1-8.

Wolf, J. P. (1985). *Dynamic soil-structure interaction.* Englewood Cliffs, N.J.: Prentice-Hall.

Wu, H., Wang, I., Abdallah, I., & Nazarian, S. (2002). A rapid approach to interpretation of SASW results. *Proceedings of 6th BCRA Conference,* (p. T.8.18). Lisbon, Portugal.

Xia, J., Miller, R. D., & Park, C. B. (1999). Estimation of near-surface shear-wave velocity by inversion of Rayleigh waves. *Geophysics, 64*(3), 691-700.

Zerwer, A. C. (2002). Parameter estimation in finite elemnt simulation of Rayleigh wave. *Journal of Geotechnical & Enviromental Engineering, ASCE, 128*(3), 250-261.

Zhang, S. X., & Chan, L. S. (2003). Possible effects of misidentified mode number on Rayleigh wave inversion. *Journal of Applied Geophysics, 64,* 691.